UNIVERSITÉ DE STRASBOURG

ÉCOLE DOCTORALE 182

Institut Charles Sadron

THÈSE présentée par :

Friedrich WALZEL

soutenue le : **04 Novembre 2024**

pour obtenir le grade de : **Docteur de l'Université de Strasbourg**

Discipline/ Spécialité : Physique

From interacting bubbles and drops to soft capsules: shape, mechanics and stability analysis

THÈSE dirigée par :

M. CHARITAT Thierry	Professeur, Institut Charles Sadron, Université de Strasbourg, France
Mme DRENCKHAN Wiebke	Directrice de recherches CNRS, Institut Charles Sadron, Université de Strasbourg, France

RAPPORTEURS :

Mme QUILLIET Catherine	Maitre de conférences, Interdisciplinary Laboratory of Physics, Université de Grenoble, France
M. RAUFASTE Christophe	Professeur, Institut de Physique de Nice France, Université de Côte d'Azur, France

---

AUTRES MEMBRES DU JURY :

M. BUTT Hans-Jürgen	Professeur, Max Planck Institute for Polymer Research, Johannes Gutenberg University of Mainz, Germany
M. HEBRAUD Pascal	Directeur de recherches, CNRS, Institut de Physique et Chimie des Matériaux de Strasbourg, Université de Strasbourg, France

Acknowledgments

The three years of my doctorate passed very quickly. Mainly because there were always new things to understand and discover. The atmosphere was very open and pleasant, with plenty of room for discussion and different opinions. I would like to thank the Institute Charles Sadron and my two teams MIM and MCUBE for this. My special thanks go to my two supervisors, Wiebke Drenckhan and Thierry Charitat. Thank you for showing me the way to become a scientist, and for all the advice and the good working atmosphere during this three years.

Many thanks also to Pierre Muller and all the advice and careful reading of my papers. Thanks to Leandro Jacomine and your help for all the performed experiments. Many thanks to Jonathan Dijoux, without whom there would be no double droploon experiments today. It was a pleasure exchanging news about the machine with you every day. Thanks to Elodie, Graith, Andres, Luca and Qiwei, the interns who worked with me and helped me to perform all this experiments. Thanks to Alice Requier, who had just as important a part in the catenoid work as I did.

Thanks to Damian Favier and Antoine Egele for 3D printing and handicrafts, which made many of my experiments only possible. Thanks to the Atelier mecanique with Francois Coutier and Christophe Lambour.

Many thanks to Jan Kierfeld and Felix Kratz for my visit to Dortmund and the many discussions and good advice.

Many thanks to the administration of ICS, especially to Virginie Oberle and Odile Lemble and your help with my contracts and missions.

Thanks to all the people of MIM, MCUBE, BJC..., you made this three years in Strasbourg to an awesome time and helped me to become a professional Babyfoot player.

Many thanks also to my family, without which I would probably never have got this far. Finally, many thanks to you Mondane for always being there for me.

Contents

Chapter 1

Introduction

Contents

1.1 Motivation

Foams and emulsions are structures with a continuous and a dispersed phase. Foam has a liquid continuous phase and a dispersed gaseous phase, the bubbles. An emulsion consists of two immiscible liquids, one being the continuous phase and the other the dispersed phase (the drops). Foams and emulsions are widely used in applications and industrial processes, such as in food industries, personal care and cosmetic products, in agrochemicals, pharmaceuticals, paints, oil industries, mining industries and recycling processes, to mention only a few. They are also frequently observed in nature, for example at the coasts after a storm in the presence of plankton, at an active volcano or in animal products like milk. It is therefore crucial to understand their properties [4, 5, 6, 7, 8].

Foams and emulsions have many advantageous properties like the macroscopic yield stress behavior, good thermal insulation, high sound absorption, the low continuous volume fraction in comparison to the total volume, the self assembly of bubbles or drops in a foam or emulsion, etc.. With help of solidification methods, some of these properties are conserved in solid foams. This extends the range of applications, for example for building materials. Other properties play a greater role there, such as the Young's modulus or the stiffness. However, this brings to light a major disadvantage, the small compression modulus and stiffness against deformation of foams. It is related to the characteristic structure of the continuous phase which is mainly defined by Plateaus' and Young-Laplace laws, discussed in more detail in Section 1.2. This makes solid foams less attractive for many applications. By modifying the bubble/bubble or drop/drop interactions in a

foam or emulsion, new structures with new properties would be accessible, which could use the advantages of foams/emulsions by minimising their disadvantages. The ERC Consolidator Grant (agreement 819511 METAFOAM) aims to understand with different model systems the influence of elasticity, adhesion and friction in interplay with interfacial tension on the final structures. Subsequently, the knowledge gained will be used to produce meta-materials with the desired material properties. The effect of mechanical self-assembly will be used in order to work reproduce-ably and cost-effectively. The first step is to find the right model system. The criteria for this are reproducibility and control of the parameter space. Important parameters that define a foam/emulsion are the continuous phase volume fraction, the bubble/drop size distribution, the interfacial tension, the attractive forces between bubbles/drops or the rheological properties of the interface/skin. Furthermore, it is desired to distinguish between the influence of elasticity, adhesion, friction and interfacial tension on the interactions of the individual bubbles/drops and on the final foam/emulsion structure. This opens up another question. Which experimental measurement method and which setup is suitable for this? This thesis is part of the Metafoam project, trying to find the right model systems and answering in the meantime the question about the experimental setup and measuring method. The complexity of foams and emulsion is undisputed. This is only intensified by elasticity and adhesion. A good approach is to split the complex system in to smaller subsystems. By investigating only one bubble/drop [9], some of the interplay between interfacial tension and visco-elasticity can be understood. But an important ingredient is missing, the bubble/bubble or drop/drop interaction. The approach in this thesis is therefore to model a foam/emulsion with a subset of two bubbles/drops in contact. Starting with two simple bubbles or drops in contact, the investigation goes up to two capsules in the same configuration. The aim is to show a continuous transition from surface tension controlled systems to fully elasticity controlled systems. The effect of adhesion between two bubbles or drops is investigated in the same manner.

The general structure of the thesis with its six chapters is illustrated in Fig. 1.1. This thesis starts with a general introduction providing a general background to this topic and ending with a conclusion and outlook, which summarise the most important findings and discuss it in context to the existing literature and possible future investigations. The main results obtained during the three years of investigation are presented in the four chapters in between. Chapter 2 talks about minimal surfaces close to the catenoid surface with help of experiments, simulations and a perturbation theory. As minimal surfaces can be used as a model system for soap films, they have a special interest for foams. The catenoid is a well investigated configuration and its understanding can be used to generate a better understanding of new surfaces, close to the catenoid. Chapter 3 treats two bubbles or drops in contact with constant interfacial tension. This configuration therefore models an ordinary foam that is only controlled by interfacial tension. It serves as a starting point for more complex systems, since the physical principles for ordinary foams are already understood. Chapter 4 shows the fabrication and mechanical characterisation of a single "capsule" or "dropbloon". The tension at the interface of a capsule is purely related to elastic tensions and for a dropbloon interfacial and elastic tension play both a significant role. The aim is to characterise as much as possible the properties of the interface in order to concentrate afterwards just on the interactions between the two capsules or dropbloons. Chapter 5 explores the interactions of two capsules in contact.

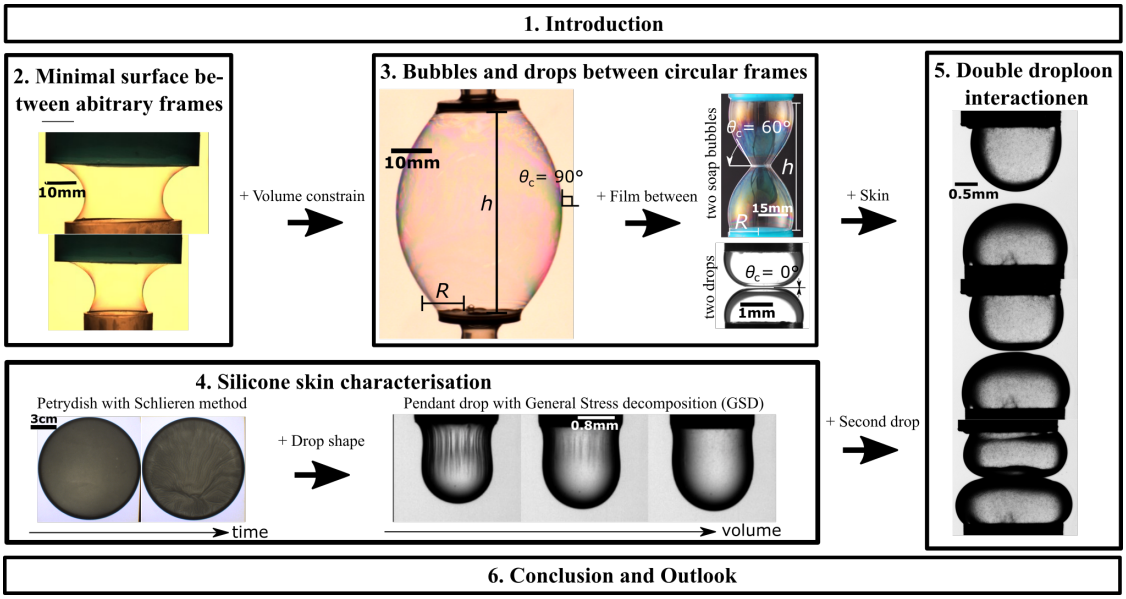

Figure 1.1: Illustrations of the general idea and structure of this thesis with the six different chapters.

1.2 General Introduction and background

1.2.1 Foams and emulsions

Different length scales play a role in foams and emulsions. The smallest length scale is that of the interface, which is at the length of molecules. It depends on the used solutions and is between 1 to 10 nm [5]. The thickness of a film separating two bubbles is commonly between 5 nm to 1 µm. It depends on the interactions between the interfaces and on the liquid fraction Φ. The size of drops and bubbles can vary between hundreds of nm and a cm. The size of the macroscopic foam or emulsion can reach the length scale of a meter. Phenomena of all length scales interact with each other, making foams and emulsions in the general case a strongly dynamic, non-linear system. Their properties depend on many parameters [4, 5], like the volume fraction of the different phases, the bubble/drop size distribution, the used surfactant, etc..

Considering for now by simplicity only foams, one very important parameter is the liquid volume fraction Φ. A critical point is where the bubbles touch each other and build a network, the jamming point, which is approximately at $\Phi = 0.36$ for a disordered and reasonably mono-disperse foam, as illustrated in Fig. 1.2. For larger liquid fractions one talks rather about bubbly liquids than about foams. If the liquid fraction tends towards zero, one talks about dry foams, which have a special equilibrium structure defined by Plateau's laws [5, 4, 10]. They state that films separating bubbles can be modeled as constant mean curvature surfaces due to the Young-Laplace law, as explained in more detail in Section 1.2.3.

In these dry foams, always three films meet each other in a line creating the Plateau borders. The angle between two films is always 120°. Four of the "Plateau borders" meet each other in a vertex with angles of 109.47°. In the limit of low liquid fraction this is exact. However, it also gives a very good approximation for foams up to a liquid fraction

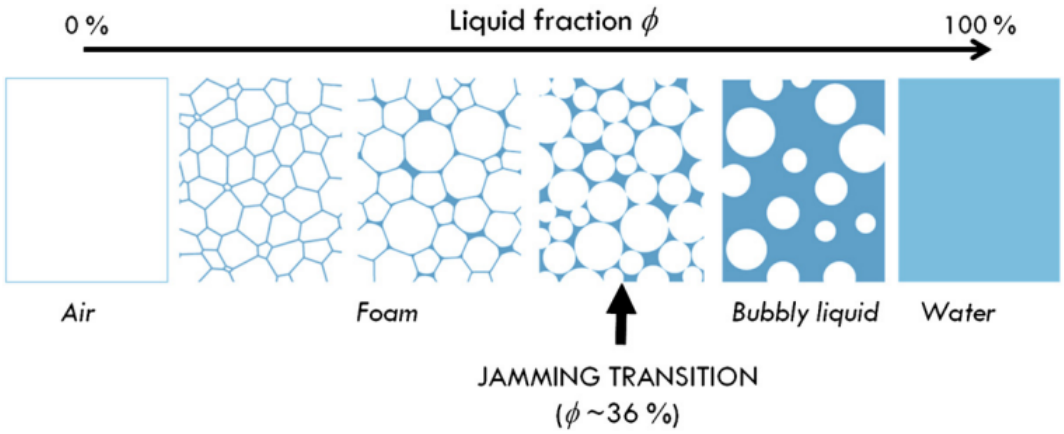

Figure 1.2: Scheme of foam aspects for different liquid volume fractions Φ, (C. Wiebke Drenckhan)

of $\Phi = 0.1$. That is why foams are called "dry" for $\Phi < 0.1$ and "wet" for $0.36 > \Phi > 0.1$. These principles are also true for emulsions. Even if they are called "high internal phase emulsions" for continuous fractions above the jamming point. Since jammed emulsions are often less stable than foams, Plateau's laws are observed mostly in foams and not in emulsions.

Foams and emulsions are in a meta-stable state and continuously changing their shape and structure, due to three mechanisms: drainage, gas or liquid diffusion and coalescence. Drainage describes the transport of liquid through the continuous phase due to gravitational and capillary forces [4]. Gas or liquid diffuses between different bubbles/drops due to Young-Laplace pressure difference. This changes the bubble/drop size distribution. Coalescence between two bubbles/drops appears if the film between them breaks. All three mechanisms influence each other.

Surfactants or emulsifiers are necessary to prevent the foam/emulsion from collapsing due to a hydrophobic and hydrophilic part in their molecular structure. Surfactants or emulsifiers absorb at the gas/liquid or liquid/liquid interface and stabilise against coalescence by reducing the interfacial energy and creating an energy barrier for film rupture.

Investigations of foams and emulsions are therefore very complex even for the "simple" case with purely liquid interfaces of constant interfacial tension. The Metafoam project aims to modify the interfaces or films, by adding elastic or adhesive contributions. Since the interfaces control the whole system, they have an impact on all phenomena discussed above. Smaller subsets of a foam or emulsion can help to simplify the system and develop a general understanding.

1.2.2 Interfacial tension and effective interfacial tension

The interfacial energy per interface area γ is the cost of energy per interface area between two phases, as sketched in Fig. 1.3. It can be an interface between phase 1 and vacuum, γ_1, or between phase 1 and phase 2, γ_{12}. The interfacial tension between phase 1 and a vacuum is a hypothetical tension important for some theoretical explanations (see Fig. 1.6). An interface between a liquid and a vacuum is not physical, as the vacuum disappears through evaporation. Since physical systems try to minimise their total energy

$\mathcal{E}$, interfaces try to minimise their total interface area A, which is proportional to the interfacial energy, i.e $\mathcal{E} = \gamma A$. The consequence is an interfacial tension tangential to the interface (Fig. 1.3b) and identical in absolute value to the energy per interface element. The interfacial energy per interface area can therefore be interpreted as interfacial tension and inverse. This is why the same formula symbol γ is used for both.

A liquid film consists of two interfaces and a small liquid phase in between. Since both interfaces of the film are very close to each other, a liquid film is often modelled as a single interface with an effective interfacial tension of $\gamma_{\text{eff}} = 2\gamma$ as illustrated in Fig. 1.3c. This is generally a good approximation if interactions between the two interfaces are negligible.

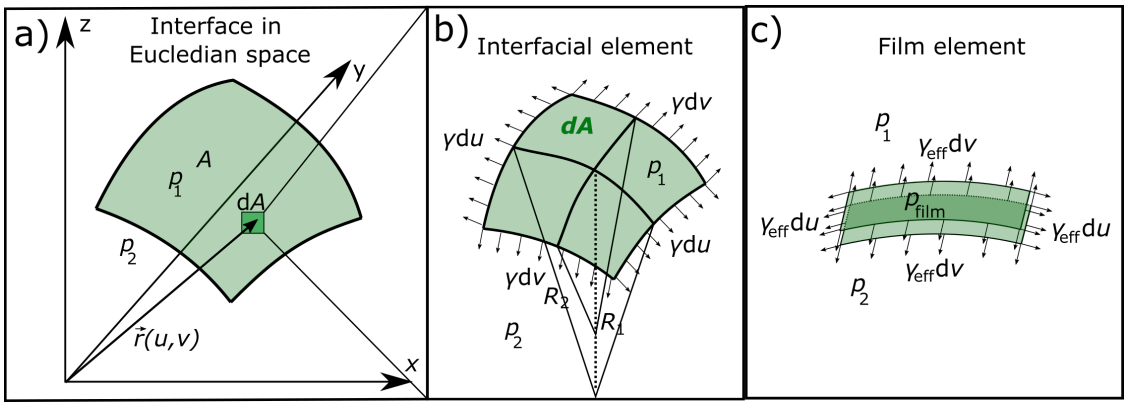

Figure 1.3: Illustration of an interface in Euclidean space in a), an interfacial element in b) and a film element in c) and their geometrical properties, $\vec{r}$ the vector description of the interface with the parametrisation u and v, A the interface area, $\mathrm{d}A$ an interfacial element, R_1 and R_2 the inverse of the principal curvatures and the forces with p_1 and p_2 the pressures on both sides of the interface or film, p_{film} the pressure inside of the film and $\gamma \mathrm{d}u$, $\gamma \mathrm{d}v$ and $\gamma_{\text{eff}} \mathrm{d}u$ and $\gamma_{\text{eff}} \mathrm{d}v$ the line tension or effective line tensions of the interface or film. The surface tension forces are always tangential to the interface/film and the pressure forces always normal. The arrows in b) and c) symbolise the direction of the interfacial tension.

1.2.3 Constant mean curvature surfaces and minimal surfaces

One important ingredient of a foam or emulsion is the interface between the discrete and the continuous phase or a film with two interfaces and their effective surface tension γ_{eff}.

A general interface in an Euclidean space is illustrated in Fig. 1.3a. If we make the assumption that γ_{eff} is constant in space, the total free energy of an open interface or film is given by

$$\mathcal{E} = \gamma_{\text{eff}} \iint_A \mathrm{d}A = \gamma_{\text{eff}} \iint_A \left\| \frac{\partial \vec{r}}{\partial u} \times \frac{\partial \vec{r}}{\partial v} \right\| \mathrm{d}u \, \mathrm{d}v = \gamma_{\text{eff}} \iint_A \mathcal{L} \, \mathrm{d}u \, \mathrm{d}v, \tag{1.1}$$

with $\mathcal{E}$ the free energy, A the surface area of the interface/film, $\vec{r}$ the surface coordinates, u and v the surface parameterisation and $\mathcal{L}$ the analog of a Lagrangian. "Open" means in this case that one can reach the other side of the film without crossing the film, i.e. the pressures on both sides are identical: $p_1 = p_2$. We are interested in physically stable surfaces in equilibrium at a local energy minimum. Equ. (1.1) shows that extremising $\mathcal{E}$ is

equivalent to extremising A. To find the extrema of Equ. (1.1), it is helpful to represent the surface $\vec{r}$ in an implicit form with Cartesian coordinates (x, y, z) with

$$r_z = f(r_x, r_y), \tag{1.2}$$

and r_j the Cartesian coordinates of $\vec{r}$. The Lagrangian becomes

$$\mathcal{L} = \sqrt{1 + f_{,x}^2 + f_{,y}^2}, \tag{1.3}$$

with $(\,)_{,j}$ the partial derivative with respect to j. The Euler-Lagrange equation is therefore

$$\frac{\partial \mathcal{L}}{\partial f} - \frac{\partial}{\partial x}\left(\frac{\partial \mathcal{L}}{\partial f_{,y}}\right) - \frac{\partial}{\partial y}\left(\frac{\partial \mathcal{L}}{\partial f_{,y}}\right) = 0, \tag{1.4}$$

and gives the differential equation for extremal surfaces

$$\left(1 + f_{,y}^2\right) f_{,xx} - 2 f_{,x} f_{,y} f_{,xy} + \left(1 + f_{,x}^2\right) f_{,yy} = 0. \tag{1.5}$$

In the literature, the obtained solutions of the differential equation are called "minimal surfaces". Sometimes, only the local minima are called minimal surfaces and sometimes all solutions, including the local maxima. We will stick to the more general case and call all solutions of Equ. (1.5) minimal surfaces. Consequently, open liquid interfaces or films in equilibrium are minimal surfaces in a local minimum. Soap films are liquid films that remain stable for a long time and are therefore predestined for analysing minimal surfaces.

Minimal surfaces are of special interest, since they are the solution of optimisation problems. The question of the existence of a minimal surface for given boundary conditions is known as the Plateau problem [11] and of particular interest. Only the minima of Equ. (1.1) are physically stable. That adds the question of stability of minimal surfaces. Soap films in equilibrium are always stable minimal surfaces (surfaces in a local minimum), which makes them even more interesting for minimal surface analysis.

Only few analytical solutions for minimal surfaces are known. That is why the known analytical solutions are of high interest. The simplest and trivial minimal surface is the plane. The catenoid, shown in Fig. 1.4, is the minimal surface connecting two coaxial circles with each other. Apart from the plane, it is the only axisymmetric minimal surface. The $r_c(z)$ profile (difined in Fig. 1.4) is the catenary

$$r_c(z) = a_c \cosh\left(\frac{z}{a_c}\right), \tag{1.6}$$

with a_c the smallest radius of the profile r_c. It can be used to model lipid membranes between colloids [12]. Besides the catenoid and the plane, there are other known, more complex minimal surfaces. The helicoid is the minimal surface obtained with a helix boundary curve [13], represented in Fig. 1.4. The Weierstrass representation produces minimal surfaces in a more general way [13] with

$$\begin{aligned} r_x &= \mathrm{Re}\left(\int o\left(1 - g^2\right) \mathrm{dw}\right), \\ r_y &= \mathrm{Re}\left(\int io\left(1 + g^2\right) \mathrm{dw}\right), \\ r_z &= \mathrm{Re}\left(\int og \mathrm{dw}\right) \end{aligned} \tag{1.7}$$

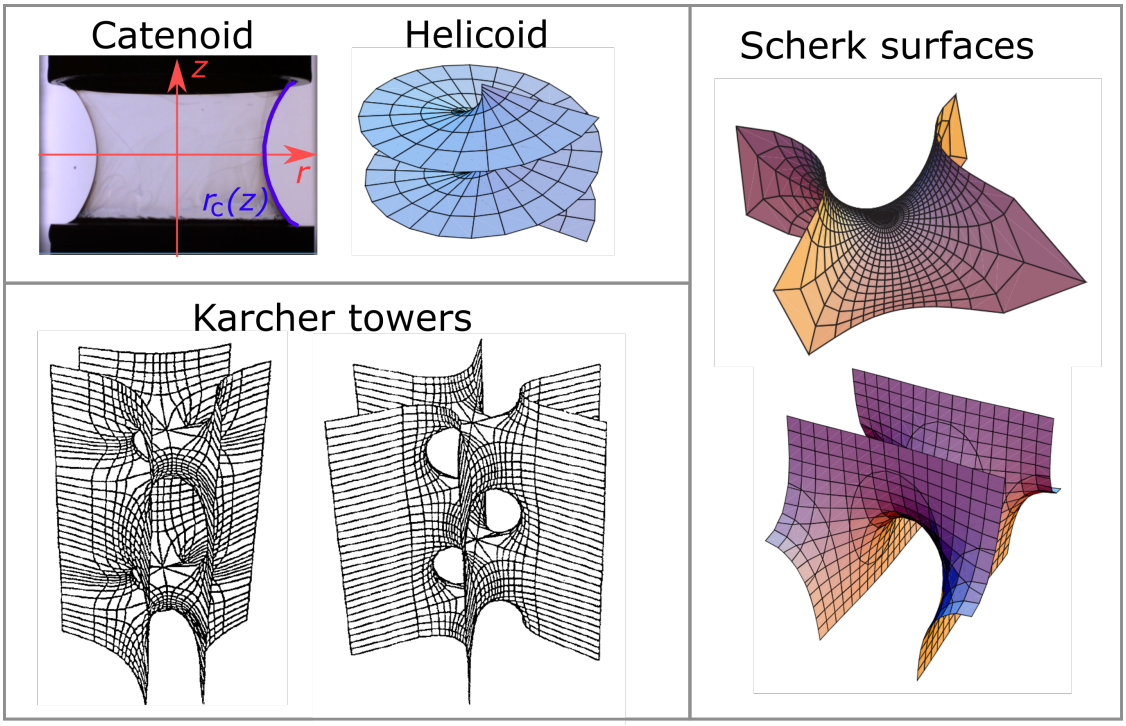

Figure 1.4: Different minimal surfaces, the catenoid, the helicoid [16], the Scherk surfaces [16] and the Karcher towers [15].

with g a meromorphic function, og an analytic function and the complex number $w = u+iv$ with i the imaginary unit [13] and u and v the parametrisation of the surface. Two examples of minimal surfaces, which are obtained with the Weierstrass representation, are the Scherk surfaces [14] and Karcher towers [15]. Both are represented in Fig. 1.4.

By adding a volume constraint to the problem in Equ. (1.1), the free energy of the system becomes

$$\mathcal{E} = \iint_A \gamma_{\text{eff}} \mathrm{dA} + \Delta \mathrm{p} \iiint_{\mathrm{V}} \mathrm{dV}, \tag{1.8}$$

with Δp the pressure difference between the two sides of the interface and V the volume of the body. The pressure difference is from the mathematical point of view the Lagrange multiplier for the volume constrain. With extremising Equ. (1.8) using the Euler-Lagrange Equ. (1.4), the differential equation

$$0 = 2\gamma_{\text{eff}} \frac{\left(1+f_{,y}^2\right) f_{,xx} - 2f_{,x}f_{,y}f_{,xy} + \left(1+f_{,x}^2\right) f_{,yy}}{\left(1+f_{,x}^2+f_{,y}^2\right)^{3/2}} - \Delta p, \tag{1.9}$$

is obtained. Comparing Equ. (1.9) with the differential equation for the mean curvature

$$H = \frac{\left(1+f_{,y}^2\right) f_{,xx} - 2f_{,x}f_{,y}f_{,xy} + \left(1+f_{,x}^2\right) f_{,yy}}{\left(1+f_{,x}^2+f_{,y}^2\right)^{3/2}}, \tag{1.10}$$

we obtain the Young-Laplace law [17, 18]

$$p_1 - p_2 = \Delta p = 2\gamma_{\text{eff}} H, \tag{1.11}$$

which relates the pressure difference Δp between the two sides of an interface or a film in equilibrium to the mean curvature H and the interfacial tension or film tension γ_{eff}. In Fig. 1.3 the different geometrical elements and forces (pressures and tensions) are illustrated for an interface in a) and b) and a film in c).

The mean curvature H is the averaged curvature κ over all directions at a point of a doubly differentiable surface

$$H = \int_0^{2\pi} \kappa(\phi) \mathrm{d}\phi. \tag{1.12}$$

It can be shown that this is equivalent to

$$H = \frac{1}{2}\left(H_1 + H_2\right) = \frac{1}{2}\left(\frac{1}{R_1} + \frac{1}{R_2}\right) \tag{1.13}$$

with H_1 and H_2 the principal curvatures and R_1 and R_2 the principal radii, of curvature.

This Young-Laplace law (1.11) is exact for a fluid interface from the continuum mechanical point of view. It therefore describes the shape of the interfaces of bubbles and drops in foams and emulsions in equilibrium. Changes in γ_{eff} and Δp along the surface are often small and can be neglected. Consequently the mean curvature H is constant along the surface and all liquid films in foams and emulsions are constant mean curvature surfaces. Even Plateau borders can be modeled with constant mean curvature surfaces.

In the special case of $\Delta p = 0$ surfaces are minimal surfaces with $H = 0$ [19], which can be also obtained by comparing Equ. (1.10) and Equ. (1.5).

In many cases, only one or two bubbles or drops are investigated in axisymmetric configuration held by frames. Then the special group of axisymmetric constant mean curvature surfaces (Delaunay Surfaces) [20] can be exploited for a better understanding of the interactions between two bubbles (drops) confined between two circular frames. Fig. 1.5 shows the four subgroups of Delaunay Surfaces: nodoids, spheres, unduloids and cylinders with the surface coordinates $r(z, \varphi)$. The catenoid is the only other axisymmetric constant mean curvature surfaces [21, 22, 23]. Equ. (1.8) is simplified with the help of the divergence theorem and the assumption of an axisymmetric surface to

$$\mathcal{E}(r) = 2\pi \int \left[\gamma_{\text{eff}} r \sqrt{1 + r_{,z}^2} - \frac{\Delta p}{2} r^2\right] \mathrm{dz}. \tag{1.14}$$

Equ. (1.9) then simplifies to

$$0 = \gamma_{\text{eff}} \frac{1 + r_{,z}^2 - r r_{,zz}}{\left(1 + r_{,z}^2\right)^{(3/2)}} - r\Delta p. \tag{1.15}$$

Integrating Equ. (1.15) over φ and z (see also Beltramy identity [24]) one obtaines

$$F_z = \pm\gamma_{\text{eff}} \frac{2\pi r}{\sqrt{1 + r_{,z}^2}} - \pi r^2 \Delta p. \tag{1.16}$$

Equ. (1.16) is the differential equation, which gives the Delaunay Surfaces. F_z is the integration constant, which is equal to the force in z-direction exerted on the upper end of the surface and composed of the the sum of pressure and interfacial tension forces. These surfaces are discussed in more detail in Chapter 3.

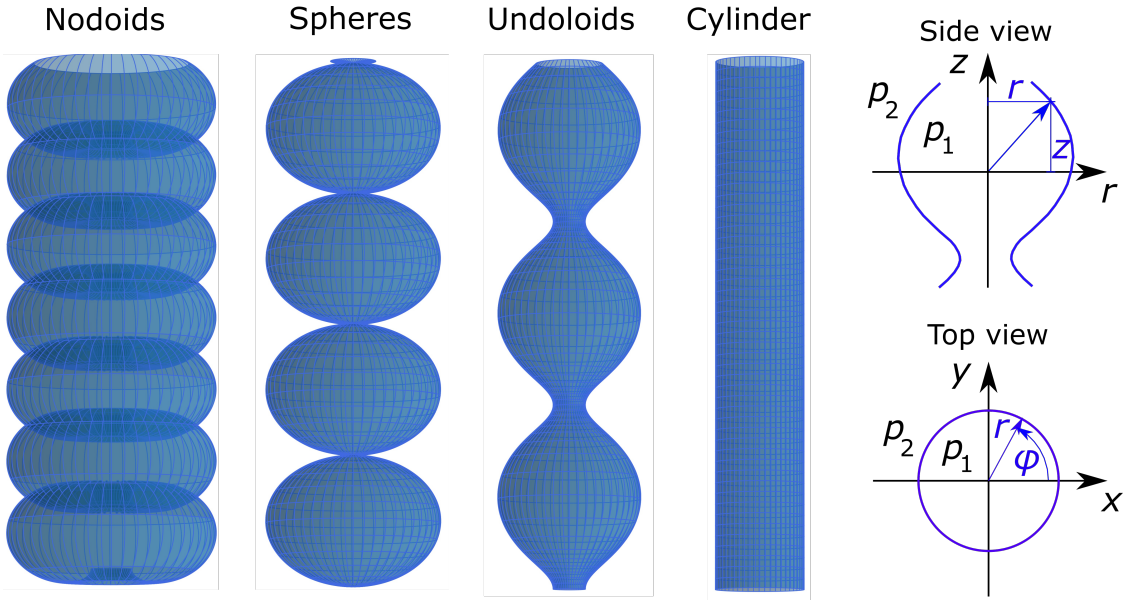

Figure 1.5: illustration of the four periodic, constant mean curvature surfaces (Delaunay surfaces): nodoids, spheres, undoluids and cylinders on the left, and a top and side view of the surface profile with cylindrical coordinates r, z and φ and the inner and outer pressure p_1 and p_2.

1.2.4 Adhesion and elasticity of interfaces

What happens now to these interfaces when adhesion or elasticity play a role? What kind of surfaces would one obtain?

1.2.4.1 Adhesion

Let us first take a closer look at the adhesion between two interfaces. Adhesion is related to the change in free energy by separating two different objects or phases [25]. The energy changes with the amount of work per unit surface W performed. One may illustrate this process as shown in Fig. 1.6a for two fluids 1 and 2. One starts with a continuous interface between the two fluids. Afterwards we create two new interfaces between phase 1 and 2 and vacuum. The free energy per surface area changes by half the work per surface area required to separate phase 1 or 2 from itself, $0.5(W_{11} + W_{22})$. The final step is to bring the two surfaces that were in contact with vacuum together and form a new interface between phase 1 and 2. The required work per surface area for this step is $-W_{12}$. One may therefore write

$$\gamma_{12} = 0.5W_{11} + 0.5W_{22} - W_{12} = \gamma_1 + \gamma_2 - W_{12}, \tag{1.17}$$

with $W_{jj} = 0.5\gamma_j$ the work needed to separate phase j and the surface energy of these phases and vacuum, W_{12} the work needed to create a new interface between phase 1 and 2 and γ_{12} the interfacial tension between this two phases [25]. The adhesion energy per surface area is therefore the surface tension between the two phases and the simplest case of adhesion between two objects, in this case two fluids. The interfacial tension between two fluids is therefore a measure of the strength of the adhesion between them.

Here we are interested in the adhesion between two interfaces. The adhesion energy between them can be defined in a similar way. Fig. 1.6b shows phase 1 as two bubbles

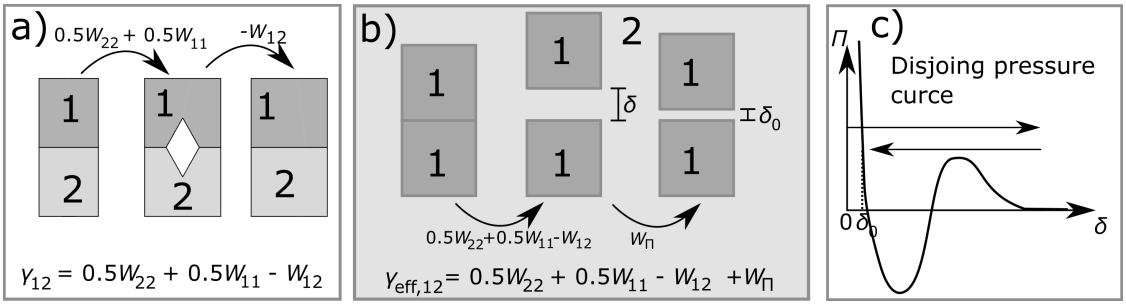

Figure 1.6: Illustrations of a) the work per surface element needed to separate a fluid interface between two phases 1 and 2, b) of the work per surface element needed to create a film in equilibrium between two bubbles or drops and c) an example of a disjoining pressure Π vs. distance δ curve.

or drops and phase 2 the continuous phase separating the two bubbles or drops with a distance δ. Since the distance δ between the two interfaces can be of the order of a nm, they interact with each other. The potential which is related to the interaction of the two interfaces is called disjoining pressure Π. It is a function of δ and depends strongly on the used surfactants, surfactants concentrations and fluids used for phase 1 and 2. An illustration of a possible disjoining pressure curve is shown in Fig. 1.6c. Possible interactions are related to Van-der-Waals forces, electrostatic forces due to charges on the interface, steric repulsive forces or depletion forces due to micelles or polymers in phase 2 [25]. Equ. (1.17) is modified to

$$\gamma_{\text{eff;12}} = 0.5W_{11} + 0.5W_{22} - W_{12} = \gamma_1 + \gamma_2 - W_{12} + 0.5W_{\Pi}, \tag{1.18}$$

with W_{Π} the work per area performed by decreasing the film thickness, from one where the interfaces do not see each other to the thickness δ_0, the final thickness, where they interact with each other. W_{Π} can be obtained with

$$W_{\Pi} = \int_{\delta_0}^{\infty} \Pi \mathrm{d}\delta. \tag{1.19}$$

The adhesion energy $\mathcal{E}_{\text{adh}}$ of two bubbles or drops is the energy which is needed to separate them. Separated in this context means the disjoining pressure and the change of the disjoining pressure with respect to δ is zero. Since before the separation and after the separation, there are two interfaces between phase 1 and 2 the energy is $\mathcal{E}_{\text{adh}} = W_{\Pi} A$. Another interpretation of $\mathcal{W}_{\Pi}$ is an effective film tension $\gamma_{\text{film}} = W_{\Pi}$ acting tangentially to the two interfaces, illustrated in Fig. 1.7a. One may write

$$\gamma_{\text{eff;12}} = 0.5\gamma_{\text{film}} + \gamma_{12}. \tag{1.20}$$

Even if a film has a $\gamma_{\text{film}} \neq 0$ the assumption of a constant mean curvature surface stays true, if $\gamma_{\text{eff;12}}$ is constant over the interface. Therefore $\mathcal{E}$ from Equ. (1.8) is proportional to $\gamma_{\text{eff;12}}$. The difference in a foam or emulsion structure can be observed at the edges of the films, shown in Fig. 1.7b. Since $\gamma_{\text{eff;12}}$ depends on Π and Π depends on δ, $\gamma_{\text{eff;12}}$ changes in the meniscus. For the length scale of the film thickness δ, this is a continuous change [26, 27], illustrated in Fig. 1.7a. For a scale larger than δ, a non zero contact angle θ_{c} between the interface at the film and the interface at the meniscus or Plateau border

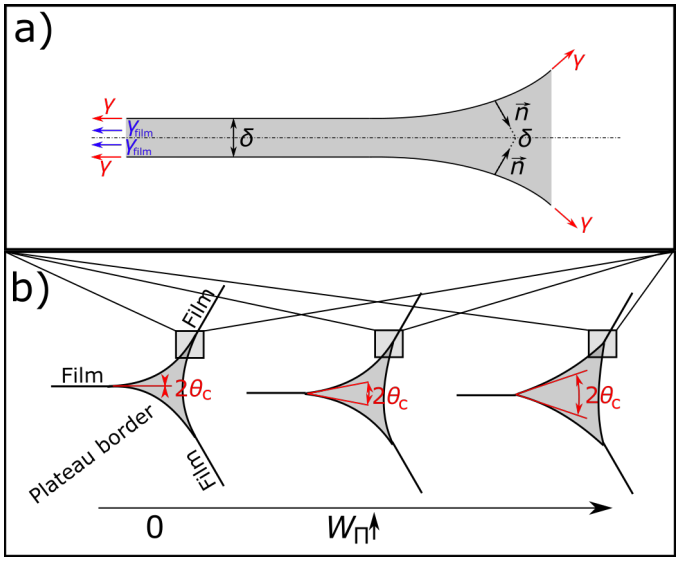

Figure 1.7: A liquid film with the transition to a Plateau border or meniscus in a) and different Plateau borders with the important geometrical parameters as $\vec{n}$ the normal vector on the interface, δ the distance between the two interfaces and θ_c the macroscopic contact angle between the interfaces at the film and Plateau border and the different tensions as γ the interfacial tension and γ_{film} the 2D film tension.

is observed [27], shown in Fig. 1.7b. This is a consequence of the force equilibrium at the film edge. Films in a foam are bounded by Plateau borders and vertices. Consequently the shape of the Plateau borders and vertices are changed in the cases, where δ is smaller than the characteristic lengths of Plateau borders or vertices and $\gamma_{\text{film}} \neq 0$. This has an influences on the global foam structure and therefore on drainage [28], the mechanical properties of the foam and more [29].

1.2.4.2 Visco-Elasticity

The energy per surface area in Equ. (1.8) becomes an integral-differential equation in space and time if visco-elasticity is considered

$$\mathcal{E} = \iint_A \gamma_{\text{eff}}(\vec{r}, \dot{\vec{r}}, \vec{r}_{,i}, ...)\text{dA} + \Delta\text{p} \iiint_\text{V} \text{dV}, \tag{1.21}$$

with $\dot{\vec{r}}$ the time derivative of the interface and $\vec{r}_{,i}$ the space derivative of the surface in the three directions in space. The energy per interfacial area has three different contributions: (1) the already discussed interfacial tension of the interface between the two phases, (2) energy due to elastic deformations and (3) the viscous dissipation energy. An interface can be elastic in a liquid state (Fig. 1.8a) or in a solid state (Fig. 1.8b). In the liquid state (Fig. 1.8a) the interface concentration of surfactants decreases and consequently, the interfacial tension γ_{12} increases, if the surface area of a liquid interface is increased and exchange of surfactants with the bulk prohibited. Going back to the original surface area one obtains again the original surfactant concentration at the interface and interfacial tension. This is referred to as Gibbs elasticity. Most of the time this process is not 100% elastic due to adsorption and desorption of surfactants at the interface. The combination of both phenomena explains the visco-elastic behavior of a liquid interface, where the resitance

against surfactant adsorption and desorption is responsible for the elastic response and the adsorption and desorption for the viscous behavior. By oscillating the surface area, the elastic and the viscous part can be measured. If the characteristic diffusion time of the surfactants at the interface is large or the surfactants are not soluble in bulk, the viscous part generally becomes negligibly small. Since the layer of surfactants is confined at the interface, one talks about two-dimensional elasticity.

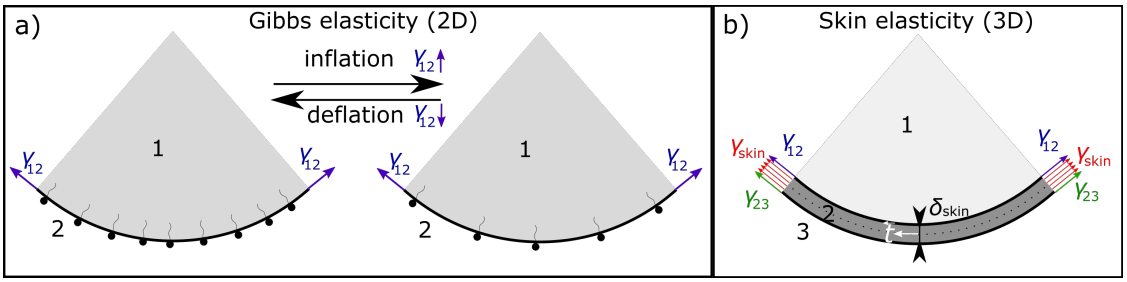

Figure 1.8: a) A scheme of the principle idea of Gibbs elasticity with phase 1 and 2, a representation of surfactants and the interfacial tension γ_{12} between the two phases. b) A scheme of a skin (phase 2) between two different fluids (phase 1 and 3) with the interfacial tensions at the interfaces γ_{12} and γ_{23} and the effective interfacial tension of the skin γ_{skin} with the geometrical properties δ_{skin} the thickness of the skin and $\vec{t}$ the tangential vector of the interface/skin.

The term "skin" is used when the interface is a solid. The skin of this thesis consists of several layers of molecules and can no longer be regarded as a two-dimensional object. Therefore, the skin has two interfaces, an inner and an outer interface as illustrated in Fig. 1.8b. The two interfacial tensions γ_{12} and γ_{23} are not the same and depend on the used gases and liquids in phase 1, 2 and 3, (Fig. 1.8). The effective interfacial tension of the skin for Equ. (1.21) is therefore

$$\gamma_{\text{eff}} = \gamma_{12} + \gamma_{23} + \gamma_{\text{skin}}, \tag{1.22}$$

assuming simple addition of all contributions. We summarise the interfacial tension parts of a skin in the following with $\gamma = \gamma_{12} + \gamma_{23}$. The skin-related tension has contribution of viscous stresses and elastic stresses and depends on the stress tensor $\underline{\sigma}$ with

$$\gamma_{\text{skin}} = \delta_{\text{skin}} \underline{\sigma} \cdot \vec{t}, \tag{1.23}$$

and $\vec{t}$ the tangential vector of the interface, consequently orthogonal to the skin thickness δ_{skin}. Equ. (1.23) assumes that the stress tensor $\underline{\sigma}$ is homogeneous across the skin thickness, which is a strong simplification. If the surface is in equilibrium the viscous stresses vanish and $\underline{\sigma}$ is purely elastic.
The stress tensor $\underline{\sigma}$ depends on the constitutive law and the deformation. If the skin thickness δ_{skin} is several magnitudes smaller than the other length scales, it can be treated as a "shell" or in special cases as a "membrane" [30]. One talks about shells if Kirchhoff's assumption are true:

- *Normals to the undeformed middle surface remain straight and normal to the deformed middle surface and undergo no extension. (This assumption implies that all the strain components, normal and shear, in the direction of the normal to the middle surface vanish* [30].

- *The transverse normal stress is small compared to other normal stress components and may be neglected.* [30]

One talks about a membrane if the bending stresses vanish and Kirchhoff's assumption for a shell are true. Therefore one distinguishes between an absolutely flexible shell ("the membrane") or the moment-less, the "membrane state of stress" [30]. In the first case, the membrane is not supporting any kind of moments. It would immediately buckle. In the second case the shell supports moments but due to the actual load, no moments are present in the structure. To summarise, all types of shells are stable under a membrane state of stress, in contrast to a state of compression in which only a shell with finite flexural stiffness resists and the membrane immediately buckles [30].
Linear elastic theory is applied if the deformation is small in comparison to the skin thickness δ_{skin}. In the other case, nonlinear elastic theory is used. Due to the small skin thicknesses δ_{skin}, linear elasticity theory gives in most cases only a first approximation for the stress and deformation state of the skin. By considering non-linear deformations, even for isotropic materials, a large number of constitutive equations are possible. By assuming only elastic deformations, one talks about "hyper-elastic" materials. An example of a constitutive law is the Neo-Hooke model, which is a special case of the Mooney-Rivelin model [31]. Both are frequently used in rubber material modelling [31]. If viscous stresses are also to be taken into account, the damped spring model would be appropriate. There, the skin's resistance to deformation is modelled using springs and dashpots in series and in parallel.

In all discussed cases (liquid elasticity, skins as a shell or membrane), it is possible to define a Young's modulus of the bulk of the skin E_{3DY} or the two-dimensional equivalent, the dilational elastic modulus K_{2D}, in the linear limit. It relates the normal strain to the normal stress with [32]

$$K_{\text{2D}} = \delta_{\text{skin}} E_{\text{3DY}} = \frac{|\underline{\sigma} \cdot \vec{t}|}{\varepsilon} \delta_{\text{skin}}, \tag{1.24}$$

with ϵ the strain of the skin. We are interested in the regime in Equ. (1.22) where the interfacial tension and the skin tension are significant. Therefore we compare K_{2D} with the interfacial tension and define the elastocapillary number α with

$$\alpha = \frac{K_{\text{2D}}}{\gamma}. \tag{1.25}$$

The interface has a constant interfacial tension with deformation if $\alpha << 1$. We will call these objects drops or bubbles. The interface is purely elastic if $\alpha >> 1$. We will call this objects capsules. If α an intermediate value, we will call these objects droploons or bubloons.

In experiments, different interfacial rheological methods are used to characterise the visco-elastic response of interfaces. Depending on how the interface is deformed, one distinguishes between dilational and shear rheological methods. Fig. 1.9 shows three examples, two dilational interfacial methods Fig. (1.9a and b) and one shear interfacial methods (Fig. 1.9c) In Fig. 1.9a a drop/bubble is quasi statically inflated or deflated. The material properties are obtained by measuring Δp and the axisymmetric drop/bubble profile and fitting it to a constitutive law [33, 34]. The software OpenCapsule can be used for this purpose [34]. In Fig. 1.9a the capsule on the right has wrinkles. Since the wrinkle wave length is small, the macroscopic shape can still be considered as axisymmetric. The

wrinkle wave length can be used to obtain the bending modulus of the skin. The software Open Capsule is able to take this into account [34]. Important for this software is a correct reference state of the capsule. It describes the shape of the capsule without elastic stresses. In Fig. 1.9b the drop or bubble is inflated and deflated sinusoidally. This method gives information about the elastic and viscous properties of the skin. It can be used to measure Gibbs elasticity, even if absorption and desorption takes place, [35] or capsule elasticity [36, 37].

In Fig. 1.9c the example of a double wall-ring geometry for "interfacial shear rheology" is shown [9, 38]. The geometry deforms the interface in-plane, resulting in a pure shear deformation. Simultaneously, the torque, due to the deformation, acting on the geometry is measured, giving information about the interfacial shear properties.

The advantage of the technique with the pendant drops is their geometrical proximity to foams and emulsions. On the other hand, non-linear geometric effects play a greater role in contrast to the rather simple planar structure in interfacial shear rheology. Their evaluation and interpretation is therefore often difficult. In general, both methods should be used in combination for a complete characterisation, since for the pendant drops the deformation is rather a dilational deformation and for the interfacial shear rheology a pure shear deformation.

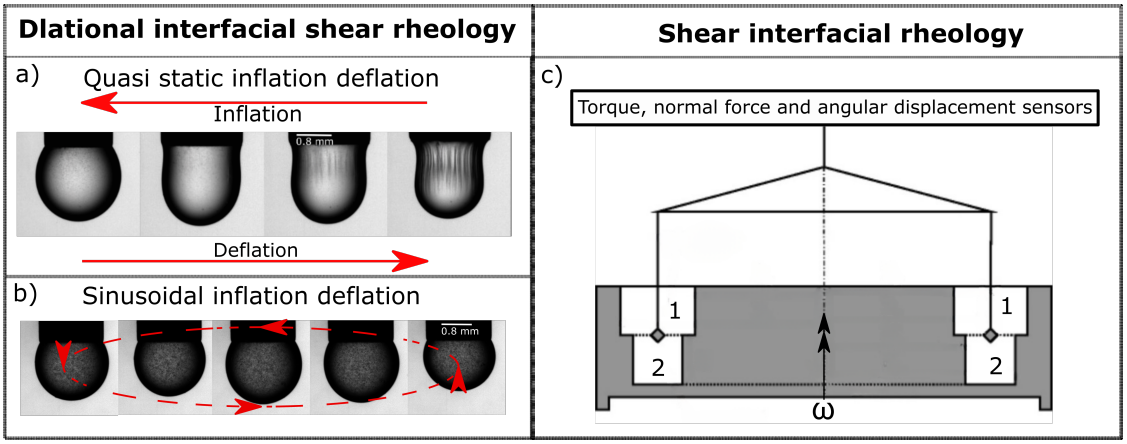

Figure 1.9: Illustration of three methods used to characterise liquid and solid interfaces. a) is the dynamic sinusoidal inflation deflation method with a silicon oil as the continuous phase, a silicon skin as the solid phase and PEG Platin catalysator emulsion as the drop phase. b) shows a quasi static inflation deflation of a pendant drop and c) an example for interfacial shear rheology [38].

1.2.5 Perturbation theory

Regardless of whether one is considering minimal surfaces, constant mean curvature surfaces or elastic skins, studies of non-axisymmetric configurations are still a challenge. This is due to the fact that they are relatively difficult to model and characterise experimentally. But non-axisymmetric solutions are not atypical. They often occur due to non-axissymmetric boundary conditions or non-isotropic or homogeneous materials. However, stable non-axisymmetric solutions can also occur with perfect axisymmetric boundary conditions and isotropic and homogeneous materials as a result of shape instabilities. An example is Euler buckling of a beam [39]. Also columns of bubbles can buckle away from the axisymmetric solution [40]. Even the simple configuration of two bubbles

confined between two axisymmetric frames can buckle [41]. In most cases, there is no analytical solution for the minimisation problem from Equ.s (1.1), (1.8) and (1.21). The known analytical solutions and most of the available numerical approaches are limited to the axisymmetric cases.

Perturbation theories are used to expand the known analytical solutions and numerical approaches to non-axisymmetric configurations. For this purpose, an analytical solution is extended by an ansatz that perturbs the known axisymmetric solution. The ansatz contains the variables to be modified. The most general ansatz is the infinite degree Tailor expansion in the perturbation term ϵ

$$f(\phi, z) = r_A(z) + \sum_{k=1}^{\infty} \epsilon^k A_k(\phi, z) \tag{1.26}$$

with $r_A(z)$ the known solution, A_k the perturbation functions and $f(\phi, z)$ the perturbed solution. In this case, r_A is perturbed in cylindrical coordinates (ϕ and z). The problem to be solved is to determine the appropriate functions $A_k(\phi, z)$. They depend on the desired boundary conditions and energy functional from Equ.s (1.1), (1.8) and (1.21). The theory is used to evaluate the stability of a known solution to an arbitrary perturbation or to generate new shapes in a new parameter space including, for example, non-axisymmetric solutions.

In general, the problem is simplified by considering only some order in ϵ in Equ. (1.26). This gives an exact result infinitesimally close to the known solution, depending on which degree in ϵ was considered. The fact that the theory is exact sufficiently close to the known solution is used to analyse stability, by comparing $\mathcal{E}$ of the original shape and the perturbed shape.

In Chapter 2 new minimal surfaces are generated by changing the boundary conditions to non-axisymmetric ones. A linear perturbation approach around the axisymmetric catenoid generates approximations for minimal surfaces.

Chapter 2

Minimal surface between arbitrary frames

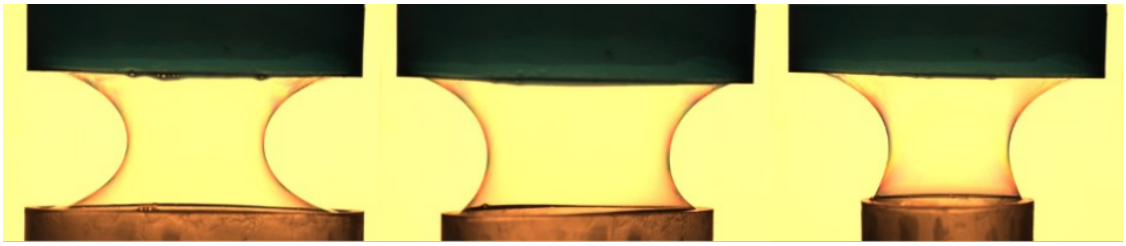

Minimal surface problems arise naturally in many soft matter systems whose free energies are dominated by surface or interface energies. Of particular interest are the shapes, stability and mechanical stresses of minimal surfaces spanning specific geometric boundaries. The "catenoid" is the best-known example where an analytical solution is known which describes the form and stability of a minimal surface held between two parallel, concentric circular frames. Here we extend this problem to non-axisymmetric, parallel frame shapes of different orientations, by developing a perturbation approach around the known catenoid solution. We show that the predictions of the perturbation theory are in good agreement with experiments on soap films and finite element simulations (Surface Evolver). Combining theory, experiment and simulation, we analyse in depth how the shapes, stability and mechanical properties of the minimal surfaces depend on the type and orientation of elliptic and three-leaf clover shaped frames. In the limit of perfectly aligned non-axisymmetric frames, our predictions show excellent agreement with a recent theory established by Alimov *et al.* (M. M. Alimov, A. V. Bazilevsky and K. G. Kornev, Physics of Fluids, 2021, 33, 052104) [1]. Moreover, we put in evidence the intriguing capacity of minimal surfaces between non-axisymmetric frames to transmit a mechanical torque despite being completely liquid. These forces could be interesting to exploit for mechanical self-assembly of soft matter systems or as highly sensitive force captors.

This chapter is based on the already published article of F. Walzel, *et al.* with the title "Perturbing the catenoid: Stability and mechanical properties of nonaxisymmetric minimal surfaces" published in the journal Physical Review E 106.1 (2022): 014803 [42].

Contents

2.1 Introduction

Minimal surfaces describe shapes of arbitrarily complex geometry which are characterised by the fact that their surface has a minimal area fixed by a set of boundary conditions. Minimal surfaces are fascinating mathematical objects introduced by the pioneering work of Euler [21], Lagrange [43] and Plateau [10]. Today, they are related to different mathematical fields such as calculus of variations, partial differential equations, differential geometry and topology, and complex analysis via the Weierstrass representation [44, 45]. Minimal surfaces have also served as models for numerous applications. Examples include architecture [46] or the development of materials combining antagonistic properties such as good mechanical rigidity and high electrical/thermal transport capacities [47, 48, 49]. We can also mention their use as scaffold for tissue engineering [50].

The relevance of minimal surfaces in different fields leads to different (yet equivalent) mathematical definitions [45]. The property of having a zero mean curvature at all points of the surface is particularly remarkable [22]. For physicists, the property of minimising the area of the surface is even more important, since it makes it possible to make the connection with physical problems where surface area can be associated with the energy

of a system which needs to be minimised. Soap films are amongst the most popular examples [10, 23].

The free energy $\mathcal{E}$ of soap films with uniform surface tension γ is given by Equ. (1.1). The equilibrium shape is then given by the minimisation of the total area A, which naturally leads to an easy realisation of minimal surfaces, discussed in more detail in the general background in Section 1.2.3.

A specific class of soap film problems was defined by Plateau. The so-called "Plateau problem" consists in studying the existence of minimal surfaces resting on given boundary conditions [10, 51, 52]. The catenoid is the classical example for this group of minimal surfaces. It consists of a minimal surface spanning two parallel circles of radius R separated by a distance h with the two centres of the circles lying on an axis orthogonal to the planes of each circle. Contrary to the majority of minimal surfaces, an analytical solution is known for the catenoid [21, 22, 53, 54]. It predicts the conditions for the existence of a solution and the exact shape of the minimal surface. The axisymmetric boundary conditions ensure that the surface is also axisymmetric. It can thus be described simply in cylindrical coordinates by a function giving the film radius r_c depending on the vertical coordinate z (see Fig. 2.1) in the range $-h/2$ to $h/2$ with Equ. (1.6) given in Section 1.2.3. The boundary conditions for the two frames are given by $r_c(z = \pm h/2) = R$. The smallest radius is found in the mid-plane ($z = 0$) and is called the neck radius. Its value, a_c, is obtained with the equation

$$R = a_c \cosh\left(\frac{h}{2a_c}\right). \tag{2.1}$$

and represented in Fig. 2.2b. This Equ. (2.1) has two solutions for $h/R < \mu^\star$, one for $h/R = \mu^\star$ and no solution for $h/R > \mu^\star$ where $\mu^\star$ is the solution of the transcendental equation $(\mu^\star/2)\sinh((\mu^\star/2)\sqrt{1+4/\mu^{\star 2}}) = 1$ leading to $\mu^\star \approx 1.33$ (illustrated in Fig. 2.2b). In the following $h^\star$ will be the critical height defined by $h^\star = \mu^\star R$. If there are two solutions, one of them always corresponds to a maximum of the area A and the other to a minimum $A_{\text{stable}} < A_{\text{unstable}}$, see Fig. 2.2a. Experimentally, only the minimum is observable since the maximum is physically unstable for open systems (Erle *et al.* [53] were able to observe the second solution in the case of closed systems. We will discuss this in Chapter 3). Close to $h^\star$, a small increase of the surface area leads to a destabilisation of the catenoid, which undergoes a topological instability leading to the so-called "Goldschmidt solution" [55] given by two disks parallel to the frames, see Fig. 2.2a.

The case of the catenoid has been much studied by physicists who have been particularly interested in the stability of the surface [56, 57, 58], in the collapse of the catenoid towards the Goldschmidt surface at the critical point [59, 60], or in the asymmetrical catenoid supported by rings of different sizes [61].

In this chapter, we extend previous studies by investigating the shape, the stability and the mechanical properties of a special group of minimal surfaces, spanning two **non-axisymmetric** closed frames, which are contained in two parallel planes. The planar boundaries $\mathcal{C}_\pm$ ($+$ and $-$ denoting the upper and lower frame, respectively) are centered on the z axis and given in polar coordinates $r_{\mathcal{C}\pm}(\varphi)$. They are separated by a distance h and rotated by an angle $\pm\varphi_0/2$ around the Oz axis. More specifically, elliptic and clover frames are used, as shown in Fig. 2.3.

Non-axisymmetric boundary conditions introduce a new degree of freedom, the angle

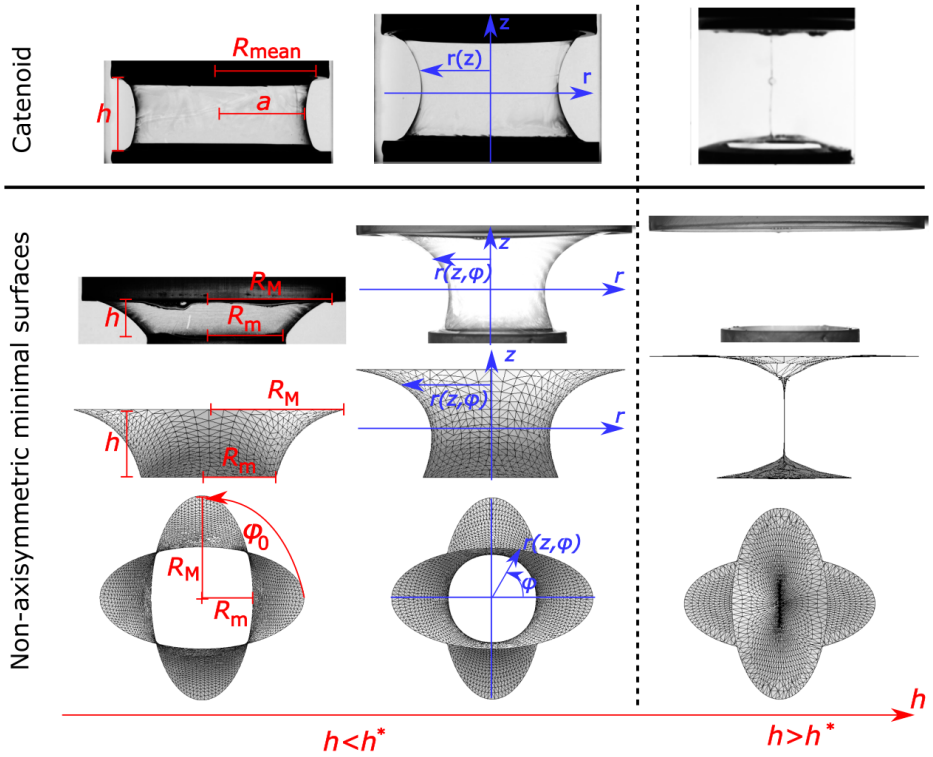

Figure 2.1: Experimental (1ste and 2nd row) and numerical (3rd and 4rd row) shapes obtained for minimal surfaces with axisymmetric circular frames (1 row) and elliptic boundary conditions (eccentricity $e = 0.866$) and for an angle $\varphi_0 = 90°$ between the main axes (2nd to 4rd row). The distance between the upper and lower frame is increasing from left to right. The rightmost images correspond to transient since h is already larger than the critical distance.

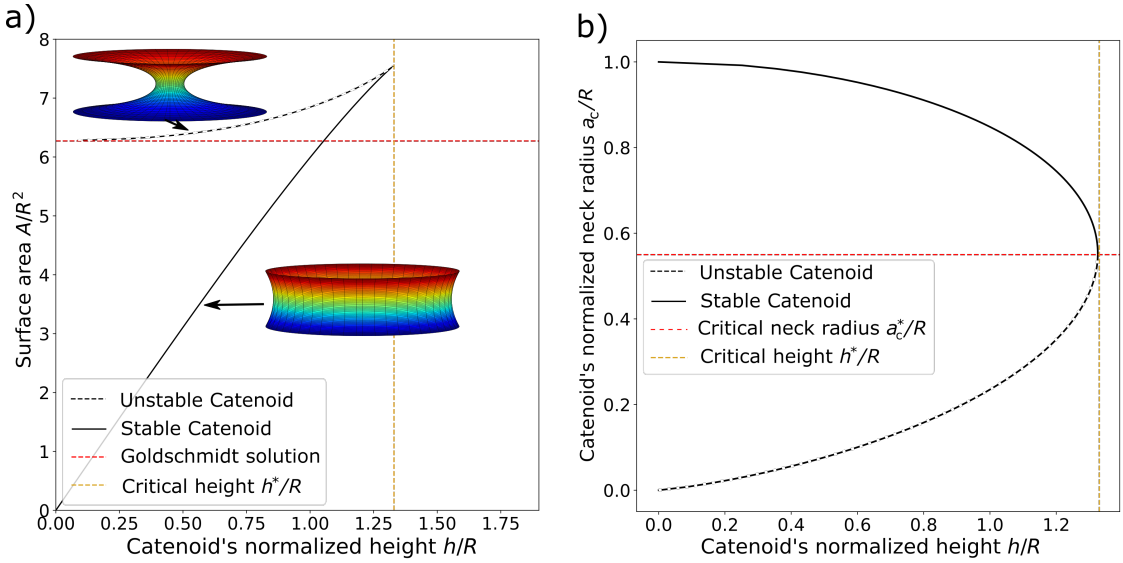

Figure 2.2: The normalized surface area in a) and the normalized neck radius a_c in b) are plotted over the normalized height for all catenoids, stable and unstable. The Goldschmidt solution is represented in a). In b) the two critical values a_c^* and h^* for the critical catenoid are illustrated with straight lines.

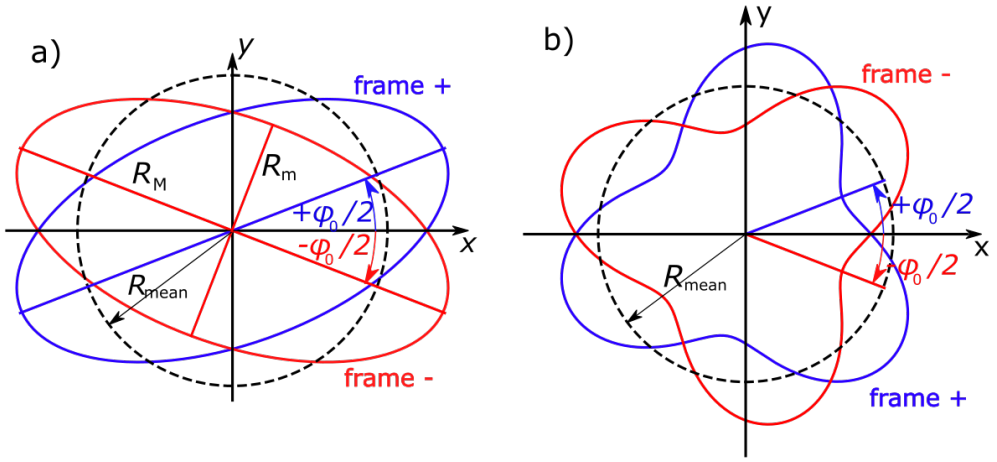

Figure 2.3: Upper (blue) and lower (red) frames, in the cases of the ellipse (a) and the clover (b), with the different associated geometric parameters R_{mean}, R_{M}, R_{m} and φ_0.

φ_0 between the upper and lower frame. This brings very interesting new properties to the minimal surface. After quantifing the influence of the angle φ_0 on the existence of the minimal surface and the associated critical height, we pay special attention to their mechanical properties. We study the forces exerted by the minimal surface on the frames. In particular, we show that besides the normal force, which pulls each frame towards the other one, non-axisymmetric shapes are also characterised by a measurable torque around the Oz axis, which tends to rotate the two frames back to the position $\varphi_0 = 0$.

To analyse the different surface properties, we combine experiments with soap films, numerical simulations using the open source software Surface Evolver [62], and theoretical modelling. The latter is a perturbation theory based on the catenoid solution. For all three approaches we study the shapes and the critical height of the minimal surfaces together with the resulting normal force and the torque on the frames. Very recently, Alimov *et al.* [63, 1] used an analogy between fluid dynamics of potential flow and minimal surfaces to provide an iterative algorithm allowing to calculate the exact surface shape between two identical convex frames. However, their theory is restricted to systems without rotation (i.e. for $\varphi_0 = 0$). In the following, it will be used as benchmark for our investigations together with the analytical predictions of the catenoid.

2.2 Materials and methods

2.2.1 Notations and boundary conditions

The shape of the minimal surface is represented in cylindrical coordinates with the vector position $\vec{r}$ given by $(x = r(\varphi, z)\cos\varphi, y = r(\varphi, z)\sin\varphi, z = z)$.

The planar boundary contours $\mathcal{C}_\pm$ ($+$ and $-$ denoting the upper and lower frame, respectively) are centered on the z axis and given in polar coordinates $r_{\mathcal{C}_\pm}(\varphi)$. They are separated by a distance h with the z coordinates $z = h/2$ and $z = -h/2$.

We assume that it is possible to do a Fourier decomposition

$$r_{\mathcal{C}_\pm}(\varphi) = R^\pm_{\text{mean}}\left(1 + \sum_{k=2}^{+\infty} a_k^\pm \cos(k\varphi) + b_k^\pm \sin(k\varphi)\right), \tag{2.2}$$

where $R^\pm_{\text{mean}}$, $a_k^\pm$ and $b_k^\pm$ are respectively the mean radius and the Fourier coefficients of $\mathcal{C}_\pm$. Note that the Fourier series starts at $k = 2$ to ensure that the frame is centered, i.e. that $\langle x\rangle = \langle r\cos\varphi\rangle = 0$ and similarly with y.

With the exception of some cases, the two frames will be identical up to a rotation of an angle φ_0, a condition which can be written $r_{\mathcal{C}\pm}(\varphi) = r_{\mathcal{C}}(\varphi \mp \varphi_0/2)$ where $r_{\mathcal{C}}(\varphi)$ is the unrotated contour defined via its Fourier decomposition

$$r_{\mathcal{C}}(\varphi) = R_{\text{mean}}\left(1 + \sum_{k=2}^{+\infty} a_k \cos(k\varphi) + b_k \sin(k\varphi)\right). \tag{2.3}$$

As shown in Fig 2.3, we use two different types of non-axisymmetric frames: elliptic shapes labelled $r_{\mathcal{C}} = r_{\text{e}}$ and clover-type shapes labelled $r_{\mathcal{C}} = r_{\text{cl}}$.

The elliptic frames are defined with an eccentricity e, major axis $2R_{\text{M}}$, and minor axis $2R_{\text{m}}$, with $e^2 = 1 - (R_{\text{m}}/R_{\text{M}})^2$ and $R_{\text{M}} = R_{\text{m}}/\sqrt{1-e^2}$ (see Fig. 2.3a). The polar equation of the non-rotated elliptic frame is given by

$$r_{\text{e}}(\varphi) = \frac{R_{\text{m}}}{\sqrt{1 - e^2\cos^2\varphi}}. \tag{2.4}$$

The first 2 coefficients from the Fourier-like expansion of the elliptic frame r_{e} are equal to

$$R_{\text{mean}}(e) = \frac{2}{\pi}K[e^2]R_{\text{m}}, \tag{2.5}$$

$$a_2(e) = \frac{2}{e^2}\left(2 - e^2 - \frac{E[e^2]}{K[e^2]}\right), \tag{2.6}$$

where $K[x], E[x]$ are the complete elliptic integrals of the first and second kind. a_k with higher k can be found in Section 2.3.7.1. Coefficients a_k with odd indices and all b_k are zero due to the symmetry at $\varphi = \pi$ and 2π of ellipses. Moreover, the perimeter of the ellipse is defined as $P = 4E[e^2]R_{\text{M}}$.

The clover frames are defined with $a_3 = -\varepsilon$ and all other Fourier coefficients from Equ. (2.3) equal to zero. The polar equation of the clover frames is given by

$$r_{\text{cl}}(\varphi) = R_{\text{mean}}(1 - \varepsilon\cos(3\varphi)). \tag{2.7}$$

2.2.2 Experiments

Minimal surfaces are studied using soap films held by 3D-printed frames with a set-up schematised in Fig. 2.4a. The position of the lower frame remains fixed during the experiment, while the upper frame, attached to a vertical translation stage, can move at variable speed between controlled positions via a home written Labview program. The lower frame is fixed on a laboratory scale (METTLER TOLEDO, precision: 0.1 g) to measure the force F_z exerted on the lower frame by the soap film in z-direction. The

ensemble is visualised from the side in front of a diffuse light source using a computer-controlled CCD camera with a spatial resolution of 50 µm. We performed experiments for two different elliptic frames: $e = 0.866$ ($R_M/R_m = 2$) and $e = 0.97$ ($R_M/R_m = 4$). The frames are fabricated by a thermoplastic 3D printer Form 2 from Formlabs. The used printing method was stereolithography with a layer thickness of 0.025 mm. The realtive deviation between the mathematical description, Equ.s (2.4) and (2.7), and the printed frame geometry is below 0.4%. Different mountings between the frame and the translation stage or the Rheometer where necessary. A picture of two frames with $e = 0.886$ and different mountings and a frame with $e = 0.97$ are shown in Fig. 2.4b. The used soap solution is optimised for film stability: 500 ml of water, 22.5 ml of the dish washing liquid "Fairy", 7.5 ml of Glycerol and 1.6 g Jlube. All ingredients are mixed for 24 hours using a magnetic stirrer. The age of the solutions is maximally three month. The surface tension is measured using a "Kibron V2" tensiometre and determined to be $\gamma = 25.7 \pm 0.5$ mN/m at a temperature of $T = 21 \pm 3\,^{\circ}\mathrm{C}$.

The minimal surface is produced by wetting the upper frame with the soap solution. Afterwards the upper frame is moved downwards until it touches the lower frame. The upper frame is moved up by a few millimetres and the lower frame is rotated by $-\varphi_0$. The distance h between the frames is then slowly increased in small intervals Δh and measurements are taken for the normal force and the shape. At each step, we checked whether the soap film still connects the two frames, since the film is draining and evaporating, which accelerate film rupture. For this reason, a humidifier was used to keep the humidity high. If the film looses the connection and a Goldschmidt solution is observed, the critical height $h^\star$ is measured by taking the average between the current h and the previous height giving a stable shape. Between each height change, at least five seconds wait time ensures static equilibrium of each shape. We improve the precision on $h^\star$ by decreasing Δh in its vicinity and by repeating measurements.

The images are treated by a home-made python code, which uses light intensity gradients to determine the distance h between the frames and the projected contour of the minimal surface.

Normal force F_z and vertical torque Γ_z are not measured simultaneously. The torque Γ_z is measured with a Discovery HR-3 hybrid rheometre holding the same bottom frame as in the normal force measurements and a frame with the same geometry but a different mounting for the top frame, see Fig. 2.4b and c. The Fig. 2.4c shows a picture of the rheometer during a measurement of Γ_z of a soap film between the two frames. The upper frame rotates with a small angular velocity during the measurement to cause a quasi-static deformation. The precision in the torque is 5 nNm. The uncertainties in the measured quantities are mainly influenced by the differences between the mathematical description of the contours and the actual shape of the frames, by imperfect alignment of the frames (centering and parallelism), the resolution and sharpness of the camera. Additional uncertainties are related to the precision of the scale. The final precision of the force F_z was around 5 μN.

2.2.3 Surface Evolver simulations

2.2.3.1 Numerical simulation

Surface Evolver is an open source Finite Element program which represents a surface via vertices, edges, facets and bodies [64]. Two vertices define an edge, three edges define a

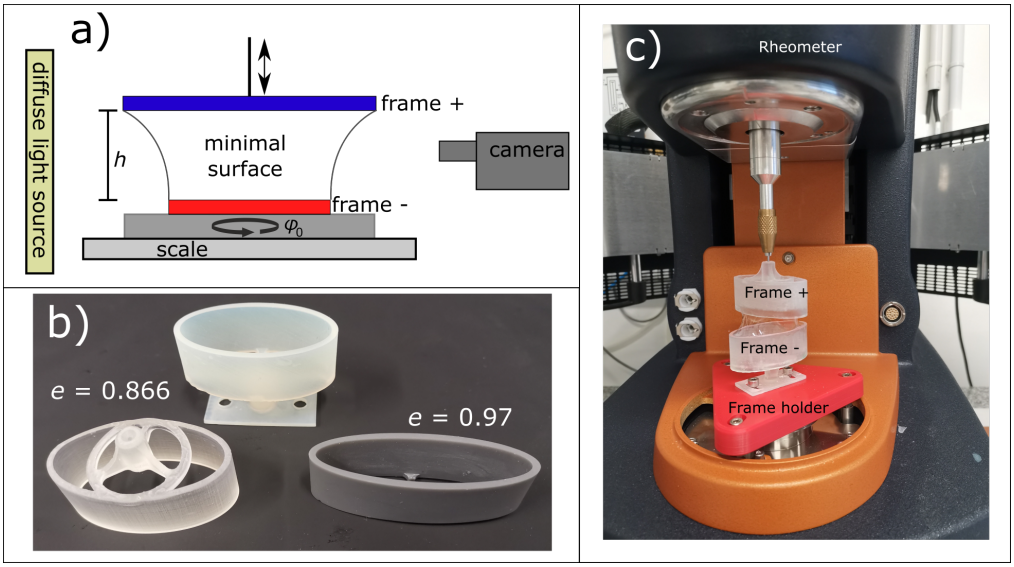

Figure 2.4: a) Scheme of the experimental set-up visualising soap films between 3D-printed identical frames whose separation is set by a vertical translation stage. The scale is used to measure the normal force F_z and a goniometer imposes a rotation angle φ_0 between the frames. b) Three examples of eliptical frames with different eccentricities and different mountings. c) The rheometer with the experimental setup to measure the torque around the z-axis.

facet and several facets define a body (Fig. 2.5. Different energy terms define the surface energy for every facet. The simplest case is if the surface energy is proportional to the facet size. Other constitutive laws are possible, which consider bending energies or surface elasticity [32]. Bodies have a specific mass, volume or pressure and are necessary to model bubbles or drops. Boundary conditions and constraints can be added. Afterwards Surface Evolver minimises the total energy by moving vertices of a defined shape in the opposite direction of the energy gradient by considering the given boundary conditions, constrains and masses, volumes and pressures.

The total energy is in the case of the catenoid proportional to the total area A, defined here as the sum of the facets areas multiplied with the surface tension. A body is not necessary since the volume or mass of the catenoid is variable and not fixed. Vertices on the frame stay fixed at the position defined by the Equ.s (2.4) or (2.7). We start with a model that fulfils only the most essential requirements, Fig. 2.5 upper left. Facets connect the two frames, whereby the vertices are fixed to the frames. The mesh is then refined and the surface is converged to a minimum, Fig. 2.5 upper right. This is repeated several times until the model has the required accuracy, Fig. 2.5 bottom. Afterwards, our simulation procedure is similar to the procedure in the experiment. The height h between the two frames is increased in small steps Δh until the surface becomes unstable. After each change of height the surface is relaxed by moving the vertices until the relative energy change is smaller than 10^{-10} after 100 such movements. The mesh is then optimised and the process is repeated until the relative change is again smaller than 10^{-10} after 100 relaxations. Iterations between these two steps stop if the convergence criterion is met twice in a row. To avoid that the system is trapped in a local minimum, all vertices are randomly moved by a small distance ("jiggled") at least twice during the relaxation process.

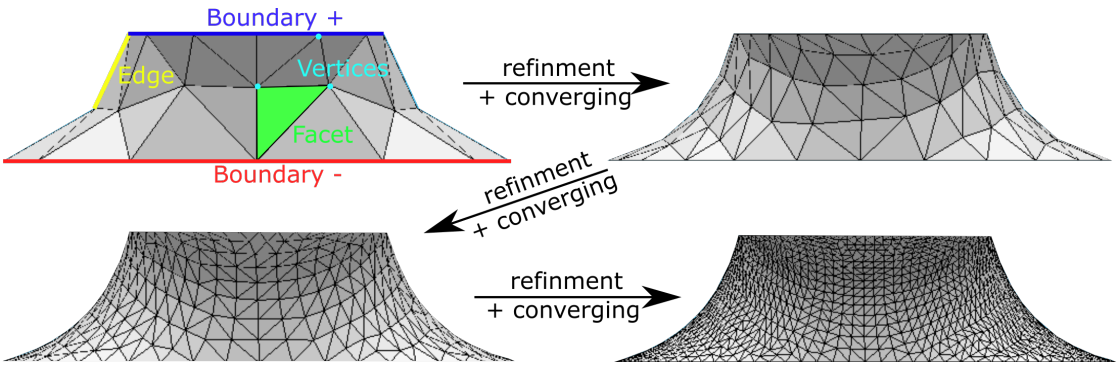

Figure 2.5: A surface evolver model at different confinement states is shown. Vertices, an edge, a facet and the upper and the lower bound at the original surface are represented in different colours.

We investigate numerically elliptic frames of various eccentricities e, clover frames with different ε and mixed frames with for example a elliptical upper and a clover bottom frame.

2.2.3.2 Stability and hessian matrix

To obtain the best precision in the critical height $h^\star$ we use the Hessian matrix $\underline{H}$ of the area functional A. The Taylor development of the area A at fixed h and φ_0 up to the second order is given by [65]

$$A(\vec{X}+\delta\vec{X}) = A(\vec{X}) + \nabla A \cdot \delta\vec{X} + \frac{1}{2}\delta\vec{X}^T \underline{H} \delta\vec{X}. \tag{2.8}$$

The free coordinates $\vec{X}$ are defined by the number of facets and their ability to change A by a small perturbation of the coordinates of the vertices. If A represents an extremal surface then $\nabla A = 0$. For it to be a minimum (and hence physically stable) all eigenvalues λ of $\underline{H}$ have to be strictly positive. Surface evolver can numerically determine any number of eigenvalues of $\underline{H}$ in ascending order. We calculated only the smallest five eigenvalues, Since the smallest eigenvalue has already all information's about the stability of the surface.

The smallest eigenvalue $\lambda_{\min}$ at a critical surface is zero. A critical surface is the first unstable extrema or the last stable extrema surface. To check the stability of the critical point, higher derivatives of A in respect to $\vec{X}$ must be analysed. If the critical area is known, the plateau problem is answered. We search the critical surface with Surface Evolver by increasing the distance between the two frames step by step and calculating the smallest eigenvalues for the converged surfaces. To get a good approximation of the critical surface the evolution of the smallest eigenvalue with increasing height of the last stable shapes is extrapolated to find the critical surface with $h(\lambda_{\min} = 0) = h^\star$.

$h^\star$ obtained with Surface Evolver depends on the number of facets. The precision increases with increasing number of facets. Fig. 2.6 compares catenoids modeled with Surface Evolver with different amounts of facets N. The evolution of λ_{min} is multiplied with the number of facets N and plotted against the relative distance to the known $h^\star$ for the catenoid in Fig. 2.6a with semilog scale and in Fig. 2.6b with loglog scale. To compare different surfaces with different amounts of facets, it is necessary to multiply

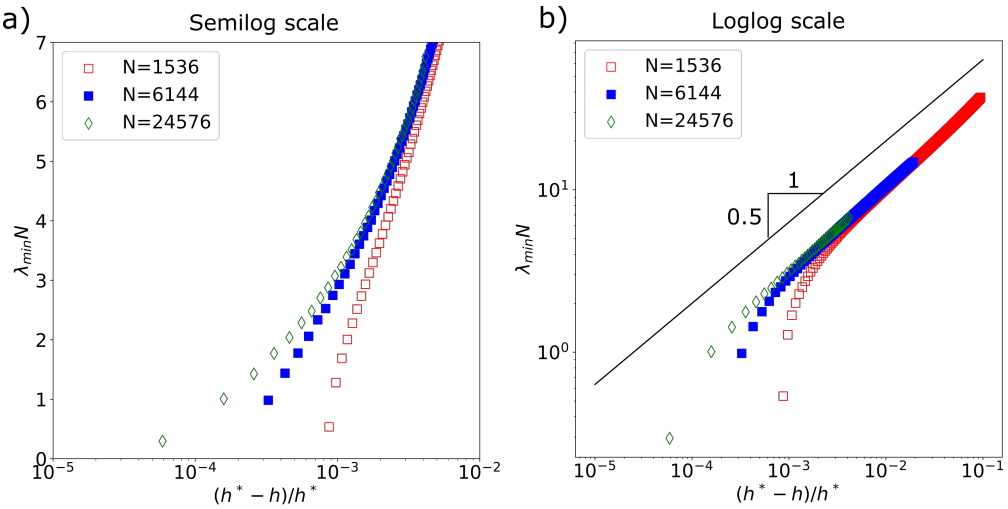

Figure 2.6: Smallest eigenvalue $\lambda_{\min}$ (multiplied by the number of facets N) of the Hessian matrix $\underline{H}$ of the total energy in Surface Evolver for different numbers of facets N in the case of the axisymmetric catenoid, as a function of the reduced height $(h^\star - h)/h^\star$, where $h^\star$ is the critical height of the axisymmetric catenoid. As the value of the latter is known exactly, the error for other simulations can be estimated depending on the number of facets used in this graph. a) and b) show the same data, a) in log scale for the x-axis and b) in log scale for both axis.

$\lambda_{\min}$ with N, since λ is proportional to N. One observes with increasing number of facets N the relative error for the obtained critical height is converging towards zero in Fig. 2.6a. It also shows that the relative error is already small ($< 0.04\%$) for a relatively small number of facets ($N = 1536$). While there is a certain flexibility as far as defining the $\delta\vec{X}$ degrees of freedom, the moment where the Hessian becomes singular should be independent of such choice, up to numerical errors. This validates the general procedure and provides at the same time an estimation of the precision of the simulation. In Fig. 2.6b we observe that $h^\star - h$ is proportional to $\lambda^2_{\min}$ close to $h^\star$.

2.2.3.3 Force and torque

The normal force F_z and the torque Γ_z on the axis passing by the two frame centers are related via

$$\gamma \mathrm{d}A = \Gamma_z(\varphi_0, h)\mathrm{d}\varphi_0 + F_z(\varphi_0, h)\mathrm{d}h. \tag{2.9}$$

The force and the torque applied on the frame are the same along the surface. The derivatives $\mathrm{d}A$, $\mathrm{d}\varphi_0$ and $\mathrm{d}h$ are approximated by finite differences of two simulated surfaces with a small change in h or φ_0. The precision of these calculations depends strongly on the precision of the total area minimum, which, in turn, depends on the number of facets and the iteration process.

2.2.4 Implementation of the Alimov *et al.* method [1]

We implemented the algorithm described in [1] using Python code. The code correctness of the implementation was tested by comparing the critical heights, critical areas and the shape parameters to the values given by Alimov *et al.* [1] in their Supplemental

Materials. All values of the table were reproduced with a relative difference smaller than 5.10^{-5}. The authors introduce a parameter called Ψ_B that we found directly proportional to the vertical component of the force exerted on the lower frame by the soap film. The convergence criterion used in the paper, which is based on the stability of the second coefficient C_2 in the Laurent series expansion had to be generalised for the clover case, for which C_2 remains zero. This method can only be used for identical, convex upper and lower frames.

2.3 Perturbation theory

Here we present a new perturbation approach to approximate minimal surfaces close to the catenoid. The two frames can be of different shapes, in contrast to the model presented by Alimov *et al.* [1].

The computation of the perturbation theory concerning the non-axisymmetric minimal surface consists in solving the minimal surface differential equation, corresponding to a vanishing mean curvature. We start by recalling the form of this partial differential equation in cylindrical coordinates, then we present in the general case the perturbative scheme we have developed to solve this equation and we discuss the conditions of the existence of a surface. Finally we show how the perturbative approach allows us to calculate the normal force and the torque exerted by the minimal surface on the contours.

2.3.1 Notations and minimal surface differential equation

First, the coordinates of the vector position $\vec{r}$ are defined as follows

$$x(\varphi, z) = r(\varphi, z)\cos\varphi \tag{2.10}$$
$$y(\varphi, z) = r(\varphi, z)\sin\varphi \tag{2.11}$$
$$z(\varphi, z) = z. \tag{2.12}$$

We will use the classical notations

$$\vec{r}_{,i}(\varphi, z) = \frac{\partial \vec{r}}{\partial i} \tag{2.13}$$
$$\vec{r}_{,ij}(\varphi, z) = \frac{\partial^2 \vec{r}}{\partial i \partial j}, \tag{2.14}$$

with $i, j = \varphi, z$. The normal vector to the surface can be calculated thanks to its definition $\vec{n} = \vec{r}_{,z} \times \vec{r}_{,\varphi} / \left\| \vec{r}_{,z} \times \vec{r}_{,\varphi} \right\|$

$$\vec{n} = \frac{1}{\left(r^2 + r_{,\varphi}^2 + r^2 r_{,z}^2\right)^{1/2}} \begin{pmatrix} -r\cos\varphi - r_{,\varphi}\sin\varphi \\ -r\sin\varphi + r_{,\varphi}\cos\varphi \\ r r_{,z} \end{pmatrix} \tag{2.15}$$

Then, the coefficients of the first fundamental form $\mathcal{F}_1$ are computed

$$E = \vec{r}_{,z}.\vec{r}_{,z} = 1 + r_{,z}^2 \; ; \; G = \vec{r}_{,\varphi}.\vec{r}_{,\varphi} = r^2 + r_{,\varphi}^2 \; ; \tag{2.16}$$
$$F = \vec{r}_{,z}.\vec{r}_{,\varphi} = r_{,\varphi} r_{,z}, \tag{2.17}$$

as well as those of the second fundamental form $\mathcal{F}_2$

$$L = \vec{r}_{,zz}.\vec{n} = \frac{-rr_{,zz}}{\left(r^2 + r_{,\varphi}^2 + r^2 r_{,z}^2\right)^{1/2}}; \tag{2.18}$$

$$N = \vec{r}_{,\varphi\varphi}.\vec{n} = \frac{r^2 + 2r_{,\varphi}^2 - rr_{,\varphi\varphi}}{\left(r^2 + r_{,\varphi}^2 + r^2 r_{,z}^2\right)^{1/2}}; \tag{2.19}$$

$$M = \vec{r}_{,z\varphi}.\vec{n} = \frac{r_{,\varphi}r_{,z} - rr_{,z\varphi}}{\left(r^2 + r_{,\varphi}^2 + r^2 r_{,z}^2\right)^{1/2}}. \tag{2.20}$$

So the expression of the mean H and Gaussian K curvature arises from these six coefficients

$$H = \frac{1}{2}\left(H_1 + H_2\right) = \frac{EN + GL - 2FM}{EG - F^2}, \tag{2.21}$$

$$K = H_1 H_2 = \frac{LN - M^2}{EG - F^2}. \tag{2.22}$$

The two principal curvatures H_1 and H_2 are then given by:

$$H_1 = H + \sqrt{H^2 - K}, \tag{2.23}$$

$$H_2 = H - \sqrt{H^2 - K}. \tag{2.24}$$

The following partial differential equation results from this vanishing mean curvature problem defining minimal surfaces (same equation as Equ. (1.5) only in cylindrical coordinates)

$$\begin{aligned} r_{,\varphi}^2 + r\Big[r\left(1 + r_{,z}^2\right) - r_{,\varphi\varphi}\left(1 + r_{,z}^2\right) - r^2 r_{,zz} \\ + r_{,\varphi}\left(2r_{,z}r_{,z\varphi} - r_{,\varphi}r_{,zz}\right)\Big] = 0. \end{aligned} \tag{2.25}$$

If we suppose that the minimal surface is invariant by rotation (corresponding to $r_{,\varphi} = r_{,\varphi\varphi} = 0$), we obtain

$$1 + r_{,z}^2 - rr_{,zz} = 0. \tag{2.26}$$

The solution of this equation is simply the symmetric catenoid for $z \in [-h/2; h/2]$, which was given in Equ. (1.6). The more general case of asymmetric minimal surface spanning on circular frames of different radius R_1 and R_2 is discussed in more detail in the following Section 2.3.2.

It is worthwhile to mention that the Equ. (2.25) corresponds to the Euler-Lagrange equations minimising the surface formula

$$S[r(\varphi, z)] = \int_{-h/2}^{h/2} \mathrm{d}z \oint \mathrm{d}\varphi \sqrt{r^2 + r_{,\varphi}^2 + r^2 r_{,z}^2}, \tag{2.27}$$

which is Equ. (1.1) in cylindrical coordinates for a catenoid. This Lagrangian interpretation of this optimisation problem allows to anticipate the conservation of a pseudo energy function, namely the fact that

$$a_h = \oint \frac{\mathrm{d}\varphi}{2\pi} \frac{r^2 + r_{,\varphi}^2}{\sqrt{r^2 + r_{,\varphi}^2 + r^2 r_{,z}^2}} \tag{2.28}$$

is a constant independent of z (along the true minimal surface). If the solution for the axisymmetric catenoid is plugged in this equation, one recovers for a_h the neck radius a_c introduced in Equ. (1.6).

2.3.2 Asymmetric catenoid

The asymmetric catenoid is important for some interpretation considering $\varphi_0 \neq 0$ and for a more general perturbation theory with non-identical top and bottom frames. For the asymmetric catenoid, we have to introduce a new constant C_c as

$$r_c(z) = a_c \cosh\left(\frac{z}{a_c} + C_c\right). \tag{2.29}$$

It shifts the neck away from mid-plane with $z = 0$. Consequently, it is zero for the symmetric catenoid. a_c and C_c are now solutions of

$$\begin{aligned} R_+ &= a_c \cosh\left(\frac{h}{2a_c} + C_c\right), \\ R_- &= a_c \cosh\left(-\frac{h}{2a_c} + C_c\right), \end{aligned} \tag{2.30}$$

with R_+ and R_- the radius of the upper and lower frame. The existence of solutions is discussed in detail in [61]. Fig. 2.7 shows how the $a(h)$ function changes with the ratio R_-/R_+, how the critical neck radius $a^\star$ and height $h^\star$ depend on each other and on R_-/R_+ and distinguish between stable and unstable asymmetric catenoids. $h^\star/a_c^\star$ for a given R_-/R_+ is obtained with [61]

$$\begin{aligned} \tanh\left(\frac{h^\star}{a_c^\star}\right) = \frac{h^\star}{a_c^\star}\left(2\frac{R_-}{R_+}\cosh\left(\frac{h^\star}{a_c^\star}\right) - 1 - \frac{R_-^2}{R_+^2}\right) / \\ \left[\frac{R_-}{R_+}\left(2\cosh\left(\frac{h^\star}{a_c^\star}\right) + \frac{h^\star}{a_c^\star}\sinh\left(\frac{h^\star}{a_c^\star}\right)\right) - 1 - \frac{R_-^2}{R_+^2}\right]. \end{aligned} \tag{2.31}$$

Equ.s (2.30) and the result of Equ. (2.31) gives the relation between the $a^\star$ and $h^\star$ for different R_-/R_+, the black dotted line in Fig. 2.7 [61].

2.3.3 General perturbative approach for arbitrary frames

We start here with a general description for the perturbation approach near the catenoid. Therefore we use the arbitrary planar closed boundary contours $\mathcal{C}_\pm$ for the upper and lower frame, given in polar coordinates $r_{\mathcal{C}_\pm}(\varphi)$, as described in Section 2.2.1 and assume that it is possible to do a Fourier decomposition, as in Equ. (2.2).

The idea of the perturbative approach is to solve Equ. (2.25) considering surfaces close to the asymmetric catenoid. Therefore we take Equ. (2.29) and write the minimal surface shape in the form of

$$r(\varphi, z) = a\cosh\left(\frac{z}{a} + C\right)(1 + f(\varphi, z)), \tag{2.32}$$

and consider $f(\varphi, z)$ as a perturbative term.

Rewriting the Equ. (2.25) on f and restricting it to the first order in f, we end up with a linear differential equation in the form (the non linear differential equation is given

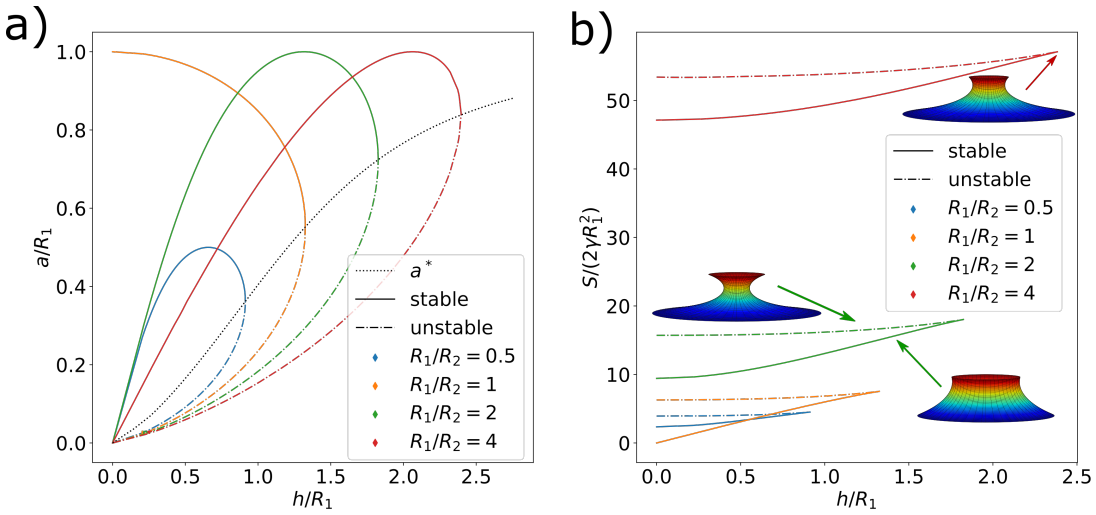

Figure 2.7: Same as Fig. 2.2 for the asymmetric catenoid. In a) the neck radius is plotted against the normalised height and in b) the free energy $\mathcal{E}$ against the height. The solid lines show the stable catenoids and the dashed lines the unstable catenoids. The different colors represent different ratio R_-/R_+. The dependency of the critical neck radius $a^\star$ on the critical height $h^\star$ is represented with the black dotted line.

only for identical frames in Section 2.3.4) [1]

$$2f(\varphi,z)+\cosh^2\left(\frac{z}{a}+C\right)\left(f_{,\varphi\varphi}(\varphi,z)+a^2 f_{,zz}(\varphi,z)\right)=0. \tag{2.33}$$

To solve this equation, let us decompose f in Fourier series

$$f(\varphi,z)=\sum_{k=1}^{+\infty}\alpha_k(z)\cos(k\varphi)+\beta_k(z)\sin(k\varphi). \tag{2.34}$$

Introducing this expansion in Equ. (2.33), we obtain the following equations for the different modes

$$\begin{aligned}\left(2-k^2\cosh^2\left(\frac{z}{a}+C\right)\right)\alpha_k(z)+a^2\cosh^2\left(\frac{z}{a}+C\right)\alpha_k''(z)=0,\\ \left(2-k^2\cosh^2\left(\frac{z}{a}+C\right)\right)\beta_k(z)+a^2\cosh^2\left(\frac{z}{a}+C\right)\beta_k''(z)=0,\end{aligned} \tag{2.35}$$

which can be solved to a given order k_0, with boundary conditions on α_k and β_k which are given by the geometry of the frames (boundary condition)

$$\begin{aligned}r(\varphi,h/2)=r_{\mathcal{C}+}(\varphi),\\ r(\varphi,-h/2)=r_{\mathcal{C}-}(\varphi),\end{aligned} \tag{2.36}$$

[1] This equation can also be obtained from the Euler-Lagrange equation of the second-order expansion of Equ. (2.27) with respect to f, which reads : $S[f]=\frac{a}{2}\int_{-h/2}^{h/2}\mathrm{d}z\oint\mathrm{d}\varphi[f_{,\varphi}^2+(af_{,z})^2-2f^2\mathrm{sech}^2(z/a)]$ plus boundary terms.

leading to, using the boundary conditions above as well as Equ.s (2.32) and (2.34)

$$
\begin{aligned}
a\cosh\left(C+\frac{h}{2a}\right) &= R^{+}_{\text{mean}}, && (2.37)\\
a\cosh\left(C-\frac{h}{2a}\right) &= R^{-}_{\text{mean}}, && (2.38)\\
\alpha_k\left(\pm h/2\right) &= a_k\pm, && (2.39)\\
\beta_k\left(\pm h/2\right) &= b_k^{\pm}. && (2.40)
\end{aligned}
$$

For the different geometries investigated below, the differential Equ.s (2.35) were solved using Python (function solve_bvp from scipy package).

Finally, It is interesting to note that for high order $k \gg 1$, Equ.s (2.35) can be simplified using $k^2\cosh^2 z/a + C \gg 2$ leading to much simpler homogeneous linear second order equations

$$
\begin{aligned}
-k^2\alpha_k\left(z\right)+a^2\alpha_k''\left(z\right)=0, && (2.41)\\
-k^2\beta_k\left(z\right)+a^2\beta_k''\left(z\right)=0. && (2.42)
\end{aligned}
$$

The solutions for these approximated differential equations are then

$$
\begin{aligned}
\tilde{\alpha}_k\left(z\right) &= \frac{a_k^{-}\sinh\left(\frac{k}{a}\left(\frac{h}{2}-z\right)\right)+a_k^{+}\sinh\left(\frac{k}{a}\left(\frac{h}{2}+z\right)\right)}{\sinh\left(\frac{kh}{a}\right)}\\
\tilde{\beta}_k\left(z\right) &= \frac{b_k^{-}\sinh\left(\frac{k}{a}\left(\frac{h}{2}-z\right)\right)+b_k^{+}\sinh\left(\frac{k}{a}\left(\frac{h}{2}+z\right)\right)}{\sinh\left(\frac{kh}{a}\right)}.
\end{aligned}
\qquad (2.43)
$$

2.3.4 General perturbation solution for identical frames with φ_0

Here we solve Equ. (2.25) considering boundary contours which are small perturbations of a circle and identical for the bottom and top frames. The Equ. (2.32) simplifies to

$$
r\left(\varphi,z\right)=a\cosh\left(\frac{z}{a}\right)\left(1+f\left(\varphi,z\right)\right), \qquad (2.44)
$$

since $C = 0$ due to $R^{+}_{\text{mean}} = R^{-}_{\text{mean}}$ and Equ.s (2.37) and (2.38). Rewriting Equ. (2.25) considering the ansatz with f from Equ. (2.44) one obtains

$$\frac{1}{2}\left(a^2 f_{,zz} - 2\cosh\left(\frac{z}{a}\right)^2 f_{,\varphi\varphi} - 4f\right) \tag{2.45}$$

$$\begin{aligned} &+ \frac{1}{2}\left[-10f^2 + 2\left(-a\sinh\left(\frac{2z}{a}\right) f_{\theta\theta} f_{,z} + \cosh\left(\frac{z}{a}\right)^2 \left(f_{,\varphi}^2 + a^2 f_{,z}^2\right) + a\sinh\left(\frac{2z}{a}\right) f_{,\varphi} f_{,z\varphi}\right)\right. \\ &+ \left. f\left(\left(1 - 3\cosh\left(\frac{2z}{a}\right)\right) f_{,\varphi\varphi} - 6a^2\cosh\left(\frac{z}{a}\right)^2 f_{,zz}\right)\right] \end{aligned} \tag{2.46}$$

$$\begin{aligned} &+ \left[-4f^3 + f\left(\left(-3 + \cosh\left(\frac{2z}{a}\right)\right) f_{,\varphi}^2 + 2a f_{,z}\left(-\sinh\left(\frac{2z}{a}\right) f_{,\varphi\varphi} + a\cosh\left(\frac{z}{a}\right)^2 f_{,z}\right)\right)\right. \\ &+ 2a\sinh\left(\frac{2z}{a}\right) f_{,\varphi} f_{,z\varphi}\Big) - 3f^2\left(\sinh\left(\frac{z}{a}\right)^2 f_{,\varphi\varphi} + a^2\cosh\left(\frac{z}{a}\right)^2 f_{,zz}\right) \\ &- \left. a^2\cosh\left(\frac{z}{a}\right)^2 \left(f_{,\varphi\varphi} f_{,z}^2 + f_{,\varphi}\left(-2f_{,z} f_{,z\varphi} + f_{,\varphi} f_{,zz}\right)\right)\right] \end{aligned} \tag{2.47}$$

$$\begin{aligned} &+ \left[-\frac{1}{2} f\left(2f^3 - f\left(\left(-3 + \cosh\left(\frac{2z}{a}\right)\right) f_{,z}^2 + 2a f_{,z}\left(-\sinh\left(\frac{2z}{a}\right) f_{,\varphi\varphi} + a\cosh\left(\frac{z}{a}\right)^2 f_{,z}\right)\right.\right. \\ &+ 2a\sinh\left(\frac{2z}{a}\right) f_{,\varphi} f_{,z\varphi}\Big) + 2f^2\left(\sinh\left(\frac{z}{a}\right)^2 f_{,\varphi\varphi} + a^2\cosh\left(\frac{z}{a}\right)^2 f_{,zz}\right) \\ &+ \left.\left. 2a^2\cosh\left(\frac{z}{a}\right)^2 \left(f_{,\varphi\varphi} f_{,z}^2 + f_{,\varphi}\left(-2f_{,z} f_{,z\varphi} + f_{,\varphi} f_{,zz}\right)\right)\right)\right] \end{aligned} \tag{2.48}$$

$$= 0,$$

with Equ. (2.45) the first order terms in f, Equ. (2.46) the second order terms in f, Equ. (2.47) the third order terms in f and Equ. (2.48) the forth order terms in f. In the following, we consider only the first order terms in f Equ. (2.45) and end up with a linear differential equation with a similar form as for the arbitrary frames in Equ. (2.33)

$$2f(\varphi, z) + \cosh^2\left(\frac{z}{a}\right)\left(f_{,\varphi\varphi}(\varphi, z) + a^2 f_{,zz}(\varphi, z)\right) = 0. \tag{2.49}$$

The procedure to solve Equ. (2.49) is the same as for Equ. (2.33), f is decomposed into a Fourier series and introduced in Equ. (2.49). One obtains Equ.s (2.35) with $C = 0$, which can be solved independently for each order k, with different boundary conditions for α_k and β_k.

The boundary conditions for the minimal surface are introduced with Equ.s (2.36), which, in the case of two identical frames, leads to

$$a\cosh\left(\frac{h}{2a}\right)\left(1 + \alpha_0(\pm\frac{h}{2})\right) = R_{\text{mean}}, \tag{2.50}$$

$$\alpha_k(\pm h/2) = a_k\cos\left(k\frac{\varphi_0}{2}\right) \mp b_k\sin\left(k\frac{\varphi_0}{2}\right), \tag{2.51}$$

$$\beta_k(\pm h/2) = \pm a_k\sin\left(k\frac{\varphi_0}{2}\right) + b_k\cos\left(k\frac{\varphi_0}{2}\right). \tag{2.52}$$

The Ansatz (2.44) embodies a small departure (with $|f| \ll 1$) from a reference catenoid characterized by its parameter a. A convenient choice for this reference catenoid is obtained by taking $\alpha_0(\pm h/2) = 0$: In this case the boundary radius of this reference catenoid is given by the mean radius R_{mean} of the actual elliptic or clover contour (compare Equ.s (2.50) with (2.1)). As the solution for $\alpha_0(z)$ is known and equal to $\alpha_0^{(1)} \tanh(z/a) + \alpha_0^{(2)}((z/a)\tanh(z/a) - 1)$ (with $\alpha_0^{(1,2)}$ some constants), the constraints $\alpha_0(\pm h/2) = 0$ imply $\alpha_0(z) = 0$. It is worth noting that this approximation entails therefore that the φ-averaged radius $(2\pi)^{-1} \oint r \mathrm{d}\varphi$ describes the reference catenoid.

For a given frame we therefore need to calculate the coefficients a_k and b_k up to an order of Fourier expansion k_M, and then solve the differential Equ. (2.35) with the boundary conditions (2.51) and (2.52). Since the shape is completely defined with a_k and b_k, all properties of the surface, like normal forces and torque can be calculated now. Equ. (2.50) (with $\alpha_0 = 0$) generalizes the condition of existence of the catenoid to more general frames leading to the theoretical critical height $h^\star_{\text{theo}}$

$$h^\star_{\text{theo}} = \mu^\star R_{\text{mean}}. \tag{2.53}$$

When $h < h^\star_{\text{theo}}$, Equ. (2.50) has two solutions for a, just like the catenoid case. By comparing Equ.s (2.50) and (1.6), one observes an equivalence between R_{mean} and r_c of the catenoid Equ. (1.6). As the zero order Fourier coefficient R_{mean} is independent of φ_0 or e, at this level of perturbation, the criterion of existence is independent of the angle φ_0 and e.

2.3.5 Force and torque predictions

The force and the torque applied by the minimal surface on the frames can also be computed thanks to the perturbation theory. The elementary surface tension force acting on a length element $\mathrm{d}\ell \vec{t}_{\mathcal{C}_\pm}$ along a contour $\mathcal{C}_\pm$ is given by

$$\mathrm{d}\vec{F}_{\mathcal{C}_\pm} = 2\gamma \vec{t}_{\mathcal{C}_\pm} \wedge \vec{n} \mathrm{d}\ell, \tag{2.54}$$

where $\vec{n}$ is the vector normal to the surface and $\vec{t}_{\mathcal{C}_\pm}$ is the tangent to the frames $\mathcal{C}_\pm$. The total force acting on the contour is obtained with

$$\frac{F_{x\mathcal{C}_\pm}}{2\gamma} = \int_0^{2\pi} \mathrm{d}\varphi \frac{-r(\varphi, \pm h/2)\, r_{,z}(\varphi, \pm h/2) \left(r'_{\mathcal{C}_\pm}(\varphi)\sin\varphi + r_{\mathcal{C}_\pm}(\varphi)\cos\varphi\right)}{\sqrt{r(\varphi, \pm h/2)^2 \left(1 + r_{,z}(\varphi, \pm h/2)^2\right) + r_{,\varphi}(\varphi, \pm h/2)^2}}, \tag{2.55}$$

$$\frac{F_{y\mathcal{C}_\pm}}{2\gamma} = \int_0^{2\pi} \mathrm{d}\varphi \frac{r(\varphi, \pm h/2)\, r_{,z}(\varphi, \pm h/2) \left(r'_{\mathcal{C}_\pm}(\varphi)\cos\varphi - r_{\mathcal{C}_\pm}(\varphi)\sin\varphi\right)}{\sqrt{r(\varphi, \pm h/2)^2 \left(1 + r_{,z}(\varphi, \pm h/2)^2\right) + r_{,\varphi}(\varphi, \pm h/2)^2}}, \tag{2.56}$$

$$\frac{F_{z\mathcal{C}_\pm}}{2\gamma} = \int_0^{2\pi} \mathrm{d}\varphi \frac{\left(r_{,\varphi}(\varphi, \pm h/2)\, r'_{\mathcal{C}_\pm}(\varphi) + r(\varphi, \pm h/2)\, r_{\mathcal{C}_\pm}(\varphi)\right)}{\sqrt{r(\varphi, \pm h/2)^2 \left(1 + r_{,z}(\varphi, \pm h/2)^2\right) + r_{,\varphi}(\varphi, \pm h/2)^2}}. \tag{2.57}$$

It is possible to give a geometrical interpretation of this force. At equilibrium, the force can be computed on any closed contour $\mathcal{C}$ not reducible to a point by calculating $2\gamma \oint_{\mathcal{C}} \vec{n} \wedge \vec{t}_{\mathcal{C}} \mathrm{d}\ell$, where $\vec{t}_{\mathcal{C}}$ is the tangent to the contour and $\mathrm{d}\ell$ is an element of length

tangent to the contour. There is a particular contour, $\mathcal{C}_{\text{neck}}$, for which at any point the normal to the surface is horizontal, which generalises the notion of the "neck" for the catenoid. In the case of a catenoid it is a circle in the mid-plane, whereas for arbitrary frames this contour is more complex, generally not restricted to the mid-plane and in some cases, can be discontinuous. When this contour is fully contained in the minimal surface, the z component of the force can be calculated using the simple expression

$$F_z = 2\gamma P_{\mathcal{C}_\parallel}, \tag{2.58}$$

where $P_{\mathcal{C}_\parallel}$ is the perimeter of $\mathcal{C}_\parallel$, the projection of $\mathcal{C}_{\text{neck}}$ onto the median plane. F_z is therefore a direct measure of the perimeter of the projection onto the median plane of the locus of points where the normal to the surface is horizontal.
The torque can be calculated using $\mathrm{d}\vec{\Gamma}_{\mathcal{C}_\pm} = \vec{r}_{\mathcal{C}_\pm} \wedge \mathrm{d}\vec{F}_{\mathcal{C}_\pm}$, leading to the components in x, y and z defined in clockwise direction with

$$\Gamma_{x\mathcal{C}_\pm} = 2\gamma \int_{\mathcal{C}_\pm} r_{\mathcal{C}_\pm}(\varphi) \sin\varphi \mathrm{d}F_{z\mathcal{C}_\pm} - z(\varphi)\mathrm{d}F_{y\mathcal{C}_\pm}, \tag{2.59}$$

$$\Gamma_{y\mathcal{C}_\pm} = 2\gamma \int_{\mathcal{C}_\pm} z(\varphi)\mathrm{d}F_{x\mathcal{C}_\pm} - r_{\mathcal{C}_\pm}(\varphi) \cos\varphi \mathrm{d}F_{z\mathcal{C}_\pm}, \tag{2.60}$$

$$\Gamma_{z\mathcal{C}_\pm} = 2\gamma \int_{\mathcal{C}_\pm} r_{\mathcal{C}_\pm}(\varphi) \left(\sin\varphi \mathrm{d}F_{x\mathcal{C}_\pm} - \cos\varphi \mathrm{d}F_{y\mathcal{C}_\pm}\right). \tag{2.61}$$

Since the perturbative theory does not give an exact minimal surface, the force equilibrium is not perfectly fulfilled and the calculated force and torque are slightly depending on the integration contour.

2.3.6 Case $h = 0$

In the case $h = 0$ the minimal surface is perfectly known. If $\varphi_0 = 0$ and the upper frame and lower frame are identical, then it is an infinitely thin cylinder generated by the frame. In that case the force is simply proportional to the perimeter of the ellipse $F_z = 2\gamma P$.

If $\varphi_0 \neq 0$ the minimal surface is planar and consists in symmetric difference $\mathcal{S}_+ \Delta \mathcal{S}_- = \mathcal{S}_+ \cup \mathcal{S}_- - \mathcal{S}_+ \cap \mathcal{S}_-$ of the surface of the two frames (see Fig. 2.8 in the elliptic case) and the force is vanishing. Therefor $\mathcal{S}_+$ is the planar surface inside of the upper frame and $\mathcal{S}_-$ of the lower frame.

In the case of elliptic frame it is easy to calculate the area of the symmetric difference that is proportional to the energy of the film

$$\begin{aligned}\mathcal{E}(\varphi_0) = \quad & 2\gamma \frac{4R_{\text{m}}^2}{\sqrt{1-e^2}} \left[\arctan\left(\frac{\cot\frac{\varphi_0}{2}}{\sqrt{1-e^2}}\right)\right. \\ & \left. + \arctan\left(\frac{\tan\frac{\varphi_0}{2}}{\sqrt{1-e^2}}\right) - \frac{\pi}{2}\right].\end{aligned} \tag{2.62}$$

By deriving this relation with respect to φ_0 (see Equ. (2.9)), we obtain the torque

$$\Gamma_z(\varphi_0) = 2\gamma \frac{8R_{\text{m}}^2 e^2 \cos(\varphi_0)}{(e^2-2)^2 - e^4\cos^2(\varphi_0)}. \tag{2.63}$$

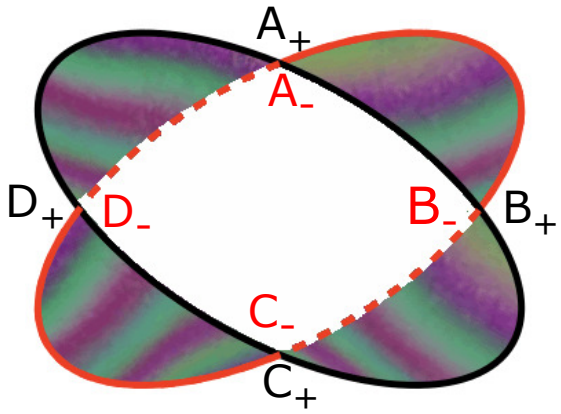

Figure 2.8: In the case $h = 0$ the soap film consists in the symmetric difference $\mathcal{S}_+ \Delta \mathcal{S}_-$ of the surface of the two frames as shown in the elliptic case. The points of intersection between the two frames for $h = 0$ become the points A_+, B_+, C_+ and D_+ (respectively A_-, B_-, C_- and D_-) for the top (respectively bottom) frame when $h \neq 0$.

2.3.7 Application to different frames

2.3.7.1 Elliptical contours

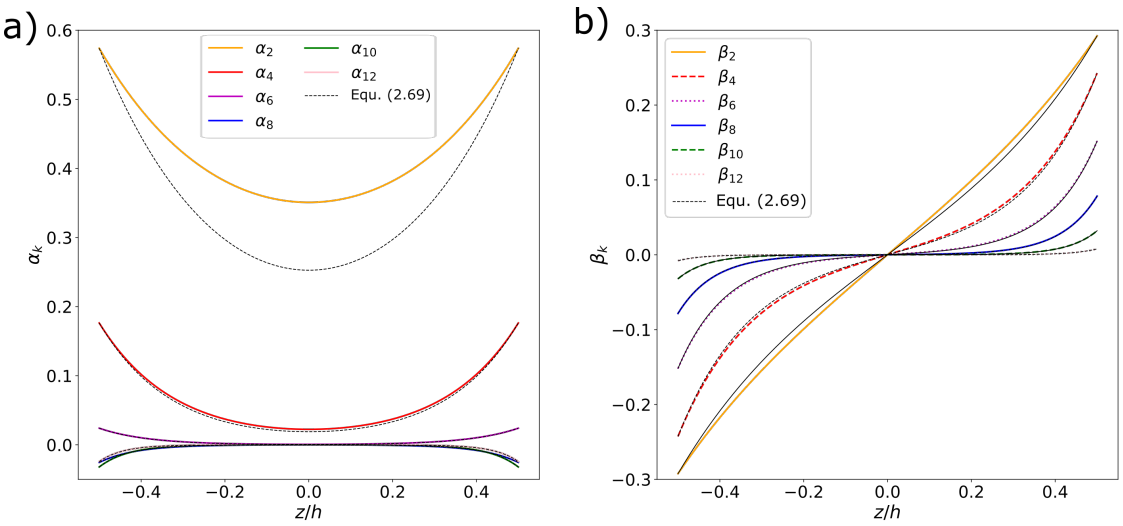

Figure 2.9: Solution of the differential Equ.s (2.35) for $\alpha_k(z)$ (a) and $\beta_k(z)$ (b) for $k \leq 12$, elliptic frames, $e = 0.97$, $h = 0.5$ ($R_{\mathrm{M}} = 1$, $R_{\mathrm{m}} = 0.24$) and $\varphi_0 = 0.3\pi/2$. The black dashed lines are the approximation for $k \gg 1$, Equ. (2.69).

A special case of the description developed above would be a minimal surface supported by ellipses of eccentricity e, major axis $2R_{\mathrm{M}}$, and minor axis $2R_{\mathrm{m}}$, introduced already in Section 2.2.1. We will also need the perimeter of the ellipse that is given by $P = 4E[e^2]R_{\mathrm{M}}$.

The Fourier transform of the ellipse gives $r_{\mathrm{e}}(\varphi) = R_{\mathrm{mean}}\left(1 + \sum_{k=2}^{+\infty} a_{\mathrm{k}}(e)\cos(k\varphi)\right)$. For odd k, $a_k(e)$ is zero due to the symmetry of the ellipse about the Ox axis. The first Fourier coefficients are equal to

$$
\begin{aligned}
R_{\text{mean}}(e) &= \frac{2}{\pi} K\left[e^2\right] R_{\text{m}}, && (2.64)\\
a_2(e) &= \frac{2}{e^2}\left(2 - e^2 - \frac{E\left[e^2\right]}{K\left[e^2\right]}\right), && (2.65)\\
a_4(e) &= \frac{2}{3e^4}\left(16 - 16e^2 + 3e^4 - 8\frac{(2 - 3e^2 + e^4)}{(1 - e^2)}\frac{E\left[e^2\right]}{K\left[e^2\right]}\right), && (2.66)\\
a_6(e) &= \frac{2}{15e^6}\left(256 - 384e^2 + 158e^4 - 15e^6\right. && (2.67)\\
&- \left. 2\left(128 - 128e^2 + 23e^4\right)\frac{E\left[e^2\right]}{K\left[e^2\right]}\right), && (2.68)
\end{aligned}
$$

where $K[e^2], E[e^2]$ are the complete elliptic integral of the first and second kind. We have computed the Fourier coefficient of the ellipse up to order 12.

Knowing the a_k coefficients, is it possible to solve differential Equ.s (2.35) on α_k and β_k with boundary conditions (2.50), (2.51) and (2.52) and $C = 0$. We have plotted the first 12 functions α_k and β_k on Fig. 2.9 for elliptic frames ($e = 0.97$, $h = 0.5$ ($R_{\text{M}} = 1$, $R_{\text{m}} = 0.24$) and $\varphi_0 = 0.3\pi/2$). The approximated solutions from Equ.s (2.43), which becomes

$$
\begin{aligned}
\tilde{\alpha}_k(z) &= \frac{\cosh\left(\frac{kz}{a}\right)}{\cosh\left(\frac{kh}{2a}\right)} \cos\left(\frac{k\varphi_0}{2}\right) a_k,\\
\tilde{\beta}_k(z) &= \frac{\sinh\left(\frac{kz}{a}\right)}{\sinh\left(\frac{kh}{2a}\right)} \sin\left(\frac{k\varphi_0}{2}\right) b_k, && (2.69)
\end{aligned}
$$

for the elliptical frames, is plotted in Fig. 2.9 given by the black dashed lines. One observes easily how the coefficients converge for higher k towards Equ.s (2.69).

A good test of the perturbation theory is to calculate the mean curvature H using Equ. (2.21). We have plotted this curvature as a function of φ for different horizontal planes $z = 0$ and $z = h/4$ in Fig. 2.10, with the principal curvatures κ_1 and κ_2. The perturbed surfaces have similar mean and principal curvatures as the corresponding catenoid. The mean curvature is not perfectly zero but has only small fluctuations around zero depending on the z and φ coordinate.

2.3.7.2 Clover contours

The results for α_k and β_k for clover frames with $\varepsilon = 0.1$, introduced in Section 2.2.1 are represented in Fig. 2.11. Since all a_k and b_k except of $k = 3$ are zero, all α_k and β_k vanish except of $k = 3$. Due to symmetries α_3 and β_3 vanish as well all 120° changes in φ_0. α_3 vanishes at $\varphi_0 = n120°$ and β_3 at $\varphi_0 = n120° + 60°$. This makes the clover frame to one of simplest configurations.

2.3.7.3 Non-identical frames

To test our approach in the case of two different frame, we used an ellipse ($e = 0.866$, $R^{+}_{\text{mean}} = 1.65$) for the top frame and a three-leaves clover ($\varepsilon = 0.3$, $R_{\text{mean}} = 1$) for the

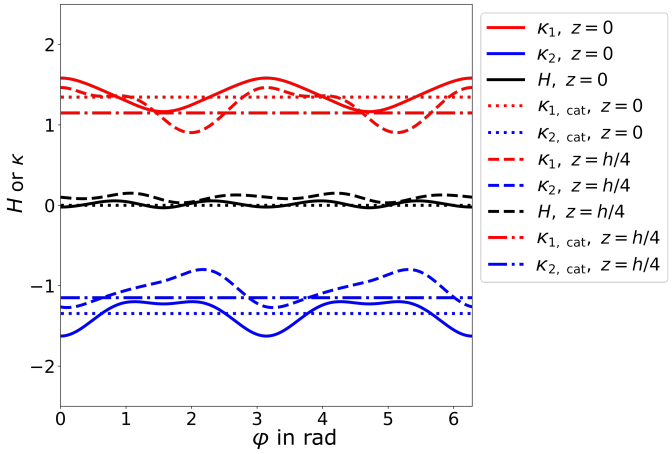

Figure 2.10: Principal curvatures κ_1 (red curves) and κ_2 (blue curves) and mean curvature (black curves) H for two horizontal planes $z = 0$ (solid lines) and $z = h/4$ (dashed lines) for $e = 0.866$, $h/R_{\mathrm{mean}} = 1.2$ and $\varphi_0 = 90°$. Dotted line gives the principal curvatures for the catenoid of the same mean radius for comparison.

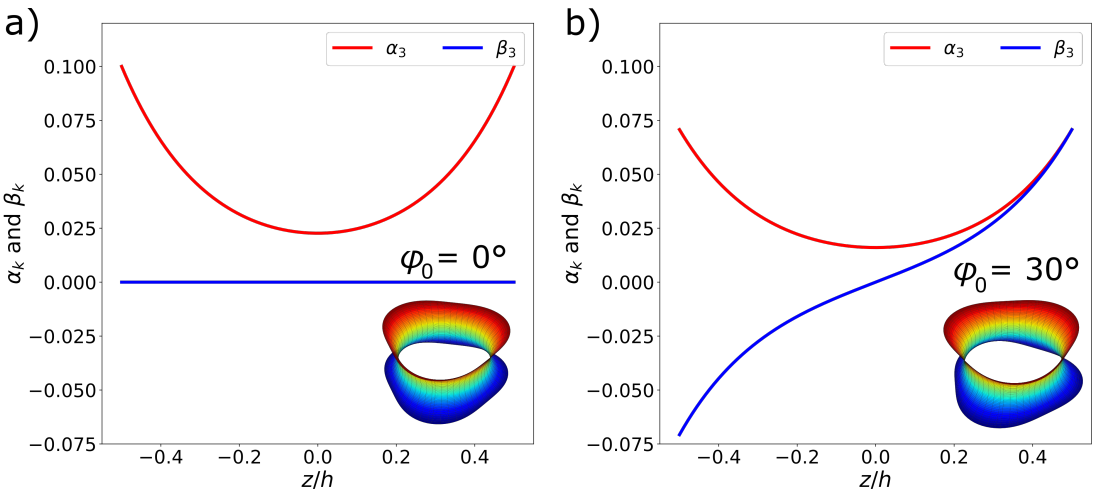

Figure 2.11: α_k and β_k for frames with clover shape with a) $\varphi_0 = 0°$ and b) $\varphi_0 = 30°$. All α_k and β_k are zero except of $k = 3$.

lower one. In that case we have solved the differential Equ.s (2.35) leading to the solution plotted on Fig. 2.12.

We also reported the shape and profiles on Fig. 2.13.

2.3.8 Forces and moments

As shown in Section 2.3.5, it is possible to calculate forces and moments which are exerted on the frames due to the minimal surface. In the case of identical frames with at least two symmetry axis only F_z and Γ_z are not vanishing. In Fig. 2.14 the argumentation for this is illustrated, with two identical frames with a rotation of $\varphi_0 \neq 0°$, one symmetry axis and an arbitrary distance h between the two frames. The force exerted by the minimal surface on the frames $\vec{F}^{\pm}$ is decomposed in a force parallel to the symmetry axis

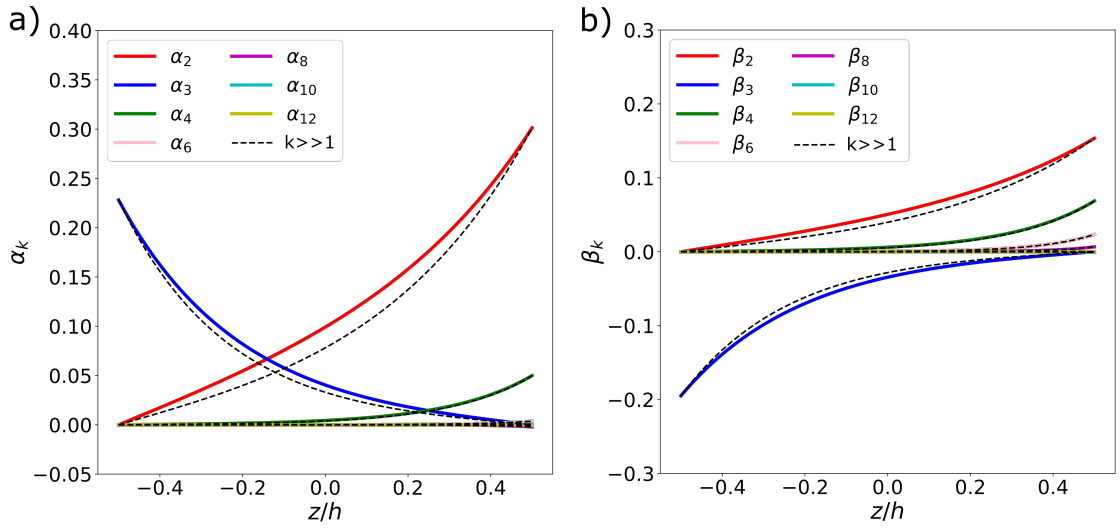

Figure 2.12: Solution of the differential equations (2.35) for $\alpha_k(z)$ (a) and $\beta_k(z)$ (b) for $k \leq 12$, in the case of an upper elliptic frame ($e = 0.866$, $R_{\mathrm{M}} = 2.4$, $R_{\mathrm{m}} = 1.2$, $R^{+}_{\mathrm{mean}} = 1.65$) and a lower three-leaves clover frame ($\varepsilon = 0.3$, $R^{-}_{\mathrm{mean}} = 1$) for $h = 1.2$ and $\varphi_0 = 0.3\pi/2$. The black dashed lines are the approximation for $k \gg 1$, Equ. (2.43).

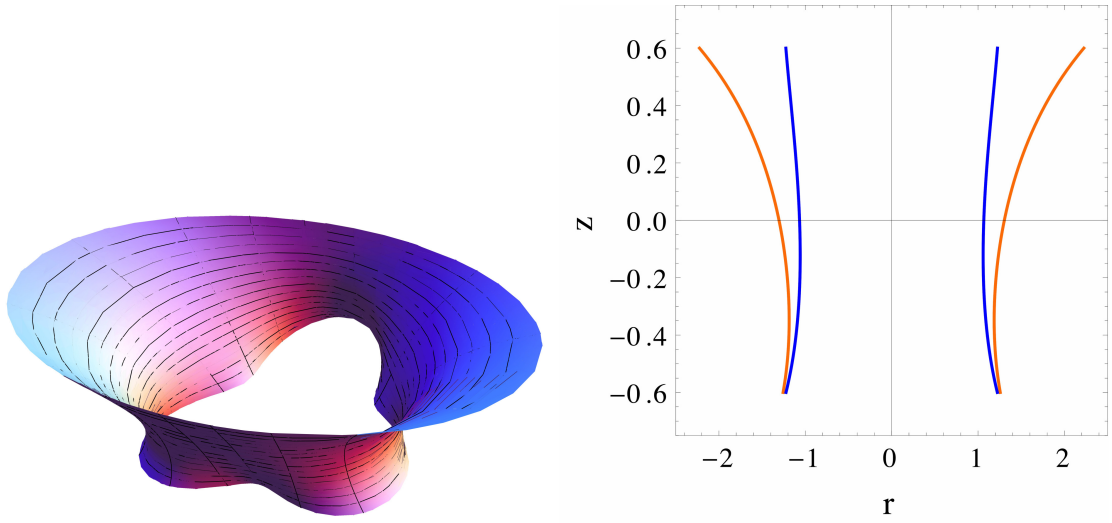

Figure 2.13: Minimal surfaces in the case of an upper elliptic frames ($e = 0.866$, $R^{+}_{\mathrm{mean}} = 1.65$) and a lower three-leaves clover frame ($\varepsilon = 0.3$, $R^{-}_{\mathrm{mean}} = 1$) for $h = 1.2$ and $\varphi_0 = 27°$: (Left): surface shape and (Right) profiles for $\varphi = 0°$ (orange) and $\varphi = 90°$ (blue).

$F^{\pm}_{\parallel}$, vertical to the symmetry axis $F^{\pm}_{\perp}$ and $F^{\pm}_{z}$. For a surface in equilibrium it is

$$\vec{F}^{+} = -\vec{F}^{-}. \tag{2.70}$$

If the frame geometry $\mathcal{C}^{+}$ has a symmetry axis as in Fig. 2.14a, all points on the frame geometry, as P^{+}_{1}, are reflected at the frame symmetry axis. If the bottom frame geometry is identical up to a rotation φ_0 there is a global symmetry axis, (see Fig. 2.14a), which reflects all points P^{+} to P^{-} on the minimal surface and the frames. Fig. 2.14a illustrates this for the points on the frames in two dimensions. In three dimensions the global

symmetry axis is in the plane $z = 0$.
We can split the frames with the global symmetry axis, by projecting the global symmetry axis in to the plane of the frames in part 1 and 2 (Fig. 2.14c, d). For the top and the bottom frame part one and two are identical except that they are mirrored on the projected global symmetry axis, Fig. 2.14c,d. We define forces which are exerted by the minimal surface on the frame part 1 (Fig. 2.14c) and 2 (Fig. 2.14d) in tangential and vertical direction to the global symmetry axis for the upper and lower frame. Due to the global symmetry, it is

$$F^+_{\parallel k} = F^-_{\parallel k}, \tag{2.71}$$

$$F^+_{\perp k} = -F^-_{\perp k}, \tag{2.72}$$

with $k \in \{1, 2\}$. Due to the Equ.s (2.70) and (2.71)

$$F^+_{\parallel} = -F^-_{\parallel} = F^+_{\parallel 1} + F^+_{\parallel 2} = -F^+_{\parallel 1} - F^+_{\parallel 2} = 0, \tag{2.73}$$

and the force $F^{\pm}_{\parallel}$ vanishes.
If a second symmetry axis is present, which is the case for two identical elliptical frames or two identical clover frames, a second component of $\vec{F}$ vanishes and $F_x = F_y = 0$. The same argumentation holds for the moments Γ_x and Γ_y.
If the upper frame and the lower frame are not identical, there are in the general case no symmetry axis. We define therefore F_r and Γ_r and φ_F and φ_Γ with (illustrated in Fig. 2.15)

$$F_r = \sqrt{F_x^2 + F_y^2}, \tag{2.74}$$

$$\Gamma_r = \sqrt{\Gamma_x^2 + \Gamma_y^2}, \tag{2.75}$$

$$\varphi_F = \arctan\left(F_y / F_x\right), \tag{2.76}$$

$$\varphi_\Gamma = \arctan\left(\Gamma_y / \Gamma_x\right). \tag{2.77}$$

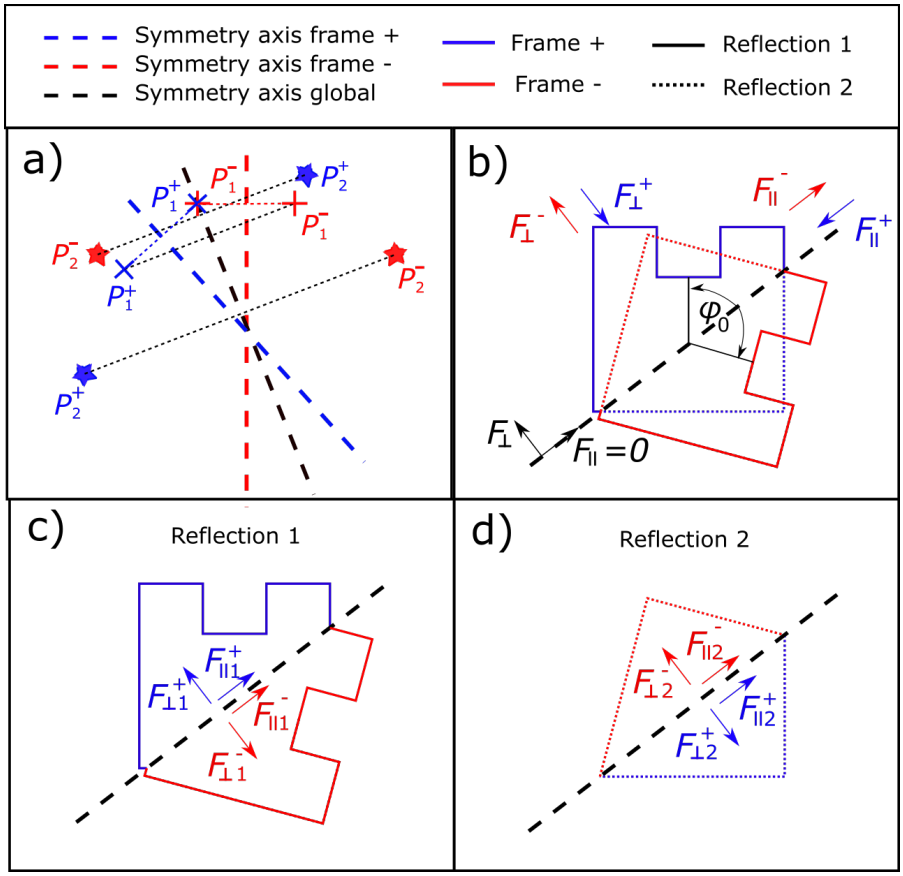

Figure 2.14: Scheme of how the frame symmetry axis interfere with each other creating a global symmetry axis in a). Scheme of two identical frames with a contour with one reflection symmetry in b), c) and d). The blue contour is the upper frame +, red is the lower frame -. The frames are shown from the top view in b) both frames completely with the symmetry axis, c) the upper frame part above the symmetry axis and the lower frame part below the symmetry axis and d) the upper frame part below the symmetry axis and the lower frame above the symmetry axis. In all the sub figures b), c) and d) the different forces with their directions acting on the different parts of the frame are illustrated.

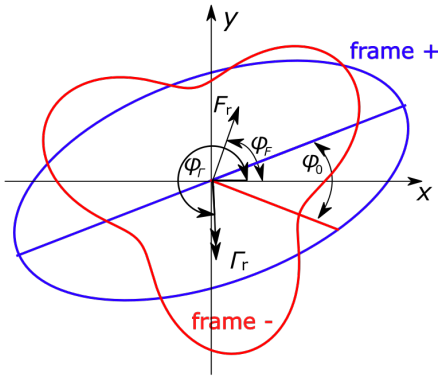

Figure 2.15: Geometrical overview of φ_F, φ_Γ, F_r and Γ_r for an elliptical upper frame and a clover bottom frame.

2.4 Results and discussions

In the following, we systematically compare the measured and calculated quantities of the soap film experiments (index "exp") and of the Surface Evolver simulations (index "SE") with the predictions of the perturbation theory (index "P") and of the algorithm provided by Alimov *et al.* [1] (index "A"). We analyse first the stability of the continuous minimal surface (Section 2.4.1) and their shapes (Section 2.4.2), investigating in detail, in the cases of elliptic and clover frames, the effect of the angle φ_0 between the frames on the critical height $h^\star$. We then turn to the analysis of the normal force (Section 2.4.3) and the torque (Section 2.4.4) exerted on the frames by the film. At the end we extend the perturbation theory to non identical frames.

2.4.1 Critical height

We first focus on minimal surfaces with elliptic boundary conditions. Fig. 2.16a displays the critical height $h^\star$ normalized by the average radius $R_{\text{mean}}(e)$ as a function of eccentricity e for $\varphi_0 = 0$. Experimental measurements, SE simulations and exact theory (Alimov *it et al.* method [1]) are in perfect agreement for all e. This confirms the validity of our experimental and numerical protocols. The perturbation theory also agrees very well with the Alimov *it et al.* method [1] over a wide range of e, but keeps as discussed a constant critical height $h^\star/R_{\text{mean}} = \mu^\star$.

The next step is to evaluate the impact of the angle φ_0 between the two elliptic frames (see Fig.2.3a) on $h^\star$ with the different approaches. As shown in the Fig. 2.16c, experiments and SE simulations show a very small variation of the critical height with the angle φ_0 (less than 2% for $e = 0.866$), compatible with a $\cos(2\varphi_0)$ variation. Experimentally, this small difference of $h^\star$ for different φ_0 is only evidenced by computation of the statistical average over repeated measurements. This variation is not predicted by the perturbative theory, as shown by equation 2.50, which systematically overestimates $h^\star$ (see Fig. 2.16c). Fig. 2.17 displays the maximum normalised variation of $h^\star$ between the different angles φ_0 expressed *via* $\Delta h^\star = \left(h^\star(\varphi_0 = 0) - h^\star(\varphi_0 = 90)\right)/R_{\text{mean}}$ as a function of eccentricity e. The impact of the angle φ_0 on $h^\star$ increases quite naturally with the increase of e.

We have extended numerically this study to other boundary conditions. Fig. 2.16b and d display the results obtained for clover frames. Again, a very small but significant variation of $h^\star$ is observed with φ_0 (Fig. 2.16b). Relative changes in $h^\star$ with the change of φ_0 are very small (Fig. 2.16d), less than 0.4% with $\varepsilon = 0.3$. As expected from the shape of the contours, we observe a three fold symmetry in the case of the clover in good agreement with a cosine variation (see Fig. 2.16d). The comparison with theoretical models is similar to the case of ellipses. Again $h^\star_{\text{P}}$ is constant for all ε, Fig. 2.16b. The Alimov *et al.* method [1], which can be applied only to convex shapes (i.e. for $\varepsilon < 0.1$ in our case), predicts again very well the variation of $h^\star$ with ε (see Fig. 2.16). For small ε values, all approaches are in good agreement with the SE simulations.

In conclusion, concerning the critical height $h^\star$, we have demonstrated both experimentally and numerically, that a small but significant dependence of $h^\star$ on the angle φ_0 between the frames exists for different contour shapes (ellipses and clovers). This variation is not predicted by the perturbative theory, and, to our knowledge, no alternative theoretical prediction exists at this stage which captures this observation. Interestingly, we can see that the perturbative theory predicts a constant critical height independently

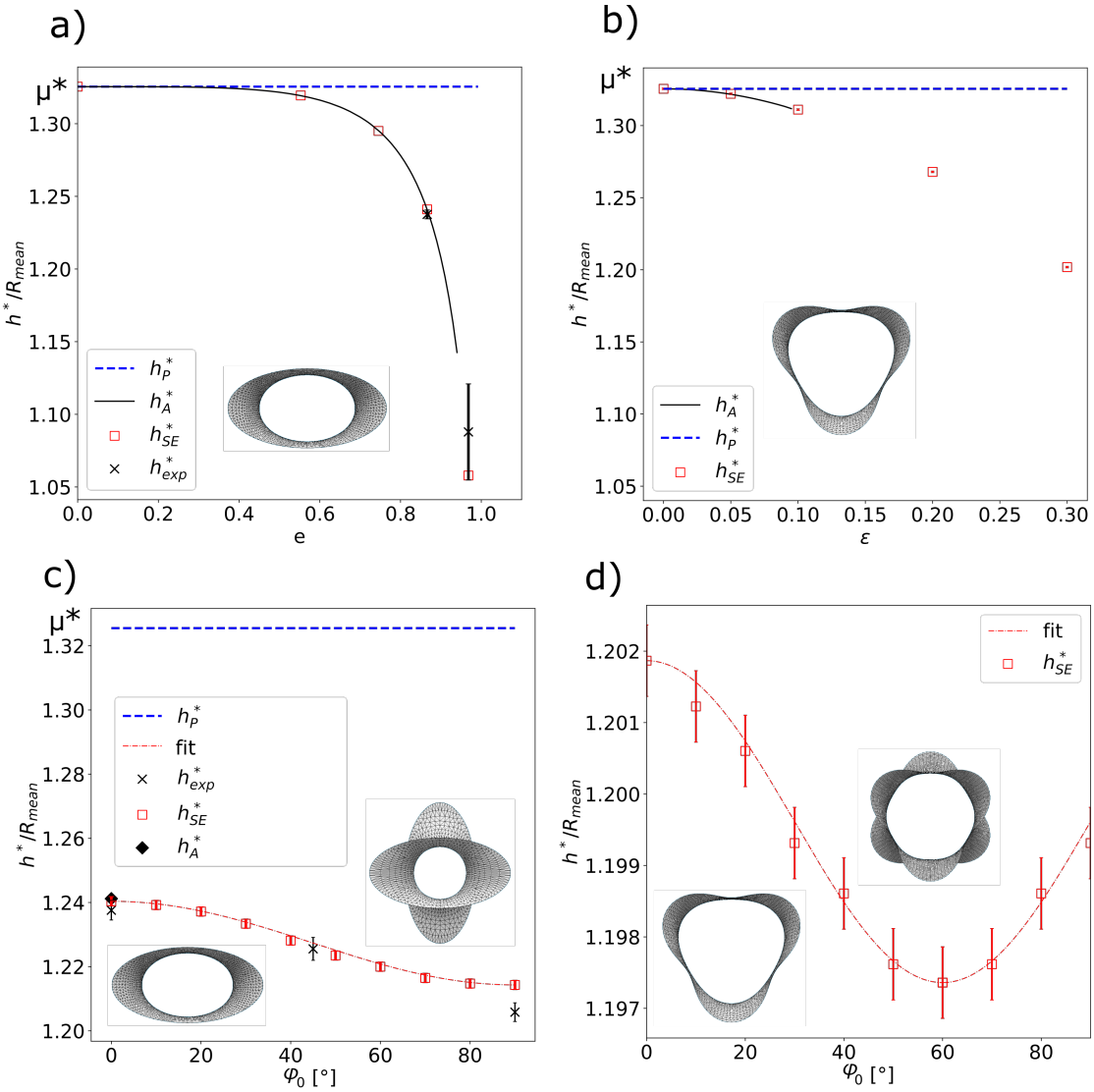

Figure 2.16: Normalized critical height ($h^\star/R_{\mathrm{mean}}(e)$) of minimal surfaces with elliptic (left) and clover frames (right) obtained with Surface Evolver simulations $h^\star_{\mathrm{SE}}$ (□), experiments $h^\star_{\mathrm{exp}}$ (×), the perturbation theory $h^\star_{\mathrm{P}}$ (dashed line) and the the Alimov algorithm $h^\star_{\mathrm{A}}$ (solid line). a) and b) show how $h^\star$ changes with e or ε for $\varphi_0 = 0°$. c) and d) show the dependence on φ_0 for constant values of $e = 0.866$ in c) and $\varepsilon = 0.3$ in d). The red dashed line in figure c) and d) is an empirical fit with a cosine function.

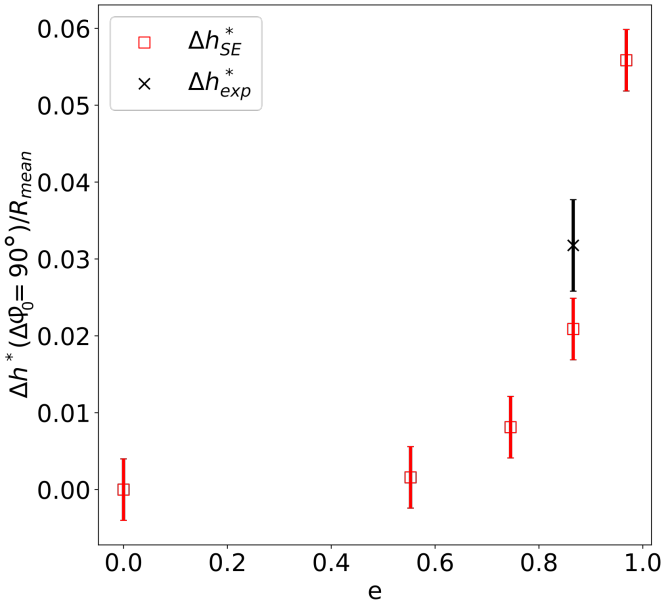

Figure 2.17: Normalized maximal variation of $h^\star$, $\Delta h^\star/R_{\text{mean}}$ for different eccentricities e. Only simulations and experiments, which are able to show these changes, are presented.

of the number of Fourier coefficients taken into account. The variation of $h^\star$ is therefore intrinsically linked to the non-linear character of the partial differential equation (2.44).

2.4.2 Shape description

In this section we focus on the shape of the minimal surfaces for $h < h^\star$. Fig. 2.18 shows the example of a minimal surface obtained via SE simulations for elliptic frames at an angle $\varphi_0 = 45°$, $h/R_{\text{mean}} = 1.02$ and $e = 0.866$. The surface is represented by plotting the vertices of the finite element mesh.

In order to make a quantitative comparison of our results, we extracted the experimental, numerical and theoretical profiles corresponding to the intersection of the surface with a vertical plane passing through the axis of rotation, and making an angle φ with the x-axis (see Fig. 2.19 for 2 values of φ_0 and φ). Experiments and simulations are in very good agreement for both profiles. Far from the critical point ($h \ll h^\star$), the perturbative theory is in very good agreement with the experimental and numerical results. Near the critical point ($h \leq h^\star$), the agreement is less convincing (See Fig. 2.19a and b), and the perturbative theory clearly overestimates the radius $r(\varphi, z)$. As we have shown before, the perturbative theory does not predict a variation of the critical height $h^\star$ with the angle φ_0. This means that this variation appears in the non-linear terms of the differential Equ. (2.25), whereas there are of course corrections to the profile that depend on φ_0 at the linear order. Rather than comparing the experimental, numerical and theoretical profiles for the same value of h/R_{mean}, as done before, we therefore compared them for the same value of $h/h^\star$, i.e. at the same relative distance to the critical point. The results presented in Fig. 2.19c and d show a good agreement for both types of profiles (top and side views), which demonstrates that the perturbative theory describes quantitatively very well the shape of the surface, even very close to the critical point, provided that

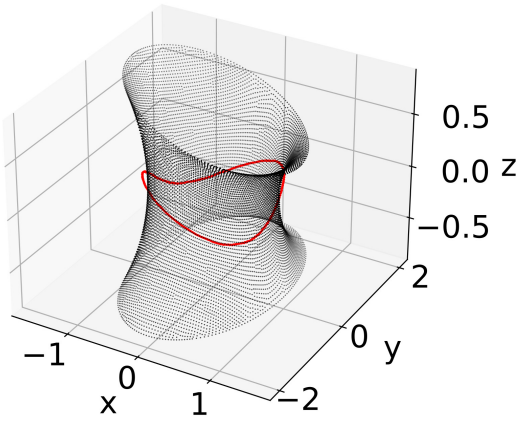

Figure 2.18: Shape of a minimal surface held by elliptic frames with $\varphi_0 = 45°$, $h/R_{\text{mean}} = 1.02$ and $e = 0.866$, obtained by SE simulations (all vertices are shown). The red solid line is the approximated neck contour of this surface.

variations of $h^\star$ are taken into account.

All profiles show a point where $r(z)$ is minimal and the normal to the surface is horizontal corresponding to the Top view (see Fig. 2.19a and c). The location of these points generalises the notion of the neck contour introduced in the case of the catenoid. For non-axisymmetric frames, it is a closed loop, which is not necessarily planar. An example is represented by the red solid line in Fig. 2.18. For large φ_0 and small h, the neck contour may lie partially outside the surface. Mathematically, the neck contour is the curve that minimises its projected perimeter in the Oxy plane $\mathcal{C}_\parallel$. From a physical point of view, the neck contour has a particularly interesting property. The total force exerted by the minimal surface on the frame is $2\gamma P_\parallel$, where $P_\parallel$ is the projected length of the neck contour in the Oxy plane $\mathcal{C}_\parallel$.

2.4.3 Normal forces on frames

We now discuss the results for the normal force F_z exerted by the soap film on the elliptic frame (Section 2.2.2). In the Alimov *et al.* method, one has to calculate a value (called Ψ_B in [1]), which is proportional to the projected neck perimeter $\mathcal{C}_\parallel$ and thus to F_z. The Alimov algorithm thus allows to compute the force $F_{z;A}$, which will serve as a reference case for $\varphi_0 = 0°$.

2.4.3.1 Force dependency on $\mathcal{C}$

The force of the perturbation theory depends on the chosen integration contour $\mathcal{C}$ in comparison to forces obtained with SE or the Alimov algorithm. Fig. 2.20 compares the force $F_{z;SE}$ obtained with Surface evolver with the force $F_{z;P}$ obtained with the perturbation theory for different φ_0. The contour $\mathcal{C}$ for Equ. (2.57) is the cross section of the surface in a plane parallel to the $z = 0$ plane with distance z. $F_{z;P}$ and $F_{z;SE}$ is plotted against the different $\mathcal{C}(z)$. For $\varphi_0 = 0°$ the agreement between simulation and

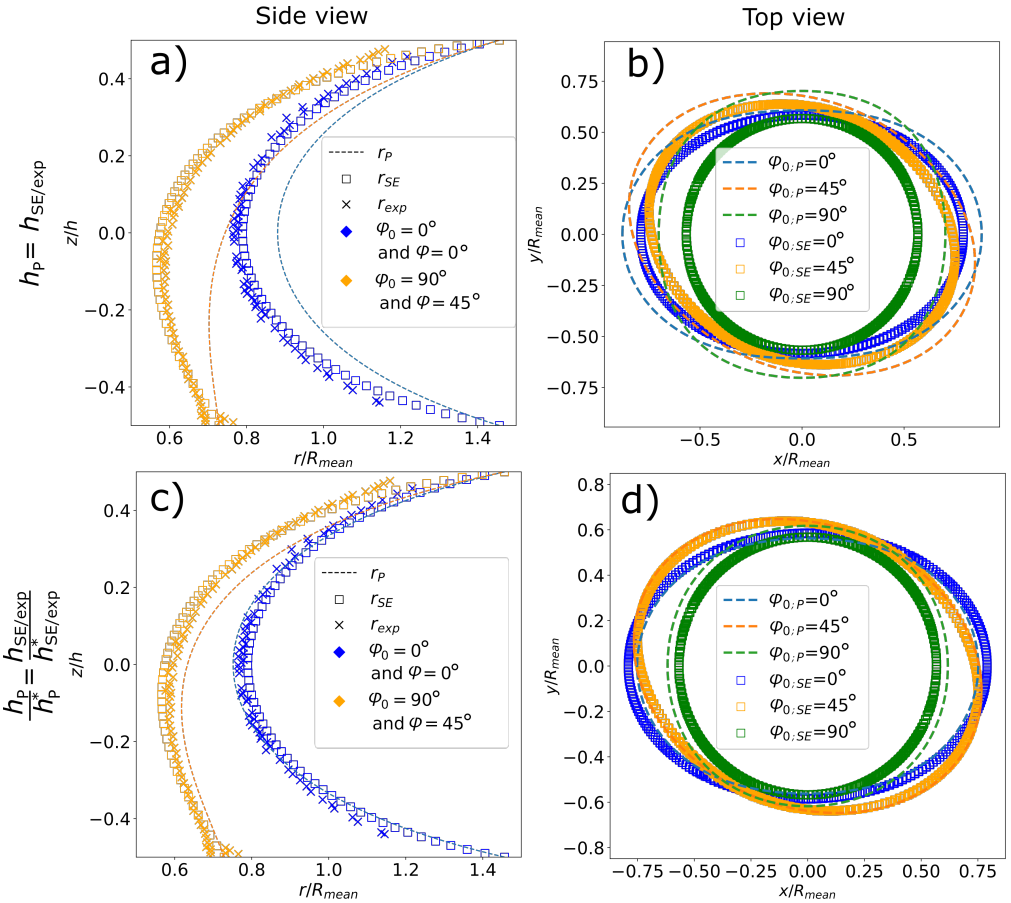

Figure 2.19: (Left) Side view (vertical profile in the symmetry plane of the surface defined by φ) and (Right) top view (projected neck contour) of a minimal surface spanning elliptic frames with $e = 0.866$ obtained with SE simulations $r_{\mathrm{SE}}(z)$, the perturbation theory $r_{\mathrm{P}}(z)$ and the soap film experiment $r_{\mathrm{exp}}(z)$ for two different angles φ_0 on the left and three on the right at a height of $h = 1.2R_{\mathrm{mean}}$. On the right, the dashed lines are the predicted neck contours of the perturbation theory and the open squares are the vertices closest to the neck contour of the Surface Evolver simulation.

theory is better for small h/h^* in comparison to larger φ_0 where the agreement is better for large h/h^*. The evolution of $F_{z;P}(\mathcal{C}(z))$ is most of the time close to the constant $F_{z;SE}(\mathcal{C}(z))$. In conclusion, we can say that the force $F_{z;P}(\mathcal{C}(z))$ depends only slightly on $\mathcal{C}(z)$ and has almost the same value as $F_{z;SE}$.

2.4.3.2 Force F_z height h dependency

In Fig. 2.21, we compare F_z obtained with all methods (exp-experiments, P-perturbation theory, SE-Surface Evolver and A-Alimov). $F_{z;P}$ is in the following the force obtained with the frame contour ($z = \pm 1/2h$). F_z depends on the distance h and the angle φ_0 between the two frames, as shown in Fig. 2.21. $\varphi_0 = 0°$, F_z is monotonically decreasing with h until it reaches $h = h^\star$. For very small h and $\varphi_0 = 0°$ the maximal force is $F_{z;\mathrm{Max}} = 2\gamma P$, where P is the perimeter of the frame.

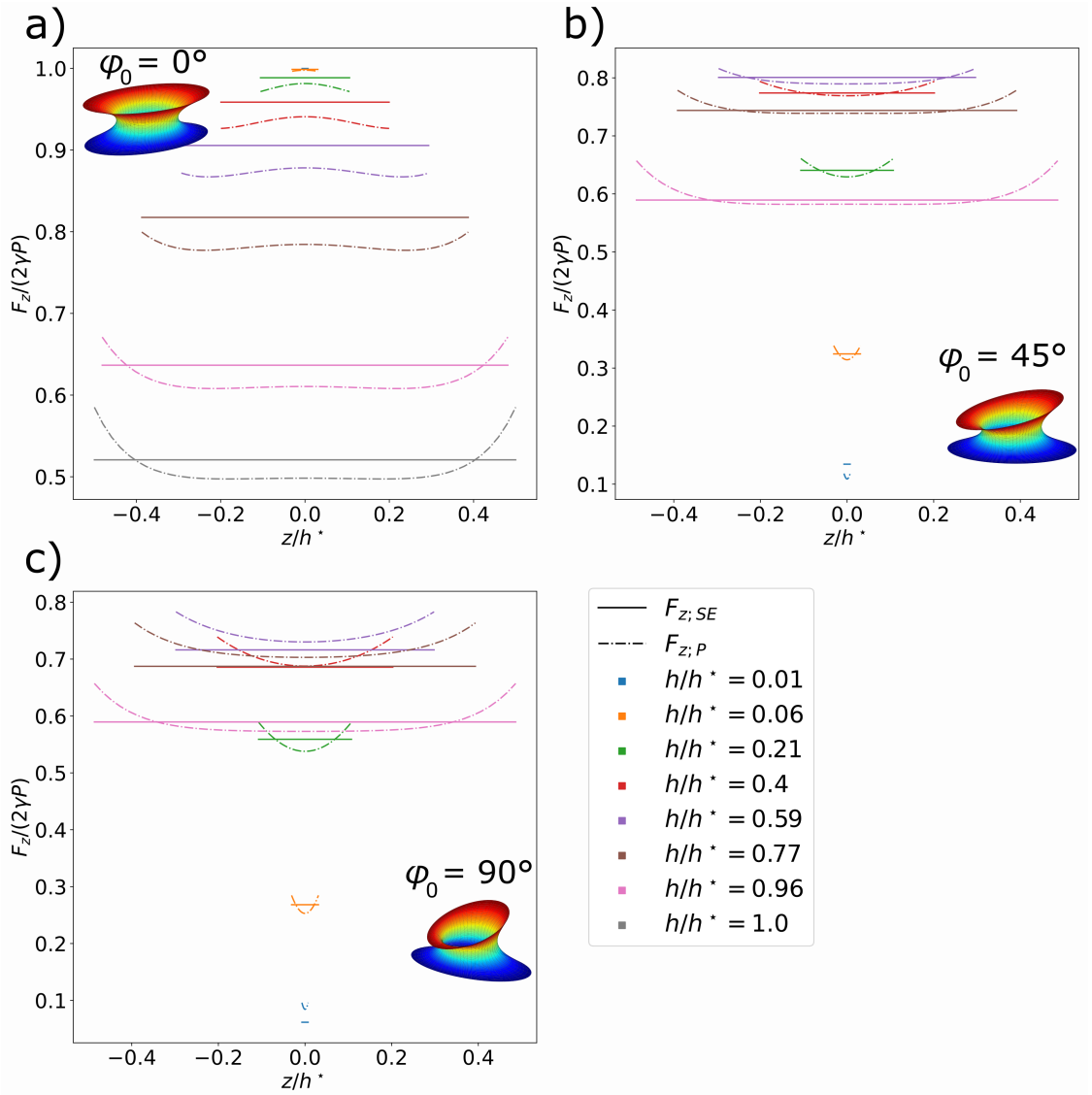

Figure 2.20: The force component F_z obtained with SE and the Perturbation theory is represented for different φ_0 (0° a), 45° b), 90°c) for different h/h^* plotted against z/h^*. The contour $\mathcal{C}$ for Equ. 2.57 is the cross section of the surface and a plane parallel to the plane $z = 0$ with distance z.

Also for $h = 0$, an infinitely small angle $\varphi_0 \neq 0$ is sufficient for the force to vanish, $F_z = 0$. This discontinuity of $F_z\,(h = 0, \varphi_0)$ for $\varphi_0 = 0$, which may seem surprising, simply reflects the fact that for $h = 0$, as soon as there is a non-zero angle between the frames, the minimal surface is made up of horizontal films (see Fig. 2.8) and the force is null.

For $\varphi_0 \neq 0$, the force increases with h until it reaches a maximum and decreases again up to $h = h^\star$. To understand this non-monotonic behavior of the force, let us first consider the axisymmetric case, a catenoid supported by two circular frames of different radii (R_- and R_+) [61] (introduced in Section 2.3.2). We are interested only in stable branches in Fig. 2.7. We can distinguish three cases: (i) the height is $h \leq h(a_c = R_{\min})$, where $R_{\min}$ is the smaller radius of R_- and R_+. In this case the force is monotonic increasing with h

until $R_{\min}$ merges with a_c. Before the neck contour is always virtual (in the prolongation of the minimal surface) and the force is always increasing monotonously as a_c in Fig. 2.7. (ii) the height $h(a_c = R_{\min}) \leq h \leq h^\star(R_-/R_+)$, the force decreases monotonously with h until $h = h^\star$, as a_c decreases in Fig. 2.7. (iii) $h^\star(R_-/R_+) < h$, there is no stable catenoid for the given boundary condition and one obtains two disks in the top and bottom frame.

In the case of an asymmetric catenoid, the maximum value of the force is proportional to the perimeter of the smaller frame, which is also the perimeter of the intersection of the surfaces bounded by the two frames. In the general case, the perimeter of $\mathcal{C}_\parallel$ is upper bounded by the perimeter of the intersection of the projection of the two frames in the mid-plane (grey area on Fig. 2.8) (It can be proven by integrating the interfacial tension force along the closed contour $(A_+ \to B_+ \to B_- \to C_- \to C_+ \to D_+ \to D_- \to A_- \to A_+$, see Fig. 2.8). By construction, the parts of the contours connecting the two frames (typically $X_+ \to X_-$ with $X = A, B, C$ or D) do not give any contribution to the vertical force, whereas the frame parts give a total vertical force which is lower than the perimeter times 2γ, because the local angle can only give lower values. As the construction of $\mathcal{C}_\parallel$ ensures that its perimeter is equal to $F_z/(2\gamma)$ it follows that the perimeter of the projected neck contour is shorter than the projected intersection perimeter. This is illustrated in the case of the elliptic frames on Fig. 2.21 which clearly shows that this theoretical upper bound gives an excellent approximation of the numerical and experimental values of the force.

At the critical point in Fig. 2.21a, the results seem to suggest that the normal forces for different angles φ_0 converge to the same value. In Fig. 2.21c, we therefore plot the normal force at the critical point $F_z^\star$ as a function of φ_0. The difference between the forces is indeed small but clearly observable with the SE simulations. The perturbation theory also predicts a change in the force but with a much smaller variation with φ_0.

In summary, sufficiently far from the critical point, experiments, SE simulations, perturbation theory and the Alimov *et al.* method [1] show excellent agreement in the prediction of the normal force exerted on the elliptic frames by the minimal surface. This was expected, since $\mathcal{C}_\parallel$ in Fig. 2.19 shows a good agreement between the different methods. Close to the critical point, excellent agreement in the dependence of the force on the angle φ_0 is obtained only between the experiments and the SE simulations, while the perturbation theory predicts only the general trend.

2.4.4 Torque on frames

An important feature of minimal surfaces spanning non-axisymmetric frames is that, despite being fully liquid, they are able to exert an important torque Γ_z on the frames. Here we investigate how this torque depends on the different frame geometries.

Fig. 2.22 summarises all our experimental, numerical and theoretical results on the torque Γ_z for elliptic and for clover frames at two different heights. The main figure plots the variation of the normalized torque $\Gamma_z/2\gamma R_{\text{mean}}^2$ with the angle φ_0. We first observe that the torque varies periodically, with a periodicity directly related to that of the frame: 180° for elliptic frames and 120° for clover.

As expected, the torque vanishes when the axes of symmetry of the upper and lower frame are parallel, corresponding to a physically stable state ($\varphi_0 = 0°$ or 180° for the ellipses and $\varphi_0 = 0°$ or 120° for the clover) or a physically unstable state ($\varphi_0 = 90°$ for the ellipses and $\varphi_0 = 60°$ or 180° for the clover). The torque thus presents two

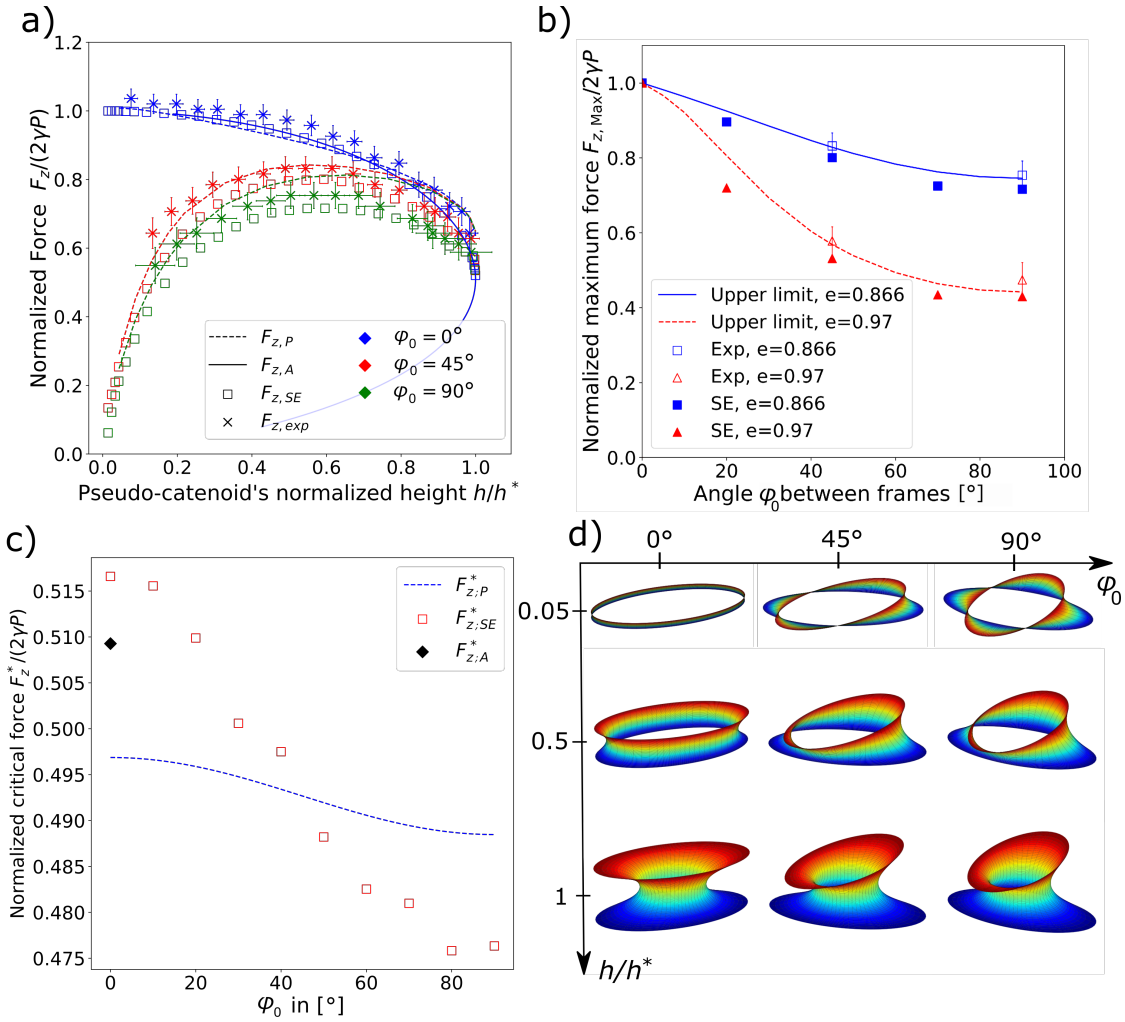

Figure 2.21: a) Normalized normal force $F_z/(2\gamma P)$ acting on elliptic frames for different heights h and angles φ_0, obtained with SE simulations $F_{z,\mathrm{SE}}$, soap film experiments $F_{z,\mathrm{exp}}$, the perturbation theory $F_{z,P}$ and the Alimov *et al.* method [1] $F_{z,A}$. All eccentricities are $e = 0.886$. b) Normalized maximum force in the case of elliptic frames ($e = 0.866$ in blue and $e = 0.97$ in red) obtained experimentally and numerically (SE). Lines correspond to the perimeter ABCD of the grey area on Fig. 2.8 normalized by the perimeter of the frame. c) Variation of the critical, normalized normal force on the elliptic frames at $h = h^\star$ with φ_0, obtained with SE simulations $F^\star_{z,\mathrm{SE}}$, the perturbation theory $F^\star_{z,\mathrm{P}}$ and the Alimov *et al.* method [1] $F^\star_{z,A}$. We remind the reader that $h^\star$ is independent of φ_0 in the perturbation theory. In the SE simulations all $F^\star_{z,\mathrm{SE}}$ belong to different $h^\star$. d) Shape diagram for two eliptical frames with $e = 0.886$ and different h and φ_0.

extrema, a maximum and a minimum over one period. The angle φ_0 at which they appear depends on h, as it is clearly shown in Fig. 2.22. The torque has a linear behavior with a torsion constant which depends on h and which increases with h until diverging for $h = 0$. Interestingly, the limit $h = 0$ allows an analytical calculation of the torque since in this case the minimal surface is composed of pieces of plane films connected by points (see top right inset of Fig. 2.22). In the case of elliptic frames, one obtains Equ. (2.63) (see also Section 2.3.6). This analytical result is represented by the black curve in Fig. 2.22 and is in perfect agreement with the perturbative theory (black $\star$). It shows that the torque

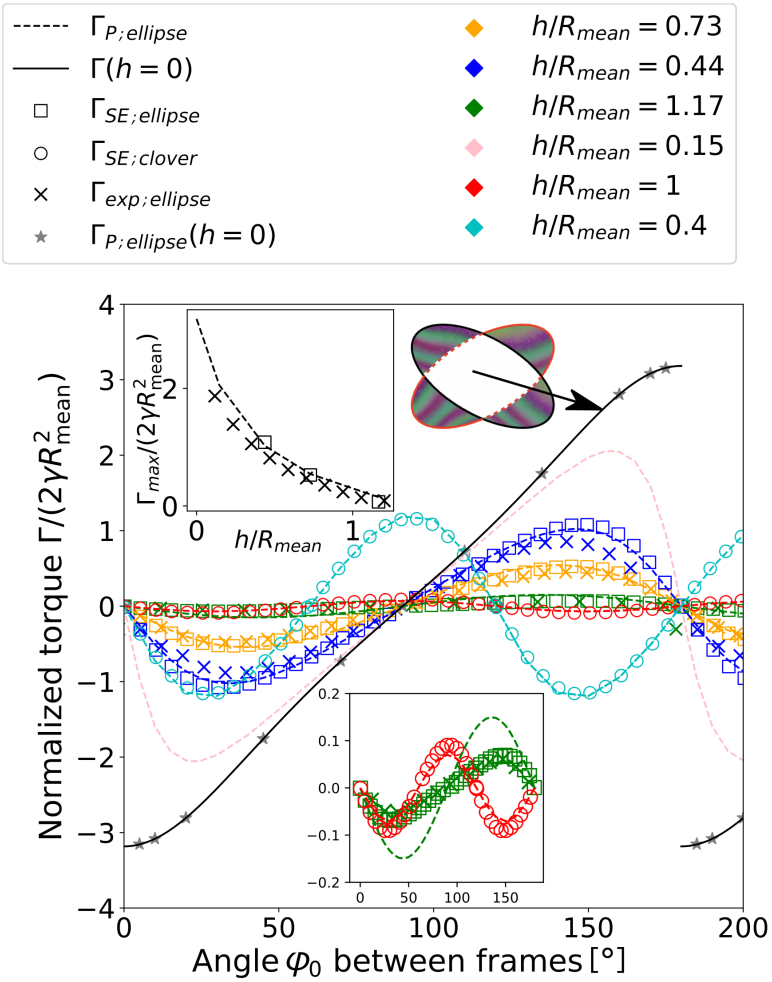

Figure 2.22: Torque on elliptic and clover frames for different h (see color code in the legend) and φ_0: experimental values Γ_{exp} for elliptic frames ($\times$), Surface Evolver simulations Γ_{SE} for elliptic frames ($\square$) and for clover frames ($\circ$), perturbative theory Γ_{P} (dashed lines) and an analytical solution for $h = 0$ with Equ. (2.63) (black solid line). The excentricity of the elliptic frame is $e = 0.866$ and $\varepsilon = 0.3$ for the clover frame. The lower inset shows a zoom for small Γ_z (same axis). The upper left inset shows how the maxima of Γ_z depend on h for the case of ellipses. The upper right inset shows an example of the configuration of the horizontal films for $h = 0$.

presents a discontinuity at $\varphi_0 = 0$ for $h = 0$. The agreement between SE simulations and the perturbation theory is very good for low h, for both elliptic and clover frames. As one approaches the critical point ($h \leq h^\star$), the torque becomes very small and the agreement with the perturbation theory is less good. The top left inset of Fig. 2.22 plots how the maxima of the torque Γ_{max} vary with h, showing again a very good quantitative agreement between the experiments, the SE simulations and the perturbation theory.

As shown in Fig. 2.22, in the case of elliptic frames, the torque tends to align the two frames along the same axis. This shows that in this case the surface energy is minimal. We do not know if it is possible to generalize this property to the general case of two identical frames of arbitrary shape, even if it is obvious that it is correct when $h \to 0$.

In summary, far from the critical point, experiments, SE simulations and perturbation

theory show excellent agreement in the description of the torque exerted by minimal surfaces on non-axisymmetric frames. Close to the critical point, the agreement with the perturbation theory remains good, if one compares shapes at the same distance to the critical point.

2.4.5 Tangential forces F_r and tilt moments Γ_r

As introduced in Section 2.3.8 non-zero forces and moments tangential to the frame plane are only possible if the frames have less than two symmetry axes. This is the case for two non identical frames. The Fig. 2.23 shows F_z in a), F_r in c), Γ_z and Γ_r in b) and the angles, φ_F and φ_Γ in b), obtained with the perturbation theory and partially with SE. The upper frame is an ellipse with $e = 0.866$ and $R^+_{\text{mean}} = 1.65$ and the bottom frame a clover with $\varepsilon = 0.1$ and $R^-_{\text{mean}} = 1$. The agreement between the normal forces is as for identical frames after the normalisation with $h^\star$ very good above the whole height (Fig. 2.23a). The overall behaviour of the function $F_z(h)$ (vanishing F_z at $h = 0$, increasing F_z until reaching a maximum, decreasing F_z until the point of instability at maximal distance $h = h^\star$) is the same as for the asymmetric catenoid or identical frames with $\varphi_0 \neq 0$, for the same reason as already discussed in Sections 2.3.2 and 2.4.3.

The force F_r in Fig. 2.23c decreases with increasing h for small h until it reaches a minimum. Afterwards it increases with increasing h reaching a maximum and decreasing again before the surface becomes unstable at $h = h^\star$. The minimum is related to a phase shift in φ_F (Fig. 2.23d). Consequently the force F_r is changing dramatically its direction close to the minimum. A geometrical explanation could be, that the neck contour for $h = 0$ is virtual, which means not between the two frames. With increasing h the neck contour becomes more and more real (between the two frames). The moment a part of the neck contour becomes real the tangential force $\mathrm{dF_r}$ at this frame part vanishes and changes direction. The minimum in the $F_r(h)$ curve could be at a height where a large part of the neck contour becomes real. This hypothesis is supported by the strong change in φ_F near the minimum (Fig. 2.23d). The general behavior and even the absolute values F_r and φ_F between Surface evolver and the Perturbation theory are in a good agreement (Fig. 2.23c and d).

Fig. 2.23b) shows the change in Γ_r and Γ_z against the normalised height $h/h^\star$. At $h = 0$ it is $\Gamma_r = 0$ and $\Gamma_z \neq 0$. Due to Equ. (2.61) and $z = 0$ and $\mathrm{dF_z}(\phi) = 0$ at $h = 0$, the moment Γ_r is vanishing. Afterwards one sees a strong increase in Γ_r, reaching a maximum far above the maximum of Γ_z. Afterwards the general trend is a decrease of Γ_r with increasing h. It cannot be ruled out that a minimum in Γ_r occurs for certain φ_0 and h. In this example, only one inflection point can be observed. The angle φ_Γ is changing continuously with h (Fig. 2.23d). For the unstable branch a phase shift as for F_r is observed. I do not dare to give an interpretation for the different phenomena happening at the moment curve, because many parameters (F_r, φ_F, F_z, $\vec{r}$) influence Γ_r and φ_Γ.

Fig. 2.24 shows the evolution of Γ_z, Γ_r and φ_Γ for different h over φ_0 between 0° and 120° for an elliptical upper frame and a clover bottom frame with different $R^\pm_{\text{mean}}$ only for the stable branches. The torques of the unstable shapes are magnitudes smaller. One observes a periodicity with a period length of 60° for Γ_z and Γ_r. That is not surprising since elliptical frames have a periodicity with 180° and clovers one of 120°. Consequently, one obtains all 60° the same configuration rotated by $\varphi = 210°$, 180° from the period of the elliptic frame and 30° from $\varphi_0/2$ the rotation of the frame. The 210° shift can be

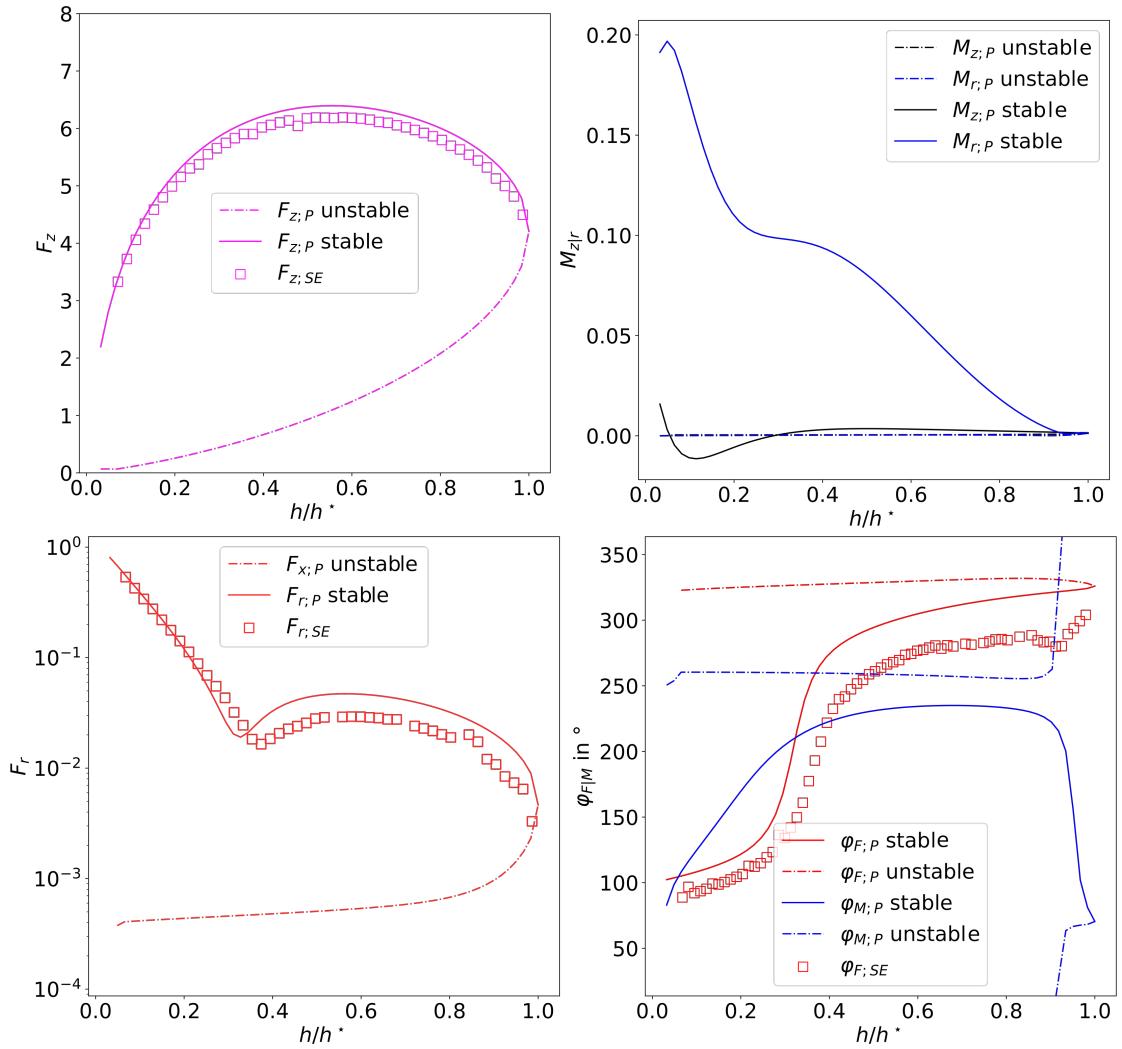

Figure 2.23: The different force components, F_z in a), F_r in c), torque components Γ_z and Γ_r in b), and angles, φ_F and φ_Γ in d), obtained with the perturbation theory are plotted against the normalized height $h/h^\star$ for an elliptical upper frame with $e = 0.866$ and $R^+_{\text{mean}} = 1.65$ and a clover bottom frame with $\varepsilon = 0.1$ and $R^-_{\text{mean}} = 1$. The angle between the two frames is $\varphi_0 = 18°$. For F_z, F_r and φ_F SE simulations are performed for a comparison.

observed in φ_Γ in Fig. 2.24d. Another general trend is the decreasing Γ_z and Γ_r in absolute values for increasing $h/h^\star$. That was already observed for identical frames, Fig. 2.22. Γ_r is never vanishing and decreases much slower than Γ_z. Another surprising observation is the change of the maximum and minimum position of Γ_r between $h/h^\star = 0.34$ and $h/h^\star = 0.58$, Fig. 2.24c. By looking at Fig. 2.24d one observes two limit cases one for $h/h^\star = 0.06$ and one for $h/h^\star = 0.58$. Both are almost straight lines, one is increasing ($h/h^\star = 0.06$) and one decreasing ($h/h^\star = 0.58$) with φ_0. Between this two heights one observes a spontaneous switch between a monotone increasing and monotone decreasing function. The reason for that is probably related to the neck contour and there position. If the neck contour changes from mainly outside the volume between the two frames to mainly inside, the direction of F_r also changes and so does Γ_r and so φ_Γ. Another

surprising observation is in Fig. 2.24c. The curve for $h/h^\star = 0.06$ has two additional local minima close to the maxima. Since they are not perfectly identically between the first and the second period, they could also be numerical artefacts related to the small height. Simulation or experiments would be interesting to verify that.

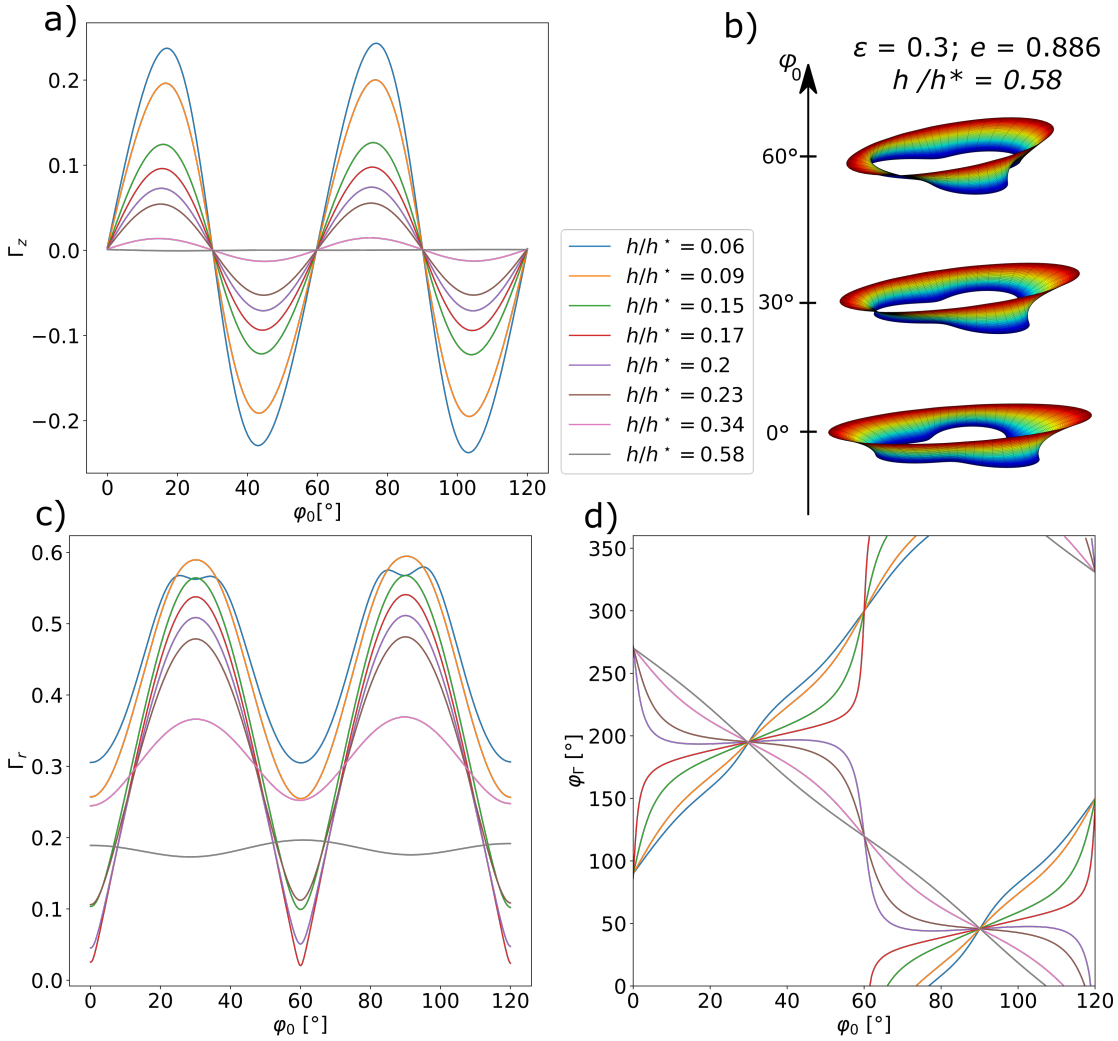

Figure 2.24: The different loads, Γ_z in a) and Γ_r in c) and angles φ_Γ are plotted against φ_0 for an elliptical top frame with $e = 0.886$ and $R^+_{\text{mean}} = 1.373$ and a clover bottom frame with $\varepsilon = 0.3$ and $R^-_{\text{mean}} = 1$. The different colors represent different $h/h^\star$. Only results for the perturbation theory are shown. The panel b) shows three illustrations of the minimal surface for different φ_0.

Even with the linearisation of the differential equation for minimal surfaces, the perturbation theory captures phenomena like forces F_r and moments Γ_z and Γ_r with a surprisingly good agreement which are not existent in the catenoid.

2.5 Conclusions and outlook

We investigated experimentally, numerically and theoretically the properties of minimal surfaces spanning two non-axisymmetric frames, with a particular focus on identical frames

specially elliptic and cloverleaf frames. We paid particular attention to the influence of the distance h and the angle φ_0 between the two frames on different properties of these surfaces. From a theoretical point of view, we propose a perturbative approach allowing to compute all the properties of the surface with good precision. The advantage of this approach in contrast to currently existing methods, such as proposed by Alimov *at al.* [1] (only for $\varphi_0 = 0°$), is that it is generalised to a wide range of frame shapes, including surfaces contained between non-identical frames.

Our experimental, numerical and theoretical study focused first on the instability of the continuous minimal surface leading to a discontinuous minimal surface (Goldschmidt surface) at a critical height $h^\star$. We have shown experimentally and numerically that, $h^\star$ depends only slightly on the angle φ_0. Perturbative theory fails to predict this non-linear effect, and to our knowledge no currently available theory predicts this variation.

We then investigated in more detail the shapes of the minimal surfaces, showing systematically excellent agreement between experiments and simulations, both agreeing very well with the prediction by Alimov *et al.* [1] for the case of $\varphi_0 = 0$. Perturbation theory is found to capture these shapes very well far from the instability. Close to the instability, this agreement is greatly improved when shapes at the same relative distance to the critical height $h^\star$ are compared, rather than shapes at the same height h. We also discussed the existence of a particular curve on the surface, consisting of points whose normal is perpendicular to the normal of the frames, which generalises the neck commonly defined for the catenoid.

We then studied the mechanical stresses (force and torque) exerted by the minimal surface on the frames. Since we consider surface tension to be constant, these physical quantities have purely geometrical interpretations. We show that they present non-trivial behavior, including a discontinuity of both the force and the torque at $h = 0$, as well as a non-monotonic character of the force for $\varphi_0 \neq 0$. Experiments, Surface Evolver simulations, perturbation theory and the Alimov *et al.* method [1] are in very good agreement.

Forces F_r and tilt moments Γ_r appear if the top and bottom frame contour are not identical or have less than two symmetries. The direction of this forces and moments depend on h and φ_0. The perturbation theory predicts well this behavior, which is verified with SE simulations.

Beyond the fundamental interest of this work, these results could pave the way for tools for future investigations. One of the most intriguing property of the non-axisymmetric minimal surfaces is its capacity to transmit not only normal stresses, but also a torque and a tilt moment despite being liquid. They could therefore be used to transmit or measure very small torques or normal forces. This could be used, for example, to investigate the visco-elastic properties of soap films. Since perturbation theory predicts the torque and normal force well, both can be determined unambiguously. By adjusting the frame geometry, the measuring range of the two quantities could be adapted.

We concentrated here on the analysis of a specific choice of shapes (ellipses and clovers), with both frames being identical, parallel and rotated around the central axis. In future work it will be interesting to investigate in more depth arbitrary shapes and also more general rotations, including the influence of the frames not being parallel. It will also be interesting to extend this work to surfaces in which surface tension depends on deformation, simulating an elastic response relevant in material design [66] or for the description of biological membranes.

Last but not least, while perturbation theory captures well a wide range of system properties, we have seen that it neglects non-linear effects which become important close to the instability. It would therefore be important to develop more accurate theoretical tools, for example in generalising the approach proposed by Alimov *et al.* [1] to more general surface shapes. Since the critcal height seems to be a characteristic length for many other properties of the surface.

Chapter 3

Bubbles and drops between circular frames

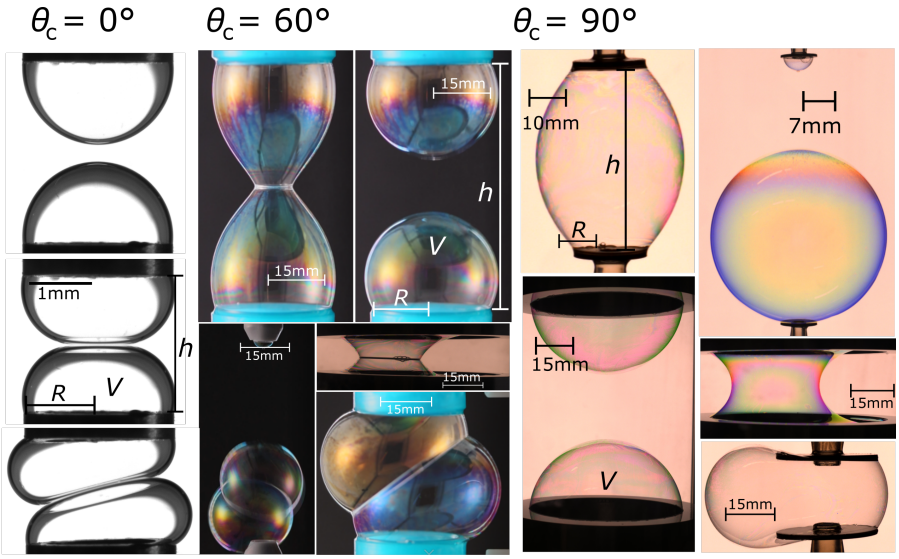

Interactions between bubbles or drops play an important role in many physical phenomena. Whether we consider the interaction between two bubbles (drops) or between many (foams or emulsions), these interactions are complex and still poorly understood. An interesting case arises when two equal- and constant-volume bubbles (drops) interact with each other while being held by two axisymetrically positioned capillaries of circular cross-section - a configuration which is frequently used in characterisation devices. The minimisation of the surface energy of this "double bubble" (or "double drop") configuration, constrained by the fixed volume and the capillary boundaries, creates a complex landscape of shape spaces where stable shapes are separated by different types of instabilities. Combining experiment, finite element simulation and theory, we provide here for the first time a complete analysis of these shape spaces, considering the adhesive energy between the bubbles or drops (expressed by the contact angle) as an additional control parameter. We provide the full shape diagrams for different contact angles (0°, 60° and 90°), including a detailed discussion of four types of instabilities. Two of these break the axisymmetry whilst the two others break the connectivity of the ensemble. As far as we are aware,

two of these instabilities have never been reported before. We accompany the shape and stability analysis with detailed mechanical characterisation using force and pressure measurements. Experiments, simulations and theory showing excellent agreement, this work will not only be useful in guiding the exploitation of double bubble (double drop) experiments on capillaries, but it also opens the possibility to exploit these configurations for the characterisation of increasingly complex bubble or drop interactions. Since the contact angle of 90° corresponds to an "imaginary" film separating the two bubbles, our analysis naturally includes the shapes and stability of a capillary bridge between two circular frames. A significant part of this chapter has been the basics for the article "Bubbles and drops between circular frames: Shape, force and stability analysis" under review in Soft Matter.

Contents

3.1 Introduction

Bubbles and drops play an important role in many physical phenomena. Their interactions control the behaviour of assemblies of bubbles or drops, ranging all the way from the simple assembly of two bubbles or two drops to the complex multi-body interactions in foams and emulsions [67, 68, 69]. One of the most commonly used techniques to characterise the properties of individual bubbles (drops) is the rising bubble (pendant drop) tensiometer [70, 71, 72], which uses the shape analysis of an axisymmetric bubble (drop) held by a capillary with circular cross-section. Here we propose to exploit this kind of configuration after the addition of a second bubble (drop) held by an axisymmetrically positioned capillary to investigate the interactions between bubbles (drops), as shown in Fig. 3.1. Similar configurations have been used in the past in order to quantify coalescence of bubbles (drops) [73, 74, 75, 76], the adhesive forces between cells [77] or the adhesive energy between bubbles, drops or vesicles [78, 79, 80], the latter being expressed by the contact angle θ_c created between the two bubbles (drops) (Fig. 3.1). However, even in the case of bubbles (drops) of equal and constant volume V, constant interfacial tension γ, fixed on identical, axisymetrically positioned capillaries with circular cross-section of radius R and separated by a distance h (Fig. 3.1), surface minimisation creates a highly complex landscape of possible shape configurations. The V-R-θ_c-h shape space contains zones with different physically stable shapes that are separated by at least four types of shape instabilities. These instabilities may either break the axisymmetry of the ensemble or its connectivity. They are sketched in Fig. 3.2 together with the convention for the naming and abbreviations which we will use throughout the chapter. One illustrative example which includes three of these instabilities is shown in Fig. 3.3 for the case of two soap bubbles in air. The two bubbles are initially separated ("Separated bubbles", SB). Upon decreasing h, they "jump" into contact ("Connected bubbles", CB) at $h = h_{SB \to CB}$ during a first shape instability, creating a contact angle $\theta_c = 60°$ due to the

natural attraction between soap bubbles in air. Further reducing h creates an increasing "flattening" deformation of the two axisymmetric bubbles, until a second shape instability is reached at $h = h_{\mathrm{CB}\to\mathrm{TB}}$ [79, 41, 81] which breaks the axisymmetry by tilting of the two bubbles ("Tilted bubbles", TB). Further decreasing h increases the tilt angle. Increasing h again, the different shape configurations are re-accessed in a fully reversible manner until $h = h_{\mathrm{SB}\to\mathrm{CB}}$. For $h > h_{\mathrm{SB}\to\mathrm{CB}}$, a range of elongated, axisymmetric bubble shapes is accessible due to the attraction between the bubbles. At another critical distance, the two bubbles may either detach from each other (top row of Fig. 3.3, "Separated bubbles", SB) or detach from the frame (bottom row of Fig. 3.3, "Detached bubbles", DB). The precise sequence of the shape configurations and the shape instabilities depends on V, R and θ_c (Fig. 3.1). For different parameter ranges, other types of instabilities may arise, which are described in more detail in Section 3.4.

In order to capture these complex behaviours for the entire V-R-θ_c-h parameter space, we combine experiments, finite element simulations (Surface Evolver) and theory (Delaunay surfaces). We provide a complete description of these "shape spaces", including the mechanical stresses created by the bubbles (drops) between the capillaries.

Other research groups conducted similar investigations with three-dimensional or quasi-two dimensional soap bubbles [82, 81, 41]. However, in most of the previous investigations, the bubbles (drops) are confined between two parallel solid walls on which the bubbles (drops) can move freely, i.e. the boundary condition is given by a fixed contact angle between the bubble (drop) and the solid surface. The fact that in our setup the bubbles (drops) are fixed by a capillary of constant radius R changes some degrees of freedom of the problem and hence the shape behaviour. While Fortes *et al.* [82] and Bohn [81] discuss also briefly this case, they do not show quantitative results. Since this configuration is relevant for many physical scenarios, it is therefore important to establish a more quantitative understanding.

In our analysis we concentrate on systems with constant interfacial tension γ. By choosing wisely the gas/liquid or liquid/liquid configuration, we have access to different contact angles θ_c between the bubbles (drops), as shown in Fig. 3.1. This contact angle can be interpreted as the change in surface energy between the contact film of effective tension γ_f and the "free" bounding surface with effective tension γ_b (discussed in more detail in Section 1.2.4). The tensions are related to the contact angle θ_c via equilibrium considerations at the contact line

$$2\gamma_b \cos(\theta_c) = \gamma_f. \tag{3.1}$$

Three different θ_c are therefore easily accessible (Fig. 3.1), since the effective film and boundary tensions are set by the number of interfaces of tension γ which they contain. The first case is the one of two bubbles or two drops in contact in a liquid, or of two drops in contact in air ("Bubble/drop" configuration in Fig. 3.1) which gives $2\gamma_b = \gamma_f = 2\gamma$ and therefore $\theta_c = 0°$. The second configuration consists of two bubbles in air ("Soap bubble" configuration in Fig. 3.1), which has a contact angle of 60° since $\gamma_b = \gamma_f = 2\gamma$. A special case is the one of an imaginary film with $\gamma_f = 0$, which gives $\theta_c = 90°$ with $\gamma_b = \gamma$ (bubble or drop in a liquid or drop in air) or $\gamma_b = 2\gamma$ (bubble in air). This corresponds in reality to one single bubble or drop, i.e. a "Capillary bridge" between the two capillaries. This little mental exercise opens a door to a slightly different configuration with different applications in nature and industry for almost the same theory and experimental setup.

In all our considerations we neglect gravity. In the experiments we ensure this by

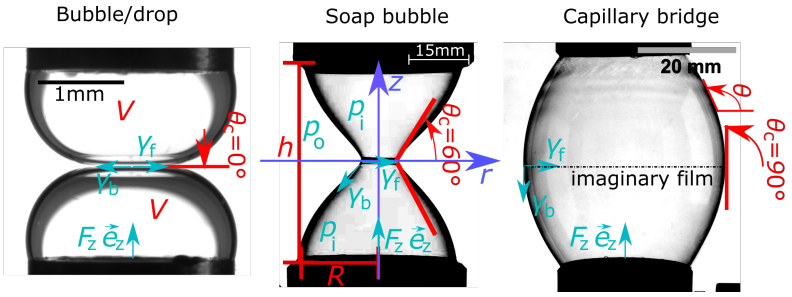

Figure 3.1: Configurations considered in this article: "Bubble/drop": two drops or two bubbles in contact surrounded by a liquid ($\theta_c = 0°$); "Soap bubbles": two bubble in contact in air ($\theta_c = 60°$); "Capillary bridge": one bubble or drop separated by an "imaginary" central film of zero interfacial tension, leading to $\theta_c = 90°$. All bubbles or drops are held by axisymmetrically positioned circular frames. The geometrical variables are: h the distance between the frames, R the frame radius, V the bubble or drop volume, θ_c the contact angle between the upper and lower bubble and θ the angle of inclination of the $r(z)$-profile, which depends on the other geometrical boundary conditions. $F_z\vec{e}_z$ is the total force in z-direction exerted on the lower bubble by the lower frame, p_i and p_o are the inner and outer pressure of the bubbles (drops), respectively, and γ_f and γ_b are the effective film and effective bubble/drop interfacial tension.

choosing configurations in which interfacial tension dominates gravity (Section 3.3.2). For this to be the case, the characteristic length of the bubbles or drops must be smaller than the capillary length, which is equivalent to a small Bond number. As the capillary length varies greatly between bubbles, drops and soap bubbles, the size of the bubbles or drops must also be adjusted. More informations the reader can find in the materials Section 3.3.2.4. All surfaces are therefore constant mean curvature surfaces given by the Young-Laplace law and the constant interfacial tension γ during one experiment. In the case of axisymmetric shapes, the external surfaces are part of the family of Delaunay Surfaces [20] whose theory we describe in more detail in Section 3.3.3.

In the following we will analyse in detail these different shape spaces by combining experiments (Section 3.3.2), finite element simulations (Surface Evolver (SE)) (Section 3.3.4) and the theory of Delaunay surfaces (DS) (Section 3.3.3). In the theoretical part we also provide the method to obtain the shapes which fit to the experiments and simulation (Section 3.3.3). We combine all three methods to analyse first the normal forces in respect

Name	Label	θ_c = 0°	θ_c = 60°	θ_c = 90°
Connected Bubbles	CB			
Separated Bubbles	SB			
Detached Bubbles	DB			
Tilted Bubbles	TB			
Shifted Bubbles	ShB			

Figure 3.2: Overview for different names of stable shapes for the three contact angles θ_c. For simplicity only "bubble" is used even though the terminology applies equally to drops.

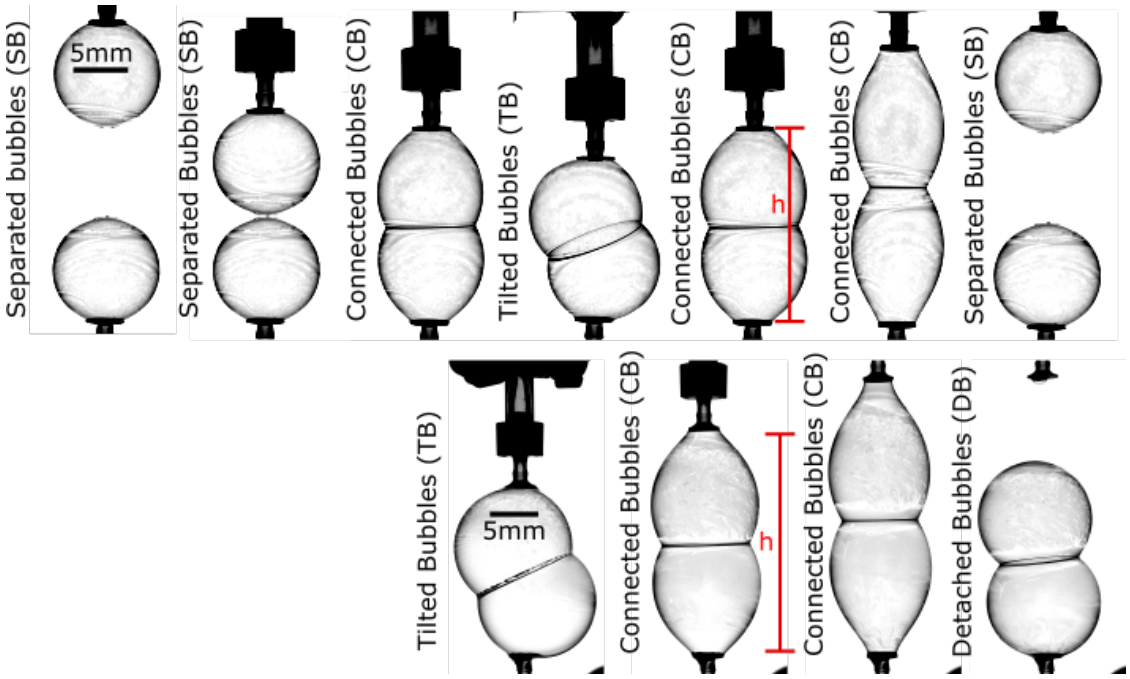

Figure 3.3: Series of photographs of soap bubble experiments where the distance h between the frames is first decreased and then increased in a quasi-static manner showing the different shapes and instabilities which can be obtained. In the bottom row, the volume V of the bubbles is larger, leading to a different instability upon increasing h

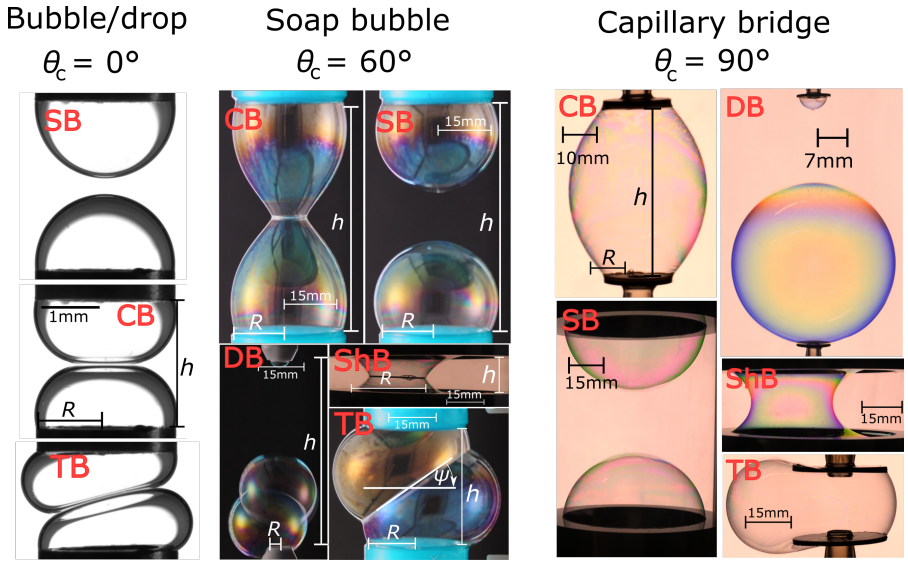

Figure 3.4: Overview of the different shape configurations for two bubbles (or drops) (left), two soap bubbles (centre) and capillary bridges (right) (see Fig. 3.1a), which appear by changing h, R, V and θ_c. One finds five different shapes witch are listed in Fig. 3.2: Connected bubbles (CB), Separated Bubbles (SB), Detached Bubbles (DB), Tilted Bubbles (TB) with the tilt angle ψ, and Shifted Bubbles (ShB).

to the frame cross-section and pressures for the different experimental configurations (Section 3.4.2). We then discuss in detail the associated shape diagrams for the three different contact angles θ_c (Section 3.4.3).

Experiment, simulation and theory showing excellent agreement, we think that this work will be useful for scientists working on double bubble (double drop) and capillary bridge problems between capillaries. It does not only provide a solid basis to start exploring more complex interactions (such as bubbles or drops with elastic interfaces), but it is also hoped to inspire more in-depth investigations of some of the instabilities which still await theoretical description.

3.2 Dimensionless lengths, forces and pressures

We combine results from three different methods to investigate the bubbles (drops) in contact and the capillary bridges: experiments (Section 3.3.2), the theory of Delaunay Surfaces (Section 3.3.3) and Surface Evolver simulations (Section 3.3.4). Since the bubble (drop) volume V and the interfacial tension γ_b remain constant during one experiment, they provide a natural length and stress scale for our specific problem. We will use them in the Result Section 3.4 to compare all three methods with each other. Therefore, we define the dimensionless lengths $\hat{L}$ (such as $\hat{r}$, $\hat{R}$ or $\hat{h}$) and forces $\hat{F}$ and pressures $\Delta\hat{p}$ with

$$\hat{L} = \frac{1}{V^{1/3}} L, \tag{3.2}$$

$$\hat{F}_z = \frac{1}{\gamma_\mathrm{b} V^{1/3}} F_z, \tag{3.3}$$

$$\Delta\hat{p} = \frac{V^{1/3}}{\gamma_\mathrm{b}} \Delta p. \tag{3.4}$$

3.3 Materials and Methods

3.3.1 Materials

For the soap bubbles we used a mixture of 30 wt% glycerol, 3 wt% Fairy dishwashing liquid and di-ionised water (Milli-Q). We mixed them for 20 minutes with a magnetic stirrer and used this solution for a period of 5 months. The interfacial tension of this solution with air is $\gamma = 26.0 \pm 0.5$ mN/m measured with pendant drop tensiometry (TRACKER device from TECLIS).

Air bubbles were also created in an aqueous solution of Sodium Dodecyl Sulfate (SDS) at a concentration of 6.5 g/L, which corresponds to 2.75 times the critical micelle concentration. The solution was mixed for a couple of hours with a magnetic stirrer. The same solution was used to create water drops with SDS in silicone oil (BLUESIL FLD 47V100, LOT 9255610). At room temperature its density was determined to be $\rho = 0.965 \pm 0.001$ kg/L using a D4 METTLER TOLEDO densimetre. The interfacial tension between the aqueous SDS solution and the silicone oil was measured to be $\gamma = 11.2 \pm 0.5$ mN/m using pendant drop tensiometry (TRACKER by TECLIS).

3.3.1.1 Frame geometries

We used different frame radii for the soap bubble setup of $R = [2.7\,\text{mm}, 3.6\,\text{mm}, 11.8\,\text{mm}, 15.0\,\text{mm}, 30.0\,\text{mm}]$. The frames were manufactured by different methods. The frames with $R = [15.0\,\text{mm}, 3.6\,\text{mm}]$ are 3D-printed with a thermoplastic 3D printer Form 2 from Formlabs (Fig. 3.5c center). The used printing method was stereolithography with a layer thickness of 0.025 mm. The deviation between a circle and the printed frame geometry is at maximum 0.4%. The frames with $R = [2.7\,\text{mm}, 11.8\,\text{mm}]$ are metal disks glued onto a microfluid connector (Fig. 3.5c left). The frame with $R = [30\,\text{mm}]$ is a numerically milled cylinder made from aluminium (Fig. 3.5c right) using a numerical milling device.

From a mathematical point of view, pinned bubbles are surfaces where some points on the surface are fixed points in space. Here the fixed points are on circular frames. The following explains how the pinning was realised in our experiments. We deal with static interfaces controlled by interfacial tension. That means the only forces exerted on the contact line between the frame and the interface are interfacial tensions. The force equilibrium at the contact line in the frame plane in radial direction is expressed with the Young-Dupré law [83]

$$\gamma_{\text{Fi}} - \gamma_{\text{Fo}} = \gamma_{\text{b}} \cos\theta, \tag{3.5}$$

illustrated in Fig. 3.5a. The interfacial tension between the frame and the inner fluid is γ_{Fi}. The interfacial tension between the frame and the outer fluid is γ_{Fo}. The interfacial tension between the inner and outer fluid is γ_{b}. Since in most cases all three interfacial tensions are constant, the angle θ at the contact line is constant as well. If now the volume or other constraints change, the contact line between the frame surface and the bubble interface can move to adapt to the new constraints. Here we want to work with pinned interfaces. This is achieved when one of the three interfacial tensions on the contact line is variable in direction or amplitude. Discontinuities in material or geometry could be seen as an infinitely strong gradient in space for the interfacial tension, as sketched in Fig. 3.5b for a geometrical discontinuity. To move the contact line above such discontinuities, the angle θ has to make a jump, which ensures for a specific range of boundary conditions a pinning of the contact line on the discontinuity. In our experiments we used only material discontinuities, since it is simpler to control the position of the discontinuity. In Fig. 3.5b a geometrical discontinuity, for example an edge, is schematically illustrated. To move the contact line over the edge of the pinning object the angle θ between the surface and the horizontal plane is free to be a value between θ_{1g} and θ_{2g} ("g" for geometrical discontinuity).

Nevertheless by making some parts of a surface hydrophobic or hydrophilic a material discontinuity could be used in the same manner. For soap films the scenario is slightly more complicated. Since the surface is a film and cannot be assigned to a specific contact point. The film will always form a meniscus at the contact to the pinning object. The geometry of the meniscus plays an important rule for the pinning strength. This geometry is influenced by the two mentioned discontinuities. But also other parameters, like the liquid fraction, play a significant rule for the geometry of the meniscus and so the pinning strength. A good approximation for the contact angle between an object and a soap film is $\theta = 90°$. It is exact for a soap film on a fully wet horizontal plane.

As we see in Fig. 3.5 the possibility to pin a liquid surface is limited to a range of θ

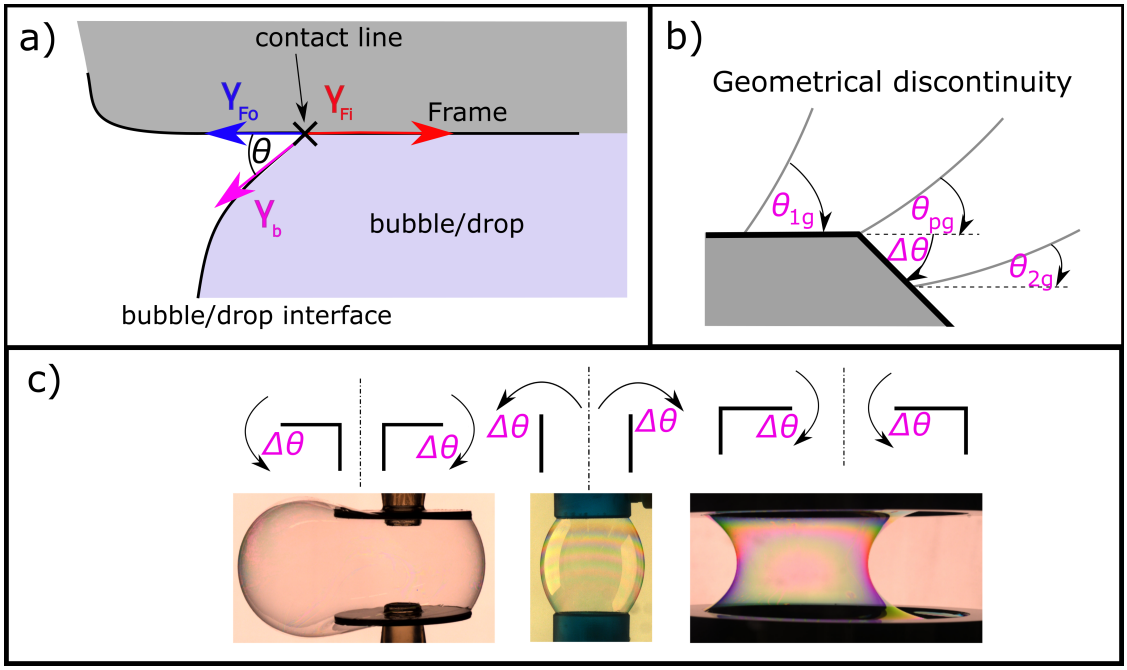

Figure 3.5: Three schemes explaining how the frame geometries are chosen. a) Force equilibrium between the different interfacial tensions at one point of the contact line between the bubble interface and the frame. γ_b is the interfacial tension between the outer and inner fluid, γ_{Fo} is the interfacial tension between the frame and the outer fluid and γ_{Fi} is the interfacial tension between the frame and the inner fluid. The contact point is part of the contact line between the frame surface and the bubble interface. b) Principal idea of pinning with help of a geometrical discontinuity. The contact line is pinned for a contact angle θ_p between $\theta_{1g} > \theta_p > \theta_{2g}$ with $\Delta\theta = \theta_{1g} - \theta_{2g}$, "g" stands for geometrical discontinuity. c) Chosen frame geometries for different boundary conditions, $\hat{h}$, $\hat{R}$ and θ_c.

depending on the discontinuities. The pinning range is

$$\Delta\theta = \theta_{1g} - \theta_{2g}. \tag{3.6}$$

The maximal $\Delta\theta$ for a geometrical discontinuity is therefore 180°. For a combination with a material discontinuity one can reach also higher $\Delta\theta$.

For our experimental setup it was important that the change in θ during the tilting instability and a detachment instability was smaller than $\Delta\theta$ defined by the setup. We used for that different frame geometries, see Fig. 3.5c. For some (R, V) we had to repeat the experiment with different frame geometries to measure the tilting instability and a detachment instability.

3.3.2 Experimental methods

We use two different setups (Fig. 3.6), one for the "Bubble/drop" configuration (Fig. 3.6 a) and one for the "Soap bubble" configuration (Fig. 3.6b). Each experiment consists of a cycle where h is varied and V, R and θ_c stay constant. The pressure changes are small compared to the atmospheric pressure. Consequently, the volume changes during an experiment are negligible.

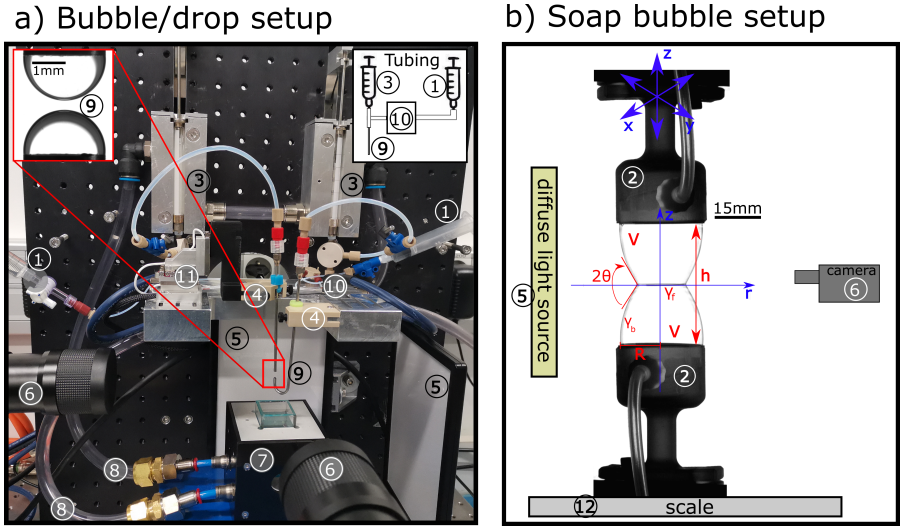

Figure 3.6: The two experiments used in this article: a) "Bubble/drop setup" and b) "Soap bubble setup". The Bubble/drop setup refers in reality to two different setups which follow the same principles. One is a modified device from TECLIS and the other one (shown in (a)) is a home-made device following the principles of the TECLIS device. In the images we can see: (1) the two syringes to charge the system with a liquid, (2) the two frames for the soap bubbles, (3) the syringes to control the volume of the drops with a linear motor, (4) the tilting mechanisms to change the angular orientation of the needles, (5) the diffusive backlights, (6) the cameras, (7) the vessel with temperature control, (8) the tubes which contain temperature controlled water, (9) the two needles (one straight the other in U-shape), (10) the pressure sensor and (11) the micro controller for a transverse displacement of the upper needle with tilting mechanism. The "Soap bubble setup" (b) has the same overall configuration. The differences are the frame size ((9) vs (2)) and the pressure sensor (10) in (a) and the normal force sensor (12) in (b).

3.3.2.1 Bubble/drop setup

We use two setups with almost the same configuration for the "Bubble/drop setup" (Fig. 3.6a). One was developed by the society TECLIS in interaction with us. It consists of a modified pendant drop tensiometre (TRACKER), to which a second syringe system was added. The second one is a fully home-built, Labview-run device (shown in Fig. 3.6a). Both devices contain two syringes (3) of max 500 μl volume, each connected to a needle (9) by a tubing system. On a sidearm of the tubing system a Miniature Low Pressure Sensor 0.5 Psi 24PCEFB6G (10) is connected to measure the pressure difference $\Delta p = p_\mathrm{i} - p_\mathrm{o}$ (see Fig. 3.1). To increase the precision of the pressure sensor, a home-made electrical circuit was used. The needles have circular cross-sections of radius R with $R = [1.2\,\mathrm{mm}, 2.15\,\mathrm{mm}]$. Each needle is fixed on a home-built tilting mechanism (4) allowing to control the orientation of the symmetry axis of the needle end, (see Appendix Section A.1). One of these tilt mechanisms is fixed on a board while the other one is fixed on a high precision micro-controller (SmarAct) (11). This micro-controller moves on command in arbitrary translational directions with a controlled speed. One of the needles has a U-shape and the other a straight shape. This allows the ends of the two needles to be positioned and moved along the same z-axis. The needle openings are immersed in a 25 mL vessel (7) with 25 mm square cross-section and 40 mm depth. The vessel, the syringes and the pressure sensor are surrounded by metal blocks through which water is flowing

continuously to maintain the temperature at 20 C° (8). The metal cube for the quartz vessel has an opening in the top and circular windows in the four horizontal directions for imaging purposes (7). Backlights (5) are positioned in front of two of these windows. On the opposite sides of the backlights, IDS U3-3800CP-M-GL R2 cameras (6) are fixed to obtain images of the two bubbles/drops from two orthogonal perspectives.

The verticality and coaxiality of the needle ends is adjusted at the beginning of each experiment with the help of the tilting mechanism, the micro-controller unit and a numerically evaluation of the images of the two cameras. The exact procedure is explained in the Appendix Section A.1. Depending on the type of experiment to be conducted, the quartz vessel was filled with an aqueous SDS solution for the investigation of bubble-bubble interactions, or with a silicone oil for the investigation of drop-drop interactions. In the first case the syringes, tubes and needles were filled with air, while in the second case they were filled with SDS solution. We decided to make water drops in silicone oil (rather than the opposite), as it is easier to clean the vessel than the syringe system. Both systems can be easily inverted to investigate water drops in air or oil drops in water.

At the beginning of each experiment the bubbles or drops were formed separately with a defined volume. With help of the cameras coupled to a PID control the volume is accurately controlled and kept constant for 60 s to allow surfactant adsorption on the bubble (drop) surface. Then the bubbles (drops) are moved against each other along the needle axis with help of the micro-controller until they touch and deform. This deformation is progressively increased until the tilting instability occurs. Then the distance between the bubbles (drops) is again increased until they detach from each other or from the needle. We make sure that the deformation is slow enough to be considered quasi-static upon using a displacement velocity of the needle of 20 µm/s. Even though the PID volume control is switched off during this part of the experiment, its duration is short enough to assume that the drop volumes remain constant. We verify this by measuring the bubble (drop) volume before and after each experiment.

3.3.2.2 Pressure measurement

Fig. 3.7 shows the two pressure sensors for the upper and bottom bubble (drop) with the important parameters which are needed to obtain the pressure difference between the inside and outside of the two bubbles (drops). Since it is impossible to place the pressure sensor directly at the interface of the bubbles (drops) there is always a distance in space between the point where we measure the pressure difference and the point where we want to know the pressure difference. In the general case these two pressures are not the same due to hydrostatic and hydrodynamic pressures. In the absence of liquid flow, the differences in pressure between the sensors and the drop interfaces are only related to hydrostatic pressures. We will start with this simple case. Afterwards we will show that for the applied flow rates we can also neglect hydrodynamic effects.

The pressure difference between the inside and outside of the lower bubble (drop) is

$$\Delta p_{\mathrm{A}}^{-} = 2H_{\mathrm{A}}^{-}\gamma_{\mathrm{b}}^{-} = p_{\mathrm{i}}^{-} - p_{\mathrm{o}} = p_{\mathrm{S}}^{-} + (L^{-} - L_{\mathrm{A}}^{-})\rho_{\mathrm{i}}g - \rho_{\mathrm{o}}g(L_{\mathrm{F}}^{-} - L_{\mathrm{A}}^{-}), \tag{3.7}$$

where the index "−" stands for "bottom", "i" for "inside", "o" for "outside", "A" for "Apex" and "b" for "bubble". p_{S}^{-} is the pressure measured at the sensor for the bottom bubble and $\Delta p_{\mathrm{A}}^{-}$ the pressure jump at the bottom bubble interface at the apex. The distances

L are illustrated in Fig. 3.7. The pressure jump at the apex is the Laplace pressure at the apex. It is proportional to the mean curvature at the apex H_{A}^{-} and the interfacial tension of the bottom bubble (drop) γ_{b}^{-}. Due to the axisymmetric shape of the bubbles the two principle curvatures at the apex are identical. That is why we took the apex as our calibration point. The two densities of the inner and outer phase, ρ_{i} and ρ_{o}, are measured independently with Mettler Toledo D4 at 20 °C. By rearranging Equ. (3.7) we obtain

$$p_{\mathrm{S}}^{-} + gL_{\mathrm{A}}^{-}(\rho_{\mathrm{o}} - \rho_{\mathrm{i}}) = 2H_{\mathrm{A}}^{-}\gamma_{\mathrm{b}}^{-} + \rho_{\mathrm{o}}gL_{\mathrm{F}}^{-} - \rho_{\mathrm{i}}gL_{-} = 2H_{\mathrm{A}}^{-}\gamma_{\mathrm{b}}^{-} + K_{\mathrm{sta}}^{-}, \tag{3.8}$$

with $K_{\mathrm{sta}}^{-} = \rho_{\mathrm{o}}gL_{\mathrm{F}}^{-} - \rho_{\mathrm{i}}gL^{-}$. Since the temperature, the bottom frame position and the liquid level of the outer liquid are constant, K_{sta}^{-} is constant as well. The liquid level stays constant if the temperature is constant and the outer liquid is not evaporating. Otherwise the liquid level has to be controlled. For the calibration of the pressure sensor the two liquid phases are chosen in a manner that γ_{b}^{-} is constant as well (high concentration of low molecular weight surfactants). In this case, one can make a linear fit between the measured H_{A}^{-} and p_{S}^{-} for quasi-static inflation and deflation of the bubble. The measured pressure of the sensor has to be corrected with $gL_{\mathrm{A}}^{-}(\rho_{\mathrm{o}} - \rho_{\mathrm{i}})$ where only L_{A}^{-} changes during the experiment and is measured optically during the calibration with a precision of 10 μm. The same procedure is applied for the upper sensor S^{+}. To obtain the respective equations one has to replace only the index "−" with "+" and change the sign in front of L_{A}^{-} in (3.8) to obtain

$$p_{\mathrm{S}}^{+} - gL_{\mathrm{A}}^{+}(\rho_{\mathrm{o}} - \rho_{\mathrm{i}}) = 2H_{\mathrm{A}}^{+}\gamma_{\mathrm{b}} + \rho_{\mathrm{o}}gL_{\mathrm{F}}^{+} - \rho_{\mathrm{i}}gL^{+} = 2H_{\mathrm{A}}^{+}\gamma_{\mathrm{b}} + K_{\mathrm{sta}}^{+}, \tag{3.9}$$

with the new constant $K_{\mathrm{sta}}^{+} = \rho_{\mathrm{o}}gL_{\mathrm{F}}^{+} - \rho_{\mathrm{i}}gL^{+}$. Since the upper frame changes position during an experiment, the constant K_{sta}^{+} changes as well. That is why we relate the variable K_{sta}^{+} to the frame distance between the bottom and top frames L_{FF} which is also measured optically. It follows

$$K_{\mathrm{sta}}^{+} = K_{0;\mathrm{sta}}^{+} + g(L_{\mathrm{FF0}} - L_{\mathrm{FF}})(\rho_{\mathrm{o}} - \rho_{\mathrm{i}}), \tag{3.10}$$

where the index "0" indicates the values at the onset of the experiment. The variables $K_{0;\mathrm{sta}}^{+}$ and L_{FF0} are constant and obtained during the pressure calibration of the upper bubble. Consequently the calibration constant K_{sta}^{+} is a function of L_{FF}. Whenever possible, the calibration was repeated before and after a set of experiments to verify that the calibration constants did not change with time. Fig. 3.8 shows an example of a typical pressure calibration inflation/deflation curve. On the left part in Fig. 3.8 the measured pressure corrected with the changing bubble height L_{A}^{-} is plotted against H_{A}^{-}. The color of the measurements symbolise the time: starting from purple at t_0, it passes through green at t_1, before ending at yellow at t_2. The red line is the obtained calibration curve, which gives K_{sta}^{-} and γ_{b}. The right part of Fig. 3.8 compares $\Delta p_{\mathrm{A}}^{-}$ obtained from image analysis with the Young-Laplace equation and the pressure sensor for the inflation and deflation. Both show excellent agreement.

3.3.2.3 Soap bubble setup

In the soap bubble setup (Fig. 3.6b) two soap bubbles ("Soap bubble" configuration) or one soap bubble ("Capillary bridge" configuration) are created in air at the outlet of air-tight frames with circular outlets of radius R, Fig. 3.5c. A soap film was first formed

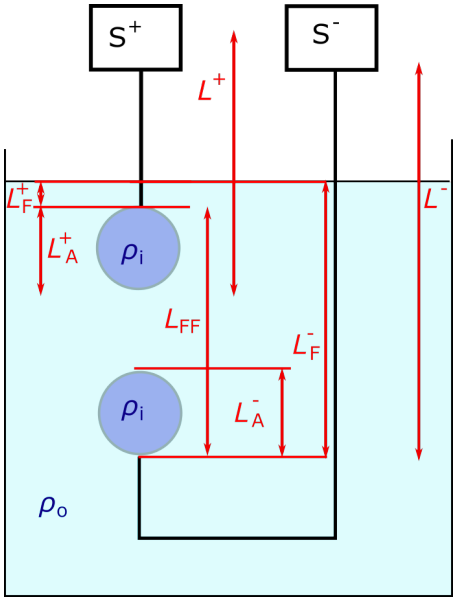

Figure 3.7: Scheme showing the relationship between the measured pressures in the Sensors S (Fig. 3.6 (10)) and the pressure difference between the inside and the outside of the bubbles. L are lengths, ρ densities and p pressures. The indices "+" and "-" stand for "top" and "bottom" respectively, "i" and "o" for "inside" and "outside", "A" for "apex" and "F" for "frame".

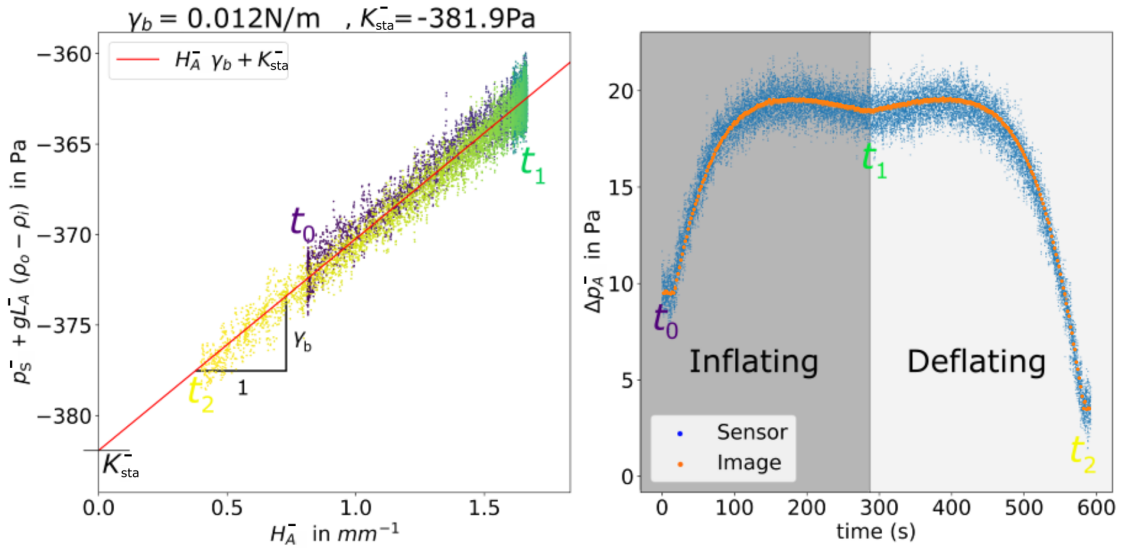

Figure 3.8: Left: measured pressure of the bottom bubble (drop) corrected with the apex height L_{A}^{-} plotted against the measured mean curvature at the bottom bubble apex H_{A}^{-} to obtain the calibration constant K_{sta}^{-} and the interfacial tension of the bottom bubble γ_b using Equ. (3.8). Right: pressure evolution at the apex of the bottom bubble obtained either with the pressure sensor or with image analysis, plotted during an inflation and deflation of a bubble/drop.

on the outlet of the frames by immersing them in the soap solution. Afterwards, a given volume of air was injected into the frames via syringes to create bubbles of volume V. The sizes of the syringes were chosen for each experiment to optimise the precision in the volume control for the desired bubble volumes, which ranged between $1\,\mathrm{ml} < V < 30\,\mathrm{ml}$.

The relative error is typically of the order of 1%. Afterwards, the bubbles were positioned on the same symmetry axis with the help of two cameras (IDS U3-3800CP-M-GL R2) positioned at an angle of 90° to each other. The upper bubble was moved in the vertical direction using a linear table CKK and a motor MSN03. The movement was smooth with a speed of 0.02 mm/s controlled by a home-made Labview program. We verified that this speed is slow enough to neglect viscoelastic contributions of the soap films.

The vertical component of the force F_z exerted on the lower bubble by the lower frame is measured by monitoring the apparent weight of the bottom frame with a high-precision scale SECURA224-1S with a precision of 0.1 µN. The force exerted by the bubble and frame weight imposes an offset which can be obtained with a precision of 1 µN. The shape of the bubbles is obtained by imaging them in front of a diffusive screen using a digital camera IDS U3-3800CP-M-GL R2. These images are also used to obtain the distance h between the frames.

At the beginning of each experiment, the distance h between the two frames is decreased until the film between the two bubbles is strongly tilted. Afterwards the measurement starts by capturing images and saving the normal force F_z every two seconds. The upper frame moves smoothly upwards. The measurement stops 10 s after the two bubbles detach or one bubble detaches from a frame. The force F_z measured after a detachment was used to calculate the offset.

The experimental procedure is the same for the Capillary bridge (contact angle $\theta_c = 90°$) only with one large bubble of volume $2V$, which connects the two frames. To create this capillary bridge with $2V$, two bubbles of the same size as before were created brought into contact. The contact film may break and a capillary bridge is created. Since it is difficult to control if the film breaks or remains intact, we started in the general case directly with the capillary bridge by starting with $\hat{h} = 0$ and increasing the distance between the two frames when injecting air at the same time.

3.3.2.4 Bond number

In order to ensure that the influence of gravity on the shape of the bubbles/drops can be neglected in our experiments, we need to work at small Bond numbers Bo. The Bond number is a dimensionless quantity measuring the importance of gravitational forces compared to surface tension forces.

In the case of bubbles/drops, it is given by

$$\mathrm{Bo} = \left(\frac{h}{\lambda_c}\right)^2 = \frac{\Delta\rho g h^2}{\gamma}, \tag{3.11}$$

where h is the characteristic length in the vertical direction, and λ_c the capillary length ($\lambda_c = \sqrt{\gamma/\Delta\rho g}$). For the silicone oil / water system one obtains $\mathrm{Bo} < 2.5\ddot{1}0^{-3}$ (see Fig. 3.9).

For soap bubbles, the average film thickness e_0 must be taken into account (see for example the work of Cohen *et al.*[84]) leading to

$$\mathrm{Bo} = \left(\frac{\Delta\rho g e_0 h}{\gamma}\right)^2. \tag{3.12}$$

In our experiments, with an estimated film thickness of 1 µm, $\mathrm{Bo} < 10^{-3}$.

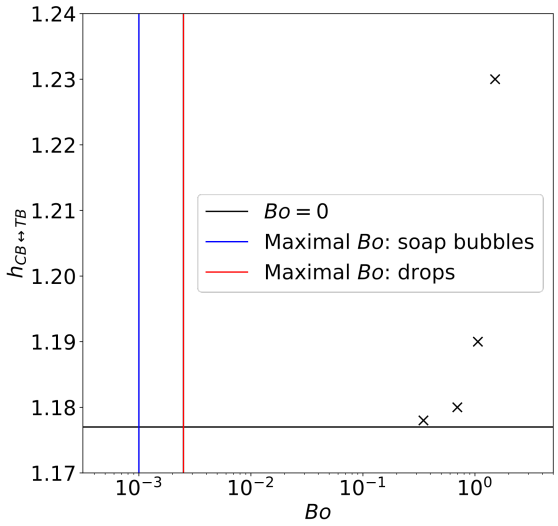

Figure 3.9: Influence of gravity (expressed by the Bond number Bo) on onset $h_{CB\longleftrightarrow TB}$ of the tilt instability for the case $\theta_c = 0°$ and $\hat{R} = 0.7$. The results are obtained with Surface Evolver. The maximal Bo encountered in the experiments for the two used systems, soap bubbles (in red) and water drops in silicone (blue), are highlighted. The influence of gravity is therefore negligible.

In both cases we obtain very small Bo and gravity is therefore negligible. The assumption of a constant Δp is therefore reasonable.

Never the less we estimate the influence of gravity for the range of Bo used in our experiments with help of Surface evolver simulations. Fig. 3.9 shows how the onset of the tilting instability $h_{\mathrm{CB}\leftrightarrow\mathrm{TB}}$ is expected to depend on Bo for the case $\theta_c = 0°$ and $\hat{R} = 0.7$. It can be seen that for soap bubbles and water drops in silicone, the influence of gravity is negligible in the range of Bo of our experiments.

3.3.3 Theoretical method: Delaunay surfaces

In the following, we only talk about bubbles to facilitate reading. However, all concepts apply equally to drops.

One can divide the films and interfaces of the two bubbles in contact into three parts: the upper bubble, the lower bubble and the film separating the two bubbles.

In all our considerations we neglect gravity. In the experiments we ensure this by choosing configurations in which interfacial tension dominates gravity, i.e. we work at sufficiently small Bond numbers Bo, as discussed in Section 3.3.2.4. We therefore assume Δp as constant along z, meaning that the upper and lower part of the bubble shape are constant mean curvature surfaces, see Section 1.2.3. If the two bubbles have the same volume and the boundary conditions are mirror symmetric, the pressure difference between both bubbles is zero and the separating film is a minimal surface. In the case where the bubble configuration stays axisymmetric, the separating film remains a horizontal, flat disk at mid-height and the upper and lower part can be described by a "Delaunay surface" [20, 85], see also Section 1.2.3.

The energy of an axisymmetric shape defined by $r(z)$ (Fig. 3.1) with constant interfacial tension γ is given in Equ. (1.14). Searching for extrema of Equ. (1.14), one obtains Equ. (1.16), the force equilibrium in z-direction. The constant F_z is equal to

the total force in the z-direction exerted on the lower bubble by the lower frame [86], as shown in Fig. 3.1a. It is constant over z. For Nodoids $r_{,z}$ has a singularity at the point where the profile becomes horizontal. That is the point where the interfacial tension part in Equ. (1.16) switches sign.

The inverse mean curvature H^{-1} is the characteristic length scale of the problem. We therefore use it to make a unique assignment between a profile $r(z)$ and a normalised force $\tilde{F}_z$, by normalising all key quantities with the absolute value of the inverse mean curvature

$$\begin{aligned} \tilde{r} &= |H|r, \\ \tilde{z} &= |H|z, \\ \tilde{h} &= |H|h, \\ \tilde{F}_z &= |H|F_z/(2\pi\gamma), \\ \Delta\tilde{p} &= |\Delta p|/(2\gamma|H|) = 1. \end{aligned} \tag{3.13}$$

Conversely, this allows us to find all possible constant mean curvature surfaces that fulfil all boundary conditions by scanning through all $\tilde{F}_z$. Since this normalisation is not valid for minimal surfaces with $\Delta p = 0$, the catenoid is treated separately in Section 3.3.3.4. A second factor $2\pi\gamma$ scales the force F_z and the pressure difference Δp and can be interpreted as the interfacial tension force of a circle of radius unity. Then, the normalised surface shape depends only on one parameter, the normalised normal force $\tilde{F}_z$ [86],

$$\tilde{F}_z = \tilde{r}^2 \mp \frac{\tilde{r}}{\sqrt{1+\tilde{r}_{,\tilde{z}}^2}}. \tag{3.14}$$

The relations given above show that two physical quantities control the mechanical and geometrical properties of these surfaces: the interfacial tension γ and the mean curvature H.

As dicussed in Section 1.2.3, four different groups of Delaunay surfaces are commonly distinguished by the choice of $\tilde{F}_z$ (see Fig. 3.10) [87, 86]: "nodoids" for $\tilde{F}_z > 0$, "spheres" for $\tilde{F}_z = 0$, "unduloids" for $0 > \tilde{F}_z > -0.25$ and "cylinders" for $\tilde{F}_z = -0.25$. The external surfaces of the bubbles or drops have to be among these five groups of surfaces (including the catenoid) if they maintain axisymmetry.

3.3.3.1 Parametrisation of Delaunay Surfaces

The five different axisymmetric constant mean curvature surfaces (nodoid, sphere, unduloid, cylinder and catenoid) can be obtained by rolling a cone section (Fig. 3.10) along the symmetry axis of the Delaunay surfaces and following one of the focal points of the cone sections. Path of the focal point then draws the profile of the surface. For example, the parametrisation of an **unduloid** is obtained by rolling an ellipse along the symmetry axis. One obtains (Fig. 3.10b)

$$\tilde{z}(\omega) = -2\tilde{F}_z \int_{\omega_0}^{\omega} \frac{\mathrm{d}u}{(1+e\cos u)\sqrt{1-e^2\cos^2 u}}, \tag{3.15}$$

$$\tilde{r}(\omega) = \sqrt{-\tilde{F}_z \frac{1-e\cos\omega}{1+e\cos\omega}}, \tag{3.16}$$

with $e = \sqrt{4\tilde{F}_z + 1}$ being the eccentricity of the ellipse and u and ω the angular position of the rolling ellipse above the symmetry axe of the Delaunay surfaces (Fig. 3.10b). ω_0 corresponds to a reference point defining the $z = 0$ plane (upper grey shaded areas in Fig. 3.10b). The implicit origin of ω in Equ. (3.16) belongs to the minimum radius of the unduloid, the point where the rolling ellipse touches the plane with the major axis and the focal point is closest to the plane.

The limit case of a **cylinder** is obtained when $e = 0$ with $\tilde{F}_z = -0.25$. Equ.s (3.16) then become

$$\tilde{z}(\omega) = -2\tilde{F}_z \int_{\omega_0}^{\omega} \mathrm{d}u, \tag{3.17}$$

$$\tilde{r}(\omega) = \sqrt{-\tilde{F}_z} = \frac{1}{2}. \tag{3.18}$$

The parametrisation of a **nodoid** is obtained by rolling a hyperbola along the symmetry axis of the nodoid and following one of the focal points. One obtains (Fig. 3.10b) [87]

$$\tilde{z}(\omega) = -2\tilde{F}_z \int_{\omega_0}^{\omega} \frac{\cos u \mathrm{d}u}{(e + \cos u)\sqrt{e^2 - \cos^2 u}}, \tag{3.19}$$

$$\tilde{r}(\omega) = \sqrt{-\tilde{F}_z \frac{e - \cos\omega}{e + \cos\omega}}. \tag{3.20}$$

The nodoid is the only Delaunay surface which exists under compression ($F_z > 0$) and with a negative pressure difference ($\Delta p < 0$). By crossing an interface of a Delaunay surface, the pressure changes by $|\Delta p|$. Depending on the direction in which the interface is crossed, the pressure jump is positive or negative. The self-intersection of the nodoids allows to cross two interfaces. Before crossing an interface $p = \tilde{p}_\infty$, after crossing the first interface $p = \tilde{p}_\infty + \Delta\tilde{p}$ and after crossing the second interface $p = \tilde{p}_\infty + 2\Delta\tilde{p}$, as shown by the pink shaded areas in Fig. 3.10b. If we now define $p_\mathrm{o} = \tilde{p}_\infty + 2\Delta\tilde{p}$ and $p_\mathrm{i} = \tilde{p}_\infty + \Delta\tilde{p}$, it is

$$\Delta p = \tilde{p}_\infty + \Delta\tilde{p} - (\tilde{p}_\infty + 2\Delta\tilde{p}) = -\Delta\tilde{p}. \tag{3.21}$$

The pressure difference changes sign. Since we also changed direction of ω, the normal force exerted on the upper frame changes also sign. The two dashed circles in the cavalier perspective at the nodoid profile in Fig. 3.10b (symbolising the beginning and the end of a bubble profile) show an example of a profile with $\tilde{F}_z > 0$, $\Delta p < 0$ and $F_z < 0$. The smallest theoretical distance between the frames is $h = 0$. This is the case when $z_1(\omega_1) = z_0(\omega_0) = 0$. For this solution to be non-trivial, $\omega_0 \neq \omega_1$ must hold. Whether there is a profile that fulfils these conditions depends on $\tilde{F}_z$ and θ_c. Profiles that fulfil these conditions always have $\tilde{F}_z > 0$ and $\theta_\mathrm{c} > 0°$.

One observes, that the eccentricity e depends only of $\tilde{F}_z$. Consequently, the mean curvature H scales the size of the conic section, and $\tilde{F}_z$ changes the angle of the cutting plane for the conic section. By increasing $\tilde{F}_z$, the plane becomes more vertical and by decreasing $\tilde{F}_z$ more horizontal. With $\tilde{F}_z = -0.25$, the plane is horizontal and cuts a circle out of the cone. H shifts the cutting plane with increasing H up and with decreasing H down, see Fig. 3.10.

If the tilt angle of the cutting plane is identical to the opening angle of the cone, then $e \to 1$ and $\tilde{F}_z \to 0$. One can distinguish two different cases. In the first case, $H \neq 0$

goes against a fixed value and we obtain a line as a conic section with a sphere as the associated surface. One obtains the unit sphere (Fig. 3.10b)

$$\tilde{z}(\omega) = \sin\omega, \tag{3.22}$$
$$\tilde{r}(\omega) = \cos\omega, \tag{3.23}$$

with $-\pi/2 \geq \omega \geq \pi/2$ and $\tilde{F}_z = 0$. For the sphere we use the same parametrisation variable ω, even if it is not the rolling parameter of the conic section.

If $H = 0$, the conic section is a parabola with a catenoid as the associated surface (Fig. 3.10a). For the catenoid we can no longer use our dimensionless representation where we multiply by the mean curvature H, since it becomes zero. Therefore, we show here the lengths with dimensions

$$\begin{aligned} z &= a\,\mathrm{arsinh}(\omega) \\ r &= a\sqrt{1+\omega^2}, \end{aligned} \tag{3.24}$$

with the neck radius $a = \lim_{H\to 0;\,\tilde{F}_z\to 0} \tilde{F}_z/H$. The catenoid is the only axisymmetric constant mean curvature surface which is not periodic. By eliminating ω in Equ.s (3.24) we obtain the classical equation of a catenoid Equ. 1.6. All five types of surfaces are present in the double bubble experiments.

3.3.3.2 Boundary conditions

In our case, for axisymmetric shapes, each bubble is described by a part of a Delaunay surface which has to fulfill a set of boundary conditions given by the experimental setup. The cylindrical coordinates of the bubble profile are defined by

$$r = f_r(\omega, \tilde{F}_z, H), \tag{3.25}$$

$$z = f_z(\omega, \omega_0, \tilde{F}_z, H), \tag{3.26}$$

where ω_0 is ω at the contact film and ω_1 is ω at the frame. The mid-plane is defined by $z(\omega = \omega_0) = 0$. The profile coordinates of Equ.s (3.25) and (3.26) are obtained with Equ.s (3.16), (3.18), (3.20), (3.23) and (3.24). The boundary conditions are given by

$$\frac{\mathrm{d}\tilde{r}}{\mathrm{d}\tilde{z}}(\omega = \omega_0) = \cot(\theta_c), \tag{3.27}$$
$$\tilde{r}(\omega = \omega_1) = |H|R, \tag{3.28}$$
$$\tilde{z}(\omega = \omega_1) = \frac{|H|h}{2}, \tag{3.29}$$
$$\int_0^{\tilde{h}/2} \pi\tilde{r}^2 \mathrm{d}\tilde{z} = |H|^3 V. \tag{3.30}$$

ω_0 is defined by the contact angle which defines the slope in $d\tilde{r}/d\tilde{z}(\omega)$ with Equ. (3.27). The radius at ω_0 has no constrains. The radius at ω_1 is defined by R with Equ. (3.28). The distance between the two frames gives the relation between $\tilde{z}$ and $\tilde{h}$ with Equ. (3.29). Finally we need to ensure volume conservation with Equ. (3.30).

$\mathrm{d}\tilde{z}$ in Equ. (3.30) can be negative for some ω at some parts of the shape in the case of a nodoid. In this case the interfacial tension is acting in the opposite direction and the

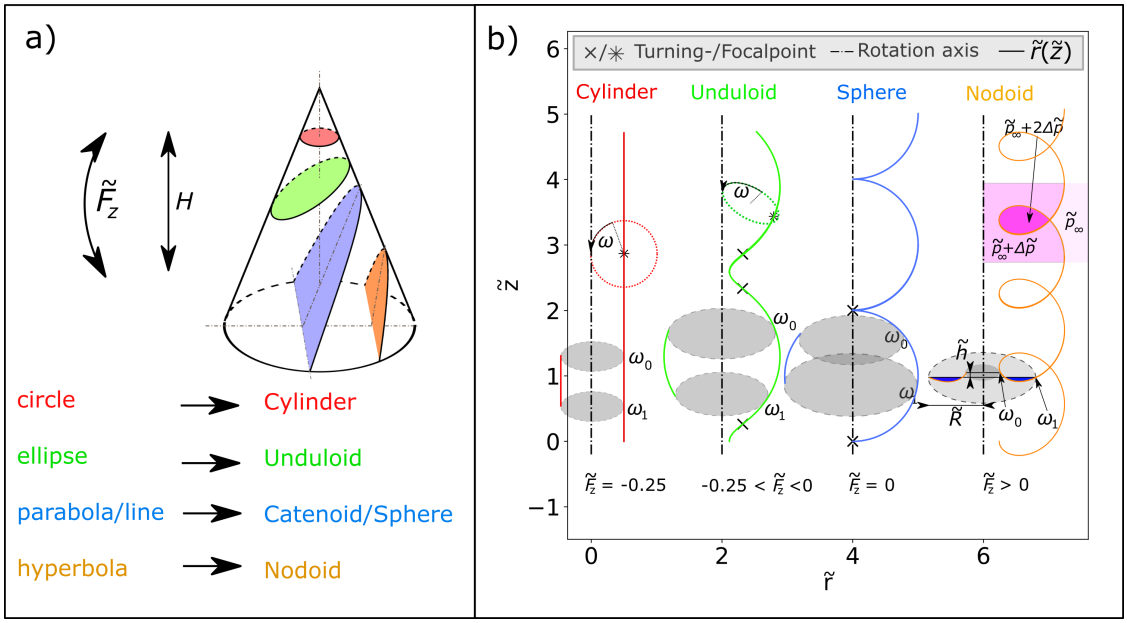

Figure 3.10: a) Cone with conic sections and the associated surfaces. $\tilde{F}_z$ rotates the cutting plane for the conic section and H shifts the cutting plane up or down. The figure is a modified figure from Wikipedia [88]. b) Examples of the normalised profiles $\tilde{r}(\tilde{z})$ of the four types of Delaunay surfaces: cylinder, unduloid, sphere and nodoid obtained with Equ.s (3.18), (3.16), (3.23) and (3.20) (shifted by $\tilde{r} = 2$ for a better visualisation). The black dash-dotted lines are the rotation axis of the shapes. The dashed, grey shaded circles in cavalier perspective are possible start and end points/planes for the Delaunay profiles/surfaces with ω_0 and ω_1. The black crosses are the turning points where the slope $d\tilde{r}/d\tilde{z}$ is maximal or minimal for unduloids and spheres. The dotted lines are cone sections rotating above the symmetry axis with the focal points on the profile. The nodoids have three pressure zones, one with $p = \tilde{p}_\infty$, one with $p = \tilde{p}_\infty + \Delta\tilde{p}$ and one with $p = \tilde{p}_\infty + 2\Delta\tilde{p}$, shown by the different pink shades. ω_0 and ω_1 show possible start and end points for surfaces.

sign in Equ.s (3.14) and (1.16) is the same as for the pressure part. The volume in Equ. (3.30) is counted negative for this part. Fig. 3.10b illustrates this for a nodoid shape. Since this provides four equations for four unknowns (ω_0, ω_1, H and $\tilde{F}_z$), we obtain a uniquely defined surface.

3.3.3.3 Delaunay Surface Algorithm used for shape prediction

Finding a suitable surface for a specific set of boundary conditions is difficult, and there is no unique solution. A more efficient method is to fix $\tilde{F}_z$ and search for all surfaces which fulfill all boundary conditions except of one, for example the volume constraint or the distance between the two frames. This gives you sets of surfaces which differ only in one boundary condition for example h. This is also the relevant consideration for our experiments, since in each experiment we change only the distance h. The exact procedure of this method is as follows.

- **Step 1: setting the problem**

  We choose a condition that changes during an experiment like h, V, R or θ_c. In our case, it is h, but the method is more general and can be applied to other cases.

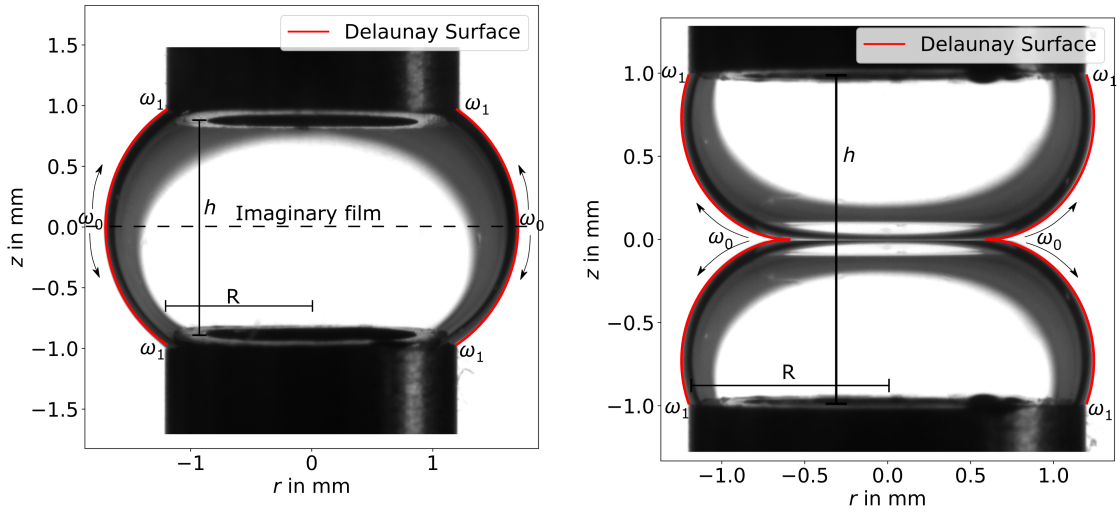

Figure 3.11: Comparison between experiments and the theoretical profile of a nodoid with $\tilde{F}_z = 0.25$ and $\theta_c = 90°$ on the left, and $\tilde{F}_z = 0.34$ and $\theta_c = 0°$ on the right, both obtained by the procedure described in Section 3.3.3.3. The parameter ω_0, ω_1, R and h are also illustrated.

- **Step 2: Accessible force range**

  We define a range of $\tilde{F}_z$ with $\tilde{F}_{z;\min} \leq \tilde{F}_z \leq \tilde{F}_{z;\max}$. $\tilde{F}_{z;\min} = -0.25$, and we have to choose a realistic value for $\tilde{F}_{z;\max}$, depending on the other boundary conditions and on the investigated problem.

- **Step 3: Setting the surface type**

  We choose a value $\tilde{F}_z \in \left[-0.25, \tilde{F}_{z;\max}\right]$, allowing to calculate the eccentricity e, and the parametrisation $\tilde{r}$, $\tilde{z}$ and $d\tilde{r}/d\tilde{z}$. This step defines if the surface is part of a cylinder, unduloid, sphere or nodoid.

- **Step 4 : Setting the starting point ω_0**

  To ensure the contact angle condition, we solve Equ. (3.27) giving all possible start points ω_0 for the given $\tilde{F}_z$ and θ_c. Depending on $\tilde{F}_z$ and θ_c, there are zero, one or two solutions for Equ. (3.27).

- **Step 5 : Setting the ending point ω_1**

  For all starting point ω_0 we have to ensure the pressure difference (mean curvature) conditions. Calculating $H(\omega)$ with

$$H(\omega)^{-1} = \sqrt[3]{\frac{V}{\tilde{V}(\omega)}}, \tag{3.31}$$

  obtained with Equ. (3.30), gives us the end point $\omega = \omega_1$ which solves Equ. (3.28). This gives us the full profile which we can compare to a profile obtained by experiments. In Fig. 3.11 we give two typical examples.

- **Step 6: Removing non-physical solutions**

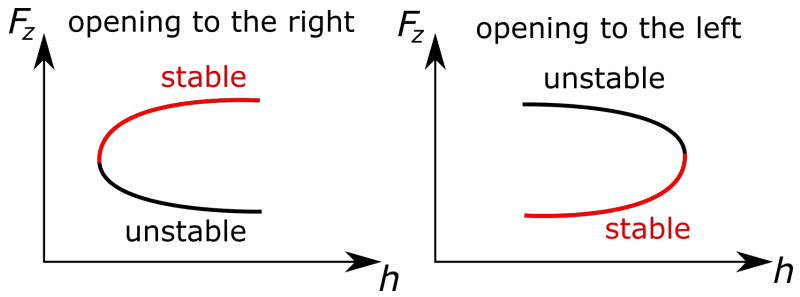

Figure 3.12: A fold with an opening to the right on the left and a fold with an opening to left on the right for a $F_z(h)$ curve [90].

Solutions defined by the values of ω_0, $H(\omega_1)$, and $\tilde{r}(\omega)$ are the Delaunay Surfaces which fulfill all boundary conditions except the one chosen at step 1 (in our case the distance between the two frames h). We have now to remove non-physical solutions.

First, It makes sense to remove solutions which include more than one period of a Delaunay Surface, since they are unstable to small perturbations [89]. We therefore eliminate all solutions with $\pi \geq |\omega_0 - \omega_1|$.

It is still possible to obtain several solutions, but in general only one corresponds to an energy minimum. Looking at the whole set of solutions which differ only in the height $\tilde{h}$, one can distinguish different branches and bifurcations in the h-F_z plane. The decision which branches are stable or unstable and to which extend is not trivial. The second derivative of the surface energy $\underline{H}$ the Hessian matrix gives a definitive answer about their stability. If one eigenvalue of the Hessian matrix is negative the surface is unstable. To calculate this matrix analytically is most of the time impossible. But we know from the publication of J. H. Maddocks [90], that any fold in the h-F_z plane of curves representing extremel surfaces, must have a change of sign of at least one eigenvalue of $\underline{H}$. If the opening of the fold is to the left (Fig. 3.12) the upper branch is unstable. One eigenvalue of $\underline{H}$ becomes negative. Consequently, we can exclude all upper branches after a fold with the opening to the left systematically

- **Choice of $\tilde{F}_{z;\min}$ and $\tilde{F}_{z;\max}$**

  To increase the accuracy and reduce the calculation time a small distance between $\tilde{F}_{z;\min}$ and $\tilde{F}_{z;\max}$ is preferred. For the different types of Delaunay surface, defined by the value of $\tilde{F}_z$, the angle $\theta = cot^{-1}(\tilde{r}_{,\tilde{z}})$ (see Fig. 3.1) varies between two extreme values $\theta_{\min}(\tilde{F}_z)$ and $\theta_{\max} = 180° - \theta_{\min}(\tilde{F}_z)$. The minimum angle $\theta_{\min}$ is plotted in Fig. 3.13 as a function of $\tilde{F}_z$. The contact angle θ_c must be included in this interval for a solution to exist. Consequently we find for $\theta_c = 0°$ only surfaces which are parts of nodoids and spheres, for $\theta_c > 0°$ also some unduloids and for $\theta_c = 90°$ all types of Delaunay surfaces, including cylinders (the cylindrical surface is only accessible in the case of "capillary bridges").

  Spherical solutions have always a $\tilde{F}_z = 0$. There is only one solution for $\theta_c = 0°$ (a simple sphere truncated by the frame) and two solutions for $\theta_c > 0°$ a simple sphere truncated by the frame and a double truncated sphere by the frame and the other bubble). Therefore, $\tilde{F}_{z;\min}$ should be selected so that $\theta_{\min}(\tilde{F}_z) \geq \theta_c$ (Fig. 3.13).

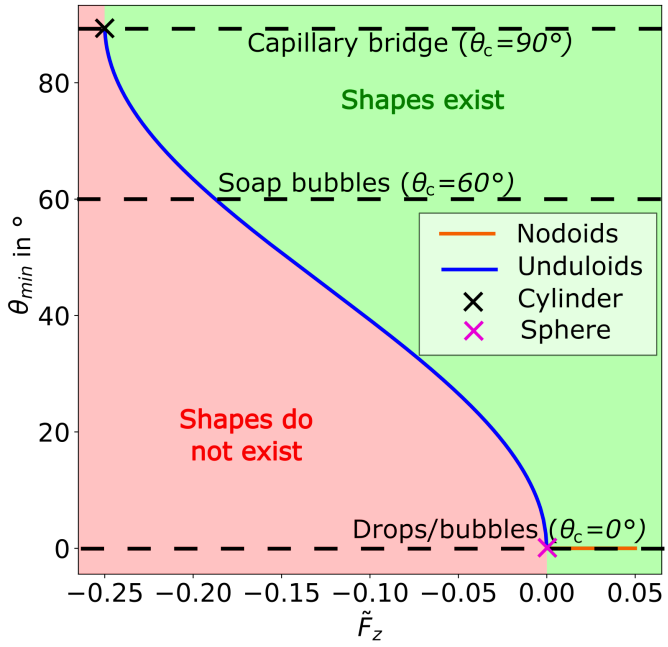

Figure 3.13: The minimal contact angle $\theta_{\min}$ is plotted for different Delaunay surfaces with different $\tilde{F}_z$. The red and green areas illustrate the inaccessible and accessible $\tilde{F}_z$ respectively for different θ_c. Only the $\tilde{F}_z$ larger than the crossing point between the horizontal dashed lines illustrating different θ_c are accessible for the specific θ_c.

$\tilde{F}_{z;\max}$ should be chosen so that all stable nodoids are taken into account. Since this depends on the position of the instabilities CB↔TB and CB↔ShB, which cannot be determined analytically, $\tilde{F}_{z;\max}$ remains to be guessed but in any case positive.

3.3.3.4 Catenoid

Since the normalized force $\tilde{F}_z$ is not defined for the catenoid (because $H = 0$) (see Section 3.3.3.1), we obtain the corresponding shapes separately from the other Delaunay surfaces. We take the parameterisation of a catenoid (Equ. (1.6)) and the derivative with respect to z

$$r_{,z} = \sinh\left(\frac{z}{a}\right). \tag{3.32}$$

The standard catenoid is obtained with $\theta_c = 90°$. With $\theta_c < 90°$ the "diabolo" catenoid [91] is obtained, (Fig. 3.14a). We are interested in the smallest R for a specific contact angle θ_c and volume V, which has a solution with $\Delta p = 0$. For larger R there are always two solutions. With other words, we are looking for the smallest $\hat{R}$ for a given contact angle θ_c and $\Delta\hat{p} = 0$. Therefore we are using for the first time the dimensionless values from Section 3.2. For larger $\hat{R}$ the pressure difference $\Delta\hat{p}$ becomes negative for some $\hat{h}$. The height of the standard catenoid (distance between the two frames, Fig. 3.14a) is

$$h_1 = 2a \ \operatorname{arccosh}(R/a). \tag{3.33}$$

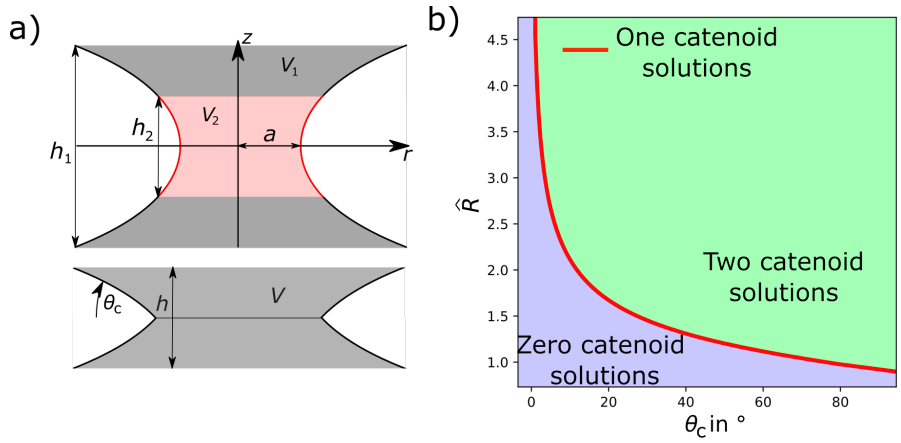

Figure 3.14: a) An illustration of the standard catenoid (top) and the diabolo catenoid (bottom) with the important geometrical parameters, explained in the text. b) The smallest $\hat{R}$ where the surface is a part of a catenoid as a function of the contact angles θ_c (One catenoid solution), separating the shape space with zero (blue area) and two (green area) catenoid solutions.

The volume of the standard catenoid (volume between one frame and the mid plane with $z = 0$, see Fig. 3.14a) is

$$V_1 = \int_0^{h_1/2} \pi r^2 \mathrm{d}z = \pi a \left(\frac{h_1}{2} + \frac{a}{2} \sinh \frac{h_1}{a} \right). \tag{3.34}$$

The diabolo catenoid is the red part subtracted from the grey part in Fig. 3.14a. The red part depends on θ_c, obtained with Equ. (3.32) and given with

$$h_2 = 2a \ \operatorname{arcsinh}(\cot(\theta_c)). \tag{3.35}$$

The volume of the red part is obtained with the same equation

$$V_2 = \int_0^{h_2/2} \pi r^2 \mathrm{d}z = \pi a \left(\frac{h_2}{2} + \frac{a}{2} \sinh \frac{h_2}{a} \right). \tag{3.36}$$

The volume of the diabolo catenoid (Fig. 3.14a) is

$$V = V_1 - V_2. \tag{3.37}$$

The distance between the two frames is

$$h = h_1 - h_2. \tag{3.38}$$

As the neck a is smaller than R, the ratio $a/R < 1$. Therefore, a similar procedure as in Section. 3.3.3.3 is used with $0 < a/R < 1$ instead of $\tilde{F}_{z;\min} \leq \tilde{F}_z \leq \tilde{F}_{z;\max}$. One obtains all possible catenoid solutions for a given θ_c. With Equ.s 3.2 and 3.37, we obtain $\hat{R}$ and $\hat{h}$. Fig. 3.14b shows this dependency of the smallest $\hat{R}$ on θ_c with $\Delta\hat{p} = 0$ (One catenoid solution). For larger $\hat{R}$ there are always two catenoid solutions (green area in Fig. 3.14b) with different $\hat{h}$ and different $\hat{a}$.

3.3.4 Computational method: Surface Evolver

The same software (Surface Evolver [64]) as for the minimal surface investigations in Chapter 2 is used. The principles of the program are explained in Section 2.2.3.

We model the bubbles or drops as two bodies with a fixed volume V and interfacial tension γ_b, Fig. 3.1. To control the contact angle θ_c the facets shared by both bodies have another interfacial tension equal to γ_f. The ratio between them defines the contact angle, as defined by Equ. (3.1). A similar procedure as for the minimal surfaces in Section 2.2.3 is used, to obtain the converged surfaces in an equilibrium. A study with a similar setup with surface evolver was performed before by Bradley *et al.* [41] in 2001.

In Surface Evolver we worked only with the dimensionless values from Equ.s (3.2), (3.3) and (3.4) from Section 3.2. The step size between two simulations is $\Delta\hat{h} = 0.0004$. The coordinates $\hat{R}$, $\hat{h}$ for the non-axisymmetric shape transitions such as CB↔TB, CB↔ShB and ShB↔CB are obtained by analysing the evolution of the two smallest eigenvalues λ_0 and λ_1 of the Hessian matrix (the second derivative of the energy with respect to the vertex coordinates) with the distance $\hat{h}$ of totally converged surfaces in Surface evolver.

Fig. 3.15a shows the evolution of λ_0 and λ_1 with respect to the frame distance $\hat{h}$ around a CB↔TB for different $\hat{R}$. For a specific height the smallest eigenvalue λ_0 and second smallest λ_1 decrease rapidly and reach almost zero. Afterwards λ_0 stays almost zero and λ_1 increases rapidly again.

If $\lambda_0 > 0$, the surface is stable and the surface energy is in a minimum. Totally converged surfaces are always stable and have consequently only positive eigenvalues. In the case of axisymmetric shapes, two eigenvalues are identically if they belong to a non-axisymmetric perturbation mode. As soon as they start to differ, the shape looses the axisymmetry. Here the point where λ_0 and λ_1 start to differ is determined as a shape transition. The branch on which the shapes in the shape diagram previously lay is now unstable and has negative eigenvalues. The shapes that are obtained now belong to another branch that was previously unstable or did not exist.

Another characteristic of a shape transition is, that at least one eigenvalue becomes zero. In the case of CB↔TB, CB↔ShB and ShB↔CB the non-axisymmetric shapes have $\lambda_0 = 0$, since the surface can rotate around the z-axis without energy change. The non-axisymmetric shapes are therefore Goldstone modes.

Both characteristics are observed for all simulations in Fig 3.15a. λ_0 is not exactly zero and not identical for the different cases in Fig. 3.15a, due to the finite discretisation of the simulation and different discretisations of the surfaces.

We define the coordinates $\hat{R}, \hat{h}$ of the shape transition at the point, where λ_0 and λ_1 start to differ more than 20%. To obtain a curve in the shape space, the frame radius $\hat{R}$ was increased by steps of $\Delta\hat{R} = 0.01$.

The precision of the tilting/shifting point in Surface Evolver can be estimated with help of a convergence study. Fig. 3.15b shows that the critical height $\hat{h}_{CB\leftrightarrow TB}$, where the surface looses the axisymmetry, converges against a value for increasing number of facets. We worked with approximately 5000-10000 facets, which gives us a precision of approximately 0.1%.

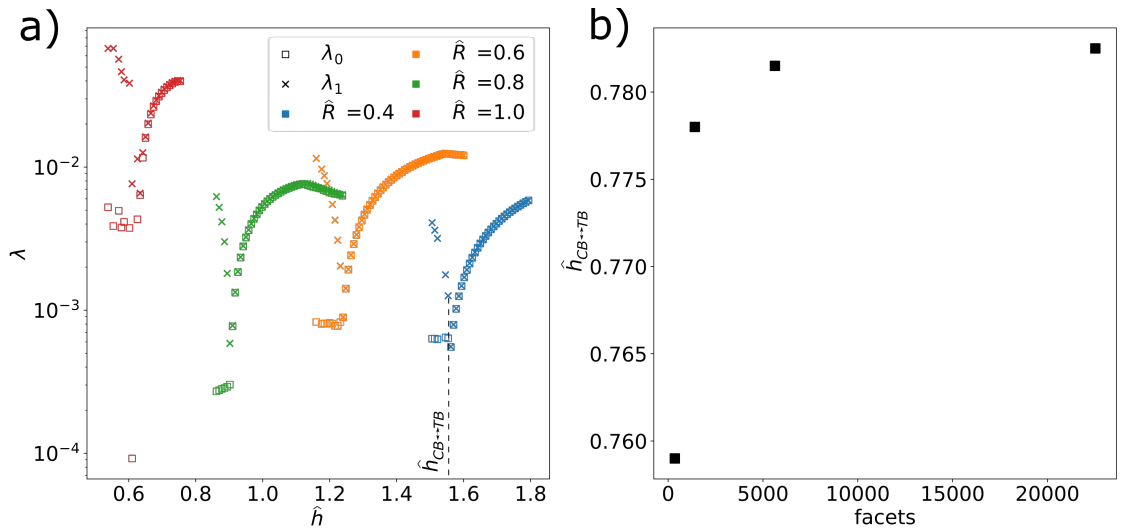

Figure 3.15: a) The two smallest eigenvalues λ_0 and λ_1 of the Hessian matrix obtained with Surface evolver for different $\hat{R}$ plotted over the frame distance $\hat{h}$. b) Height $\hat{h}_{CB\leftrightarrow TB}$ where the surface looses the axissymetry for a simulation in Surface evolver with different number of facets ([352, 1408, 5632, 22528]), $\hat{R} = 0.4$, $\theta_c = 60°$.

3.4 Results and discussion

3.4.1 General observations

In order to describe the different stable shapes and instabilities, we use the following naming convention, which is summarised schematically in Fig. 3.2 with corresponding images given in Fig. 3.4 for the three contact angles θ_c. The detailed example for one contact angle is given in Fig. 3.3. For simplicity, we only use the word "bubble" here, but most of these configurations can also be obtained using drops. The initial configuration is given by two axisymmetric "Separate Bubbles", which we label "SB". When these are put in contact by decreasing h, they "jump" into a new configuration, creating axisymmetric "Connected Bubbles" ("CB"). The instability between these two is labelled "SB→CB". By increasing h of a CB configuration with sufficiently large R (depending on θ_c) one observes that the bubbles separate ("CB→SB"). This instability is also observed in the work of Bohn [81] and Fortes *et al.* [82] in the case where the bubbles are confined between two parallel walls. By decreasing h in the CB configuration for any R and θ_c, the axisymmetry is lost and one observes "Tilted Bubbles" ("TB") for $\theta_c = 0°$ and $\theta_c = 60°$, and a mirror symmetric buckling for $\theta_c = 90°$. Even if for $\theta_c = 90°$ the shape after the transition has characteristic differences, we want to group it with the other tilting instabilities since all of them appear only if the bubbles are under compression. The onset of this tilting is a well-defined instability "CB→TB", which is also observed in the case of bubbles confined between two parallel walls [81]. Bradley *et al.* [41] conducted also Surface Evolver simulations of this problem. The difference with our configuration is that for bubbles confined between two walls the point of instability is always at a double truncated sphere [81, 82]. A geometrical explanation is given in the work of Bohn [81], illustrated in Fig. 3.16. The total surface area and consequently the total free energy $\mathcal{E}$ stays constant between the two illustrated configurations in Fig. 3.16. The surface area is

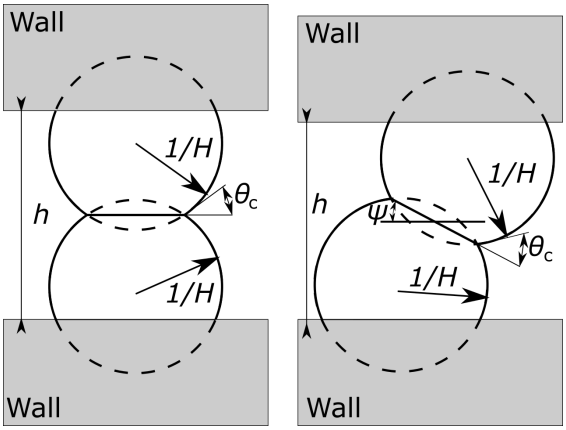

Figure 3.16: Two double truncated spherical bubbles or drops in contact with an contact angle θ_c and mean curvature H confined between two walls are illustrated with two different distances h between the walls. The total surface area of both configuration is the same. For larger distance, the bubbles or drops stay axisymmetric. For the smaller distance, the bubbles or drops are tilted with the tilt angle ψ [81].

for both two times the surface of a sphere with mean curvature H minus the surface of the spherical cups with the dashed lines.

Besides these two known instabilities, pinning the bubbles on frames creates new instabilities for certain parameter ranges of h, R, V and θ_c, which are reported here for the first time in detail. The article of Frostad *et al.* [79] observed for some experiments Detached Bubbles. The Detached Bubbles DB are observed by increasing h coming from a CB ("CB→DB"). For this instability to arise, R has to be small enough depending on θ_c. For perfectly symmetric systems, this detachment should arise on both frames. However, in reality, it typically arises only on one frame, as shown in Fig. 3.3b or 3.4. For $\theta_c = 0°$ this instability does not exist due to the lack of attractive forces between the bubbles (drops), (contact angle of $\theta_c = 0°$). The second new instability is a bubble shifting ("ShB") away from the CB upon decreasing h, i.e. CB→ShB. There the film between the two bubbles is shifted away from the z-axis, while maintaining the mirror symmetry in the xy-mid plane. This instability is observed only for R above a critical value which depends on θ_c and converges against infinity for $\theta_c = 0°$.

We combine results from three different methods to investigate the bubbles (drops) in contact and the capillary bridges: experiments (Section 3.3.2), the theory of Delaunay Surfaces (Section 3.3.3) and Surface Evolver simulations (Section 3.3.4).

Since the bubble (drop) volume V and the interfacial tension γ_b remain constant during one experiment, they provide a natural length and stress scale of the problem, as already mentioned in Section 3.2. Since they are more readily accessible than the mean curvature H used in Section 3.3.3, we use them here to normalise all lengths L (such as r, R or h) and forces F and Δp as in Equ.s (3.2), (3.3) and (3.4). To obtain the pressure difference $\Delta\hat{p}$ predicted by Delaunay Surfaces, Δp and V in Equ. (3.4) have to be replaced by $2\Delta\tilde{p}$ and $\tilde{V}$. In the following we will work only with the normalised values from Equ.s (3.2) - (3.4), which allow us to provide a coherent picture combining experiments, theory and simulation. We discuss first the forces and pressures arising in the system (Section 3.4.2) before turning to a detailed analysis of the shapes and their stability (Section 3.4.3).

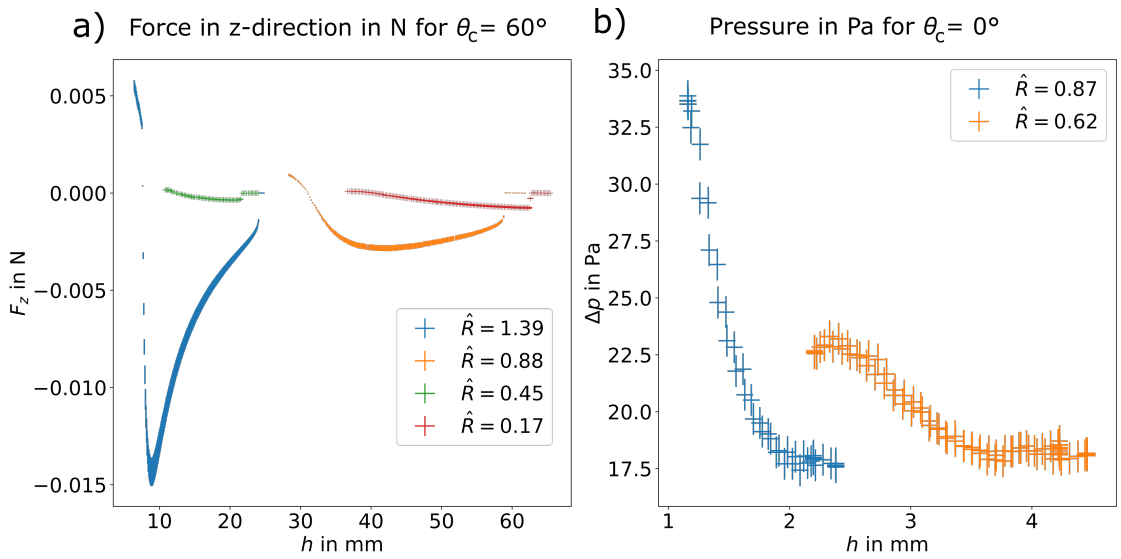

Figure 3.17: a) Force in z-direction measurements for the soap bubble setup for four different radii $\hat{R}$ plotted against the physical distance between the frames h. b) Pressure difference Δp for two drops in contact for different $\hat{R}$.

3.4.2 Force and pressure characterisation

This subsection compares forces and pressures obtained by experiments, simulations and theory. In the case of soap bubbles and soap bubble capillary bridges, we measured directly the force F_z, since it is proportional to the system size and hence large enough to be measured directly (Section 3.3.2 and Fig. 3.17a). In the case of the bubble/drop configuration, we have to work with much smaller systems to be able to neglect gravity. This makes the forces too small to be measured directly. We therefore measure the pressure difference between the bubbles (drops) and the surrounding liquid (Section 3.3.2 and Fig. 3.17b). It is inversely proportional to the system size and therefore large enough to be measured with sufficient precision. To give the reader an order of magnitude of the physically measured values of the pressure and normal forces, Fig. 3.17 shows the real measured values plotted against the real frame distance. The measured normal forces and pressure differences typically are in the range -0.005 N $< F_z <$ 0.005 N and -50 Pa $< \Delta p <$ 50 Pa.

In Fig. 3.18, the normalised pressure difference $\Delta\hat{p}$ is plotted over the normalised distance $\hat{h}$ between the frames for the three methods (experiments, simulations and theory) and for two contact angles ($\theta_c = 0°$ in Fig. 3.18a,b and $\theta_c = 90°$ in Fig. 3.18c,d). In Fig. 3.19, the normalised force $\hat{F}_z$ is plotted over the normalised distance $\hat{h}$ between the frames for the three methods (experiments, simulations and theory) and for two contact angles ($\theta_c = 60°$ in Fig. 3.19a,b and $\theta_c = 90°$ in Fig. 3.19c,d). In both figures, the panels a,c show in detail how the pressure or the force depend on the distance between the frames for the example of one frame radius $\hat{R}$, indicating the different shapes and transitions via arrows and a colour shading. The sub-panels b,d plot the pressure- or force-height relation for different frame radii $\hat{R}$ represented by different colours. The theory (solid lines) shows the pressures and normal forces for all possible Delaunay surfaces which meet the boundary conditions. They are not necessarily physically stable shapes. The

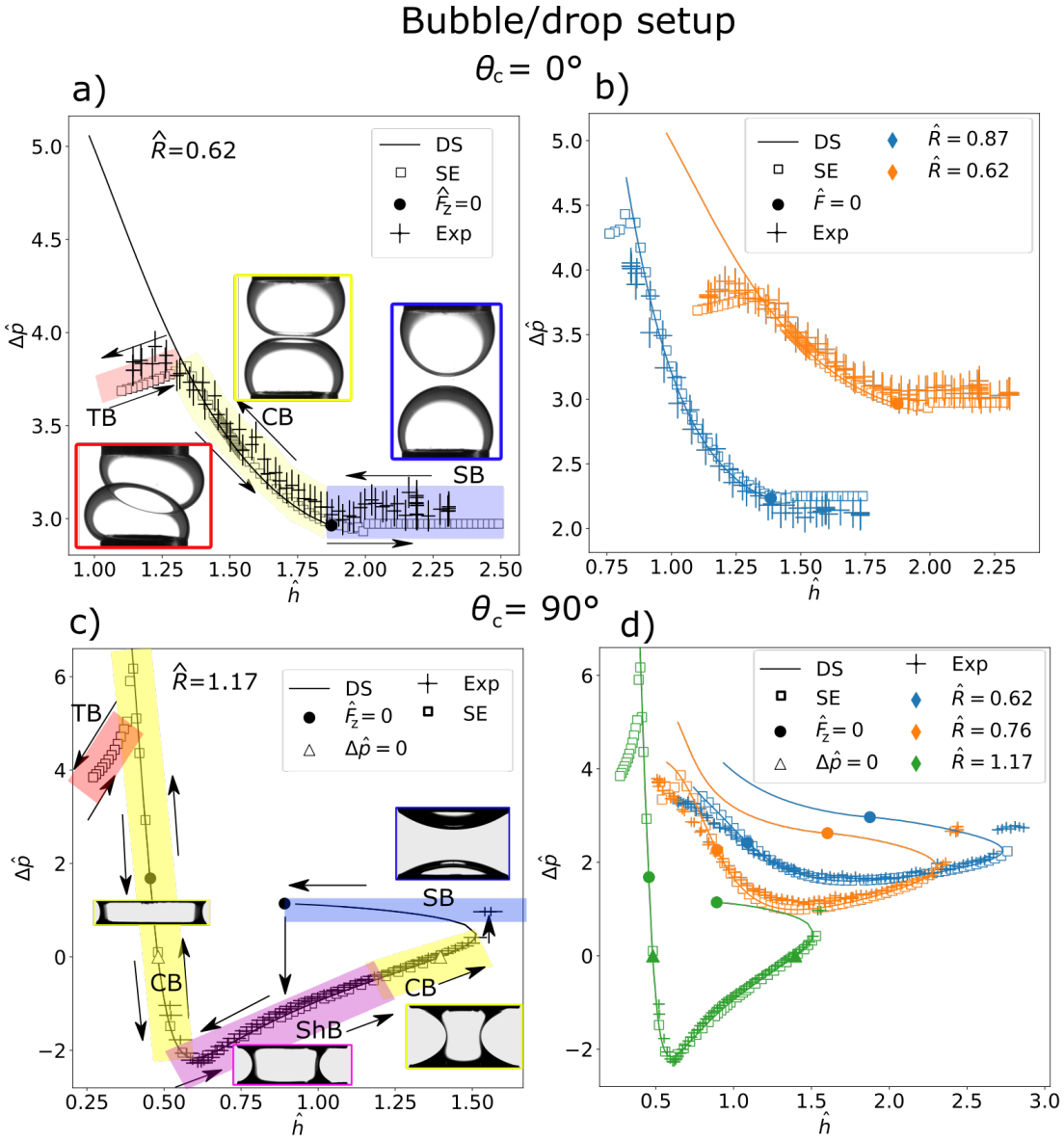

Figure 3.18: Different dimensionless pressure differences $\Delta\hat{p}$ are plotted over the dimensionless height $\hat{h}$ for water drops in silicone oil. For the two figures a) and b) the contact angle is $\theta_c = 0°$ and for the figures c) and d) $\theta_c = 90°$. The figures a) and c) illustrate the different shapes and the path related to the pressure measurements during one measurement, and the figures b) and d) show how $\Delta\hat{p}$ changes with $\hat{h}$ for different frame radii $\hat{R}$. In all figures, experimental data (Exp) is compared to simulations (SE) and the theory of Delaunay surfaces (DS). In the theoretical curve spherical ($\hat{F}_z = 0$) and catenoid ($\Delta\hat{p} = 0$) solutions are highlighted with a filled circle and an open triangle respectively. Force jumps are related to bubbles coming in to contact SB $\rightarrow$ CB, a bubble bubble detachment CB $\rightarrow$ SB for larger frame radii or a bubble frame detachment CB $\rightarrow$ DB for smaller frame radii. The ShB appears only for $\Delta\hat{p} < 0$. The change in pressure is fairly small and in most cases almost the same as for the axisymmetric solution. Consequently, the shape transition CB $\leftrightarrow$ ShB is only optically clearly observable.

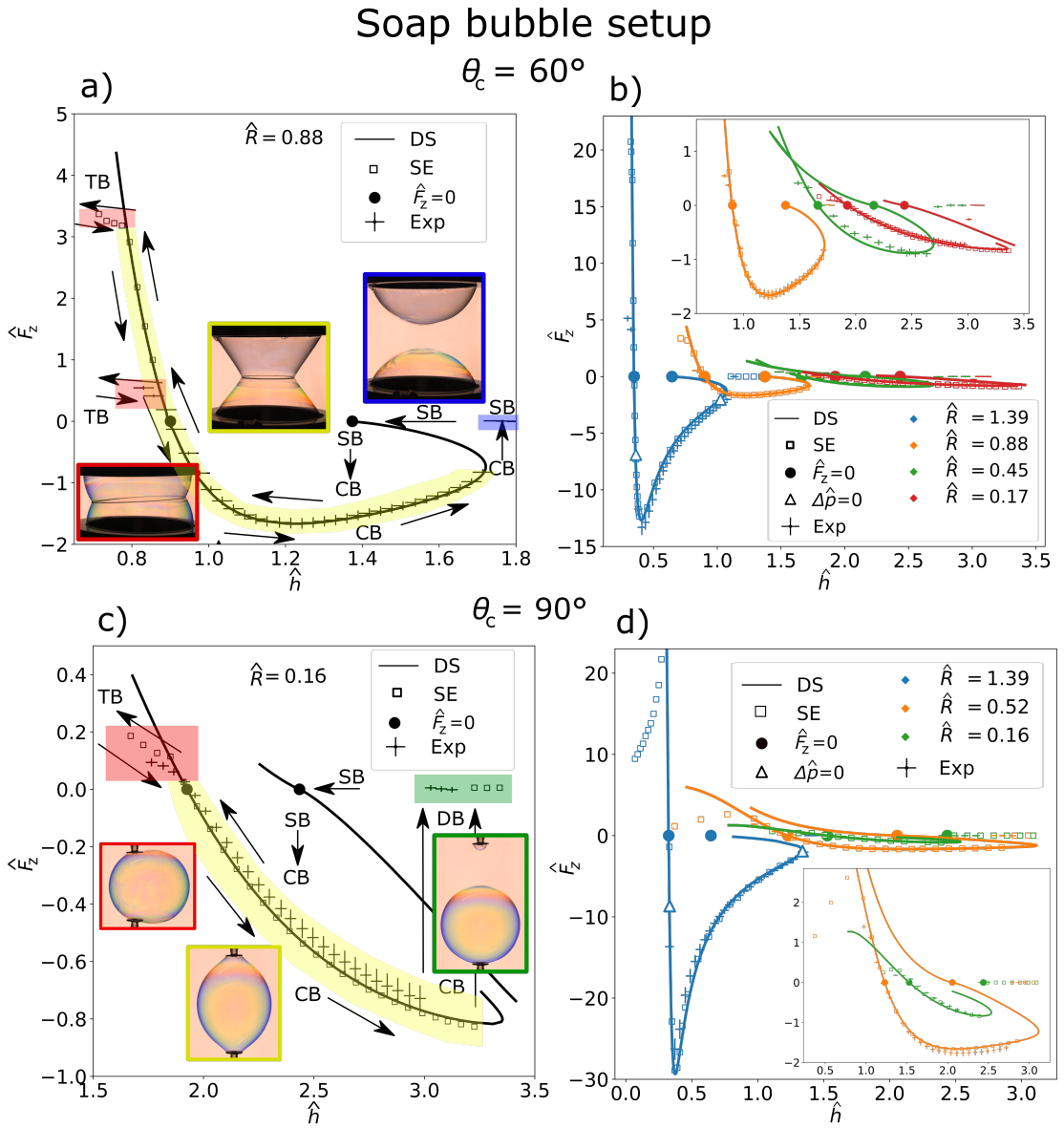

Figure 3.19: Different normalised force $\hat{F}_z$ measurements are plotted over the normalised height $\hat{h}$ for soap bubbles. In the two figures a) and b) the contact angle is $\theta_c = 60°$ and in the two figures c) and d) $\theta_c = 90°$. The figures a) and c) illustrate the different shapes and the path related to the force measurements during one measurement and the figures b) and d) show how $\hat{F}_z$ changes with $\hat{h}$ for different frame radii $\hat{R}$. In all figures, experimental data (Exp) is compared to simulations (SE) and the theory of Delaunay surfaces (DS). In the theoretical curve spherical ($\hat{F}_z = 0$) and catenoid ($\Delta\hat{p} = 0$) solutions are highlighted with a filled circle and an open triangle respectively. Force jumps are related to bubbles coming in to contact SB → CB, a bubble bubble detachment for larger frame radii or a bubble frame detachment for smaller frame radii. The largest $\hat{R}$ where a bubble frame detachment appears depends on θ_c. The tilt instability appears only if the bubbles are under compression with $\hat{F}_z > 0$. The instability presents a discontinuity in $\mathrm{d}\hat{F}_z/\mathrm{d}\hat{h}$.

simulation and the experiments show only pressures and forces of stable shapes.

Let us start by considering more closely the pressure-height cycle shown in Fig. 3.18a

for the case of $\hat{R} = 0.62$ and $\theta_c = 0°$. By starting at a point of two Separated Bubbles (SB) the pressure difference $\Delta\hat{p}$ stays constant by decreasing $\hat{h}$ until the two drops touch each other. One obtains Connected Bubbles (CB) with the transition SB↔CB. Then $\Delta\hat{p}$ increases smoothly by decreasing $\hat{h}$. This changes at the Tilted Bubbles shape transition CB↔TB, where $\mathrm{d}\Delta\hat{p}/\mathrm{d}\hat{h}$ is discontinuous. By increasing $\hat{h}$ one goes the same way back, i.e. for $\theta_c = 0°$ the pressure-height cycle has no hysteresis. In Fig. 3.18b one observes the influence of different needle radii. The general behavior stays the same. With increasing $\hat{R}$ the slope, $\mathrm{d}\Delta\hat{p}/\mathrm{d}\hat{h}$, increases in absolute value for CB, but $\Delta\hat{p}$ for SB decreases. $\Delta\hat{p}$ at CB↔TB increases with increasing $\hat{R}$.

An example of a force-height cycle is shown in Fig. 3.19a for the case of $\hat{R} = 0.88$ and $\theta_c = 60°$. This corresponds to a sequence as the one shown in the top row of Fig. 3.3. Starting at a point with two Separated Bubbles (SB), the distance $\hat{h}$ is decreased (going from right to left) until the bubbles touch each other. Since $\theta_c > 0°$, the bubbles are attractive and there is a jump to negative values of $\hat{F}_z$, corresponding to the transition SB→CB. Continuation of approaching the frames leads to a decrease in force reaching a minimum in $\hat{F}_z$ and then an increase in force if SB→CB was before the force minimum. Otherwise the force only increases after the SB→CB for approaching frames. Whether the SB→CB is before or after the minimum depends on $\hat{R}$. At this stage, we lack a physical interpretation for this observation. In both cases, an axisymmetric shape is maintained reaching positive values of $\hat{F}_z$. When a critical distance is reached, the axisymmetry is broken leading to the Tilted Bubble state (TB) via the tilt instability (CB↔TB). We assume that at this point a second order shape transition takes place, since the first derivative of the energy with respect to $\hat{h}$ ($\hat{F}_z$) is identical before and after the shape instability, as shown in Fig. 3.19 for the experiments and simulations. This interpretation is discussed in more detail in Section 3.4.3.

Since $\hat{F}_z$ changes strongly at CB↔TB, experiments tend to show strong fluctuations for the onset of this instability in comparison to the simulations. This instability cannot be described by the Delaunay theory. In the TB, the tilting angle ψ increases with decreasing $\hat{h}$ (see Fig.s 3.4 and 3.23) and $\mathrm{d}\hat{F}_z/\mathrm{d}\hat{h}$ changes. The tilting would increase until the contact film touches the frame boundary. This behavior is similar to the behavior of two bubbles confined between two parallel walls (Fig. 3.16). If a bubble touches the other frame, the deformation often becomes irreversible due to the pinning of the bubble on the frame geometry. That is why before reaching this point, we increase $\hat{h}$ again (withdrawing the frames from each other). The system follows again the TB and CB branch moving back into negative $\hat{F}_z$ which reaches a minimum before increasing again. In the case of attractive bubbles ($\theta_c > 0°$), we observe a hysteresis, i.e. we have access to stable CB shapes which we did not see upon decreasing the distance $\hat{h}$. Upon increasing $\hat{h}$ further, the bubbles detach from each other (CB→SB) and the force vanishes, $\hat{F}_z = 0$. We have therefore returned to the initial configuration and can start another cycle. Depending on θ_c and $\hat{R}$, the final instability can also evolve towards a bubble detachment from the frame (CB→DB), as shown in the bottom sequence of Fig. 3.3. The overall shape of the $\hat{F}_z(\hat{h})$ curve depends on $\hat{R}$. Different examples are plotted in Fig. 3.19b. They show that with increasing $\hat{R}$ the distance $\hat{h}$ for a CB→SB decreases and the minimal and maximal $\hat{F}_z$ increases in absolute values. Catenoid shapes appear for larger frame radii as well.

A very similar cycle is obtained for the capillary bridge with $\theta_c = 90°$ shown in Fig. 3.18c,d and 3.19c,d. Detailed examples of these cycles are given in Fig. 3.18c for $\Delta\hat{p}(\hat{h})$ and in 3.19c for $\hat{F}_z(\hat{h})$. Let us consider first the cycle of Fig. 3.19c with $\hat{R} = 0.17$: We

start with two Separated Bubbles (SB) and decrease $\hat{h}$ (approaching frames). When the two bubbles touch each other, we observe the instability SB→CB. In this case, the film between the two bubbles may break and one obtains a capillary bridge. Continuing approaching the frames, we observe again the instability CB→TB, which looks in this case more like a shifting, see Fig. 3.4. Then we increase $\hat{h}$ again (withdrawing the frames from each other). The system follows again the TB and CB branch moving back into negative $\hat{F}_z$. Depending on $\hat{R}$ one observes a CB→SB, or, like in the case of Fig. 3.19c, a CB→DB. A hysteresis would also be possible between the DB and CB, but is rarely observed in experiments since the DB configuration is often unstable due to gravity.

The pressure-height cycle in Fig. 3.18c has a $\hat{R} = 1.17$. This is a regime where experiment and simulation can differ in their shape transitions, since in the experiment the boundary conditions are never perfectly axisymmetric in comparison to the simulations and the energies of the shapes ShB and CB are in this regime very close to each other. Consequently we observe a SB→ShB in the experiment and in the simulation a SB→CB. That adds for the experiment the shape transition ShB↔CB and CB↔ShB for the approaching-withdrawing cycle. The simulation shows the same behavior for larger $\hat{R}$. The rest of the cycle is similar to the cycle shown in Fig. 3.19a.
With increasing $\hat{R}$ the minimum of $\Delta\hat{p}(\hat{h})$ decreases and reaching also zero and negative values (Fig. 3.18d). The absolute values of $\Delta\hat{p}(\hat{h})$ decrease with decreasing $\hat{R}$ (see Fig. 3.18d).

3.4.3 Shape instabilities and shape diagrams

In what follows, we discuss in more detail the different instabilities that occur during the approaching-withdrawing cycles. For a given bubble volume, the equilibrium forms are characterised by the two scaled parameters $\hat{h}$ (scaled distance between frames) and $\hat{R}$ (scaled frame radius), and by the contact angle θ_c. In principle, θ_c can vary continuously from 0° to 90°. Theoretically and numerically this is not difficult. Experimentally, we have only studied the cases $\theta_c = 0°$, 60° and 90°, but we could imagine accessing other angles by tuning the effective interfacial tension of the different interfaces. It is therefore interesting to discuss in a general manner the different states of the system in the phase space $\theta_c - \hat{h} - \hat{R}$. The instabilities are then given by surfaces ($f\left(\theta_c, \hat{h}, \hat{R}\right) = C^{te}$) whose traces we can observe experimentally in the planes $\theta_c = 0°$, 60° and 90°. We plot the shape diagrams for these three cases in Fig. 3.20 and discuss in detail the different shape transitions, given again by experiment, simulation and (in most cases) by theory.

3.4.3.1 Contact instability SB→CB

If we decrease the distance $\hat{h}$ between two initially separated bubbles whose surfaces correspond to spherical sectors, there is a value $\hat{h}_{SB\to CB}$ for which they come into contact (SB→CB in Fig.s 3.18 and 3.19, and and blue dashed line in Fig. 3.20). The theoretical prediction of this surface instability is trivial and twice the height of the no-deformed bubbles (drops). Even though it is in very good agreement with experiment we do not plot the experimental data here to keep the focus of the graphs on the less trivial instabilities. When the bubbles are attractive ($\theta_c > 0$), the system jumps to a new equilibrium shape satisfying the contact angle θ_c and the boundary conditions. The associated contact force can also be predicted exactly by Delaunay theory, as shown in Section 3.4.2.

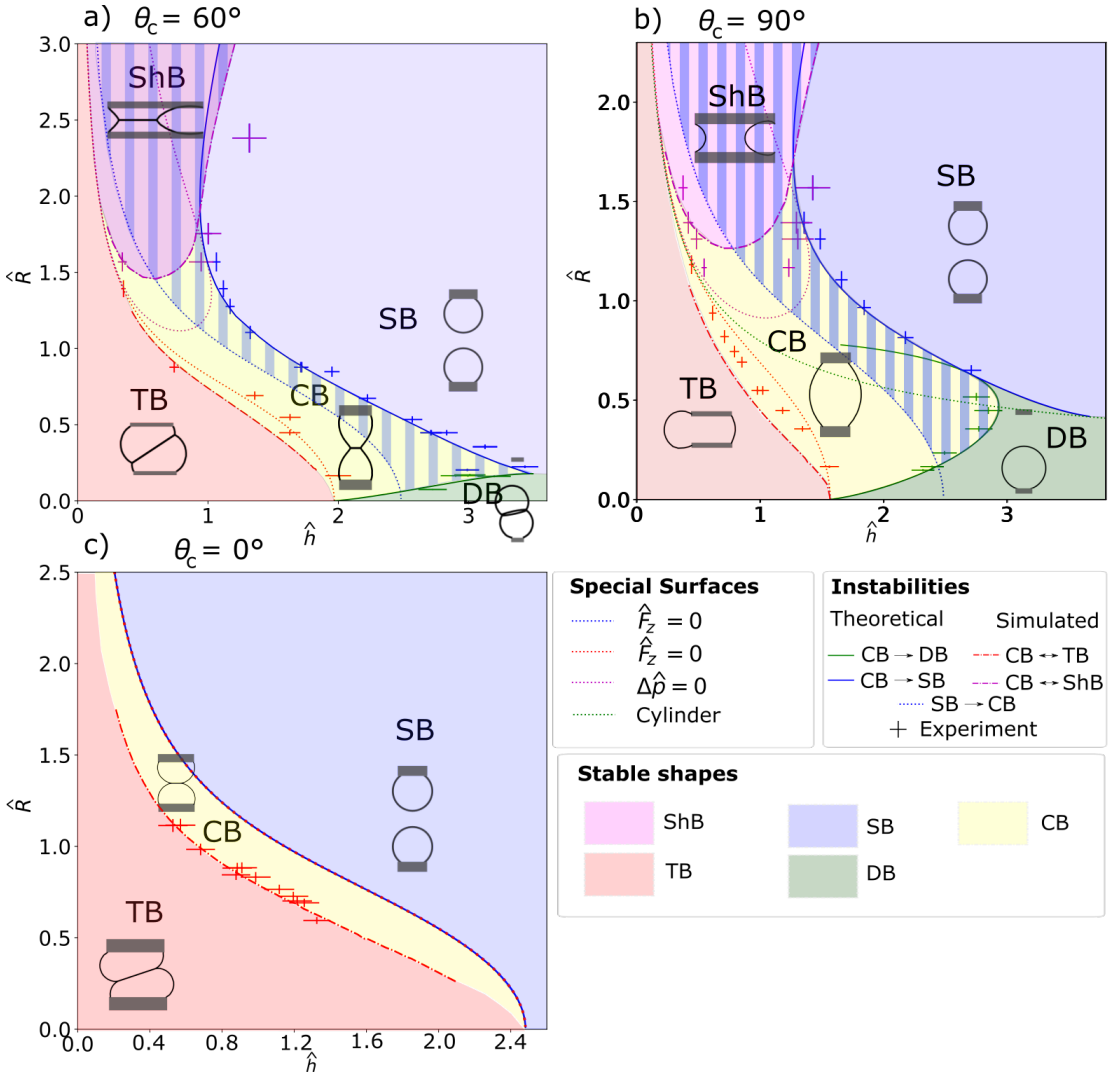

Figure 3.20: Three shape diagrams for the $\hat{h} - \hat{R}$-plane corresponding to different contact angles θ_c for (a) two soap bubbles ($\theta_c = 60°$), for (b) capillary bridges ($\theta_c = 90°$) and for (c) two bubbles or drops in a liquid $\theta_c = 0°$. The solid lines are predicted shape transitions due to the theoretical Delauney Surfaces, the dotted dashed lines are shape transitions obtained with help of Surface Evolver. The dotted lines are special Delaunay surfaces, blue spherical cups which touch each other in one point ($\hat{F}_z = 0$), red spherical double truncated surfaces in contact ($\hat{F}_z = 0$) and magenta catenoid surfaces ($\Delta\hat{p} = 0$). The different colors of the experimental points refer to the different phase transitions and show at which point the respective phase transition was observed in the experiment. In the yellow area the Surface is a Connected Bubble (CB). In the blue area one observes Separated Bubbles (SB), in the green area Detached Bubbles (DB), in the red area Tilted Bubbles (TB) and in the magenta area Shifted Bubbles (ShB). The blue yellow and the blue magenta pattern area symbolize the history dependency of the shape. If one comes from a complete blue area the shape will be a SB if one comes from complete yellow or magenta area the shape will be a CB or a ShB.

3.4.3.2 Tilt instability CB↔TB

Upon decreasing the distance $\hat{h}$ beyond the contact point, the force $\hat{F}_z$ increases and crosses zero. At this crossing point, the corresponding shape is composed of double truncated spheres (see Fig. 3.19 and the red dotted line in Fig. 3.20). However this time the bubbles are fully connected, i.e. this point is always at a distance $\hat{h} < \hat{h}_{\mathrm{SB}\to\mathrm{CB}}$. For even smaller $\hat{h}$, $\hat{F}_z$ becomes positive and the axisymmetric solutions are parts of nodoids. At a specific $\hat{h}_{\mathrm{CB}\leftrightarrow\mathrm{TB}}$, depending on $\hat{R}$ and θ_c, the axisymmetry is broken and the film between the two bubbles begins to tilt in a random direction(CB↔TB in Fig. 3.19 and red dash dotted line in Fig. 3.20). The force measurements show this time not a jump as for the SB→CB, the CB→DB or the CB→SB (see below) instabilities. Instead, one observes merely a change in slope (Fig.s 3.18 and 3.19). The TB for the capillary bridge looks more like a shift with a bulge formed in a random direction (Fig. 3.20). But since the main characteristics, such as the nodoidical shapes before the shape instability at $\hat{F}_z > 0$, or the change in the slope of $\mathrm{d}\hat{F}_z/\mathrm{d}\hat{h}$, are the same for the capillary bridge and for two bubbles, we decided to treat them together.

We determined the point of instability numerically, with help of the eigenvalues of the Hessian matrix in Surface Evolver (Section 3.3.4), and experimentally by direct visualisation (Section 3.3.2). The shape diagrams in Fig. 3.20 show the experimental points for the CB↔TB with red crosses and the simulated points as a red dash-dotted line, as already mentioned above. All simulated and almost all experimental points are on the left side of $\hat{F}_z = 0$ (the red dotted line in Fig. 3.20). It follows that $\hat{F}_z > 0$ when the tilt instability occurs. The difference between the simulation and the experiments is due to geometric inaccuracies in the experiments and the difficulty to determine precisely a rather smooth shape transition.

In contrast to the case of two bubbles confined between parallel plates [82, 81, 41], some nodoids are stable when the bubbles are pinned on frames. In the case of two bubbles between plates, the always spherical solution can be rotated and shifted in a manner that for a decreasing distances between the plates h the surface (and hence the surface energy) stays the same until the contact film touches the plates [82] (Fig. 3.16). This is not possible for pinned bubbles. This is why the CB↔TB appears only for $\hat{F}_z > 0$ and the contact film between two tilted, pinned bubbles in contact is not flat, as discussed in more detail in Section 3.4.4. The pinning adds an energy barrier for a shift of the contact area between the bubble and the frame, which does not exist for the bubbles between parallel walls.

3.4.3.3 Bubble-bubble detachment CB→SB and Bubble-frame detachment CB→DB

Starting with Tilted bubbles (TB), and increasing $\hat{h}$ (withdrawing frames), we first come back to the axisymmetric Connected Bubbles (CB) without any hysteresis. Further withdrawing can lead to two different behaviours depending on the value of the frame radius $\hat{R}$. When $\hat{R} > \hat{R}_{\mathrm{Tr}_1}(\theta_c)$, an instability is observed where the two bubbles detach from each other (bubble-bubble detachment CB→SB in Fig.s 3.18 and 3.19, blue solid line in Fig. 3.20). When $\hat{R} \leq \hat{R}_{\mathrm{Tr}_1}(\theta_c)$, we observe an instability where the bubbles detach from the frame (bubble-frame detachment CB→DB in Fig.s 3.18 and 3.19, and green solid line in Fig. 3.20). In theory, the detachment should occur from both frames simultaneously. However, in the experiment it occurs always from the upper frame, because of gravity.

The value of $\hat{R}_{\mathrm{Tr}_1}(\theta_c)$ can be obtained both numerically and theoretically and corresponds to a triple point in the phase diagram $\hat{h} - \hat{R}$ for a given θ_c (crossing point of green and blue solid line in Fig. 3.20). The theoretically and computationally obtained values for the $\hat{R}_{\mathrm{Tr}_1}$ and $\hat{h}_{\mathrm{Tr}_1}$ of these triple points are listed in Table 3.1. The points are part of a triple line in the $\theta_\mathrm{c} - \hat{h} - \hat{R}$ space.

The bubble-bubble detachment instability CB→SB is observed when the theory of Delaunay surfaces predicts the maximal distance $\hat{h}$, corresponding to the point where the compressibility $\partial\hat{h}/\partial\hat{F}_z$ of the system changes sign. We obtained this point numerically by converging the function $\hat{h}(\tilde{F}_z)$ to a maximum. The point of instability for both, simulation and experiment, agree within the uncertainties, see Fig.s 3.18 and 3.19 CB→SB, and Fig. 3.20 (blue solid line). If one moves the frames up and down, exceeding the height where the CB→SB occurs and going below the height of the simple truncated spherical solution (SB→CB), one obtains a hysteresis already discussed with Fig.s 3.18 and 3.19, and shown in Fig. 3.20 by the zone with blue and yellow stripes.

By observation we found out that the bubble-frame detachment CB→DB always occurs when $\hat{r}_{,\hat{z}}(\pm 0.5\hat{h}) = 0$, which is equivalent with a vertical interface at the frame. Fig. 3.22d shows some examples for vertical interfaces at the frame, which is equivalent to a contact angle to the frames of $\theta(z = \hat{h}/2) = 90°$. For the case of a cylindrical capillary bridge (green dotted line in Fig. 3.20b) this is always the case. The cylindrical capillary bridge becomes unstable at $\hat{h} = 2\pi\hat{R}$ with $\hat{R} = 0.4662$ (where the green dotted line and the green solid line meet each other in Fig. 3.20b). This cylinder height is also known as the critical length of the Rayleigh instability for capillary bridges after which the surface is physically unstable to small fluctuations [92]. It is also the $\hat{h}$ of one period of the Delaunay surface with $\tilde{F}_z = -0.25$, i.e. $\omega_1 - \omega_0 = \pi$. Unduloids are also unstable with respect to small fluctuations if they exceed one period [89, 93]. The solid green line in Fig. 3.20b shows the function $\hat{R}(\hat{h})$ for one period of a Delaunay surface for all $\tilde{F}_z < 0$, if one starts at an extremum of the profile $\hat{r}(\hat{z})$. Since there is always a maximum and a minimum in the profile $\hat{r}(\hat{z})$ (except for the cylinder) one finds two solutions for one $\hat{h}$, one with a smaller $\hat{R}$ (the lower branch) and one with a larger $\hat{R}$ (the upper branch). Theoretically also all other $\hat{R}$ in between the upper and lower branch are possible shapes. But they are not mirror symmetric to the xy-plane. All of those shapes are already unstable due to small fluctuations. The upper and lower branch meet each other at the cylindrical shape of one period (the shortest unstable cylinder).

Since in experiments all frames have a rim thickness, the upper and lower pinning positions are not necessarily the same, giving rise to Delaunay surfaces without mirror symmetry (two different $\hat{R}$). They occur only if this configuration has less surface area for the same $\hat{h}$ in comparison to the mirror symmetric solution and if one of the angles $\theta^{\pm}$ between the bubbles and the upper and lower frame (Fig. 3.5) is outside of the pinning range $\Delta\theta$ (Equ. (3.6)). This is, for instance the case for soap film capillary bridges close to the cylindrical solution. An example of a non-axisymmetric capillary bridge is represented in the Fig. 3.21. It is still a Delaunay Surface with two different $\hat{R}^{\pm}$.

The solid green line in Fig. 3.20a shows the curve $\hat{R}(\hat{h})$ for $\theta_\mathrm{c} = 60°$ and all $\tilde{F}_z < 0$ where $\hat{r}_{,\hat{z}}(\pm\hat{h}/2) = 0$ and the total surface of both bubbles include at least one complete period of a Delaunay surface. It follows that

$$\omega_1 = \pi \tag{3.39}$$

$$|\omega_1 - \omega_0| > \pi. \tag{3.40}$$

Figure 3.21: A Delaunay Surfaces obtained with a capillary bridge, which is not mirror symmetric to the xy-mid plane.

Basically they are the same surfaces as for $\theta_c = 90°$ only a little longer due to the change in contact angle. Fig. 3.22 gives with the sub-figures a, b, c, d and e an overview about the shapes and the position in the shape diagrams of CB→DB and the triple point Tr_1 of CB, SB and DB for different θ_c. Fig. 3.22a and b show the upper and lower branches for CB→DB and the beginning of CB→SB with the intersection of CB→DB and CB→SB, the triple point Tr_1. Different colors represent different θ_c. Some examples of shapes on CB→SB for different θ_c are represented in Fig. 3.22d. As already discussed, the upper branch (Fig. 3.22a blue dashed line) for CB→DB with $\theta_c = 90°$ has a maximum in $\hat{r}(\omega_1)$ and a minimum at $\hat{r}(\omega_0)$, the lower branch (Fig. 3.22a blue solid line) has a minimum at $\hat{r}(\omega_1)$ and a maximum at $\hat{r}(\omega_0)$. In order to have a $\theta_c < 90°$, $\hat{r}$ must increase with changing $\hat{z}$ at least in the close neighbourhood to $\hat{z} = 0$. Consequently, ω_0 moves away from the maxima and minima in $\hat{r}$ with decreasing θ_c. In order to fulfill the condition of Equ. (3.39) and the condition of Equ. (3.40), the upper branch is folded to larger $\hat{h}$ and smaller $\hat{r}$ for $\theta_c < 90°$ (Fig. 3.22a). As θ_c decreases, the upper and lower branches approach each other and become shorter (Fig. 3.22a).

One observes that Tr_1 is within the precision of the calculation on the point, where the upper and lower branch meet each other. The shapes related to this intersection have a $\tilde{F}_z(\theta_{min} = \theta_c)$ from Fig. 3.13 and fulfill Equ.s (3.39) and (3.40). They are unique shapes for a specific contact angle θ_c. An exception is the case of a capillary bridge. The triple point is not at the intersection of the upper and lower branches. It is inside of the upper branch. The part of the upper branch above Tr_1 is part of the unstable branch of a typical withdrawing approaching experiment, see, for example, Fig. 3.19c and d.

Furthermore, a region in the phase diagrams in Fig. 3.22a and b close to Tr_1 with $\theta_c < 90°$ (shaded area in Fig. 3.22b) is not accessible for a typical withdrawing approaching experiment. The size of this region decreases dramatically with a decreasing θ_c. To quantify this decrease, we calculated the relative difference between the coordinates $(\hat{R}, \hat{h})$ of the maximum in $\hat{R}$ and Tr_1 and plot it against θ_c in Fig. 3.22c. $\Delta\hat{R}/\hat{R}_{Tr_1}$ and $\Delta\hat{h}/\hat{h}_{Tr_1}$ decrease exponentially with decreasing θ_c. Numerical and experimentally we did not succeed to verify without doubt the stability in the shaded region in Fig. 3.22b. In the experiments ($\theta_c = 60°$), this region is already very small, below our measurement precision. In the simulations, the converging process turned out to be difficult for these shapes. The difference between stable shapes and unstable shapes is very small in this region. This makes it necessary to use a high number of facets to be able to distinguish between them. Therefore, the shapes need a lot of calculation time to converge against a

	Tr_1		Tr_2	
θ_c	$\hat{R}$	$\hat{h}$	$\hat{R}$	$\hat{h}$
0°	0.0	2.4814		
60°	0.1782 ± 0.0001	3.48 ± 0.01	1.91 ± 0.01	0.939 ± 0.005
90°	0.632 ± 0.005	2.69 ± 0.02	1.70 ± 0.01	1.27 ± 0.01

Table 3.1: shows points in the $\hat{R} - \hat{h} - \theta_c$ shape space, where three shape configurations meet. We call them triple points. There are two triple points, Tr_1 between CB, SB and DB, Tr_2 between CB, SB and ShB. The points are listed for $\theta_c = 0°$, $\theta_c = 60°$ and $\theta_c = 90°$.

minimum. A complex convergence study is needed to answer the problem with certainty, which we have not done. It remains an open question, if the shaded region in Fig. 3.22b belongs to stable or unstable shapes. It will be interesting to do this convergence study in future work, to answer this question with certainty.

For $\theta_c = 0°$ the CB→DB does not exist, since there are never attractive forces between the bubbles. Consequently there are no unduloids fulfilling all boundary conditions. The upper and lower branch vanish in the triple point $\mathrm{Tr}_1(\theta_c = 0°)$, which corresponds to the shape of two spheres in contact in a point.

3.4.3.4 Shift instability CB↔ShB↔CB

Depending on $\hat{R}$, θ_c and $\hat{h}$, the pressure difference $\Delta\hat{p}$ between the inside and the outside of the bubbles can become zero and negative. This is shown by the magenta dotted line for $\Delta\hat{p} = 0$ and the area above the magenta dotted line for $\Delta\hat{p} < 0$ in Fig. 3.20a and b. If $\Delta\hat{p} = 0$ the surface is a part of a catenoid. The only axisymmetic constant mean curvature surfaces with $\Delta\hat{p} < 0$ are nodoids, see Section 3.3. Some of them are unstable against non-axisymmetric perturbation, like in the case for the TB. In this case the film between the two bubbles is shifted away from the frame axis, as shown in the ShB examples of Fig. 3.4. The mirror symmetry to the xy-plane remains, as in the case for the TB with $\theta_c = 90°$. However, here the contact film for two bubbles stays horizontal and flat. We can identify a critical needle radius $\hat{R}_{\mathrm{Tr}_2}$ such that: If $\hat{R} \leq \hat{R}_{\mathrm{Tr}_2}$ we go from CB↔ShB and back from ShB↔CB before we obtain a CB→SB. If $\hat{R} \geq \hat{R}_{\mathrm{Tr}_2}$ we go from CB↔ShB and than directly to ShB→SB. Therefore $\hat{R}_{\mathrm{Tr}_2}$ is representing the triple points where the dash dotted magenta line and the solid blue line meet each other in the shape diagrams in Fig. 3.20 and the triple line for the same shapes in the θ_c-$\hat{R}$-$\hat{h}$-space. The numerically obtained values of $\hat{R}_{\mathrm{Tr}_2}$ and $\hat{h}_{\mathrm{Tr}_2}$ associated with Tr_2 can be found in Table 3.1. The theoretical prediction for the CB→SB starts to be wrong at the Tr_2 line. Simulations are necessary to obtain the real point of detachment.

The last stable catenoid is the point in Fig. 3.20 where the dotted magenta line (for catenoids) and the blue solid line (CB→SB) are tangential to each other. Starting from this point, all catenoid solutions clockwise on the magenta dotted line are stable and unstable counter clockwise. This is fundamentally different from the stable catenoid solution without a volume constraint [53], see Chapter 2.

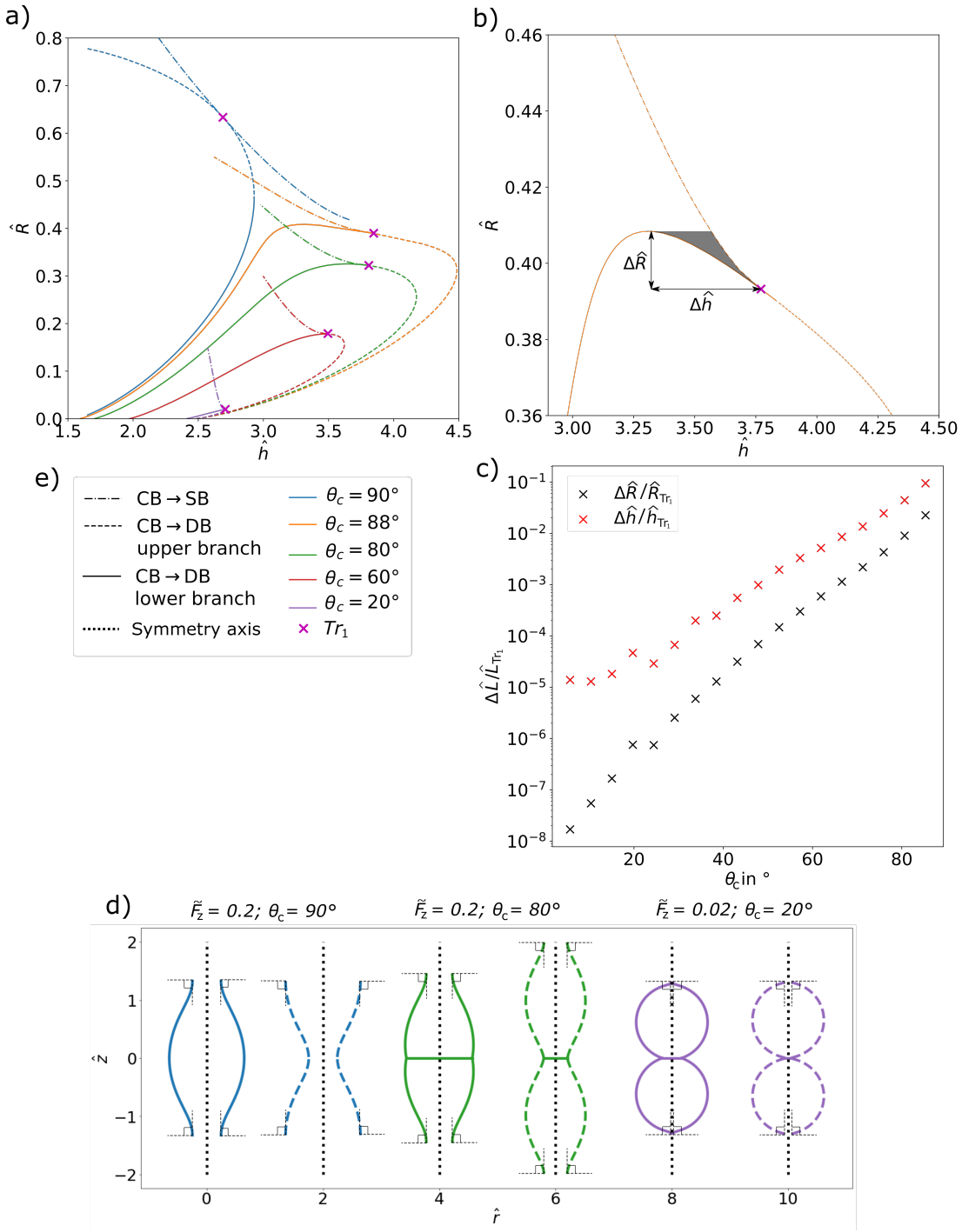

Figure 3.22: a) Lines and points in the phase diagram $\hat{R}$ over $\hat{h}$ for different θ_c, such as the $\hat{R}(\hat{h})$ for CB→SB and CB→DB, where the latter has been split into an upper and lower branch. The intersection of CB→SB and CB→DB (Tr_1) is also shown. b) A zoom in to the triple point Tr_1 for $\theta_c = 80°$ with the definition of $\Delta\hat{R}$ and $\Delta\hat{h}$. c) The evolution of $\Delta\hat{R}/\hat{R}_{Tr_1}$ and $\Delta\hat{h}/\hat{h}_{Tr_1}$ with increasing θ_c. d) Shapes with different θ_c and $\tilde{F}_z$, which fulfill the conditions of Equ. (3.39) and (3.40) shifted horizontally for a better visualisation. e) The legend for all sub figures.

3.4.4 Shape of the tilted film and Landau approach

In the following we analyse more close the non-axisymmetric instabilities CB↔TB, CB↔ShB and the non-axisymmetric shapes. We use an approach known from Landau's Theory, which normally describes phase transitions, to model our shape transitions. We will start with CB↔TB.

The surface and the contact film of tilted bubbles is shown in Fig. 3.23a for two different θ_c. It has to be a minimal surface since the pressure difference between the two bubbles is zero. However the surface is not a plane anymore, as can be seen in Fig. 3.23a. For a better representation we use a new coordinate system (x', y', z') (Fig. 3.23a). $\vec{e}_{z'}$ is the normal vector to the best fitting plane of the contact surface. ψ is the angle between $\vec{e}_{z'}$ and $\vec{e}_z$ defined by

$$\cos(\psi) = \vec{e}_z \cdot \vec{e}_{z'}. \tag{3.41}$$

As the difference to a plane is only very small (note the different scaling for the z' axis in Fig. 3.23a), the undulations in the z' direction could not be observed in the experiments. In the simulations, one clearly observes a three undulated shape with a triple saddle point in the origin, which was in this form unexpected.

The second observation for CB↔TB was the continuity of F_z across the instability, which suggests a second order shape transition. In the following we model the energy $\mathcal{E}$ close to CB↔TB with a Landau approach to quantify ψ and the undulations of the contact film, which were in this form unexpected. Therefore we describe the shape of the contact film in cylindrical coordinates (z, r and φ) as a complex Fourier series in φ and polynom in r

$$z = \sum_{n}^{\infty} P_n r^n \sum_{-\infty}^{\infty} A_k e^{ik\varphi}, \tag{3.42}$$

with A_k the complex Fourier coefficients and P_n the prefactor of the polynomial in r. We know that $A_0 = 0$, since the contact plane is not shifted along z. A_k is always the conjugate complex of A_{-k} ($A_k = \overline{A}_{-k}$), since z is always real. First, we make the assumption of a flat tilting plane and consider only the first mode A_1 and A_{-1}, and $P_1 = 1$. All other P_n and A_k are zero. Consequently, $|A_1|$ can be interpreted as the tilt angle with

$$\sin(\psi) = |A_1|. \tag{3.43}$$

It is therefore the mode, that best describes the instability and lends itself as an order parameter. We can then write the Landau potential as

$$\mathcal{E} = a_1(\hat{h})|A_1|^2 + b_1(\hat{h})|A_1|^4. \tag{3.44}$$

The height $\hat{h}$ can be interpreted as a temperature and the tilt angle ψ or $|A_1|$ as the order parameter if we compare it with the classical Landau approach for phase transitions. For $|A_1|^2$ we can write

$$|A_1|^2 = A_1 A_{-1} e^{i\varphi - i\varphi} = A_1 A_{-1}. \tag{3.45}$$

Consequently, the Landau potential given in Equ. (3.44) is independent of φ and symmetric to $z \to -z$. These two symmetries are required for the instability. As long a_1 and b_1 are positive in Equ. (3.44), the only extremal point and minimum is at $|A_1| = \sin(\psi) = 0$. At a point of instability, a_1 must change sign. Close to the point of instability we can make

the approximation

$$\begin{aligned} a_1 &= a_1^*(\hat{h} - \hat{h}_{\mathrm{CB}\leftrightarrow\mathrm{TB}}), \\ b_1 &= b_1^*, \end{aligned} \tag{3.46}$$

with a_1^* and b_1^* two constants. Differentiating Equ. (3.44) with respect to $|A_1|$ after inserting Equ. (3.46) we obtain

$$\frac{\mathrm{d}\mathcal{E}}{\mathrm{d}|\mathrm{A_1}|} = 2a_1^*(\hat{h} - \hat{h}_{\mathrm{CB}\leftrightarrow\mathrm{TB}})|A_1| + b_1^* 3|A_1|. \tag{3.47}$$

The bubble shape is stable if the energy (Equ. (3.44)) is in a minimum, therefore Equ. (3.47) must be zero and the second derivative positive. We obtain

$$|A_1| = 0 \quad \text{for } \hat{\mathrm{h}} > \hat{\mathrm{h}}_{\mathrm{CB}\leftrightarrow\mathrm{TB}}, \tag{3.48}$$

$$|A_1|^2 = -\frac{a_1^*}{b_1^*}\left(\hat{h} - \hat{h}_{\mathrm{CB}\leftrightarrow\mathrm{TB}}\right) \quad \text{for } \hat{\mathrm{h}} < \hat{\mathrm{h}}_{\mathrm{CB}\leftrightarrow\mathrm{TB}}. \tag{3.49}$$

Fig. 3.23c compares the $\sin\psi = |A_1|$ for $\hat{R} = 0.4$ for θ_c between 0° and 90° with the Landau approach from Equ. (3.49). $-a_1^*/b_1^*$ and $\hat{h}_{\mathrm{CB}\leftrightarrow\mathrm{TB}}$ are therefore fitting parameters. One observes for all θ_c a quadratic increase in $|A_1|$ for $\hat{h} < \hat{h}_{\mathrm{CB}\leftrightarrow\mathrm{TB}}$ as aspect. The precision decreases with approaching $\theta_\mathrm{c} = 90°$, because the contact film represents smaller energies, which makes it more complicate for surface evolver to converge the contact film correctly (Fig. 3.23c for $\theta_\mathrm{c} = 80°$ and 85°). There is no contact film for $\theta_\mathrm{c} = 90°$. Consequently, this approach is not working for $\theta_\mathrm{c} = 90°$.

In Fig. 3.23d, a_1^*/b_1^* and $\hat{h}_{\mathrm{CB}\leftrightarrow\mathrm{TB}}$ are compared for $\hat{R} = 0.4$ and different θ_c. a_1^*/b_1^* increases in absolute value approaching $\theta_\mathrm{c} = 90°$ and $\hat{h}_{\mathrm{CB}\leftrightarrow\mathrm{TB}}$ makes a jump from $\theta_\mathrm{c} < 90°$ to $\theta_\mathrm{c} = 90°$. The increasing a_1^*/b_1^* versus $\theta_\mathrm{c} = 90°$ and the jump at $\theta_\mathrm{c} = 90°$ are related to each other: To change the surface area of a surface element, it has to be stretched or compressed in one of the tangential directions ($\vec{r}_{,\varphi}$ or $\vec{r}_{,z}$). The tilting stretches or compresses the surface in $\vec{r}_{,z}$ direction where the two bubbles are in contact. The inverse ratio of a_1^*/b_1^* can be interpreted as the resistance against tilting, which decreases with increasing θ_c and vanishes at $\theta_\mathrm{c} = 90°$ since all stretched surface elements are compensated by all compressed surface elements. Consequently, the tilting has no effect on the shape for $\theta_\mathrm{c} = 90°$ and we cannot observe it. The jump in $\hat{h}_{\mathrm{CB}\leftrightarrow\mathrm{TB}}$ at $\theta_\mathrm{c} = 90°$ confirms that. In reality, we observe another instability with other shape characteristics, which is much closer to the shift instability CB↔ShB at this point.

Let us now expand the Landau potential from Equ. (3.44) to higher order in $|A_k|$. The new potential still has to respect both symmetries, invariant to a rotation φ in direction $\vec{e}_z$ and mirror symmetry to the middle plane with $z = 0$. All quadratic terms like $|A_k|^2$ respect both, (Equ. (3.45)). But since only one term can destabilise ($a_k(\hat{h})$ crosses zero), we are interested in the coupled terms, as

$$|(A_1^2 A_{-2} + A_{-1}^2 A_2)e^{i2(\varphi-\varphi)}|. \tag{3.50}$$

This term is invariant to rotation but not mirror symmetric, due to the power three in the $A_1^2 A_{-2}$ term. Consequently, a coupling between the second and the first order, which respects all symmetries, happens only at higher order. For odd k the first coupling which respects all symmetries is

$$|(A_1^k A_{-k} + A_{-1}^k A_k)e^{ik(\varphi-\varphi)}|. \tag{3.51}$$

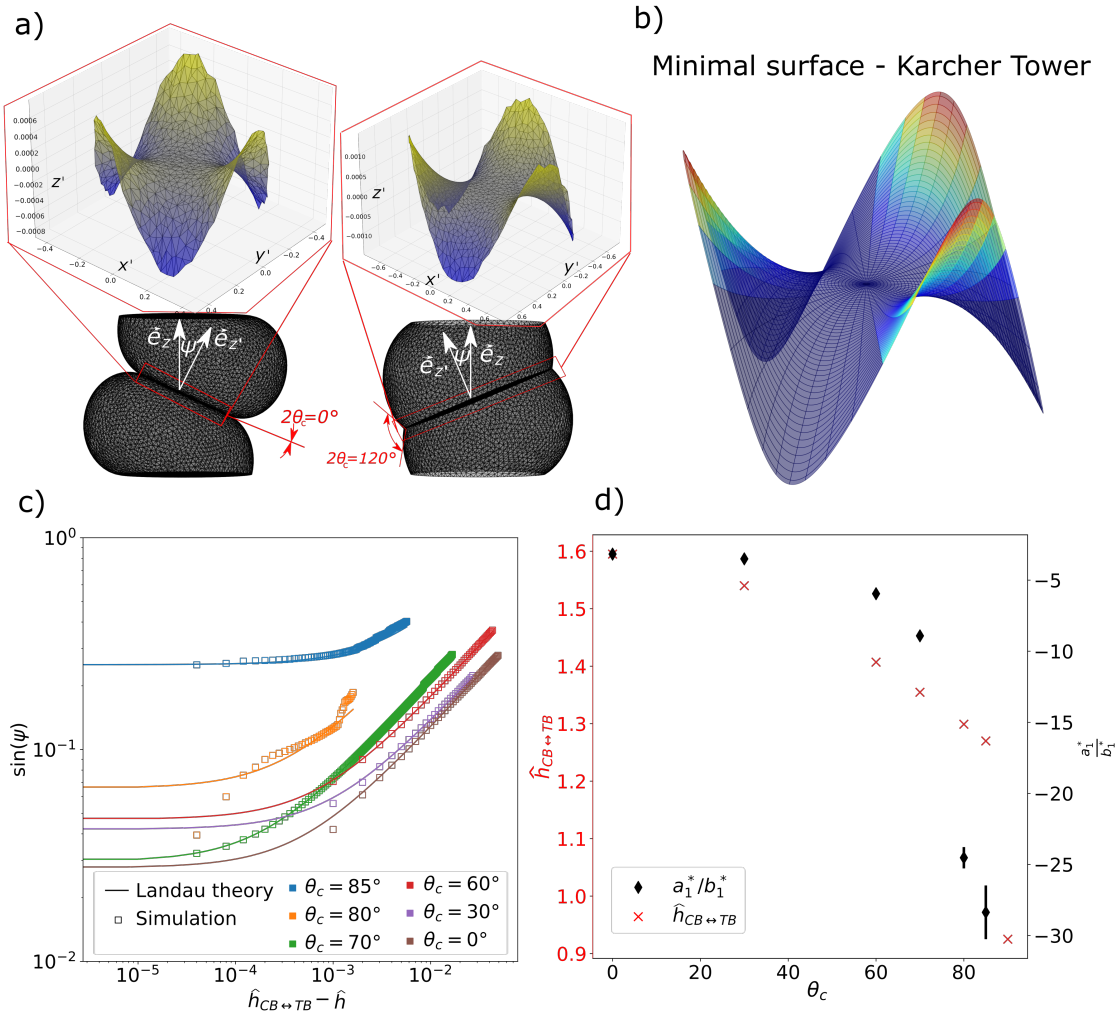

Figure 3.23: a) Two examples of tilted bubble simulated in Surface Evolver. Left: $\theta_c = 0°$. Right: $\theta_c = 60°$. The upper part of the figure shows the shape of the contact film in the (x',y',z') coordinate system which has been rotated by ψ. b) An example of the minimal surface type Karcher tower [15]. c) $\sin\psi = |A_1|$ plotted against $\hat{h}_{\mathrm{CB}\leftrightarrow\mathrm{TB}} - \hat{h}$ for different θ_c and $\hat{R} = 0.4$, compared with the fit to the minima of the Landau potential (Equ. (3.49)). d) Values for $a_1^\star/b_1^\star$ and $\hat{h}_{\mathrm{CB}\leftrightarrow\mathrm{TB}}$ for $\hat{R} = 0.4$ for different θ_c.

At the beginning we will consider only the third order ($k = 3$), since we observe it clearly in the tilted contact surface (Fig. 3.23) and it is the smallest odd k after one. We will consider only the term where the two couples with the lowest power, since $|A_1|$ and $|A_3|$ should be small close to $\hat{h}_{\mathrm{CB}\leftrightarrow\mathrm{TB}}$. We obtain the new Landau potential

$$\mathcal{E} = a_1(\hat{h})|A_1|^2 + b_1(\hat{h})|A_1|^4 + a_3(\hat{h})|A_3|^2 + b_3(\hat{h})|A_3|^4 + 2c_3|(A_1^3 A_{-3} + A_{-1}^3 A_3)|. \quad (3.52)$$

Since $A_1 = \overline{A}_{-1}$ and $A_3 = \overline{A}_{-3}$, we can write

$$\mathcal{E} = a_1(\hat{h})|A_1|^2 + b_1(\hat{h})|A_1|^4 + a_3(\hat{h})|A_3|^2 + b_3(\hat{h})|A_3|^4 + c_3(\hat{h})|A_1^3 A_3| \quad (3.53)$$

We want to describe the same instability as with the Landau approach from Equ. 3.46, we again assume that a_1 becomes negative and so the energy minimum shifts. This time

we are looking for two unknown, $|A_1|$ and $|A_3|$. Differentiating the potential with respect to the two variables gives us

$$\frac{\partial \mathcal{E}}{\partial |A_1|} = 2a_1^*(\hat{h} - \hat{h}_{\mathrm{CB}\leftrightarrow\mathrm{TB}})|A_1| + 4b_1^*|A_1|^3 + 3c_3^*|A_1|^2|A_3| = 0, \tag{3.54}$$

$$\frac{\partial \mathcal{E}}{\partial |A_3|} = 2a_3^*|A_3| + 4b_3^*|A_3|^3 + c_3^*|A_1|^3 = 0. \tag{3.55}$$

As before we obtain for $\hat{h} > \hat{h}_{\mathrm{CB}\leftrightarrow\mathrm{TB}}$

$$|A_1| = 0 \text{ and } |\mathrm{A}_3| = 0. \tag{3.56}$$

For $\hat{h} < \hat{h}_{\mathrm{CB}\leftrightarrow\mathrm{TB}}$ we obtain

$$|A_1| = -\frac{3c_3^*|A_3|}{4b_1^*} \pm \left(\left(\frac{3c_3^* A_3}{4b_1^*} \right)^2 - \frac{a_1^*}{2b_1^*}(\hat{h} - \hat{h}_{\mathrm{CB}\leftrightarrow\mathrm{TB}}) \right)^{0.5} \tag{3.57}$$

Close to $\hat{h}_{\mathrm{CB}\leftrightarrow\mathrm{TB}}$, $|A_3| << 1$ and we obtain Equ. (3.49) again. Furthermore, we can neglect higher orders of $|A_3|$ in Equ. (3.55) to obtain

$$2a_3^*|A_3| = -c_3^*|A_1|^3. \tag{3.58}$$

Consequently, $|A_3|$ should be proportional to $|A_1|^3$. To verify this, we fitted the contact film to Equ. (3.42) up to the order $k = 5$ and plotted the evolution of A_k against $A_1 = \sin\psi$ in Fig. 3.24a. The proportionality between $|A_3|$ and $|A_1|^3$ is clearly observed. Even for $k = 5$ the expected proportionality to $|A_1|^5$ is visible. The even orders ($k = 2$ and 4) are small in comparison to the odd k.

Every mode has a direction φ_k in the complex plane defined via

$$\tan\varphi_k = \frac{\mathrm{Im}[A_k]}{\mathrm{Re}[A_k]}. \tag{3.59}$$

In Fig. 3.24b the difference $\varphi_k - \varphi_1$ is plotted against $\hat{h} - \hat{h}_{\mathrm{CB}\leftrightarrow\mathrm{TB}}$. Since the Landau potentials are invariant to rotation only the differences between the φ_k are of interest. Only $\varphi_3 - \varphi_1$ was accurate enough and remains constant with approximately 25° over all investigated $\hat{h}$.

In Fig. 3.24c, the fitted surfaces of Equ. (3.42) for $\varphi = 0$ are represented. One observes with increasing ψ and decreasing $\hat{h}$ an increase in $\hat{z}'(\varphi = 0)$ of the modulation. Since the curves seems to be self similar and the leading term $|A_3|$ for $\hat{z}'$ is proportional to $|A_1|^3$, we normalise the curves from Fig. 3.24c with $|A_1|^3$ and obtain the master curve with the uncertainty environment of one standard derivation in Fig. 3.24d.

Consequently, all forms are similar regardless of the distance to $\hat{h}_{\mathrm{CB}\leftrightarrow\mathrm{TB}}$. A completely analytical solution to this problem therefore seems realistic. In addition, the contact film can be more easily compared to other minimal surfaces, such as the Karcher tower in Fig. 3.23b.

3.4.4.1 Laundau approach for ShB

To use the same approach for CB↔ShB and ShB↔CB we have to compare the shifted surfaces (obtained with Surface evolver) with the axisymmetric surfaces (a Delaunay

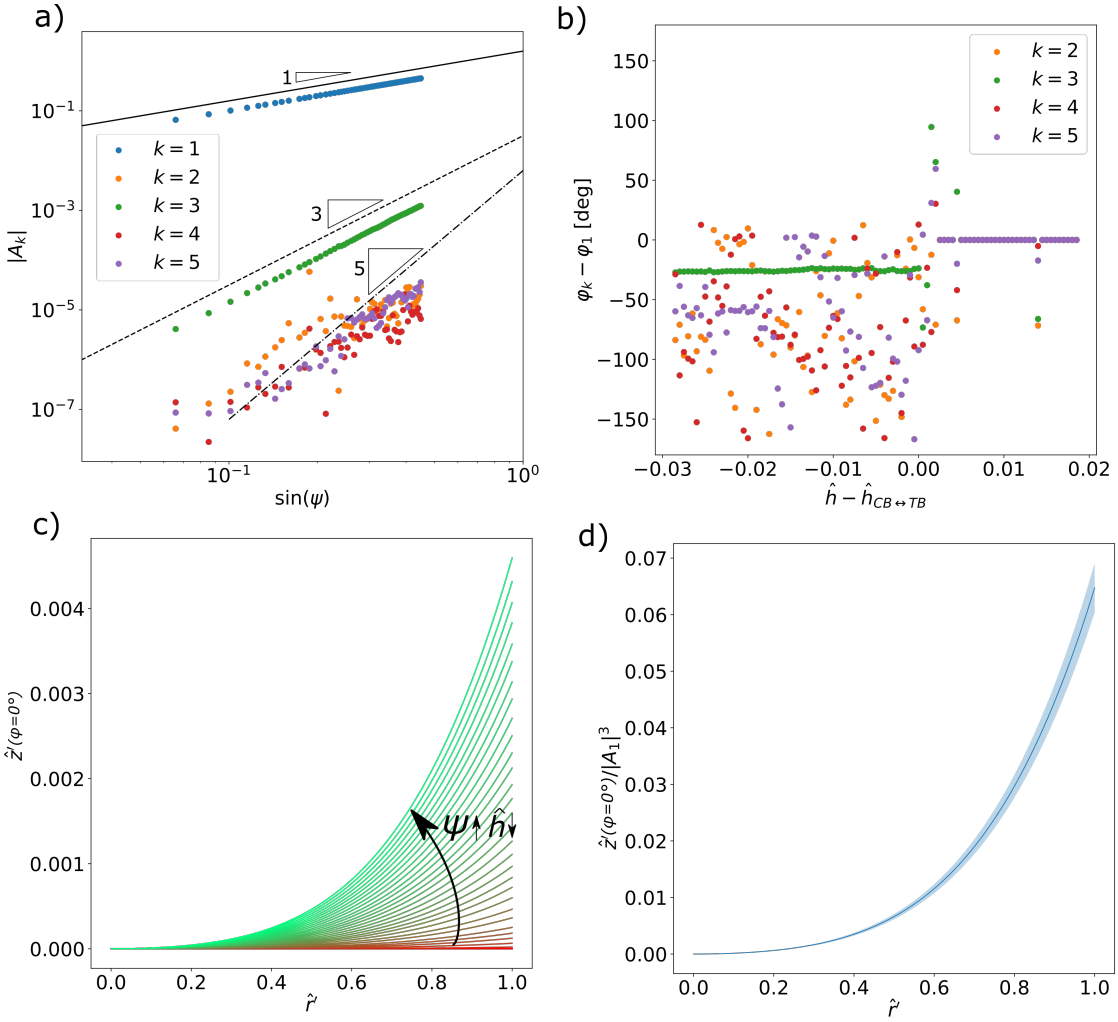

Figure 3.24: a) Absolute values of the complex Fourier coefficients $|A_k|$ up to the order $k = 5$ plotted against $\sin\psi$, the best fitting tilt angle, with $|A_1| = \sin\psi$, which is also the case. b) The change in phase shift φ_k of the complex Fourier coefficients between the first (φ_1) and the other orders (φ_k with $k > 1$). c) $\hat{z}'$ plotted against $\hat{r}'$ for different $\hat{h}$ and ψ, first part of Equ. (3.42) for $\varphi = 0$. d) Master curve for curves from c) normalized by $\sin\psi^3 = |A_1|^3$ with an uncertainty environment of one standard derivation.

Surface). CB↔ShB stands for the instability where $\hat{h}$ decreases and one goes from CB to ShB. ShB↔CB stands for the instability where $\hat{h}$ decreases and one goes from ShB to CB. Before we compare them with each other we obtain the critical distances $\hat{h}_{\mathrm{CB}\leftrightarrow\mathrm{ShB}}$ and $\hat{h}_{\mathrm{ShB}\leftrightarrow\mathrm{CB}}$ by looking at the smallest eigenvalues, which are plotted in Fig. 3.25a. Afterwards we compare two surfaces with the same $\hat{h}$ obtained with Surface Evolver simulations (SE) and the theory of Delaunay Surfaces (DS), using

$$\Delta\hat{r} = \hat{r}_{\mathrm{SE}}(\hat{z}, \varphi) - \hat{r}_{\mathrm{DS}}(\hat{z}). \tag{3.60}$$

An example of $\Delta\hat{r}$ as a function of $\hat{z}$ and φ with $\hat{h} = 0.265$ is shown in Fig. 3.25b. The red points represent the vertices of the Surface Evolver model. The blue surface is a surface fitted to the SE points. We notice that $\Delta\hat{r}$ depends only slightly on $\hat{z}$ and quickly

becomes zero approaching the frame. It is periodic in φ. Therefore, we take Equ. (3.42) and replace $\hat{z}$ with $\Delta\hat{r}$ and $\hat{r}$ with $\hat{z}$,

$$\Delta\hat{r} = \sum_{n}^{\infty} P_n \hat{z}^n \sum_{-\infty}^{\infty} A_k e^{ik\varphi}. \tag{3.61}$$

Since $\Delta\hat{r}$ depends mostly only on φ, we neglect higher orders of P_n and use only the first term with $P_0 = 1$. An example of the fitted surface with Equ. (3.61) is represented in Fig. 3.25b as the blue surface, which fits rather well. We immediately obtain the different $|A_k|$ and φ_k from the fit. The $|A_k|$ are represented in Fig. 3.25c, e and f, the φ_k in Fig. 3.25d. In all cases, the range of $\hat{h}$ is chosen in a manner that both instabilities (CB↔ShB and ShB↔CB) are represented. In the general case, $\hat{h}$ increases from the left to the right, except in Fig. 3.25e, where it increases from the right to the left. With increasing k the $|A_k|$ become smaller. In general they all follow the same tendency. If $|A_1|$ increases or decreases the other $|A_k|$ also increases or decreases respectively. An exception is $|A_3|$, which has a singularity in between the two critical distances $\hat{h}_{\mathrm{CB}\leftrightarrow\mathrm{ShB}}$ and $\hat{h}_{\mathrm{ShB}\leftrightarrow\mathrm{CB}}$, see Fig. 3.25c,e and f. We do not have an explanation for that. It is really surprising, since all other modes behave as before, which means the behavior of $|A_3|$ is independent of the other modes in this region. Farther investigations are necessary to understand this phenomena.

The shift $\varphi_k - \varphi_1$ in Fig. 3.25d is difficult to interpreted, due to a lot of noise. It is represented mainly to complete the data set. Nevertheless we see for the smaller k in some regions a dependency on $\hat{h}$. The jumps can be explained with symmetries between the different modes. All modes are invariant to a phase shift of $2\pi/k$. Consequently, the shift $\varphi_k - \varphi_1$ has k possibilities with an identical configuration.

Fig. 3.25e and f show the behavior of the different $|A_k|$ as a function of $\hat{h}$ close to the critical distances $\hat{h}_{\mathrm{ShB}\leftrightarrow\mathrm{CB}}$ and $\hat{h}_{\mathrm{CB}\leftrightarrow\mathrm{ShB}}$ in log-log scale. Close to $\hat{h}_{\mathrm{ShB}\leftrightarrow\mathrm{CB}}$, $|A_1|^2$ is proportional to $\hat{h}_{\mathrm{ShB}\leftrightarrow\mathrm{CB}} - \hat{h}$ as for the CB↔TB (Fig. 3.23c). Therefore, $|A_1|$ is again a suitable order parameter. It would be interesting to find other coupled modes as for the CB↔TB using the different slopes in Fig. 3.25e. The slope of 0.8 for $|A_2|$ is difficult to relate to a specific mode since it does not scale with 0.5. The slopes of 1.0 for $|A_3|$ and $|A_4|$ propose a proportionality between $|A_1|^2$ and $|A_3|$ or $|A_4|$. There are no simple modes with this dependency which respect the different symmetries of the problem. We therefore stop here with our investigations. For the second instability represented in Fig. 3.25f, we do not find an order parameter, due to the slopes unequal to 0.5. The question automatically arises as to whether the Landau approach is still the right one here, or whether we should proceed differently.

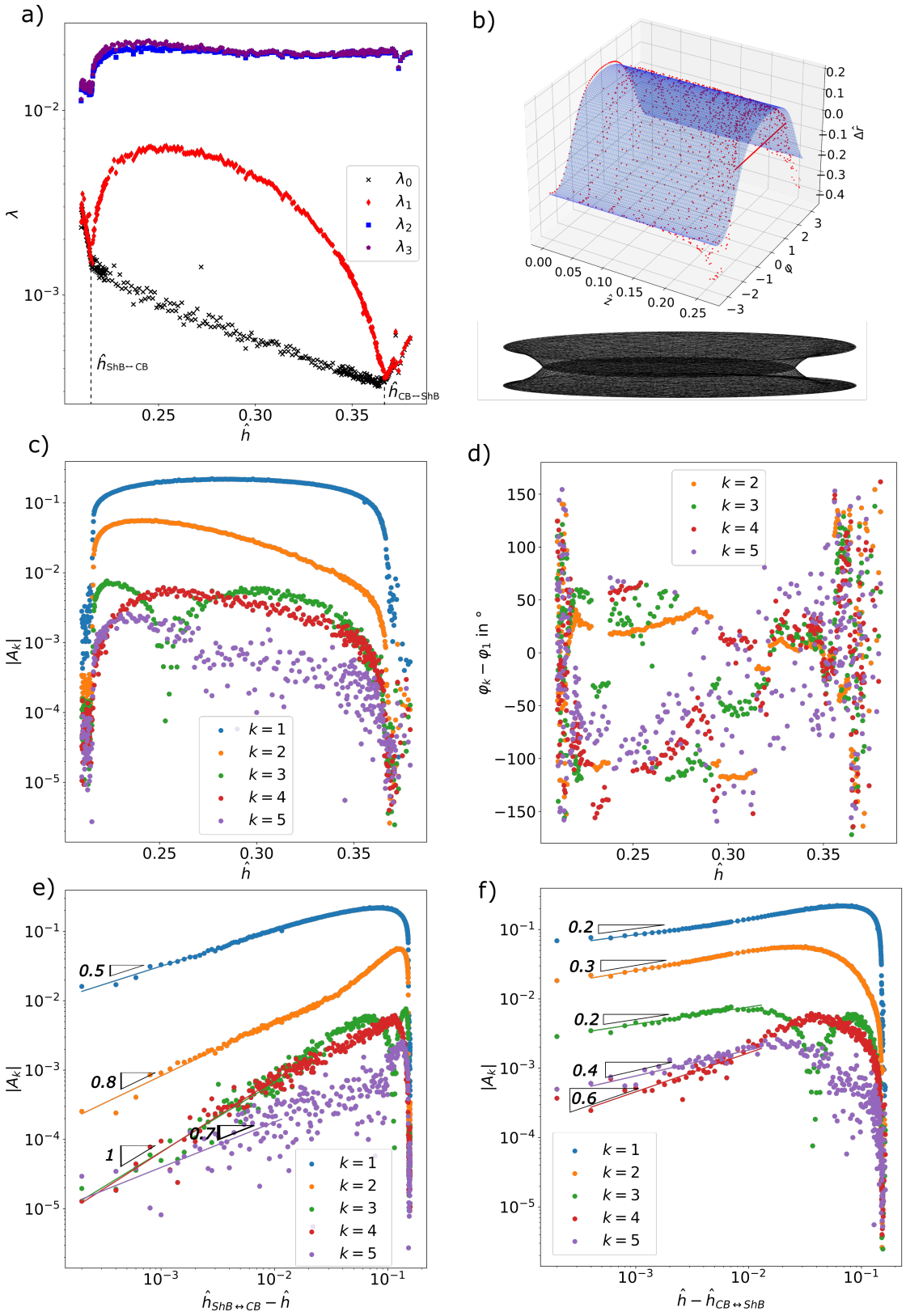

Figure 3.25: The data for all sub-panels is obtained with a Surface Evolver simulation, with $\hat{R} = 1.5$, $\theta_c = 60°$ and different $\hat{h}$. a) The five smallest eigenvalues λ of the hessian matrix are plotted against $\hat{h}$. The instabilities CB↔ShB and ShB↔CB with their critical distances $\hat{h}_{\mathrm{CB}\leftrightarrow\mathrm{ShB}}$ and $\hat{h}_{\mathrm{ShB}\leftrightarrow\mathrm{CB}}$ can be read off. b) A representation of the radial difference between a Delaunay Surface and the simulated surface with the same $\hat{h} = 0.265$ in the top and a representation of the corresponding Surface Evolver model. c) $|A_k|$ plotted against $\hat{h}$ in semi-log scale. d) $\varphi_k - \varphi_0$ plotted against $\hat{h}$. e) $|A_k|$ plotted against $\hat{h}_{\mathrm{ShB}\leftrightarrow\mathrm{CB}} - \hat{h}$ in log-log scale. f)$|A_k|$ plotted against $\hat{h} - \hat{h}_{\mathrm{CB}\leftrightarrow\mathrm{ShB}}$ in log-log scale.

3.5 Conclusion

In this chapter we investigated the shape, stability and mechanical properties of two interacting bubbles or drops pinned on parallel, circular frames. These include capillary bridges, which may be considered as two bubbles (drops) separated by a film of zero surface energy.

In contrast to some previously investigated cases of bubbles or drops interacting between two parallel plates [81, 93], the constraints imposed by the pinning create complex shape spaces separated by different types of instabilities. We investigate here in detail the force-shape-deformation relations using as control parameters the volume of the bubbles (drops), the radius of the circular frames, the distance between the frames, and the contact angle between the bubbles (drops). Whenever the surfaces are axisymmetric, we combine systematic experiments and computer simulations (Surface evolver [64]) with the Delaunay theory of constant mean curvature surfaces [20]. In all cases, experiment, simulation and theory show very good agreement, generally within the experimental/numerical errors. In the case of non-axisymmetric surfaces (TB and ShB), for which no analytical theory exists to our knowledge, we have limited ourselves to a comparison between experiments and numerical simulations. Once again, the agreement is very good and within the experimental and numerical errors.

As shown in Fig.s 3.2 and 3.20, we find five different types of physically stable shapes characterised by different force/pressure-deformation relations: Connected bubbles (CB), Separated bubbles (SB), Detached bubbles (DB), Tilted bubbles (TB) and Shifted bubbles (ShB). The system moves between these shapes through approaching and withdrawing the frames from each other, passing through different types of instabilities which are discussed in detail in Section 3.4. The theory of Delaunay Surfaces explains the other three types of shapes and the instabilities between them. To the best of our knowledge, it is the first time that DB and ShB - and the associated instabilities - are mentioned and investigated. ShB only exist for bubbles (drops) pinned on frames and not for bubbles (drops) interacting between parallel plates. The TB, CB and SB are also observed for bubbles (drops) interacting between parallel plates [81, 82], but the detailed behaviour is different. For example, for the case of the instability CB↔TB, which is already known from previous investigations between parallel plates [81, 82, 41], we show that the bubbles (drops) remain stable at higher compression $\hat{F}_z > 0$ if they are pinned on frames. We show in Section 3.4.4 that this instability can be described as a second order shape transition and that the tilted film become undulated with a three-fold symmetry. We are able to describe and explain the three-fold symmetry with a Landau approach for a second order shape transition. With the same approach the CB↔ShB was modelled. In comparison to CB↔TB this approach was not able to explain the instability in detail. Future work will establish the theoretical prediction of this instability and the associated film shapes.

While we concentrated for practical reasons on three different contact angles $\theta_c = 0^o, 60^o, 90^o$ between the bubbles (drops), our calculations include naturally the intermediate contact angles, which are of increasing interest for communities working on adhesive foams or emulsions [94, 29, 95].

The interest of the provided shape and force/pressure diagrams goes well beyond general curiosities. Bubbles or drops in contact held by frames are increasingly used to quantify the highly non-local interactions between bubbles (drops). Our work can therefore be used to cleanly design and analyse experiments which investigate bubble or

drop interactions.

While the presented investigations explore interactions between "simple" bubbles (drops) of constant interfacial tension, future work will extend this work to interactions between bubbles (drops) with complex interfacial properties, including the presence of an interfacial elasticity.

3.6 Outlook

The boundary conditions of two bubbles in contact on circular frames, as described in this chapter, are similar to a circular film limited by a liquid meniscus attached to circular boundary conditions, demonstrated by Fig. 3.26b. This configuration resembles the setup of a Thin Film Pressure Balance (TFPB in Fig. 3.26a), which is used to analyse thin films, for example to determine the disjoining pressure Π between two interfaces [96, 97, 98]. The problem of the classical TFPB is, that a big part of the disjoining pressure curve is unstable (difference between red and black curve in Fig. 3.26a). For now only Atomic force measurements are able to obtain a full disjoining pressure curve [99]. But this is expensive and no visually access of the film is possible in comparison to a TFPB. Only by changing the geometry of the meniscus boundary conditions to one as in Fig. 3.26b, parts of the unstable branch become stable (Fig. 3.26b) under the condition that the contact angle θ_c is large enough in function of the ratio $\hat{h}/\hat{R}$. The dependencies between the minimal stable pressure $\Delta\hat{p}_{\min}$, $\hat{h}/\hat{R}$ and θ_c are predicted with the theory of Delaunay from Section 3.3.3. In this case it is V and θ_c which are changing and not h. Fig. 3.26c shows a first experimental setup, which was build to demonstrate this also experimentally. But for now our fabrication precision is not precise enough to reach the interesting regimes with $\Pi = \Delta p < 0$ as illustrated in Fig. 3.26b, and to keep at the mean time smooth circular boundary conditions. Future work could optimise the current setup and investigate so far unknown phenomena in thin films as instabilities which should appear if we reach the minimum in Π in the film.

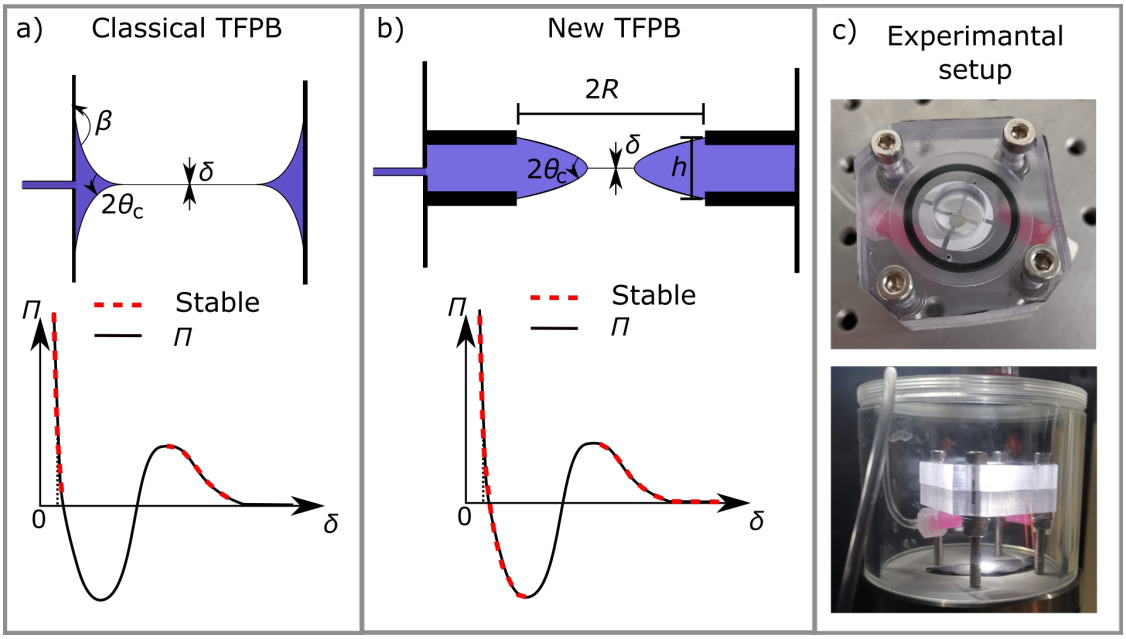

Figure 3.26: a) A scheme of a classical TFPB with a disjoining pressure curve Π. The red curve highlights the stable pressures for the TFPB. b) The new TFPB with boundary conditions as in Chapter 3 with the same disjoining pressure curve and the highlighted red part for the stable pressures. c) Our first proposition of a new TFPB.

Chapter 4

Silicone skin characterisation

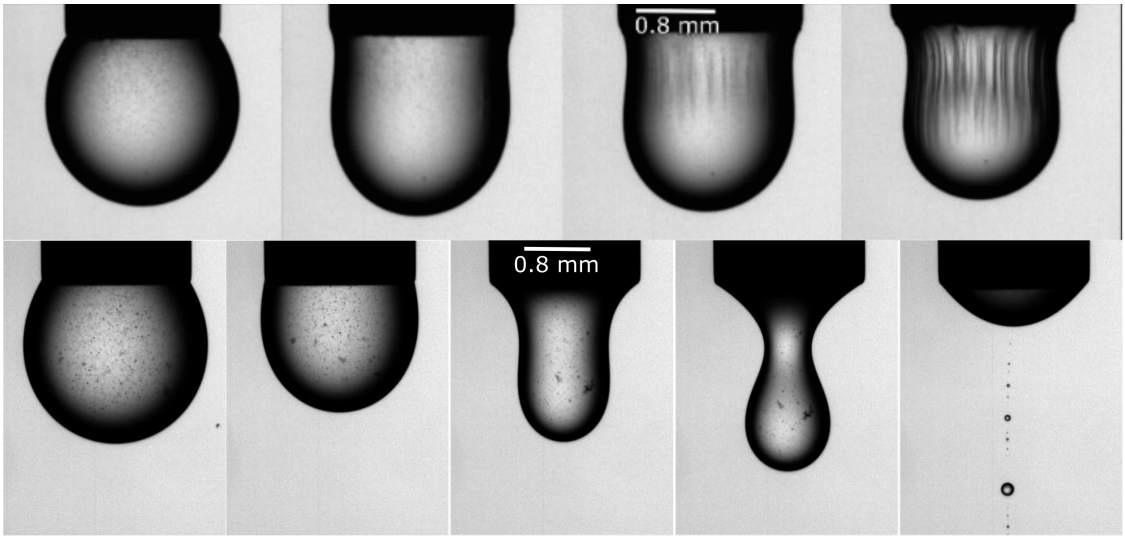

Contents

4.1 Introduction

Capsules find use in many different applications such as pharmacy [100, 101], food industry [102, 103], agriculture [104, 105], cosmetics [106], textile industry [107], printing [108], biosensor engineering [109], active coatings [110] or construction [111]. In most cases, they are not used individually but as a accumulation, such as shown in Fig. 4.1. This brings a comparison with foams or emulsions close. In contrast, the interfacial tension plays a minor role in most cases with capsules, due to high elasto-capillary numbers, $\alpha >> 1$ (Equ. (1.25)). Consequently, the assemblies behave differently from foams and emulsions. In order to optimise the previously mentioned application areas and to benefit simultaneosly from capsule properties and foam or emulsion properties, elastic interfacial forces could be combined with interfacial tension forces by tuning the skin properties (intermediate elastocapillary numbers $\alpha \approx 1$). We are interested in a general understanding of the influence of the interfacial modification from a inelastic fluid interface to a purely elastic solid-like interface and all intermediate states, as discussed in the general introduction in Section 1.2.4. Therefore we look for a suitable model system with tune-able skin properties and associated characterisation methods. A single bubble/drop, droploon/bubloon or capsule must first be characterised, in order to understand the global material behaviour of accumulations of bubbles/drops (foam/emulsion), droploons/bubloons or capsules. The definitions of bubble/drop, droploon/bubloon or capsule are given in Section 1.2.4.

There are different methods to characterise capsule mechanics for different force magni-

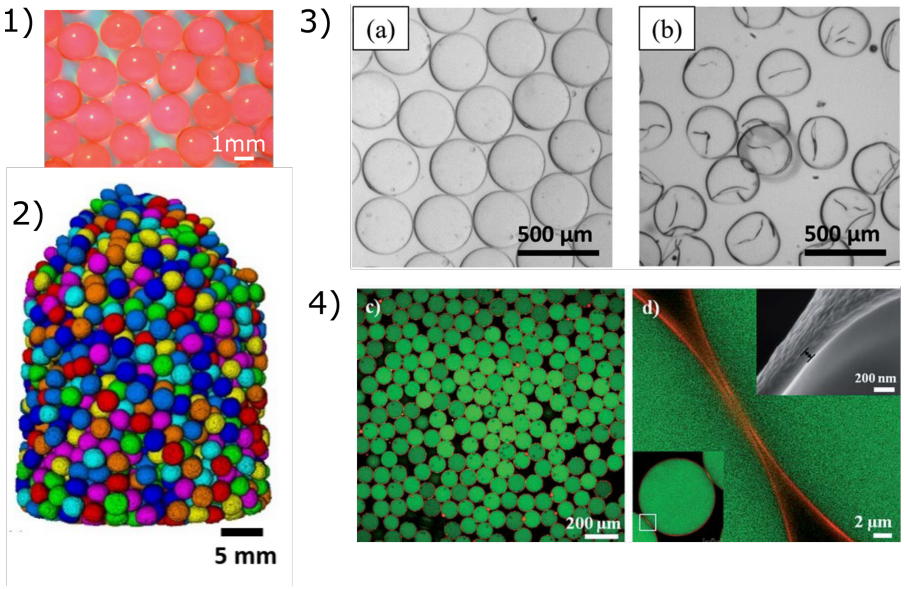

Figure 4.1: Different capsule or droploon/bubloon accumulations: 1) Encapsulation of oil in ca-alginate capsules (photographs of dry capsules under an optical microscope) [112]. 2) 3D volume rendering of a PEG-in-silicone emulsion stabilised by a cross-linked silicone skin obtained from X-ray tomography [2]. 3) Capsules with aqueous core and continuous phase, separated by solid PDMS skin with different levels of deflation: (a) Spherical capsules after fabrication (b) Capsules deflated by 36% [113]. 4) Double emulsion drops, having an ultra thin cross-linked wall as an outer layer [114].

tudes, for example with opitical tweezers, micropipettes, shear flows, AFM or micromanipulations. They are summarised in the article of M. Neubauer *et al.* [115]. To relate the global deformation with the applied force, a constitutive equation is necessary to obtain the stress-strain relation. In most of the methods known to us, including those from the article of M. Neubauer *et al.* [115], the constitutive law of the interface/skin is only indirectly obtained by fitting the results to theoretical models. An exception are direct interfacial rheology experiments. In the general introduction (Section 1.2.4) two examples with the dilational interfacial shear rheology (Fig. 1.9a) and the shear interfacial rheology (Fig. 1.9b) are introduced. In contrast to other methods, there the stress-strain relation is measured directly for a specific deformation. The dilational interfacial shear rheology works directly with bubbles/drops, bubloons/droploons or capsules. This makes this method the most suitable for us. For a full picture of the problem both dilational and shear interfacial rheology are necessary. We also plan to perform shear interfacial experiments in near future. Dilational deformation dominate the main part of our problems. Another reason to start with dilational experiments.

Our chosen model system consists out of two immiscible liquids. The first liquid is a reactive silicone oil, a mixture of two different silicones, a vinyl-terminated PDMS with two functional vinyl groups (Fig. 4.3a) and methylhydrosiloxane (MHDS, Fig. 4.3b) with functional Si-H groups. The second liquid is a catalyst-in-PEG emulsion made with polyethylene glycol (PEG, Fig. 4.3c) and a platinum catalyst, solved in a vinyl-terminated PDMS (Fig. 4.3d). The catalyst forms small droplets in the PEG phase. The two functional groups, the Si-H and the vinyl groups, react with each other in the present of the catalyst.

Fig. 4.2 shows two of our setups, where we create an interface between the catalyst-in-PEG emulsion and the reactive silicone oil. They have different initial shapes. Fig. 4.2a shows the planar setup with an initially flat interface. Fig. 4.2b shows the pendant drop setup with an initially spherical interface. In both setups the emulsion droplets diffuse in the PEG phase and release the catalyst into the silicone phase once they come into contact with the interface. The released catalyst then diffuses in the silicone phase and starts the reaction between the two functional groups building an increasingly cross-linked polymer network. The "skin" is formed with a growing skin thickness δ (Fig. 4.2). Depending on the interface shape, different phenomena can be observed: a wrinkling and folding for the flat interface (Fig. 4.2a) and a buckling for the spherical interface (Fig. 4.2b). A similar formulation was used before by Anais Giustiniani *et al.* [2] and Gael Ginot *et al.* [3]. Their works are summarised in Section 4.2.1 and Section 4.2.2, respectively.

First, we present in Section 4.2 all known information from previous studies [2, 3] about our chosen model system. Second, we characterised and optimised the catalyst-in-PEG emulsion production to ensure that it is reproducible and sufficiently stable. In all previous studies, the emulsion was never properly characterised and controlled. However, it influences many processes at the emulsion-silicone interface, such as the reaction rate or skin growth. Afterwards, we use the optimized catalyst-in-PEG emulsion to investigate the interface between this emulsion and the reactive silicone blend in the material and method Section 4.3. For this purpose, we use the two interface shapes shown in Fig. 4.2. The planar setup helps us to quickly determine interesting parameter spaces due to its simplicity. It also provides initial information about the mechanical properties of the skin through wrinkling and their wavelength. The pendant drop setup can then be used to characterise the interesting parameter spaces more intensively, for example with dilational interfacial shear rheology. Therefore, we exploit a newly developed method, called General stress decomposition (GSD) [116, 37, 36] and use it for the first time at a liquid/liquid interface, to determine the temporal evolution of the viscou-elastic properties of the polymer skin. In Section 4.4 we show our measurement results and try to interpreter them by comparing them with existing theories. At the end we give a conclusion in Section 4.5.

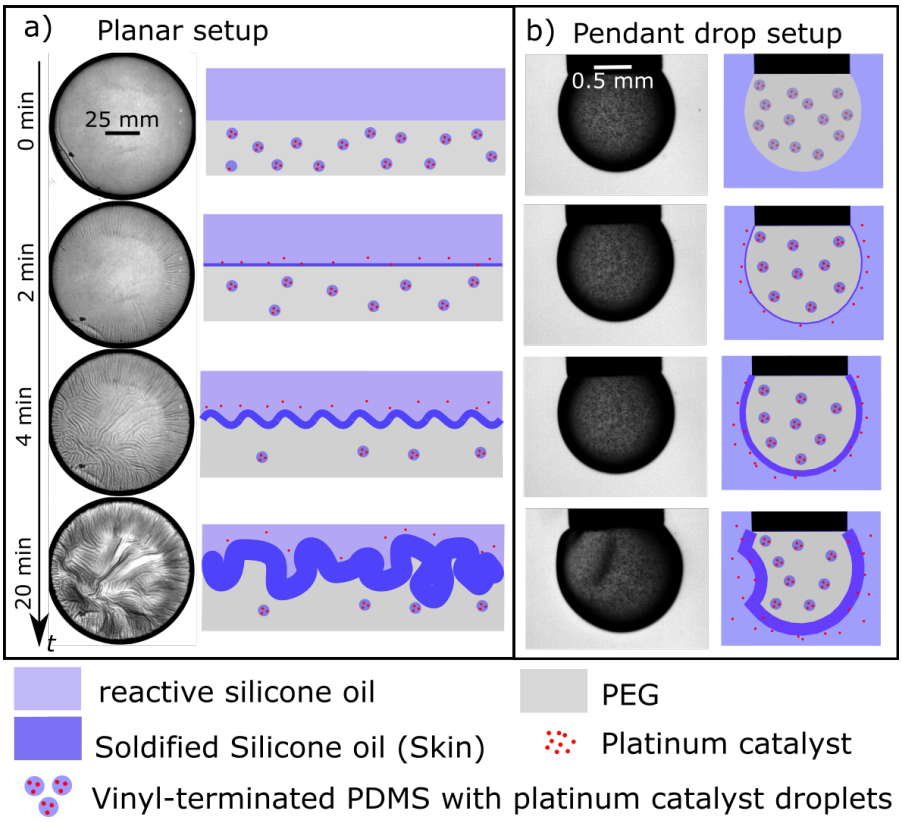

Figure 4.2: A scheme and a experimental example of (a) the planar setup (Petri dish) and of b) the pendant drop setup. First, the interface between the catalyst-in-PEG emulsion and the reactive silicone oil is liquid. The droplets with the catalyst diffuse in the emulsion phase and come into contact with the emulsion/silicone interface. Second, the catalyst starts to diffuse in the silicone phase and starts the reaction. A thin solid silicone phase (the skin) is created at the interface. Third, the skin thickness δ increases with time. The interface winkles in a) and buckles in b) after a characteristic time, which depends on the chosen silicone blend, the catalyst concentration and the shape of the interface.

4.2 Droploon model system

Ultimately, we are looking to create droploons with fully controlled and predictable mechanical properties. To achieve this, we need to understand and control the various influencing factors. For example, the reaction speed, the molecular weight of the polymer, the distribution, number and ratio of the functional groups, the skin thickness δ, the reaction homogeneity, the structure of the final polymer network, the temperature, to name the most important ones. The ratio between the functional groups is

$$S = \frac{mN_{\text{MHDS}}}{2N_{\text{vinyl}}}, \tag{4.1}$$

with N_{vinyl} the number of polymers of vinyl-terminated PDMS, N_{MHDS} the number of MHDS polymers and m the average number of Si-H groups in the MHDS polymer (Fig. 4.3). If $S = 1$ there is exactly the same number of Si-H groups and vinyl groups in the blend. For $S > 1$, there are more Si-H than vinyl groups and for $S < 1$ more vinyl than Si-H groups.

We profit from previous work by Anais Giustiniani *et al.* [2] (Section 4.2.1), and Gael Ginot *et al.* [3] (Section 4.2.2), to obtain some first information about the different influencing factors.

4.2.1 Anais Giustiniani *et al.* [2]

In her work the continuous phase is in contrast to our system only made out of MHDS. The discrete drop phase is as in our case a catalyst-in-PEG emulsion. Instead, the amount of vinyl-terminated PDMS in the drops with the platinum catalyst in the PEG phase (Fig. 4.2) is changed. The amount of vinyl-terminated PDMS controls the final skin thickness δ, since the reaction stops when all vinyl groups reacted with Si-H groups. The resulting skin thicknesses are rather thin. The ratio between the Si-H and vinyl groups is not controlled and unknown locally in the skin. The amount of vinyl groups should decrease with increasing distance to the skin-PEG interface. Consequently the ratio S cannot be used to control the mechanical properties of the skin in this setup.

4.2.2 Gael Ginot *et al.* [3]

In his work the continuous phase consists of three silicone oils: MHDS, vinyl-terminated PDMS (Fig. 4.3) and a non-reactive PDMS. The emulsion in the drops is the same as in our case. The reaction is stopped with the injection of an inhibitor (Dimethyl maleate), which occupies the docking points of the catalyst. The inhibitor is injected after different reaction times to obtain different skin thicknesses. The ratio S was kept constant at 1 and only the mass fraction

$$\Phi_r = \frac{m_{\text{MHDS}} + m_{\text{vinyl}}}{m_{\text{total}}}, \tag{4.2}$$

of the reactive silicones (m_{MHDS} and m_{vinyl}) in comparison to the total mass m_{total} (with the non-reactive PDMS included). The polymer network should be softened differently by the different ratios, with the non-reactive polymers filling in places of reactive polymers. Indeed, the mechanical properties changed with different non-reactive PDMS concentrations. But it could not be completely clarified how the non-reactive groups participate in the polymer network of the skin. Possible scenarios include

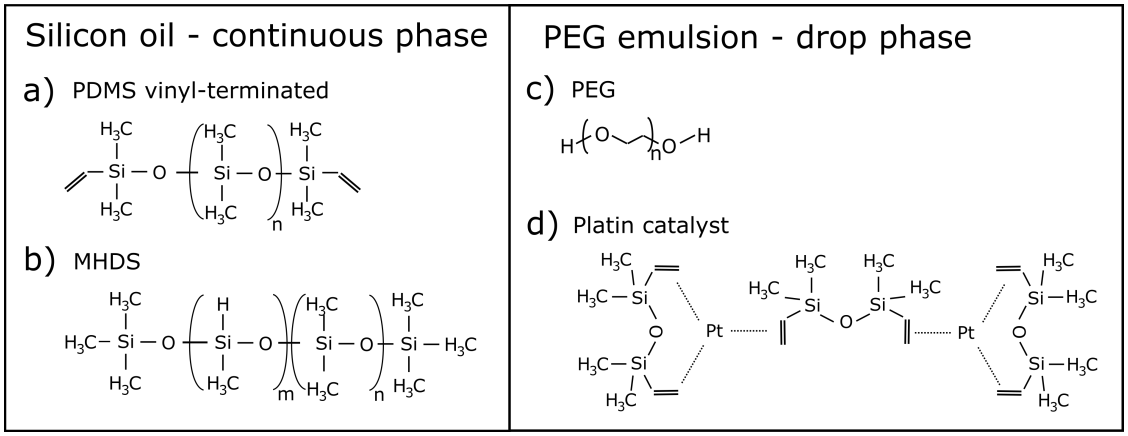

Figure 4.3: Fischer projection of the chemical components of the chosen model system. On the left side the continuous phase (silicone oil) with a) a vinyl-terminated PDMS with two functional vinyl groups at the end of the polymer and b) methylhydrosiloxane (MHDS) with m functional Si-H groups and n non-functional groups. On the right side the components of the catalyst-in-PEG emulsion with c) polyethylene glycol (PEG) and d) the platinum catalyst as a complex with vinyl-terminated PDMS.

- the non-reactive PDMS is trapped in the polymer network and participates to the elastic stresses only by swelling the cross-linked network like a solvent.
- the non-reactive PDMS is pushed out of the skin and slows down the skin growth and influences so the mechanical properties of the skin.

Several droploons were produced using the system of G. Ginots at the outset of this thesis. Afterwards we analysed the interfaces using the beamline ANATOMIX at the Syncrotron SOLEIL [117]. As this system was not used further on and differs from the main system used in this thesis due to the non-reactive silicones, we decided to present the results separately in the Appendix A.2. A characteristic profile could be identified at all interfaces. However, this was not analysed further.

4.2.3 System used in this thesis

Here we use only reactive silicone oils in the continuous phase, but we change S, the ratio between the reactive Si-H and vinyl groups and defined in Equ. (4.1). We use a dilute catalyst-in-PEG emulsion with a defined drop size distributions and volumetric droplet fraction,

$$\Phi_{\mathrm{d}} = \frac{V_{\mathrm{droplets}}}{V}, \tag{4.3}$$

with V the volume of the emulsion phase and V_{droplets} the total volume of all catalyst droplets in the emulsion. We define the local catalyst concentration $\Phi_{\mathrm{cat}}(x, y, z)$ in the silicone phase (droplets or continuous phase) with

$$\Phi_{\mathrm{cat}}(x, y, z) = \frac{V_{\mathrm{cat}}}{V_{\mathrm{silicone}}}, \tag{4.4}$$

with V_{silicone} a volume fraction of the continuous phase or the volume of the droplets V_{droplets} in the case of the emulsion. Therefore, V_{cat} is the volume occupied by the catalyst

in the droplets of the emulsion or in the volume fraction of the continuous phase. We do not know the exact platinum catalyst concentration in the solution we bough from Gelest. They claim that the catalyst concentration in their solution is 3% of catalyst, but we could not check it and do not trust the information 100%. We therefore define $\Phi_{\text{cat}} = 1$ for the solution we bought from Gelest. The same definition was used in the studies by G. Ginot *et al.* [3] and A. Giustiniani *et al.* [2]. Using dilution, Φ_{cat} in the emulsion droplets becomes an additional control parameter.

We want to measure the mechanical properties of the silicone skin and its evolution with time during the skin growth. Finally we stop the reaction with an inhibitor, when the desired properties are achieved. We aim to understand the influence of

- the molecular weight of the chosen polymers and their relative concentrations given by S with Equ. (4.1),
- the initial catalyst concentration Φ_{cat} (Equ. (4.4)) and catalyst droplet fraction Φ_{d} (Equ. (4.3)) in the catalyst-in-PEG emulsion,

on

- the reaction speed and the skin growth,
- elastic properties of the skin (Youngs modulus and compression modulus in two and three dimensions) during skin growth and after stopping the reaction,
- buckling and winkling instabilities.

4.2.3.1 Bulk properties of the silicone phase

Before characterising the skin properties, we determine the bulk properties of solid silicone obtained for different S and Φ_{cat}. Luca Fiorucci carried out rheological and mechanical tests on the same silicone for his master's thesis. All used silicone with their measured molar mass, functionalization degree, density at 20 °C and their viscosity at 20 °C are presented in the Table 4.1. A "short" MHDS (HMS301), a "long" MHDS (HMS082), a "short" vinyl terminated PDMS (DMSv21) and a "long" (DMSv31) were used for this studies. "Short" and "long" refer to the molar mass. The molar mass was measured with a Steric Exclusion Chromatography (SEC) in toluene using PDMS standards by the Carmac platform at the ICS. The functionalization degrees were obtained by NMR spectroscopy (400MHz in $CDCl_3$). We assume the repartition of the functional groups along the polymer chain to be stochastic. The density was measured with a Mettler Toledo density meter D4. The viscosity was measured with a DHR3 rheometer with a cone-plate configuration. The temperature was controlled with a Peltier plate.

Fig. 4.4 shows the measured Shore hardness (Fig. 4.4a) determined with a Hildebrand durometer [118] and the Young's modulus E (Fig. 4.4b) determined with a flat punch indentation method [119]. One observes a maximum around $S = 1$ and a continuously decreasing function away from the maximum for both measured quantities.

In order to understand the processes at the interface between the catalyst-in-PEG emulsion and the reactive silicone oil, the gelation process in the reactive silicone oil is important, especially the transition from liquid to solid. The gelation time t_g indicates, when a continous polymer network is present for a given S and Φ_{cat}. Consequently, the solution is fluid for $t < t_g$ and solid for $t > t_g$. t_g was measured for different S and Φ_{cat}

with oscilatory rheology using a DHR-3 rheometer with a parallel plate geometry. t_g is defined at the point where the derivative of the complex viscosity of the silicone blend is maximal. Fig. 4.5 shows the measured t_g for different catalyst concentration and S. With increasing S and Φ_{cat} the gelation time t_g decreases. The measured data is compared to the fitted empirical model

$$t_g = A_1 S^{n_1} \Phi_{\text{cat}}^{n_2}, \tag{4.5}$$

with the fitting parameters $A_1 = 10^{-7.92}$, $n_1 = -1.15$ and $n_2 = -2.48$ in Fig. 4.5. The measurements were limited to a small range in Φ_{cat}, due to the too slow or fast reactions for lower or higher Φ_{cat}. The relative precision of Φ_{cat} decreases with decreasing Φ_{cat}. This is why we decided to use the model of Equ. (4.5), even if it does not manage to display the exponent for S with $\Phi_{\text{cat}} = 0.00001$ correctly (Fig. 4.5b).

Table 4.1: The used reactive silicones and polyethylene glycol (PEG) with their short names, complete names and measured molar mass (g/mol), functionalization degree (Si-H or C=C), density and viscosity at 20 °C, all measured by us.

Short name	Complete name	Molar mass (g/mol)	Functionalization degree (Si-H)	Density at 20 °C	Viscosity at 20 °C (Pa s)
HMS301	25% - 35% methylhydrosiloxane	5470	0.26	0.972	0.032
HMS082	7% - 9% methylhydrosiloxane	14970	0.07	0.972	0.150
			(C=C)		
DMSv21	vinyl terminated polydimethylsiloxane	7990	0.015	0.968	0.092
DMSv31	vinyl terminated polydimethylsiloxane	29480	0.004	0.974	1.144
PEG400	Poly(ethylene glycol)			1.126	0.104

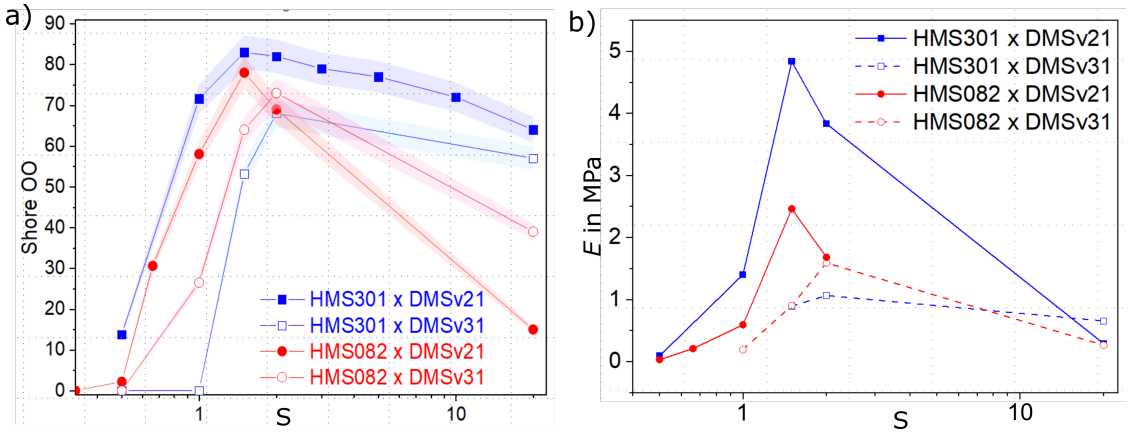

Figure 4.4: Mechanical properties of solidified silicone for different S and different MHDS (HMS301 and HMS082) and vinyl-terminated PDMS (DMSv31 and DMSv21) blends. In a) the Shore hardness and in b) the Young's modulus E.

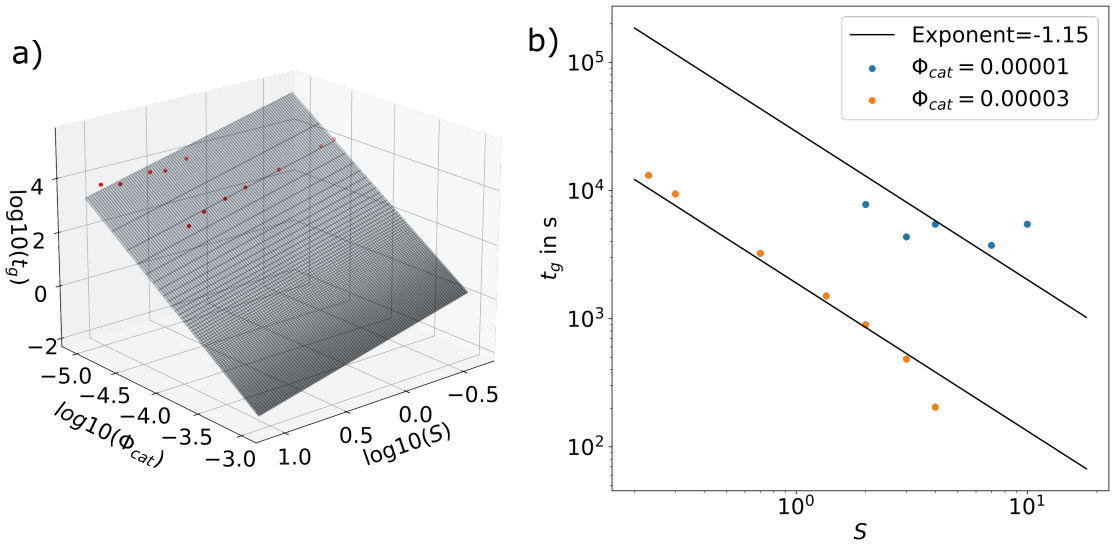

Figure 4.5: a) Comparison of the measured gelation times t_g (red points) with the fitted empirical model from Equ. (4.5). b) The gelation time t_g is plotted against S for two different Φ_{cat} and compared to the empirical model of Equ. (4.5) obtained with the 3D fit from a).

4.3 Material and methods

4.3.1 Materials

We used industrially available silicone oils listed in Table 4.1. All of them were ordered from Gelest and used as provided. The poly(ethylene glycol) (PEG400, Table. 4.1) was ordered from Sigma Aldrich. Before use, the PEG was dried by evaporating the potentially dissolved water in a vacuum oven at 40°C and pressure of 5 Pa for 4 hours. Higher temperatures would damage the PEG polymers. The PEG was then sealed airtight and protected with a layer of argon. Removing water is necessary to avoid additional reactions involving water [3]. The Karstedt platinum catalyst was ordered from Gelest. The complete name is "Complexe platine(0)-1,3-divinyl-1,1,3,3-tétraméthyldisiloxane solution", where the platinum molecules take approximately 3% of the solution as mentioned in Section 4.2.

4.3.2 Generation of the catalyst-in-PEG emulsion

The optimized protocol for the generation of the catalyst-in-PEG emulsion was obtained by Qiwei Li (M2 student) [120] and Leandro Jacomine, by analysing the evaluation of the droplet size distribution with Dynamic Light Scattering (DLS) [121] and optical microscopy for different generation methods. Here we introduce only the method, which was identified as most suitable for us and which was used exclusively for all further experiments.

We take the desired volume of the catalyst solution with a micro pipette and 60 ml of the dried PEG to obtain the desired Φ_d in the final emulsion. If $\Phi_{cat} < 1$ is desired, the solution is mixed with vinyl terminated PDMS (DMSv21, Table 4.1) so that in the end Φ_{cat} and Φ_d are as desired. Second, we mix the PEG with the immiscible catalyst solution with the double syringe method at least 40 times: We transfer rapidly the total liquid trough a small connection from one syringe to another syringe with 60 ml volume [122]. Third, the created emulsion is transferred to another vessel cooled with ice to 0°C and mixed with an Ultra-Turrax with a rotor diameter of 25 mm and a rotation speed of 6000 rpm. The obtained drop size distribution starts at radii of 300 nm and stops at radii of 2000 nm. For Brownian diffusion to outweigh gravitational effects of the droplets to obtain a stable emulsion, the droplet radius must be smaller than 1300 nm [120]. That is the case for the majority of drops as shown in the internship report of Qiwei Li [120]. The drop size distribution changes slightly within one day. Therefore, we repeat the third step of the emulsion preparation in the morning before we start our experiments, to keep the drop size distribution the same between different experiments.

4.3.3 Planar setup

Since phenomena such as buckling and winkling are shape dependent, we decided to perform experiments with different interface geometries. The first interface geometry is a planar interface in a circular Petri dish of 111 mm diameter as shown in Fig. 4.6. We fill the Petri dish with the catalyst-in-PEG emulsion until it has a depth of 5 mm. Then we let the silicone blend flow over a paper onto the catalyst-in-PEG emulsion surface until it has approximately also a depth of 5 mm and pull out slowly the paper afterwards. This allows to maintain the flat interface. The reaction starts as soon as the two liquids are in

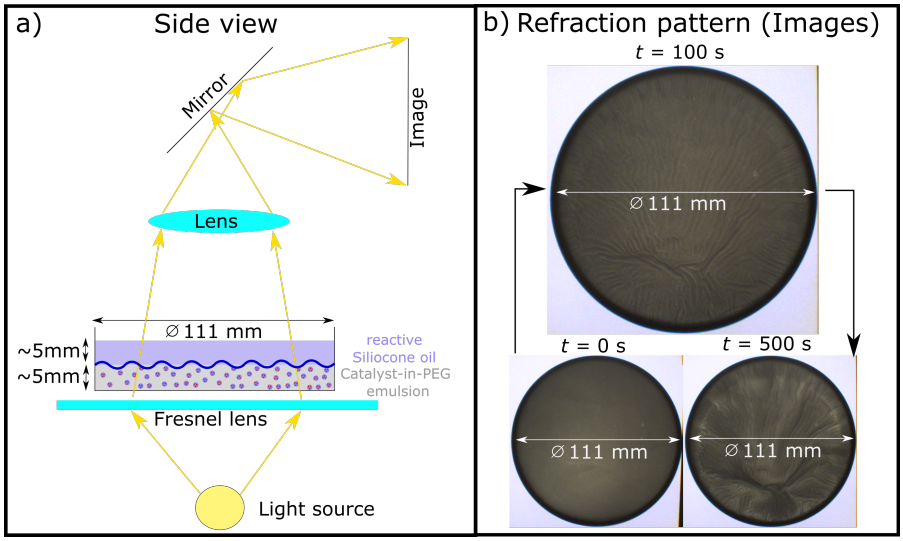

Figure 4.6: a) Scheme of the planar setup, with a light source below a Petri dish filled with the catalyst-in-PEG emulsion as a first layer and the reactive silicone oil as a second layer, separated by an already solidified skin. The skin shows a periodic deformation after a given time, at which the light beams are transmitted, reflected and refracted. The transmitted and refracted light when through a Fresnel lens, the Petri dish, a second lens and is finally projected on a white wall by a mirror. b) the refraction patterns obtained with the camera from the transmitted and refracted light.

contact. We make all 10 s an image of the projected refraction pattern via an overhead projector, as sketched in Fig. 4.6a. At the beginning of the reaction, the interface is a flat disk and the light is reflected or transmitted homogeneously. Due to the polymerisation at the interface, the interface starts to deform. The light rays are now not only reflected and transmitted, they are also refracted, which leads to intensity patterns emphasised by the overhead projector. The deformations increase with advancing reaction time as shown by the photographs in Fig. 4.6b.

4.3.4 Pendant droploon setup

We use the same setup as in the Chapter 3, shown in Fig. 3.6a. This allows us to analyse two identical droploons at the same time, one hanging and one sitting. The droploon phase is the catalyst-in-PEG emulsion and the continous phase the reactive silicone blend.

Before we start the experiment, we measure the interfacial tension γ between the emulsion and the reactive silicone oil. Since the chemical reaction at the interface due to the diffusion of the catalyst changes the effective interfacial tension, we consider only the first seconds after the drop creation, during which the tension stays constant. We obtain an interfacial tension, independent of S, of 11 ± 0.5 mN/m, which is the same as in the literature [2]. Gravity can be neglected in our measurements, due to the small drop size and the small density difference between the PEG and Silicone as discussed in Section 3.3.2.4. However, it is necessary for measuring the interfacial tension with pendant drop tensiometry. Therefore, we measure the interfacial tension with larger drops and thus larger bond numbers, than the ones used for the skin growth measurements.

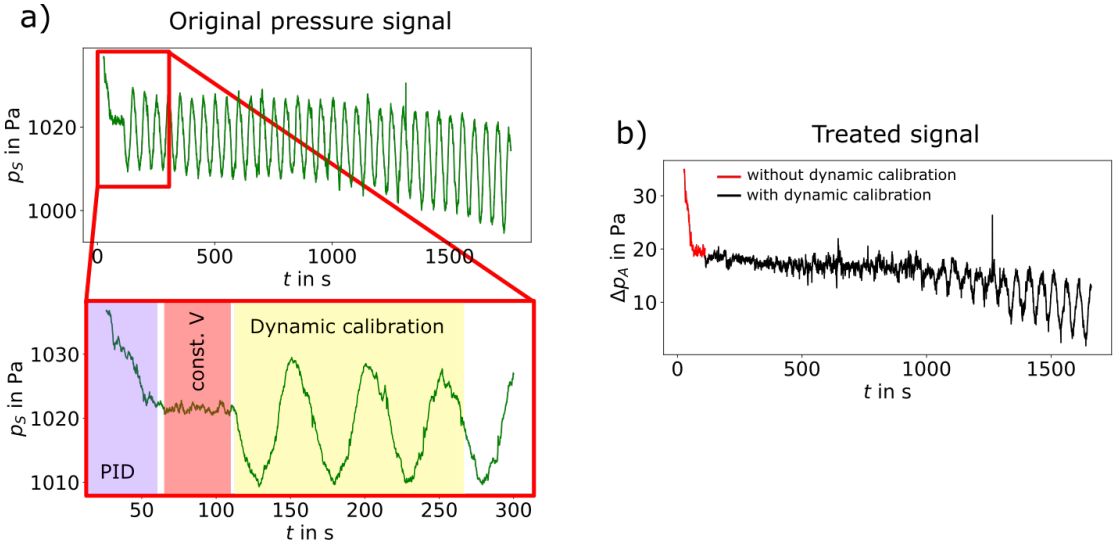

Figure 4.7: a) An example of a raw pressure signal $p_S(t)$. In the zoom, the different steps of the experiment are illustrated: First, the control with a PID to obtain the initial volume. Second, a small time period at which the volume is constant and not controlled for the static calibration. Third, the volume oscillates around the initial volume for the dynamic calibration. b) The pressure difference at the apex $\Delta p_A(t)$ obtained with the static and dynamic calibration.

An example of a pressure measurement with the different steps for a typical interfacial dilational rheology experiment is shown in Fig. 4.7. At the first step (Fig. 4.7a purple zone), we define an initial drop volume V_0 of 3 μl for the hanging and sitting drop. Then, we control the drop volume for 50 s with a PID (Proportional Integral Differential control), which uses the drop profile of the cameras as input and the piston position of the syringes as output. Then we stop the control by the PID. It gives almost spherical drops, where gravity plays a negligible rule. In the second step, the static calibration is carried out as described in Section 3.3.2 (Fig. 4.7a red zone). As discussed above, the chemical reaction at the interface changes the effective interfacial tension with time. A quasi-static inflation and deflation as in Section 3.3.2 is therefore not possible before γ_{eff} changes. Therefore, we take the measured data only over a small time period (Fig. 4.7a the red zone), at the beginning of the measurements, when the interface is still liquid and the interfacial tension 11 mN/m. From this static pressure calibration we obtain K_{sta}, which is the same constant as in Section 3.3.2. The time period, where the interfacial tensions remains constant, depends on the used silicone blend (S) and the two volume fractions Φ_{cat} and Φ_{d}. It goes from 1 s to 300 s. During this time period all volume controls are switched off, since the smallest movement of the syringe piston would affect the pressure measurement. Afterwards the dynamic calibration described in Section 4.3.6.1 (yellow zone in Fig. 4.7a) takes place. Then we start to characterise the skin (Section 4.3.6).

4.3.5 Optical skin thickness measurements

Due to a small changes of the refraction or attenuation index of the polymerized skin in comparison to the liquid reactive silicone oil, the skin becomes visible for some S as shown in Fig. 4.8. The reason is not yet fully clear to us, but it seem correlated with the pressure of mechanical constraints. In this case the skin thickness δ was measured at

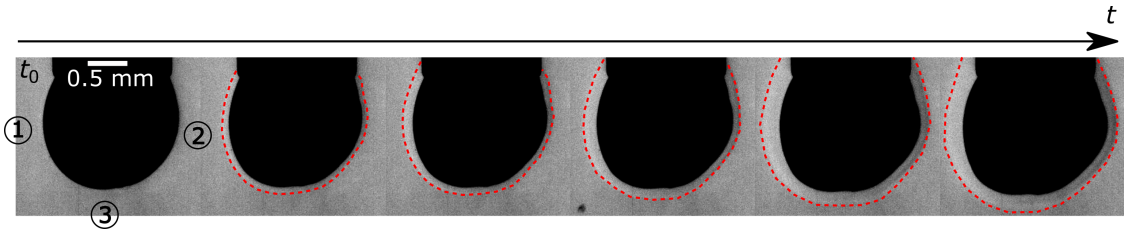

Figure 4.8: Evolution of a drop of catalyst-in-PEG emulsion in the reactive siliocne blend. The contrast was increased to observe the skin and to measure the skin thickness δ as a function of time at position 1, 2 and 3, indicated in the first figure. The skin boundary is shown by the red dashed line.

different positions of the pendant drop using ImagJ. This measurement is not very precise due to the small difference in the refraction or attenuation index between the solid and liquid silicone and that the skin thickness can rarely be measured perpendicular to the solid liquid interface, as the drops buckle or otherwise deform as shown in Fig. 4.8. But it allows us to obtain an approximate evolution of the skin thickness δ as a function of time.

4.3.6 Interfacial dilational rheology between two viscous fluids

After the catalyst-in-PEG emulsion drop is in place in the reactive silicone blend, as described in Section 4.3.4, we start with the dilational interfacial shear rheology to obtain the rheological skin properties as a function of time. Therefore, we oscillate sinusoidally the volume V of the drop

$$V(t) = V_0 + \Delta V \sin \frac{2\pi t}{T}, \tag{4.6}$$

with ΔV the amplitude of the oscillations and T the oscillation period. The pressure and all geometrical parameters of the drop, such as the drop volume V, the drop surface area A and the apex radius R_A were measured as a function of time t with a sampling rate of 5 per s.

We aim to determine the rheological properties of the interface with an elastic skin by relating the measured pressure to the measured deformation of the drop. As seen in Fig.s 3.6a and 4.9, the pressure sensor is not located on the interface. In Section 3.3.2 we showed how the measured pressure can be related to the pressure drop at the apex for a static measurement. Here, the dynamic effects (viscosity and inertia effects) of the dispersed phase are too large to be neglected for the selected oscillation periods, amplitudes, liquids and setup. For smaller amplitudes the pressure changes are to small to be measured correctly. For larger periods times the skin growth is to fast to capture all important features. We therefore established the measurement conditions, which have as little flow resistance as possible. We identified the following conditions as the best compromise: $\Delta V = 0.4\,\mu$l and $T = 50$ s. These were used in all investigations, stated otherwise. Nevertheless, important dynamic pressure effects remain and need to be separated from the effects of the skin in a dynamic calibration discussed in Section 4.3.6.1.

4.3.6.1 Dynamic calibration

Fig. 4.9a shows a scheme with the tube system (connecting the syringe, drop and pressure sensor), the emulsion in the tube system, the vessel filled with silicone oil and all important physical quantities, such as the liquid velocity $v(\xi,t)$, the different pressures p and different vertical coordinate z in the setup. The Bernoulli equation

$$\frac{\rho v(\xi,t)^2}{2} + gz(\xi)\rho + p(\xi,t) + \int_{\xi_0}^{\xi} C(v(\xi,t),\xi)d\xi = const(t), \tag{4.7}$$

relates the different quantities at the different points with each other along the streamline at the position coordinate ξ (red in Fig. 4.9a). The first term in Equ. (4.7) is the dynamic pressure, the second the hydrostatic pressure, the third the pressure and the forth the pressure lost due to viscous forces. $C(v,\xi)$ is the local system resistance due to viscous forces. ξ_0 is at the syringe if the syringe is pushing and at the apex if the syringe is withdrawing, since ξ is define in a manner that it always increases in the direction of flow. First, we estimate the influence of the dynamic pressure at the height $z = z_1$ in Fig. 4.9a. At the apex and the sensor, the dynamic pressure is negligible, since the apex and the syringe piston is moving only a few microns up and down during one period (Fig 4.9a). The flow rate is the derivative of Equ. (4.6) with respect to t

$$\frac{dV}{dt} = \frac{2\pi\Delta V}{T}\cos\left(\frac{2\pi t}{T}\right). \tag{4.8}$$

Since the flow rate is constant across the tube cross section, we obtain for the maximal velocity at the height $z = z_1$ in Fig. 4.9a during the oscillation period

$$v_{1;\max} = \frac{2\pi\Delta V}{T\pi R_{\text{tube}}^2}, \tag{4.9}$$

for $R_{\text{tube}} \approx 1$ mm, $T = 50$ s and $\Delta V = 0.4$ μl the estimated dynamic pressure from inertia contributions is therefore

$$\frac{v_{1;\max}^2 \rho_{\text{PEG}}}{2} \approx 10^{-6}\text{Pa} \tag{4.10}$$

for the density ρ_{PEG} from Table. 4.1. The characteristic overall pressure is a few Pa. Consequently, it can be neglected. But it is therefore important to have a large connection between the pressure sensor and the tube between the syringe and the needle with the drop, keeping $v_{1;\max}$ small. Therefore, all dynamic pressure corrections are of viscous nature.

We are interested in the pressure difference across the interface with a skin at the apex $\Delta p_A = p_{Ai} - p_{Ao}$ and how the pressure is related to the measured pressure difference $p_S = p_1 - p_\infty$ between the environmental pressure p_∞ and the pressure in the sensor p_1 (Fig. 4.9a). The outer pressures p_{Ao} and p_∞ are not influenced by the flow in the tube system. We can therefore use the same procedure as in Section 3.3.2 to relate them with each other. The inner pressures p_{Ai} and p_1 are related with each other via Equ. (4.7). We obtain

$$\Delta p_A^{\pm}(t) = p_S^{\pm}(t) - K_{\text{sta}}^{\pm} - K_{\text{dyn}}^{\pm}(t) \pm gh^{\pm}(\rho_{\text{PEG}} - \rho_{\text{cat}}), \tag{4.11}$$

with "$\pm$" the index representing the upper or lower drop respectively and h the vertical distance between the apex and the opening of the needle. The calibration constant K_{sta}

is from Section 3.3.2 and $K_{\mathrm{dyn}}(t)$ is the integral

$$K^{\pm}_{\mathrm{dyn}}(t) = \int_1^{A^{\pm}} C^{\pm}(\xi, v(\xi,t))\mathrm{d}\xi. \tag{4.12}$$

Since the apex position changes slightly during an oscillation, we take the needle opening as a reference height for K_{sta} to be constant, as in Section 3.3.2. $K_{\mathrm{dyn}}(t)$ depends on C, which depends on the tube system and the local velocity $v(\xi,t)$. $v(\xi,t)$ in turn depends on the selected oscillation amplitude ΔV and period time T. For the chosen flow rates the assumption of a laminar flow in the tube system is correct. For one tube system, fluid (catalyst-in-PEG emulsion), ΔV and T, $K_{\mathrm{dyn}}(t)$ remain identical.

Two different methods can be used to obtain K_{dyn}. In both methods the procedure to obtain K_{dyn} follows the general procedure: A drop is created with the PID control (Fig. 4.7a purple zone). H_{sta} is obtained, during a time at which V stayed constant (Fig. 4.7a red zone). The oscillation starts, following Equ. (4.6). The difference between the two methods is, that in one case we used for the continuous phase a non-reactive silicone (standard PDMS) of the same viscosity and in the second case we used a reactive silicone blend for the continuous phase. With the non-reactive silicone the drop interface stays liquid and the effective interfacial tension constant. $\Delta p_A(t)$ can then be measured with help of the apex radius and the Young-Laplace law. We obtain

$$K^{\pm}_{\mathrm{dyn}}(\Delta V, T, t) = \int_1^{A^{\pm}} C^{\pm}(\xi,t)d\xi = p^{\pm}_{\mathrm{S}}(t) - K^{\pm}_{\mathrm{sta}} - \Delta p^{\pm}_{A}(t) \pm g h^{\pm}(\rho_{\mathrm{PEG}} - \rho_{\mathrm{cat}}). \tag{4.13}$$

An example of $K_{\mathrm{dyn}}(t)$ for $T = 50$ s and $\Delta V = 0.4\,\mu$L is shown in Fig. 4.9b. In the case of a calibration with non-reactive silicone oil, $K_{\mathrm{dyn}}(t)$ is obtained from the periodic averaged value of at least 10 periods. In Fig. 4.9b, $K_{\mathrm{dyn}}(t)$ shows two sharp peaks when the volume becomes minimal or maximal. These peaks are setup-dependent and appear when the syringe pistons change their direction of movement. We have problems to interpret them. We suspect that it has something to do with the motor of the syringe pump or the structure of the syringes, but we cannot say for sure. Since they are very reproducible and at the largest and smallest deformation of the drop, they do not influence our evaluations.

The second method with the reactive silicone follows the same logic and assumes, that for the first oscillation periods the interface stayed liquid with a constant interfacial tension. The first periods are used in this case to obtain K_{dyn}.

The advantages of the method with the non-reactive silicone are:

- The interfacial tension stays constant during all measurements,
- oscillations can be repeated to increase accuracy.

The advantages of the method with the reactive silicone are:

- It is very efficient, since all calibrations and measurements are made in the same experiments. This makes changes in T and ΔV easy.
- Exactly the same configuration of the setup is used for the measurements with silicone skin and for the calibrations. That increases the accuracy of the measurements.

It is preferred to use the calibration with reactive silicone, but if the reaction is to fast the calibration with non-reactive silicone must be used.

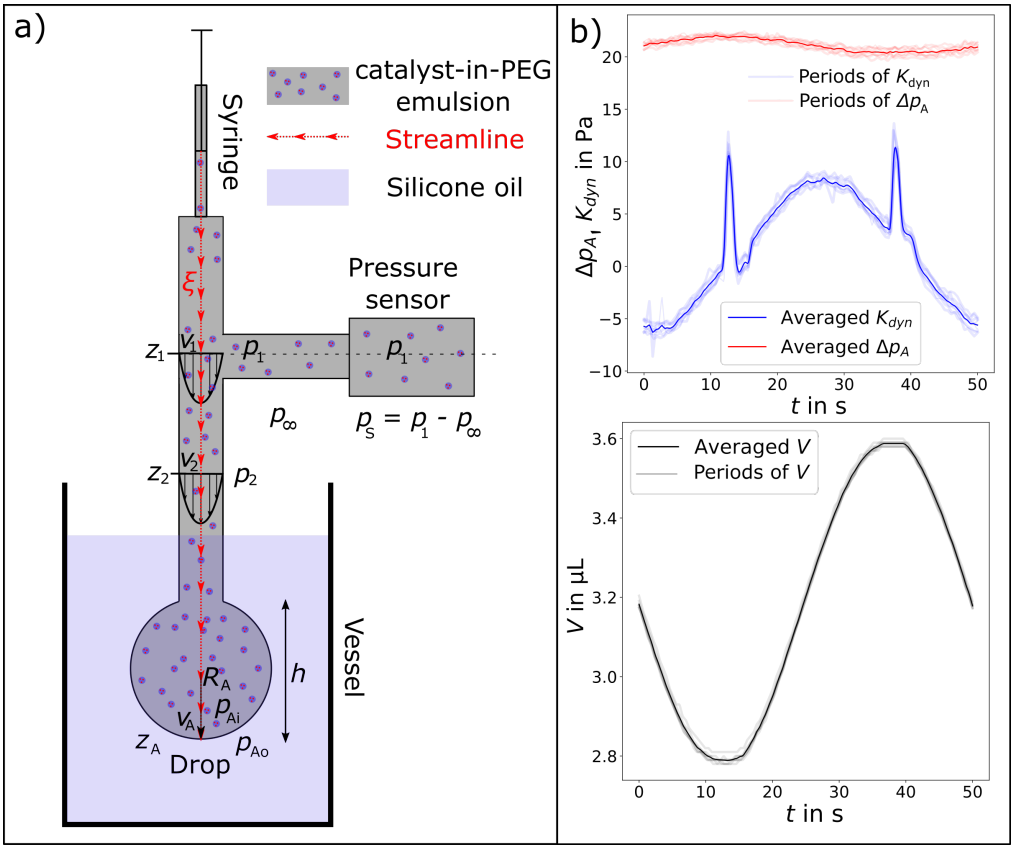

Figure 4.9: a) Scheme of the dynamic pressure measurement of the pendant droploon setup. The important physical quantities are the vertical z coordinate, the local flow velocity v, the local pressures p, the apex radius R_A, one streamline in red with the coordinate ξ. b) Top: $K_\mathrm{dyn}(t)$ plotted for one period with $T = 50$ s and the corresponding Young-Laplace pressure at the apex Δp_A measured with the pressure sensor after correction. Bottom: the corresponding volume. The gray lines are the measured data at several periods, the solid black line the periodic averaged values.

4.3.6.2 General stress decomposition (GSD)

In order to determine the skin properties, the pressure drop $\Delta p_\mathrm{A}(t)$ between the PEG phase and the liquid silicone phase separated by the solid silicone skin, obtained with the procedure explained in Sections 4.3.4 and 4.3.6.1, is treated with a method called General Stress Decomposition (GSD) [116, 37], whose underlying concepts are introduced in this section. We assume an isotropic, homogeneous skin and deformation. As discussed in Section 4.3.4, we work only at very small Bo, which allows us to neglect gravity. But even if gravity is neglected, the skin deformation is disturbed by the fixed boundary on the needle which creates inhomogeneous deformation close to the needle due to the clamping of the skin to the needle [32]. Through the work of G. Ginot *et al.* [32], we choose the volume of the drop in relation to the diameter of the needle so that we can approximate the deformations as homogeneous deformation. That is equivalent to a approximation of the droploon shapes with a spherical deflation and inflation. Therefore, we can define the

homogeneous global and local strain as

$$\lambda_A(t) = \frac{A(t)}{A_0}, \tag{4.14}$$

with $A(t)$ the interfacial area at time t and A_0 initial interfacial area in the reference state. The effective tension γ_{eff} introduced in Section 1.2.4 and Fig. 1.8 is therefore

$$\gamma_{\text{eff}} = \frac{\Delta p_A}{2R_A}. \tag{4.15}$$

The effective interfacial tension γ_{eff} should be determined at the apex, because in contrast to fluid interfaces, the interfacial tension is generally not isotropic. However, in the case where the two principal curvatures are equal, γ_{eff} is isotropic for an isotropic material. Because of the axisymmetry of the pendant droploon, this is always the case at the apex. Since we know that the deformation is not perfectly homogeneous (in comparison to what we approximate previously), the investigation at the apex gives more accurate results. Consequently, the following analysis is only correct if the droploon remains axially symmetric. The interfacial stress γ_{eff} can now be linked to the surface strain at the apex λ_A. The GSD assumes a sinusoidal deformation of the type

$$\lambda_A(t) = \lambda_0 + \Delta\lambda_A \sin\left(\frac{2\pi t}{T}\right). \tag{4.16}$$

If we are interested in the mechanical properties of the skin around the reference state, we deform the drop around the reference state with $\lambda_0 = 1$. In the work by S. Pivard *et al.* [36] and A. Groot *et al.* [37] the surface area (and therefore via Equ. (4.14) also λ_A) was controlled with a PID to obtain a deformation as described in Equ. (4.16). For a liquid/liquid system like the one we used, this is not possible, as every intervention by the PID controller changes the flow conditions in the tube system and thus the dynamic pressure calibration $K_{\text{dyn}}(t)$ (Section 4.3.6.1). S. Pivard and A. Groot worked with bubbles, which gives negligible K_{dyn} due to the small viscosity of the gas compared to a liquid. We avoid this problem by directly in passing the volume change. For this purpose, the speed of the syringe piston moved in form of a sin-wave, so that we obtain a sinusoidal change in volume as described in Equ. (4.6). Now, it has to be shown that this leads to a sinusoidal deformation as in Equ. (4.16).

Aproximating the shapes of the droploons with spherical caps during the whole process of deformation, we show that even with very large amplitudes ΔV in Equ. (4.6) and different needle radii R, the difference of $A(t)$ (and with Equ. (4.14), also $\lambda_A(t)$) to a sine function remains negligible. Therefore, we calculate the volume for a spherical cap as shown in Fig. 4.10a with

$$V = \frac{1}{6}\pi h(R^2 + h^2). \tag{4.17}$$

with the needle radius R and the spherical cap height h, represented in Fig. 4.10b. The interfacial area of the same cap is

$$A = \pi(R^2 + h^2). \tag{4.18}$$

We obtain $h(t)$ with Equ.s (4.6) and (4.17) for a given R and V_0, which gives us $A(t)$ with Equ. (4.18). Afterwards we can compare $A(t)$ with a sinus function with

$$\Delta_{\text{sin}} = \frac{A(t) - A_m}{\max(A(t) - A_m)} - \sin(\omega t), \tag{4.19}$$

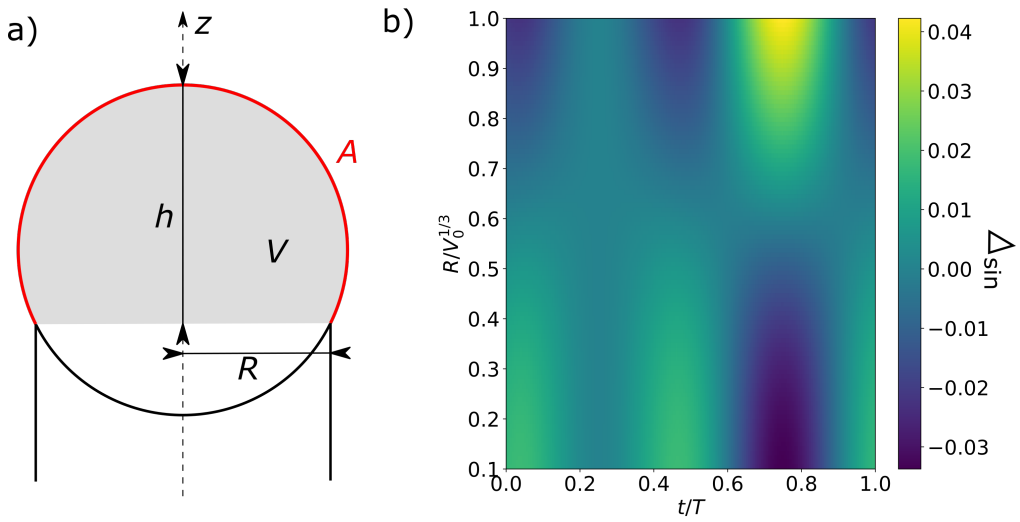

Figure 4.10: b) Scheme of a spherical cap truncated by a needle with the cap volume V, the cap interfacial area A, the needle radius R and the cap height h. b) $\Delta_{\sin}$ (defined in Equ. (4.19)) plotted for different normalized needle radii $R/V_0^{1/3}$ and normalised time t/T, where T is the oscillation period.

with A_m the averaged interfacial area for one period. Fig. 4.10b plots $\Delta_{\sin}$ for $\Delta V = 0.2V_0$ for different normalised needle radii $R/V_0^{1/3}$. If $\Delta_{\sin} = 0$ the deformation is perfectly sinusoidal. Even for very small or very large $R/V_0^{1/3}$ the surface area dependence in time stays almost sinusoidal (Fig. 4.10b). In our experiments we worked at $R/V_0^{1/3} \approx 0.6$, where $\Delta_{\sin}$ is always below 0.0005. The uncertainty due to this $\Delta_{\sin}$ is far below what we can achieve with the volume control of our setup.

We showed that for our chosen system with the applied deformations the assumptions

- sinusoidal deformations $\lambda_A(t)$ at the apex,
- the same $K_{\text{dyn}}(t)$ for different oscillation periods,

are correct if

- the droploon keeps a spherical shape and the influences due to gravity (small Bo) and clamping at the frame [32] are small,
- the volume $V(t)$ changes sinusoidally and $\Delta_{\sin}$ is small (Fig. 4.10),
- the droploon stays axisymmetric (no buckling or other non axisymmetric deformations).

Consequently, we can use GSD to analyse our measurements.

To perform the GSD we apply the procedure explained in the publication of W. Yu *et al.* [116] for the case of bulk rheology. First, the signal is divided into individual periods of length T. Afterwards the individual periods are represented in a Fourier series

$$\gamma_{\text{eff}}(t) = \sum_{k=0}^{\infty} q_k \sin(k\omega t + \phi_k), \tag{4.20}$$

with $\omega = 2\pi/T$ the angular velocity of the volume oscillation, and q_k and ϕ_k the amplitudes and phase shifts of the k-st order, respectively. With the Chebyshev polynomials [116] the signal is represented as

$$\frac{\gamma_{\text{eff}}(x,y)}{\lambda_0} = \sum_{k=0}^{\infty} b_{2k+1}x^{2k+1} + \sum_{k=0}^{\infty} a_{2k+1}y^{2k+1} + xy\sum_{k=0}^{\infty} c_{2k}y^{2k} + \sum_{k=0}^{\infty} d_{2k}y^{2k}, \tag{4.21}$$

with $x(t) = \sin(\omega t)$ and $y(t) = \cos(\omega t)$ and a_{2k+1}, b_{2k+1}, c_{2k}, and d_{2k} constants. The different stresses are defined with

$$\tau_1 = \sum_{k=0}^{\infty} b_{2k+1}x^{2k+1}, \tag{4.22}$$

$$\tau_2 = \sum_{k=0}^{\infty} a_{2k+1}y^{2k+1}, \tag{4.23}$$

$$\tau_3 = xy\sum_{k=0}^{\infty} c_{2k}y^{2k}, \tag{4.24}$$

$$\tau_4 = \sum_{k=0}^{\infty} d_{2k}y^{2k}. \tag{4.25}$$

The advantage of the division into the different τ's is that they can be assigned to specific phenomena. τ_1 is the purely elastic component, since the stress is in phase with the deformation. τ_2 is the purely viscous component, since the stress is in phase with $\mathrm{d}\lambda(\mathrm{t})/\mathrm{dt}$. τ_3 and τ_4 couple viscous and elastic components [116, 37, 36], such as plastic deformations etc. Their precise interpretations is still lacking.

The linear elastic and viscous dilatational two-dimensional modulis K'_{2D} and K''_{2D} are given by [116, 37, 36]

$$K'_{2D} = \frac{2}{T\lambda_0}\int_{-T/2}^{T/2} \sin(\omega t)\tau_1(t)dt, \tag{4.26}$$

$$K''_{2D} = \frac{2}{T\lambda_0}\int_{-T/2}^{T/2} \cos(\omega t)\tau_2(t)dt. \tag{4.27}$$

In our experiments the τ's are obtained for each oscillation period. Therefore, we split the total signal $\gamma_{\text{eff}}(t)$ in the individual periods as for Equ. (4.20). Afterwards we define for every period

$$s_1 = \gamma_{\text{eff}}(t), \tag{4.28}$$

$$s_2 = \gamma_{\text{eff}}(-t), \tag{4.29}$$

$$s_3 = \gamma_{\text{eff}}(T/2 - t), \tag{4.30}$$

$$s_4 = \gamma_{\text{eff}}(T/2 + t). \tag{4.31}$$

The τ's are obtained by simple subtraction and addition of s_1, s_2, s_3 and s_4 as

$$\tau_1 = \frac{1}{4}\left(s_1 - s_2 + s_3 - s_4\right), \tag{4.32}$$

$$\tau_2 = \frac{1}{4}\left(s_1 + s_2 - s_3 - s_4\right), \tag{4.33}$$

$$\tau_3 = \frac{1}{4}\left(s_1 - s_2 - s_3 + s_4\right), \tag{4.34}$$

$$\tau_4 = \frac{1}{4}\left(s_1 + s_2 + s_3 + s_4\right), \tag{4.35}$$

by exploiting different symmetries of the stresses from Equ. (4.21) [116].

4.4 Results and discussion

First, we compare the measured skin thickness $\delta(t)$ with a modelled skin thickness with a finite volume method in spherical coordinates in Section 4.4.1. Afterwards we give an overview of all measurements of the planar (Section 4.4.2) and the drop setup (Section 4.4.3) described in Sections 4.3.3 and 4.3.4. At the end we relate the measured skin thickness and the measured mechanical properties of the skin with the observed shape instabilities in the two setups in Section 4.4.4.

4.4.1 Skin growth modelling

The skin thickness $\delta(t)$ is an important parameter to characterise the mechanical properties of the silicone skin and as well the droploon. We could optically measure δ as a function of the reaction time in some cases (Section 4.3.5), due to a small change in the refractive index of the solidified silicone in comparison to the liquid silicone. Fig. 4.11 shows all measured $\delta(t)$ for different S and Φ_d. In the measured time interval, all measurements fall on the same empirical power law

$$\delta(t) = C_\delta t^{n_\delta}, \tag{4.36}$$

regardless of S and Φ_d. Fitting all data points in Fig. 4.11 to Equ. (4.36) gives an exponent of $n_\delta = 0.44$. A very similar exponent was found by G. Ginot *et al.* using X-ray tomography and electron microscopy [3]. It is surprising, that in the experiments C_δ seems to be independent of S and Φ_d. The skin thickness $\delta(t)$ could not be measured for $\Phi_\mathrm{cat} = 0.1$ and $\Phi_\mathrm{d} = 0.003$. Probably because it was too thin in the considered time period. To obtain a better understanding of the skin formation process, we model with a continuum mechanical approach the diffusion of the droplets with catalyst in the emulsion, the diffusion of the catalyst in the silicone phase and the solidification of the silicone with help of the empirical law from Equ. (4.5).

The modelled volume is a sphere with radius R_max, divided into two regions, an inner sphere with radius R_d in the centre of the modelled volume and the rest of the modelled volume, as sketched in Fig. 4.12. The inner sphere represents the catalyst-in-PEG emulsion drop. The second region is the silicone blend, separated from the drop by the emulsion-silicone interface. First, we use the definition of Φ_d and Φ_cat from Equ.s (4.3) and (4.4) respectively and extend it to the continuum mechanical approach with

$$\Phi_\mathrm{d}(r,t) = \frac{\mathrm{d}V_\mathrm{droplet}(r,t)}{\mathrm{d}V_\mathrm{emulsion}}, \tag{4.37}$$

and

$$\Phi_\mathrm{cat}(r,t) = \frac{\mathrm{d}V_\mathrm{cat}(r,t)}{\mathrm{d}V_\mathrm{silicone}}. \tag{4.38}$$

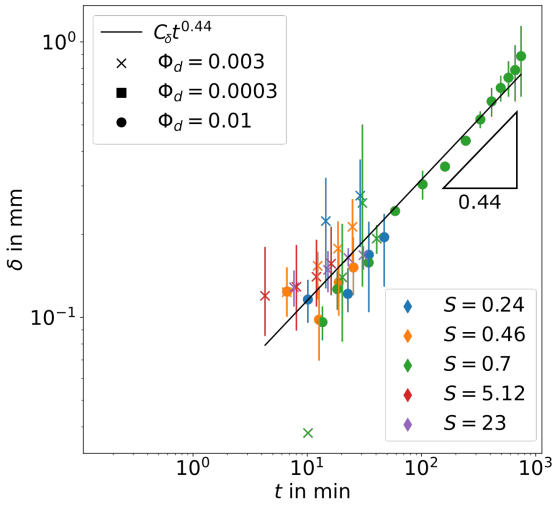

Figure 4.11: The optically measured skin thickness δ for different S and different Φ_d is plotted against the time of reaction t.

r is the radial coordinate of a spherical coordinate system, $\mathrm{d}V_\mathrm{droplet}(r,t)$ is the local amount of droplets in the local volume of emulsion $\mathrm{d}V_\mathrm{emulsion}$ and $\mathrm{d}V_\mathrm{cat}(r,t)$ is the local amount of catalyst in the local volume of silicone $\mathrm{d}V_\mathrm{silicone}$.

The diffusive flux of the catalyst droplets in the emulsion drop and the catalyst itself in the reactive silicone blend is modelled with Fick's first law of diffusion [123]

$$J = -D\frac{\mathrm{d}\Phi}{\mathrm{d}r}, \tag{4.39}$$

with J the flux and D the diffusion coefficient. The diffusion coefficient is determined by the Stokes-Einstein equation [124]

$$D = \frac{k_B T}{6\pi r_H \nu}, \tag{4.40}$$

with k_B the Boltzmann constant, T the temperature, r_H the hydrodynamic radius of the diffusive object and ν the dynamic viscosity of the surrounding liquid (PEG or silicone oil). The hydrodynamic radius of the droplets in the emulsion (inner region in Fig. 4.12) was determined with 200 nm$< r_d <$ 2000 nm in Section 4.3.2. This droplet size is small enough to consider thermal motion as the main mechanism of propagation and that gravitational creaming can be neglected. We can then determine the diffusion coefficient of the droplets as $10^{-15}\,\mathrm{m}^2/\mathrm{s} < D_d < 6 * 10^{-15}\,\mathrm{m}^2/\mathrm{s}$ with Equ. (4.40). In the silicone phase, the molecule complex with the catalyst (Fig. 4.3d) itself diffuses. Its hydrodynamic radius r_cat was estimated by calculating an approximated size of the molecule complex with the three vinyl-terminated PDMS polymers (Fig. 4.3). If we assume that all bonds have and angle of 180°, the complex is 6 nm long. We therefore use 3 nm as an upper limit for r_cat. This gives $8 * 10^{-13}\,\mathrm{m}^2/\mathrm{s} < D_\mathrm{cat}$.

If the droplets come into contact with the interface between the emulsion and the silicone blend at $r = R_d$, they release the catalyst and disappear. Consequently it is

$$\Phi_\mathrm{d}(r = R_d) = 0, \tag{4.41}$$

and

$$J_{\mathrm{cat}}(r = R_d) = J_{\mathrm{d}}(r = R_d)\Phi_{\mathrm{cat}}(\Phi_{\mathrm{d}}), \tag{4.42}$$

as shown in Fig. 4.12a. $\Phi_{\mathrm{cat}}(\Phi_{\mathrm{d}})$ is the catalyst concentration in the emulsion droplets. The modelled volume is a closed system. No material enters or exists. Consequently, the catalyst flow at $r = R_{\max}$ is

$$J_{\mathrm{cat}}(r = R_{\max}) = 0. \tag{4.43}$$

We assume an initially homogeneous distribution of droplets in the emulsion

$$\Phi_{\mathrm{d}}(0 < r < R_d, t = 0) = \Phi_{\mathrm{d};0}, \tag{4.44}$$

and no catalyst in the silicone blend

$$\Phi_{\mathrm{cat}}(R_d < r < R_{\max}, t = 0) = 0. \tag{4.45}$$

The condition of solidification is

$$\int_0^t \frac{\mathrm{dt}}{t_g(\Phi_{\mathrm{cat}}(t))} > 1, \tag{4.46}$$

with $t_g(\Phi_{\mathrm{cat}}, S)$ being the gelation time given by Equ. (4.5). The equations are solved with a one dimensional finite volume method with a lab-made python code. The radius of the PEG drop was set to $R_d = 500\,\mu$m and the radius of the modelled volume to $R_{\max} = 20R_d$. The radii R_d and $R_{\max}$ are chosen so that they have no influence on the diffusion process in the time span of the experiment (maximally a few hours). Fig. 4.12b shows the $\Phi_{\mathrm{cat}}(r)$ profiles for different times. Since the diffusion of the droplets is much slower than the diffusion of the catalyst, the concentration in the PEG drop stays almost constant. Only close to the interface we observe a decrease in concentration due to the strong gradient in Φ_{d}. In the silicone phase the catalyst concentration Φ_{cat} stays very small, below 10^{-4}, which is in our interest, since we want a rather slow solidification to have enough time to measure the mechanical properties of the skin with the GSD. Fig. 4.12c compares $\delta(t)$ for different radial step sizes Δr of the finite volume method by holding the parameters D, Δt, $\Phi_{\mathrm{d}}(t = 0\,\mathrm{s})$ and S constant. With decreasing Δr the skin growth starts earlier. With advancing time the different profiles $\delta(t)$ converge towards the same prediction. The chosen $\Delta r = 2.5\ \mu$m is a compromise between calculation time and precision. The chosen time step $\Delta t = 0.05$ s is the largest time step before the simulation becomes unstable for the chosen Δr and diffusion coefficients.

Fig. 4.12d compares the influence of different r_{d} and r_{cat} on the diffusion process, since the droplet radius r_{d} is not uniform and $r_{\mathrm{cat}} = 3$ nm only an upper bound. The best fitting radii for an experiment with $S = 0.7$ and $\Phi_{\mathrm{d}}(t = 0\,\mathrm{s}) = 0.01$ are $r_{\mathrm{d}} = 300$ nm and $r_{\mathrm{cat}} = 0.3$ nm. Both are of the same order of magnitude. The diffusion of the catalyst droplets is controlled by the smallest droplet size. $r_{\mathrm{d}} = 300$ nm is therefore reasonable. The difference between the estimated upper limit and the obtained best fitting radius of r_{cat} is rather large.

In Fig. 4.13 we exploit systematically the parameter space of the diffusion process with the chosen Δr, Δt, r_{d} and r_{cat}: Fig. 4.13a varies Φ_{d}, Fig. 4.13b varies S, Fig. 4.13c varies Φ_{cat} in the emulsion droplets and Fig. 4.11 shows all measured experimental data. As expected the simulation shows an increase in skin growth velocity for an increase in Φ_{d}, Φ_{cat} and S. We expect an increase in skin growth velocity for an increasing S, since

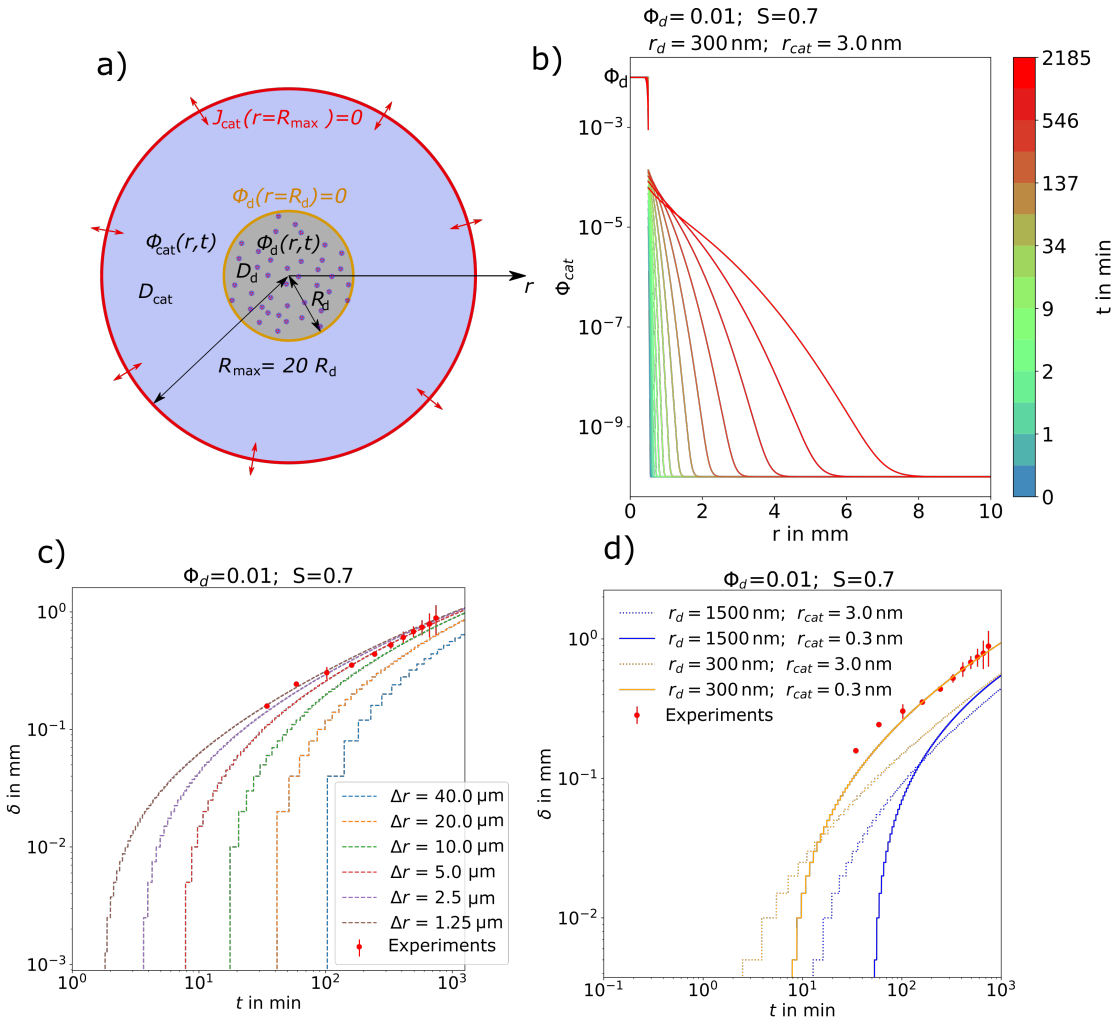

Figure 4.12: a) A scheme of a catalyst-in-PEG emulsion drop in a silicone blend. The index "d" stands for droplets in the emulsion phase. The index "cat" stands for catalyst in the silicone phase. D is the diffusion coefficient (Equ. (4.40)), J the flux (Equ. (4.39)), Φ the concentration. The model size R_{max} is 20 times larger than the emulsion drop radius R. The diffusion in the emulsion drop is bounded by a fixed $\Phi_{\mathrm{d}}(r = R) = 0$. The diffusion of the catalyst in silicone is bounded by a vanishing flux with $J_{\mathrm{cat}}(r = R_{\mathrm{max}}) = 0$. b) An example of the time evolution of the Φ_{cat} profiles. c) A convergence study of the radial step size Δr. d) The skin growth obtained with the diffusion model and the gelation time from Equ. (4.5) in comparison to optically measured skin thicknesses as a function of time for $S = 0.7$. The calculation is repeated for different r_{cat} and r_{d}.

the gelation time t_g decreases with increasing S (Section 4.2.3.1, Fig. 4.5). Independently of S, r_{cat}, r_{d}, Φ_{d} and Φ_{cat}, the simulation give an exponent of the empirical function from Equ. (4.36) of approximately $n_\delta = 0.45$, shown in Fig. 4.13d, e and f. Fig. 4.11 confirms this exponent with optical measurements for different parameters even if these measurements are rather imprecise. As said previously, in the experiments C_δ of Equ. (4.36) was independent from Φ_{d} and S. The simulation predicts in all cases a significant change in C_δ as shown in Fig. 4.13a,b and c. Even if the influence of S seems to play a minor role and therefore probably could not be observed in the experiments (Fig. 4.13b). The experimental behaviour could therefore only partly confirmed.

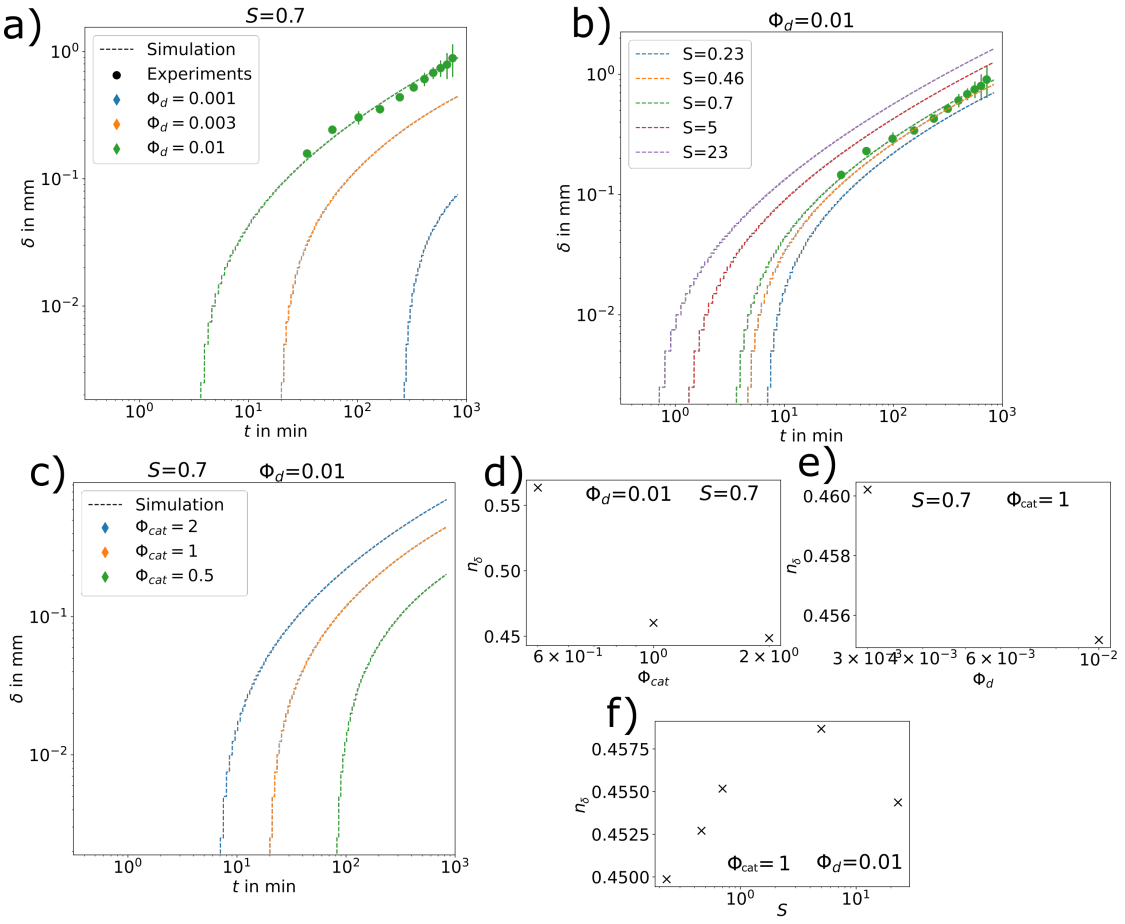

Figure 4.13: a) Simulated skin growth for $r_\mathrm{d} = 300\,\mathrm{nm}$, $r_\mathrm{cat} = 0.3\,\mathrm{nm}$, $S = 0.7$, droplet catalyst concentration $\Phi_\mathrm{cat} = 1$, and different initial Φ_d. b) Simulated skin growth for $r_\mathrm{d} = 300\,\mathrm{nm}$, $r_\mathrm{cat} = 0.3\,\mathrm{nm}$, $\Phi_\mathrm{cat} = 1$, $\Phi_\mathrm{d}(t_0) = 0.01$ and different S. c) Simulated skin growth for $r_\mathrm{d} = 300\,\mathrm{nm}$, $r_\mathrm{cat} = 0.3\,\mathrm{nm}$, $S = 0.7$, $\Phi_\mathrm{d} = 0.01$ and different $\Phi_\mathrm{cat} = 0.01$. d, e, f) The at long times fitted exponent n_δ for the simulated $\delta(t)$ to the empirical Equ. (4.36) for different d) Φ_cat, e) Φ_d and f) S.

Apart from minor inconsistencies, such as

- too fast diffusion (rather to small r_cat in the model)
- little to no influence of skin growth $\delta(t)$ by the parameter Φ_d,

it could be shown that

- Fick's diffusion Equ. (4.39) combined with an empirical law for gelation time Equ. (4.5) are able to model the skin growth $\delta(t)$,
- and to give the exponents n_δ observed in the experiments for Equ. (4.36) (Fig.s 4.11 and 4.13).

Ultimately, the question must be asked at what point the physical processes described in the modelling do not reflect the true events in the experiment. Since diffusion is

understood at this length scale, only the influence of the interface between the emulsion and silicone and the gelation process remains as a cause. For example, the influence of the change in viscosity in the silicone oil on the diffusion process due to the chemical reaction is not considered in the model. In addition, only very few catalyst droplets, which were all localised initially close to the interface, reach the interface (Fig. 4.12b). It is possible that other processes influence the movement of the droplets in this length scale. For example, the deformation of the interface at the moment the droplets reach it. For longer times, we compare mainly with a single dataset. But especially in the first hour the measurements of the skin thickness are relatively inaccurate due to small δ. At longer times, the droploons are often already very deformed, which makes the measurements difficult or even impossible.

4.4.2 Skin formation in planar setup

With the help of Andres Guerrero (M2 intern in the team), we performed the experiments described in Section 4.3.3 for different stoichiometries $S = [0.24; 0.46; 0.7; 5; 23]$, initial droplet concentrations $\Phi_d(t = 0) = [0.003; 0.0003]$ in the catalyst-in-PEG emulsion at $\Phi_{cat} = 1$. We also varied $\Phi_{cat} = [1, 0.1]$ in the droplets of the emulsion while holding $\Phi_d(t = 0) = 0.003$. We distinguish different characteristics for the interfacial evolution, which are represented in Fig 4.14. They show the development of the skin as a function of time for $S = 0.46$ (Fig. 4.14a) and $S = 23$ (Fig. 4.14b) respectively. Similar representations for all experiments can be found in the Appendix in Section A.3 in Fig. A.5 for $\Phi_d = 0.003$, $\Phi_{cat}(\Phi_d) = 1$ and all S, in Fig. A.6 for $\Phi_d = 0.0003$, $\Phi_{cat}(\Phi_d) = 1$ and all S, and in Fig. A.7 for $\Phi_d = 0.003$, $\Phi_{cat}(\Phi_d) = 0.1$ and all S.

The reaction starts at t_0, which is the moment, when the catalyst-in-PEG emulsion comes into contact with the reactive silicone blend. First, wrinkling at the edges of the Petri dish at a time which we will call "t_1" is observed. They are always perpendicular to the edges and stop at a clear boundary, (yellow zone in Fig 4.14). Outside of this zone the surface stays initially flat. We think that the boundary is not circular, because the paper that separates the two liquids before the two liquids come into contact, must be pulled out in one direction. This probably leads to heterogeneity at the edges. This hypothesis is supported by the fact that the yellow zone in Fig 4.14 is always deformed in the direction in which the paper was pulled out. At a later time, which we will call "t_w", the wrinkling also starts in the center of the Petri dish. Within a few seconds, the entire interface is full of wrinkles. Most of the times it is possible to distinguish between the inner (green) and outer (yellow) zones, as the folds have arbitrary directions in the central zone while they are parallel to each other and perpendicular to the edges in the outer zone. In many cases, two characteristic wrinkle wave lengths λ could be observed in the central part. This became particularly clear for $S = 23$ shown in Fig. 4.14b. Since they appear at different times, we define two t_w. Sometimes the wrinkles with the short wave length λ_{short} appear first and sometimes the wrinkles with long wave length λ_{long} appear first. As they overlap, it is difficult to analyse them separately. Their appearance and behavior is probably strongly coupled. If only one wavelength was identifiable, we call it λ_{short}. The wave lengths λ are measured manually using ImageJ by searching for periodic patterns in the refraction image. We tried to analyse the images with a FFT analysis. But the contrasts of the patterns were not height enough. For each time step, at least five such wave lengths were measured and averaged. It was ensured that they

had at least one centimetre distance to the edge in order to neglect boundary influences. All wavelengths λ and initial wrinkling times t_w are summarised in Fig. 4.15. We restrict ourselves to the inner zone for the wavelength measurements, as we expect that the outer zones are influenced by the edges.

At an even later time, called "t_3", at least one fold increases its amplitude considerably compared to the others and forms a large fold. For an example see the blue area at t_3 in Fig 4.14. "t_4" is the moment at which we stop interpreting the skin deformation, as the deformations are too far away from the initial plane interface.

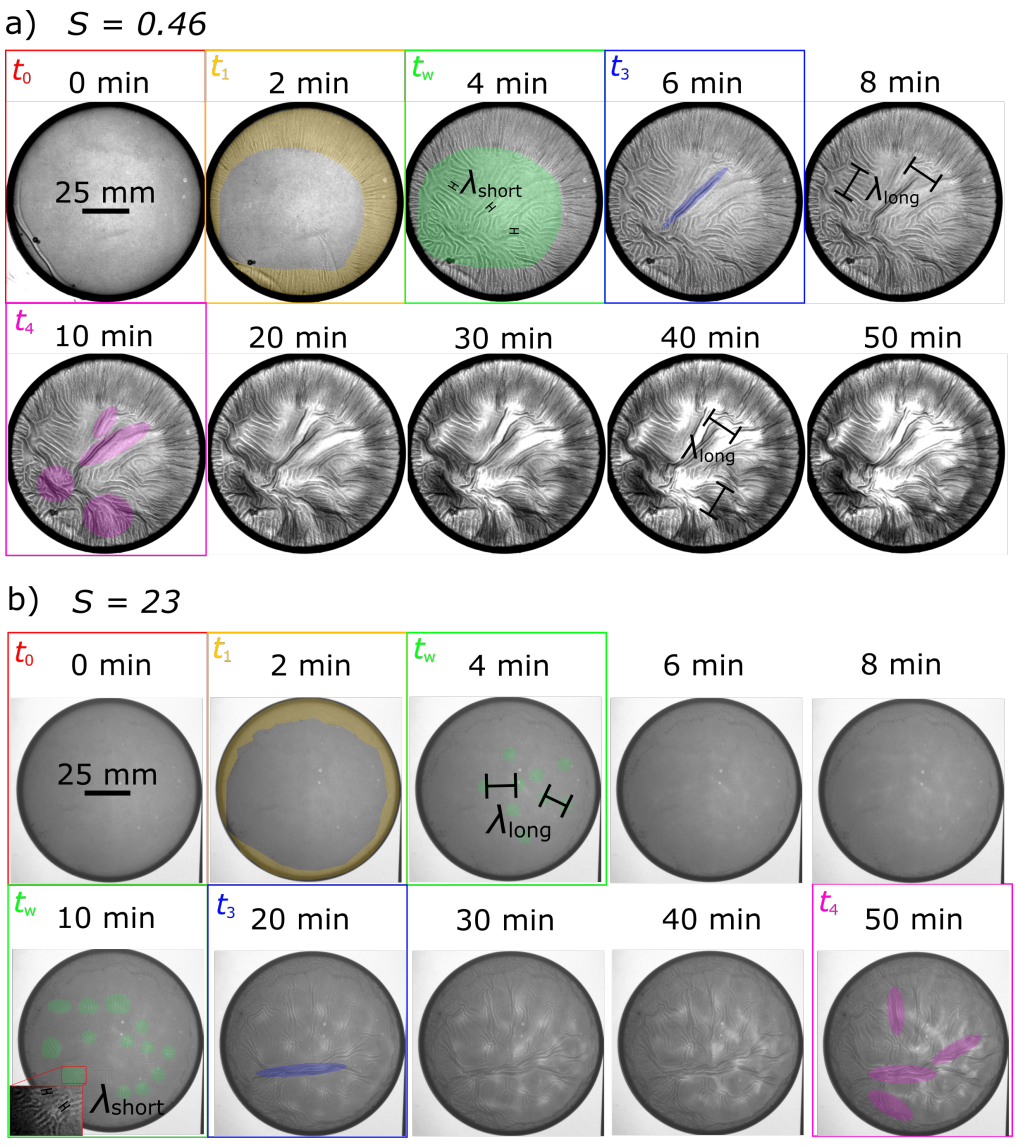

Figure 4.14: The evolution of a skin in a planar setup with a) $S = 0.46$, $\Phi_{cat} = 1$ and $\Phi_d = 0.003$ and b) $S = 23$, $\Phi_{cat} = 1$ and $\Phi_d = 0.003$. Different characteristic times are highlighted: t_0 the time of the reaction start, t_1 the time where the winkling appears the first time close to the border, t_w where the winkling with short wavelength λ_{short} or long λ_{long} appears the first time in the center, t_3 where the large folds appear the first time and t_4 where large deformation with length scales of the Petri dish appear the first time. The contrast was increased for the zoom at minute 10 to increase the visibility of the small wrinkles.

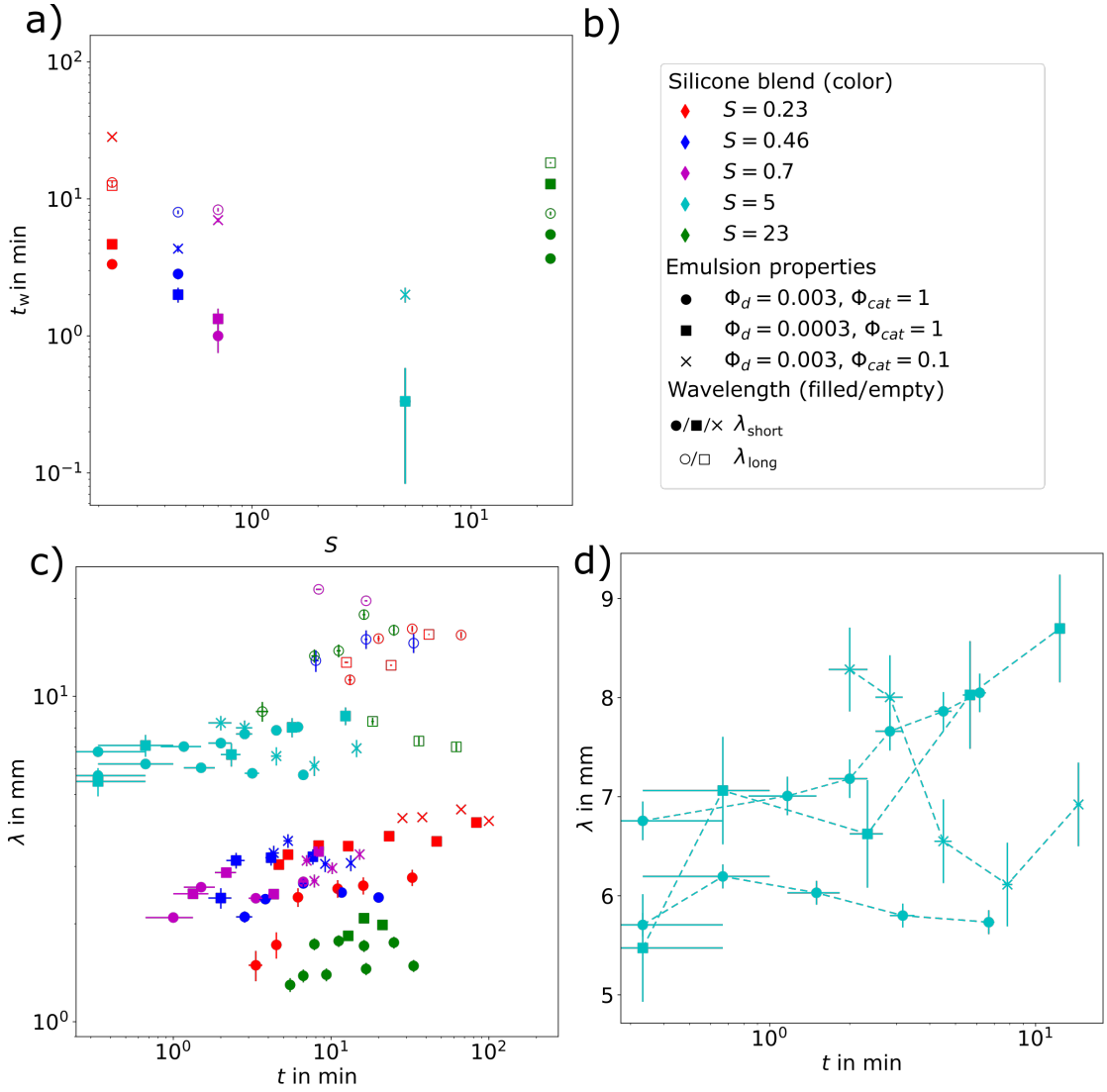

Figure 4.15: a) t_w for different stoichiometries S and emulsion properties for short λ_{short} and long λ_{long} wave length. b) Legend for figure a, c and d. c) The two wrinkle wave length λ_{short} and λ_{long} are plotted as a function in time t. The different colors represent different stoichiometries S, the different symbols different droplet concentrations in the emulsion Φ_d or catalyst concentrations in the droplets Φ_{cat}. Filled symbols represent λ_{short} and empty symbols λ_{long}. d) Zoom into c) for all λ with $S = 5$ with linear y-axis.

We measured the wrinkling onset t_w for the short and long wrinkles whenever possible for the five S, two Φ_d and two Φ_{cat} (Fig. 4.15a). All t_w follow the same behavior. They decrease with increasing S until they reach a minimum and increase again. The minimum is between $0.7 < S < 5$ and could not be measured since the reaction was to fast. For $S = 5$ it was difficult to distinguish between t_1 and t_w since the perpendicular wrinkling starting from the edges occupied almost the full interface (Fig. A.5). Consequently, we used t_1 instead of t_w in Fig. 4.15a. Φ_d has no measurable influence on t_w. In contrast, a smaller Φ_{cat} greatly delays the appearance of the wrinkles (Fig. 4.15a).
By comparing the different measured wrinkle wave lengths λ in Fig. 4.15c and d, we observe that in most cases λ increases slightly with time, reaches a maximum and decreases

in the following. In some cases, λ seems to converge against an upper limit. But the variations in time are in all cases rather small. The zoom on the example of $S = 5$ in Fig. 4.15d demonstrates this behaviour very well. However, it is noticeable that even with the same emulsion properties and the same reactive silicone blend, different behaviours are observed, Fig. 4.15d. Both λ_{short} and λ_{long} have only small differences for the same S and different Φ_d and Φ_{cat}. They are independent of the emulsion properties, only their time of appearance depends on them. $\lambda_{short}(S)$ (solid symbols in Fig. 4.15c) increases with decreasing $t_w(S)$ (Fig. 4.15c). This observation seems similar for λ_{long} (empty symbols in Fig. 4.15c) but is less clear due to the little data.

We can summarise that:

- The wrinkling appears after a characteristic time t_w, which depend on Φ_{cat} and S. It has a minimum between $S = 0.7$ and $S = 5$ (Fig. 4.15a);
- The wrinkle wave length λ_{short} goes through a maximum in S which seems to be the same as the minimum for t_w (Fig. 4.15c)
- A second longer characteristic length or wave length λ_{long} is present in most of the Petri dish experiments (Fig.s 4.14 and 4.15c);
- The amplitude of the wrinkles increases until larger folds appear at t_3. Unfortunately, we could not measure the amplitude in our experiments;
- At a time t_4 the interface lost most of its periodicity and is strongly deformed.

We cannot explain the appearance of the wrinkling with 100% certainty, but we will give some interpretations in Section 4.4.4.

4.4.3 Skin formation on a drop

Firstly, let us take a look at the droploon shapes. Only axisymmetric shapes can be analysed with the GSD introduced in Section 4.3.6.2. Fig. 4.16 shows the evolution in time of pendant catalyst-in-PEG emulsion drops with different S at $\Phi_d = 0.003$ and $\Phi_{cat} = 1$. At the beginning, except for $S = 5$, all shapes are axisymmetric (Fig. 4.16) claimed by direct observation with the two cameras. For $S = 5$ the reaction is to fast to create a spherical drop controlled by interfacial tension before the skin starts to grow. During the creation of the drop through the syringe, a skin is already formed which significantly influences the shape of the droploon as it is deformed by the further increase in droploon volume. At a time, which we will call "t_b", the droploons lose their axisymmetry. Fig. 4.17 shows for different Φ_d, Φ_{cat} and S the time t_b. t_b was measured visually. One observes a similar behavior as for the wrinkling appearance t_w from Section 4.4.2 (Fig. 4.15a):

- The minimum for t_b is in between $S = 1$ and $S = 5$,
- Φ_d has a no measurable influence,
- and Φ_{cat} shifts t_b to significantly higher values.

The non-axisymmetric drop shapes differ significantly between each other. We distinguish different characteristic shapes by direct observations, shown in Fig. 4.18. First, the "axisymmetric spherical" shape, which we are looking for to perform the GSD from Section

4.3.6.2. Second, the "buckled shape", which is typical for spherical droploons under compression and observed in many experiments [125, 126] and well understood also from the theoretical point of view [127, 128]. Third, the "potato shape", at which the interface is not any more homogeneously curved. Locally increased curvatures, which almost appear like edges or corners, are typical of the potato shape. Forth, the "mushroom shape", in which the droploon maintains an overall nearly spherical shape but significantly reduces its curvature, and compensates this by curving around the edge of the needle.

The buckled shape is typical for $S \leq 0.7$. It speaks for isotropic skin properties. The potato shape is typical for $S > 0.7$. We suspect that the reaction is too fast for these stoichiometries (see Fig.s 4.5, 4.11 and 4.13) to form a drop with a complete liquid interface before a skin forms on it. Therefore, the skin is not isotropic from the start, which may explains the non-homogeneous deformations. The mushroom shapes are observed for all S but more often and more pronounced for sitting drops (Fig. 4.18). It becomes clear that small changes such as sitting and hanging or the needle radius have an influence on the later shape, probably due to the influence of gravity. Another factor, which is difficult to control, is the spreading behaviour of the catalyst-in-PEG emulsion in the reactive silicone oil on the needle surface. Often the droplet did not have perfect axisymmetric boundary conditions on the needle.

4.4.3.1 Interfacial rheology of droploons via GSD

Only droploons which keep a spherical shape can be evaluated with a GSD. The mushroom shapes can be evaluated under the condition that the curving around the needle deforms only slightly during the volume oscillation and that the main part of the interface stays spherical and axisymmetric (For example Fig. 4.18b the second sitting droploon from the left). In this case, the lower part of the mushroom shape can be ignored and only the upper spherical part can be analysed under the same conditions as discussed in Section 4.3.6. From Fig.s 4.15a and 4.17 we observe that a lower Φ_{cat} ($\Phi_{\text{cat}} = 0.1$) slows down the skin growth, which allows a better calibration and gives more time for the analysis before the droploon starts to buckle. Some experiments with $\Phi_{\text{cat}} = 1$ and $\Phi_{\text{d}} = 0.0003$ are also suitable. But the emulsion properties are less reproducible (since the amount of catalyst is very small, which has an influence on the mixing procedure and the precision of Φ_{d}) and consequently the GSD experiments as well. Therefore, we chose $\Phi_{\text{cat}} = 0.1$ and $\Phi_{\text{d}} = 0.003$ to analyse the skin with a GSD. Since our final goal is to study the interactions of two droploons, we perform the experiments directly on the double bubble setup of Fig. 3.6a. Consequently, the two initial droploons are almost identical. Their volume oscillation starts at the same time, they have the same emulsions, the same temperatures, the same environmental pressures, the same silicone blend, only one droploon is hanging and the other is sitting. But this has almost no influence on the initial shape, since the Bond number Bo is small. From Fig. 4.18 we know, that even this small influence changes the shape evolution with time. Fig.s 4.19 and 4.20 have both the same structure respectively for the hanging and sitting droploon and show the results of a double droploon GSD for $S = 0.7$, $\Phi_{\text{cat}} = 0.1$ and $\Phi_{\text{d}} = 0.003$ with: in a) the effective interfacial tension of Equ. (4.15), in b) a color time scale for the different volume oscillations together with photographs of the investigated droploons for the different times, in c) τ_1 from Equ. (4.32), in d) τ_2 from Equ. (4.33), in e) τ_3 from Equ. (4.34) and in f) τ_4 from Equ. (4.35). We observe for the hanging and sitting droploon a similarly behavior.

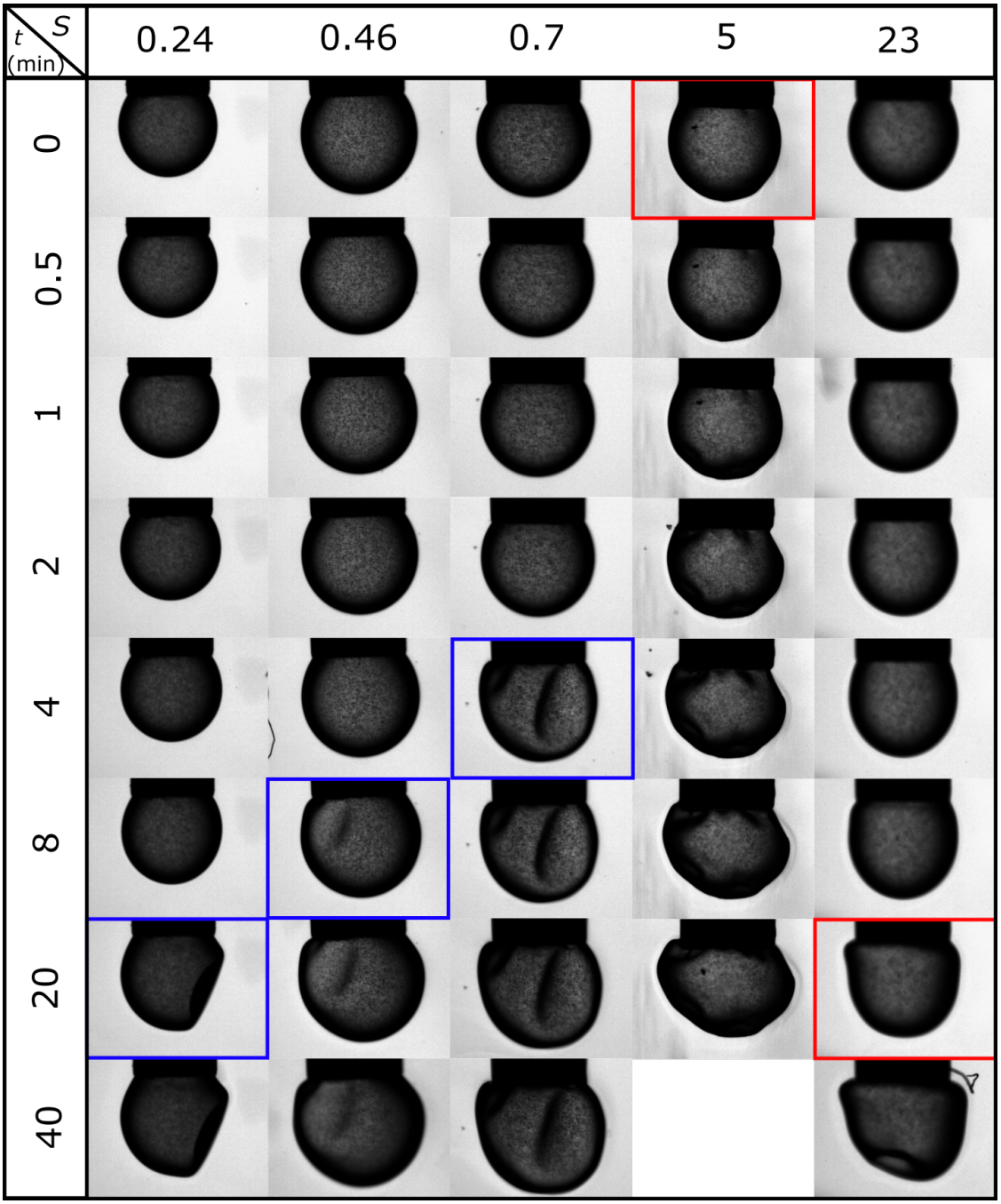

Figure 4.16: The evolution in time of catalyst-in-PEG emulsion drops in a silicone blend with different S and $\Phi_{\mathrm{d}} = 0.003$ and $\Phi_{\mathrm{cat}} = 1$. The first non-axisymmetric shape is highlighted in blue if it buckles and in red if it deformed in another manner.

The influence of λ_A on γ_{eff} increases with time and the mean effective interfacial tension,

$$\gamma_{\mathrm{eff};0} = \frac{1}{T}\int_0^T \gamma_{\mathrm{eff}} \mathrm{d}t, \tag{4.47}$$

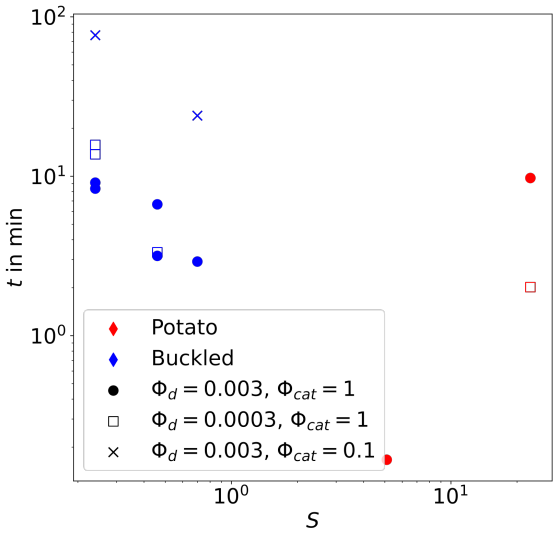

Figure 4.17: The time at which a pendant catalyst-in-PEG emulsion drop in a silicone blend with stoichiometry S under a periodic deformation as described in Section 4.3.6 with $\Delta V = 0.4\,\mu$l and $T = 50$ s looses its axisymmetry due to buckling (in blue) or due to other deformations for example a "potato" shape (in red).

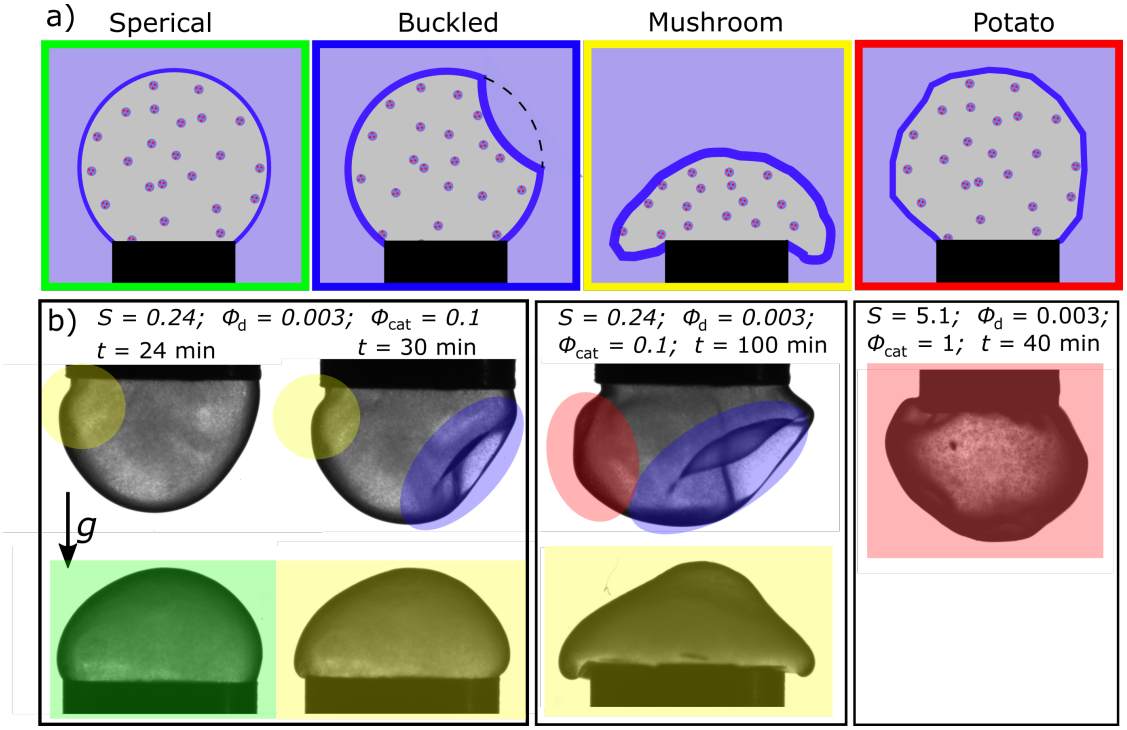

Figure 4.18: a) Four different types of droploon shapes as a scheme and b) examples of experiments showing simultaneously the top and bottom drop: Nearly spherical shapes (green), which are observed at the beginning of each experiment. Buckled shapes (blue), which are observed mostly for $S \leq 0.7$. Potato shapes (red), which are observes mostly for $S > 0.7$. Mushroom shapes (yellow), which are observed mostly for sitting droploons.

decreases with time (Fig.s 4.19a and 4.20a). The functions of τ_2 and τ_3 in Fig.s 4.19 and 4.20d and e are very noisy and have small amplitudes for $t < 23$ min in comparison to τ_1 and τ_4 in Fig.s 4.19 and 4.20c and f. We conclude that τ_1 and τ_4 contain the important information for these measurements and τ_2 and τ_3 have negligible influence on γ_{eff}. In τ_1 we find the influence of λ_A on γ_{eff} and in τ_4 the falling mean effective interfacial tension $\gamma_{\text{eff;0}}$ (Fig.s 4.19 and 4.20c and f).

For reaction times longer than $t > 23$ min, the droploon starts to buckle for the hanging droploon (Fig. 4.19b). This also has an influence on the measured (calculated) γ_{eff} and thus on the different τ_k. However, since the droploon is no longer axisymmetric and the measured surface area is not considering the buckled part correctly, this behaviour can no longer be used to determine the skin properties. We can still try to understand the different components in general terms. First we observe, that γ_{eff} stays constant after the shape is buckled. λ_A at which the shape starts to buckle and reaches the constant γ_{eff} in one period becomes larger with time (Fig. 4.19a). Secondly, the changes in the elastic component τ_1 in time become smaller, since it connects only the maximal and minimal γ_{eff}. Third, we observe an increase in the dependency of τ_3 and τ_4 on λ_A (Fig.s 4.19e and f). They are necessary to compensate the kink of the function γ_{eff} (Fig. 4.19a).

The sitting droploon does not buckle and keeps an axisymmetric shape until the end of investigations. But we observe a slow transition from a spherical shape to a mushroom shape (Fig. 4.18 for the mushroom shape and Fig. 4.20b for the shape evolution). This has an influence on λ_A. The mean curvature of the mushroom head decreases. Consequently, the same volume change results in a smaller area change, which explains the decrease in λ_A in time in Fig. 4.20. Since the shape stays axisymmetric and most of the surface spherical, we can evaluate all volume oscillations with the GSD for the sitting droploon (Fig. 4.20).

In Fig. 4.21, we compare $\gamma_{\text{eff;0}}$ (Fig. 4.21a) and the dilational interfacial elasticity K'_{2D} (Fig. 4.21b) as a function of time for different S and for the hanging and sitting droploon. Since τ_2 is negligible, K''_{2D} is negligible too. The complete results of the GSD as for $S = 0.7$ in Fig.s 4.19 and 4.20 are shown in the Appendix in Section A.4 for the other stoichiometries S. We can recognise the temporal characteristics of the skin growth of the different S, which we know from the Petri dish experiments (t_{w} in Fig. 4.15a) and from the buckle times (t_{b} in Fig. 4.17). $\gamma_{\text{eff;0}}$ decreases earlier and faster while K'_{2D} increases earlier and faster by going closer to the minimum in t_{w} and t_{b} (Fig.s 4.15a and 4.17) at stoichiometries between $S = 0.7$ and $S = 5.1$. The behavior for the sitting and hanging droploon is almost identically for both quantities, $\gamma_{\text{eff;0}}$, K'_{2D}, and all S. The kink at the end of the data for the hanging droploon and $S = 0.7$ is related to the buckling (Fig. 4.19). For the data with $S = 0.24$, we observe a small variation between the hanging and sitting droploon. Also the data for the sitting droploon is more noisy for $\gamma_{\text{eff;0}}$ and K'_{2D}. Looking at the GSD results in Fig.s A.8 and A.9 for $S = 0.24$, one observes, that the hanging droploon is very spherical and the sitting droploon has some small defects at the interface, which ultimately cause buckling. This could explain the difference between the hanging and sitting droploon in $\gamma_{\text{eff;0}}$ and K'_{2D} for $S = 0.24$ in Fig. 4.21.

To compare the measured data with existing theories for buckling and wrinkling [127, 128, 129, 130, 131, 132], we fit $\gamma_{\text{eff;0}}$ and K'_{2D} to the empirical laws

$$\gamma_{\text{eff;0}} = \gamma_{\text{eff;0}}(t = 0) - C_\gamma t^{n_\gamma}, \tag{4.48}$$

with $\gamma_{\text{eff;0}} = 11$ mN/m the interfacial tension between the catalyst-in-PEG emulsion and

the silicone blend and C_γ and n_γ two fitting parameters. We also fit

$$K'_{2D} = C_K t^{n_K}, \tag{4.49}$$

with C_K and n_K two fitting parameters. The obtained values for the different fitting parameters can be found in Table 4.2. The fitted curves are compared in Fig. 4.21a and b with the experimentally obtained values from the GSD. These will be used in Section 4.4.4 for a more in-depth analysis.

S	C_γ in $\frac{mN}{ms^{n_\gamma}}$	n_γ	C_K in $\frac{mN}{ms^{n_K}}$	n_K
0.23	$2.7\cdot 10^{-6}$	1.7	$4.3 \cdot 10^{-12}$	3.5
0.7	$1.6\cdot 10^{-7}$	2.3	$4.7 \cdot 10^{-11}$	3.8

Table 4.2: Empirical parameter for different S for Equ.s (4.48) and (4.49).

We can summarise that

- The droploons stay axisymmetric or even spherical for a time $< t_b$ (Fig. 4.17)
- Different shape types are observed (Fig. 4.18).
- For some emulsions and silicone blends GSD is capable to measure K'_{2D} and $\gamma_{eff;0}$ (Fig. 4.21a and b).
- The time period at which measurements are possible with the GSD are rather small due to the fast decrease of $\gamma_{eff;0}$ leading to buckling phenomena.
- The response of the skin can be considered purely elastic with τ_2 (and hence K''_{2D}) being negligible small in the measured parameter range.
- For all parameters the skin is expanding isotropical within the interface, which causes a shape transition from a spherical shape to buckled, mushroom or potato shape depending on silicone blend and the catalyst-in-PEG emulsion properties.

4.4.4 Interpretations of the skin growth, wrinkling and buckling

We are not able to show what causes the expansion of the skin during growth. For this reason, we limit ourselves here to a hypothesis for an explanation that needs to be proven in future work. Our first observation: In all experiments in which the catalyst was homogeneously distributed in the silicone phase from the beginning, we could not detect any expansion (all bulk experiments of Section 4.1). That was confirmed by a Petri dish experiment, where the silicone blend was premixed with the catalyst. There no wrinkling was observed, even after the total silicone phase was solidified. That let us believe that the expansion of the skin is related to the catalyst gradient or the diffusion of the catalyst in the silicone phase. The gradient in S vertical to the interface due to the diffusion of the droplets in the catalyst-in-PEG emulsion could also have an influence. It can be said with certainty that solidification takes place very quickly near the interface, as there is a high catalyst concentration at the beginning. As the distance to the interface increases, the solidification process slows down. This creates a gradient in the material properties of the skin vertical to the interface. Near the interface, the skin has no time to relax while the reaction takes place. Perhaps the subsequent relaxation of the skin

leads to an expansion. The reaction gradient is important so that the expansion has a favoured direction and does not behave isotropically. We hardly see any differences between the optical properties of the solid and liquid silicone blend, which is why skin thickness measurement is so difficult. Presumably the densities of the two phases are also very similar. An expansion in one direction must therefore be accompanied by a shrinking in another direction. This is only possible in a non-isotropic state, which could explain the different solidification behavior between silicone with an initial homogeneous distribution of the catalyst (isotropic) and silicone where the catalyst diffuses from an interface. The gradient in Φ_{cat}, S or both could causes this non-isotropic state.

Even if we are not able to prove our hypothesis for the expansion of the skin, we can interpret the resulting phenomena as the wrinkling of the skin from Section 4.4.2 and the buckling from Section 4.4.3. Therefore we relate and compares our observations to existing theories for similar problems. In the first part we present a theory explaining the wrinkling, in the second part a theory explaining buckling and in the last part we compare the theories to our measurements.

4.4.4.1 Wrinkling of flat elastic sheets

Wrinkling of elastic sheets on liquid interfaces was observed in different studies [129, 130, 131, 132]. In the work by E. Brau *et al.* [129] and the thesis of E. Jambon-Puillet [130] the wrinkling is causes by uni-axial compression and a density difference between the upper and lower liquid phase. The studies of J. Huang *et al.* [131, 132] investigate a similarly phenomenon, where additionally interfacial tension is significant. In our case, the elastic sheet is the growing skin with thickness $\delta(t)$. Interfacial tension $\gamma_{\text{eff};0}(t=0)$ is of the same order of magnitude as the elastic stresses. We do not compress the interface by reducing the intefacial area. However, the interface is limited by the Petri dish. We hypothesise that by a mechanism unknown to us the skin expands in a direction parallel to the interface, as the interface between the emulsion and the silicone grows continuously once the reaction has started. We also hypothesise that this expansion occurs isotropically within the interface. This assumption is supported by macroscopically isotropic patterns of the folds in the circular Petri dishes for the start of the wrinkling around t_{w} (Fig.s 4.14, A.5, A.6 and A.7). This leads to compressive stresses, as in the studies of F. Brau, E. Jambon-Puillet and J. Huang [129, 130, 131, 132]. In our work, the compression is not uni-axial, it is isotropic. Despite the different stress state, we want to compare the wave lengths with the theory from F. Brau *et al.* [129]. It considers the total energy consisting of the bending energy of the elastic sheet and the potential energy, due to the density difference $\Delta\rho$ between the upper and lower liquid phase. It then compares the energies of the wrinkled and flat state of the interface. We only show the important quantities here and interpret them directly to match our system and setup. The sheet will winkle when the energy of the winkled state is lower than of the flat state. This leads to a the critical surface pressure given by

$$\gamma_{\text{eff;w}} = 2(B_{\text{w}}\Delta\rho g)^{1/2}, \tag{4.50}$$

with B_{w} the bending modulus of the skin at the moment when the interface starts to wrinkle, corresponding to t_{w} (Fig. 4.15a). The predicted wave length at t_{w} for a uni-axial state of stress is

$$\lambda_{\text{w}} = 2\pi \left(\frac{B_{\text{w}}}{\Delta\rho g}\right)^{1/4}. \tag{4.51}$$

The bending modulus of an isotropic thin sheet is given by

$$B = \frac{E\delta^3}{12(1-\nu^2)}, \tag{4.52}$$

with E the Young's modulus and ν the Poisson ratio in bulk. Since we are measuring only two-dimensional material properties with the GSD in Section 4.4.3.1, we rewrite the bending modulus with $K'_{2\mathrm{D}} = E\delta$ and use the assumption of an incompressible rubber-like skin with $\nu = 0.5$

$$B = \frac{K'_{2\mathrm{D}}\delta^2}{9}. \tag{4.53}$$

Inserting B in Equ.s (4.50) and (4.51) gives

$$\gamma_{\mathrm{eff;w}}(\delta) = \frac{2}{3}(K'_{2\mathrm{D;w}}\delta^2\Delta\rho g)^{1/2}, \tag{4.54}$$

and

$$\lambda_{\mathrm{w}}(\delta) = 2\pi\left(\frac{K'_{2\mathrm{D;w}}\delta^2}{9\Delta\rho g}\right)^{1/4}. \tag{4.55}$$

4.4.4.2 Buckling of droploons

The transition from spherical to buckled droploons, observed for some of our experiments (Fig.s 4.18 and 4.17), has been investigated theoretically [127] and experimentally [133]. The buckled and spherical states can also be compared energetically. The transition takes place at a critical buckling pressure, which depends on the properties of the skin, with thickness and Young's modulus again being of particular importance. The critical buckling pressure at which the transition from spherical to buckled shapes occurs, is [127]

$$\Delta p_b = E\left(\frac{\delta}{R_d}\right)^2 \tag{4.56}$$

with R_d the spherical droploon radius. The pressure Δp_b can be used to measure the Youngs modulus E if δ and R_d is known [133]. Inserting Equ. (4.56) in Equ. (4.15) gives the effective interfacial critical buckling tension

$$\gamma_{\mathrm{eff;b}} = -\frac{R_A E}{2}\left(\frac{\delta}{R_A}\right)^2 = -\frac{K'_{2D}\delta}{2R_A} \tag{4.57}$$

with $R_A = R_d$ for the assumption of a spherical shape and K'_{2D} the elastic two-dimensional dilatational modulus from Equ. (4.26).

4.4.4.3 Comparison with experiments

To obtain the critical wrinkling and buckling effective interfacial tension $\gamma_{\mathrm{eff;w}}$ (Equ. (4.54)) and $\gamma_{\mathrm{eff;b}}$ (Equ. (4.57)) all values are direct measurements from the GSD except of δ. Nevertheless, to make a comparison with the measured wavelengths and critical times, $\delta(t)$ is modelled with Equ. (4.36). The empirical Equ. (4.36) is based on experiments with an emulsion of $\Phi_{\mathrm{d}} = 0.003$ or $\Phi_{\mathrm{d}} = 0.0003$ and $\Phi_{\mathrm{cat}} = 1$. However, the GSD results are based on an emulsion with $\Phi_{\mathrm{d}} = 0.003$ and $\Phi_{\mathrm{cat}} = 0.1$. We know from the Petri dish

and pendant drop experiments, that this significantly slows down the skin growth. To compensate for this difference, we correct Equ. (4.36) with the factor C_{cor} and obtain

$$\delta(t) = C_{\mathrm{cor}} C_\delta t^{n_\delta}. \tag{4.58}$$

From Section 4.4.1 we know, that the exponent n_δ in Equ. (4.36) is independent of the emulsion and silicone blend properties. To obtain C_{cor} we compare t_{w} and t_{b} for the two emulsions from Fig.s 4.15a and 4.17 and obtain

$$C_{\mathrm{cor}} = \frac{t_{\mathrm{w/b}(\Phi_{\mathrm{d}}=0.003,\Phi_{\mathrm{cat}}=0.1)}}{t_{\mathrm{w/b}(\Phi_{\mathrm{d}}=0.003,\Phi_{\mathrm{cat}}=1)}} = 8 \pm 1. \tag{4.59}$$

Finally, we obtain $\gamma_{\mathrm{eff;w}}$ from Equ. (4.54) and $\gamma_{\mathrm{eff;b}}$ from Equ. (4.57) with the empirical Equ.s (4.59) for $\delta(t)$ and (4.49) for $K'_{2\mathrm{D}}(t)$. They are plotted against the time in Fig. 4.21c and compared with $\gamma_{\mathrm{eff;0}}$ from Equ. (4.48) for different S. If $\gamma_{\mathrm{eff;w}}$ or $\gamma_{\mathrm{eff;b}}$ and $\gamma_{\mathrm{eff;0}}$ overlap, the system starts to wrinkle or buckle respectively (asterisk in Fig. 4.21c). As long as $\gamma_{\mathrm{eff;0}} > 0$ the flat or spherical shape is always the preferred state. The interfacial tension γ creates a positive offset in $\gamma_{\mathrm{eff;0}}$, which stabilises the flat and spherical state.

$\gamma_{\mathrm{eff;w}}$ is for the full considered time scale very small and mostly below our measurement precision. The crossing between $\gamma_{\mathrm{eff;w}}$ and $\gamma_{\mathrm{eff;0}}$ is small enough to approximate it with $\gamma_{\mathrm{eff;w}} = 0$ mN/m. We obtain the critical wrinkling time t_{w} and the critical wrinkling wave length λ_{w} from the model (Fig. 4.21a and c). We compare the theoretical obtained values with the measured values from Fig. 4.15a and c in Fig. 4.22. Fig. 4.22 is identical to Fig. 4.15 with additionally the theoretical values. The solid lines in Fig. 4.22a are the function $\lambda_{\mathrm{w}}(t_{\mathrm{w}})$ from Equ. (4.55) with the empirical Equ.s (4.49) and (4.59) for two different S. The asterisk in Fig. 4.22 are theoretical critical predictions at which the wrinkled state is the energetically favoured state. We observe in Fig. 4.22b, that the theoretical predicted t_{w} are delayed in comparison to the measured t_{w}, but they follow the same tendency in respect to S. The predicted wave length λ_{short} in Fig. 4.15c tend to be too large, but they are in the right order of magnitude.

$\gamma_{\mathrm{eff;b}}$ and $\gamma_{\mathrm{eff;0}}$ do not intersect with each other in Fig. 4.21c. This is in agreement with the measurements, since the theory does not take into account the periodic volume change, which is necessary for the GSD. If we look at Fig. 4.19, it is also noticeable, that the drop shape has never buckled during a complete period, but only when $\gamma_{\mathrm{eff;0}} \approx 0$. For this early time span, as for $\gamma_{\mathrm{eff;w}}$, $\gamma_{\mathrm{eff;b}}$ is very small and can be approximated with $\gamma_{\mathrm{eff;b}} = 0$ mN/m. It is apparent in Fig. 4.21c that $\gamma_{\mathrm{eff;b}}$ and $\gamma_{\mathrm{eff;0}}$ do not have to intersect and if they do intersect, they do it twice. This behaviour is partially confirmed in the experiments, as not all drop shapes started to buckle, although a very negative $\gamma_{\mathrm{eff;0}}$ was measured in some cases (Fig. 4.21a). The behaviour, that a buckled shape changed back to a spherical shape, was not observed, but can be explained by the fact, that buckling influences skin growth due to the changed shape. We believe that $\gamma_{\mathrm{eff;b}}(t)$ and $\gamma_{\mathrm{eff;0}}(t)$ are very close and therefore small differences between the drops, such as whether they are hanging or sitting, can lead to an intersection between them, which causes buckling.

Fig. 4.21d shows an hypothetical Young's modulus E of the skin with the assumption, that the skin growth as with Equ. (4.59) predicted and the skin is an isotropic material, so that applies $E = K'_{2\mathrm{D}}(t)/\delta(t)$ with $K'_{2\mathrm{D}}(t)$ from Equ. (4.49). For a homogeneous skin that is deformed around its reference state, E should remain constant. This is obviously not the case (Fig. 4.21d). Two possible reasons for that are: the skin is not

homogeneous and the skin is not deformed around its reference state. The second is definitely the case, since $\gamma_{\text{eff};0}$ is decreasing. Non-linear material behaviour could harden the skin, when it is under compression. However, neither of these effects can explain the extremely large or extremely small E in Fig. 4.21d (Attention in both cases it is an extrapolation). We suspect that the skin growth by Equ. (4.59) is not appropriate for the measured time period in the drop shape experiments. Due to the oscillations, the catalyst-in-PEG emulsion silicone blend interface moves by a few μm back and forth, which greatly influences the diffusion of the catalyst and finally the skin growth in this area. Fig. 4.12b shows, that for $t > 15$ min most of the catalyst is only a few μm away from the interface.

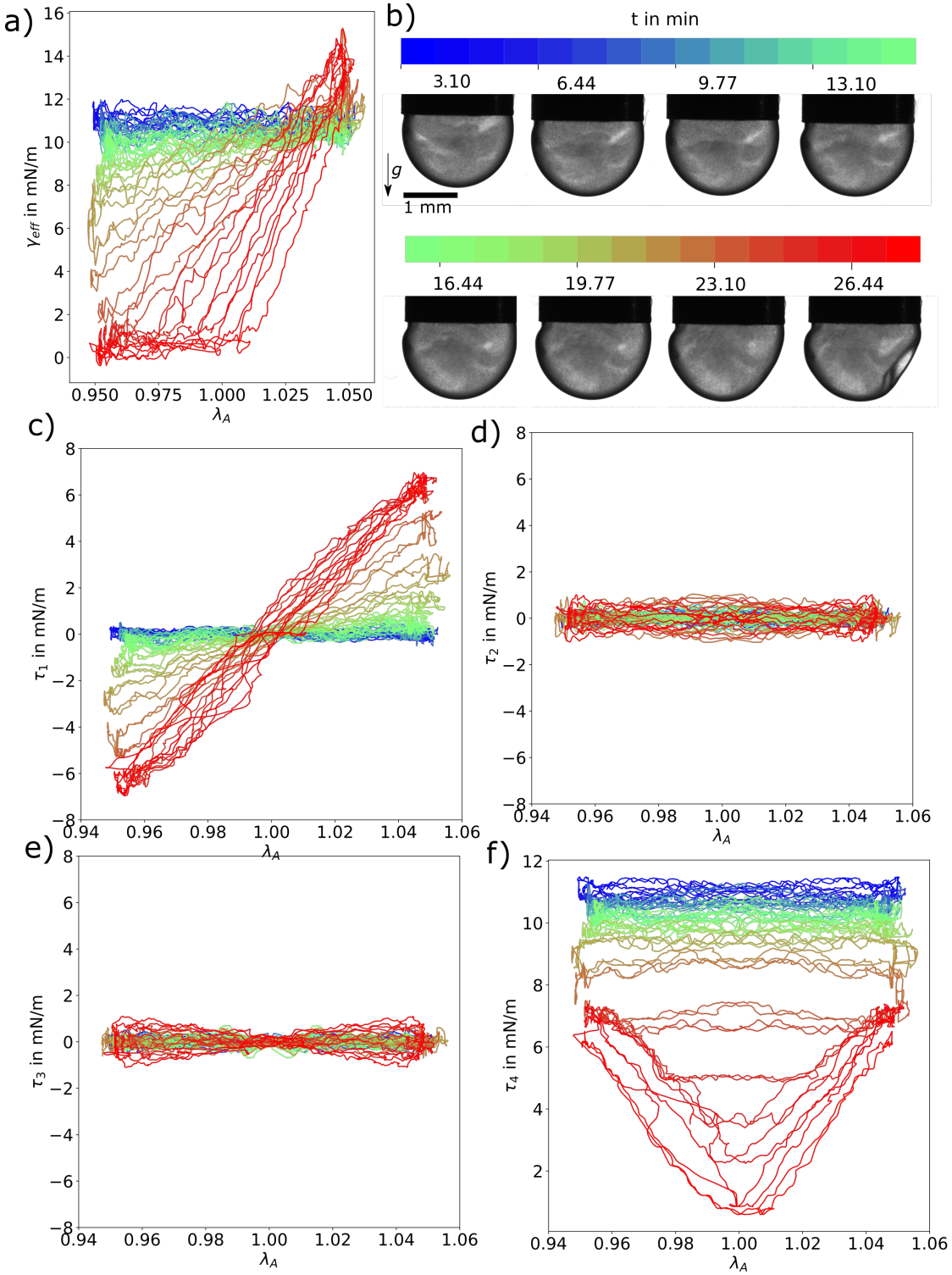

Figure 4.19: Results for dilational interfacial shear rheology (Section 4.3.6.2) for $S = 0.7$, $\Phi_d = 0.003$ and $\Phi_{cat} = 0.1$ of a hanging droploon: a) γ_{eff} from Equ. (4.15), b) Time legend with a series of images of the corresponding droploons, c) τ_1 from Equ. (4.32), d) τ_2 from Equ. (4.33), e) τ_3 from Equ. (4.34) and f) τ_4 from Equ. (4.35).

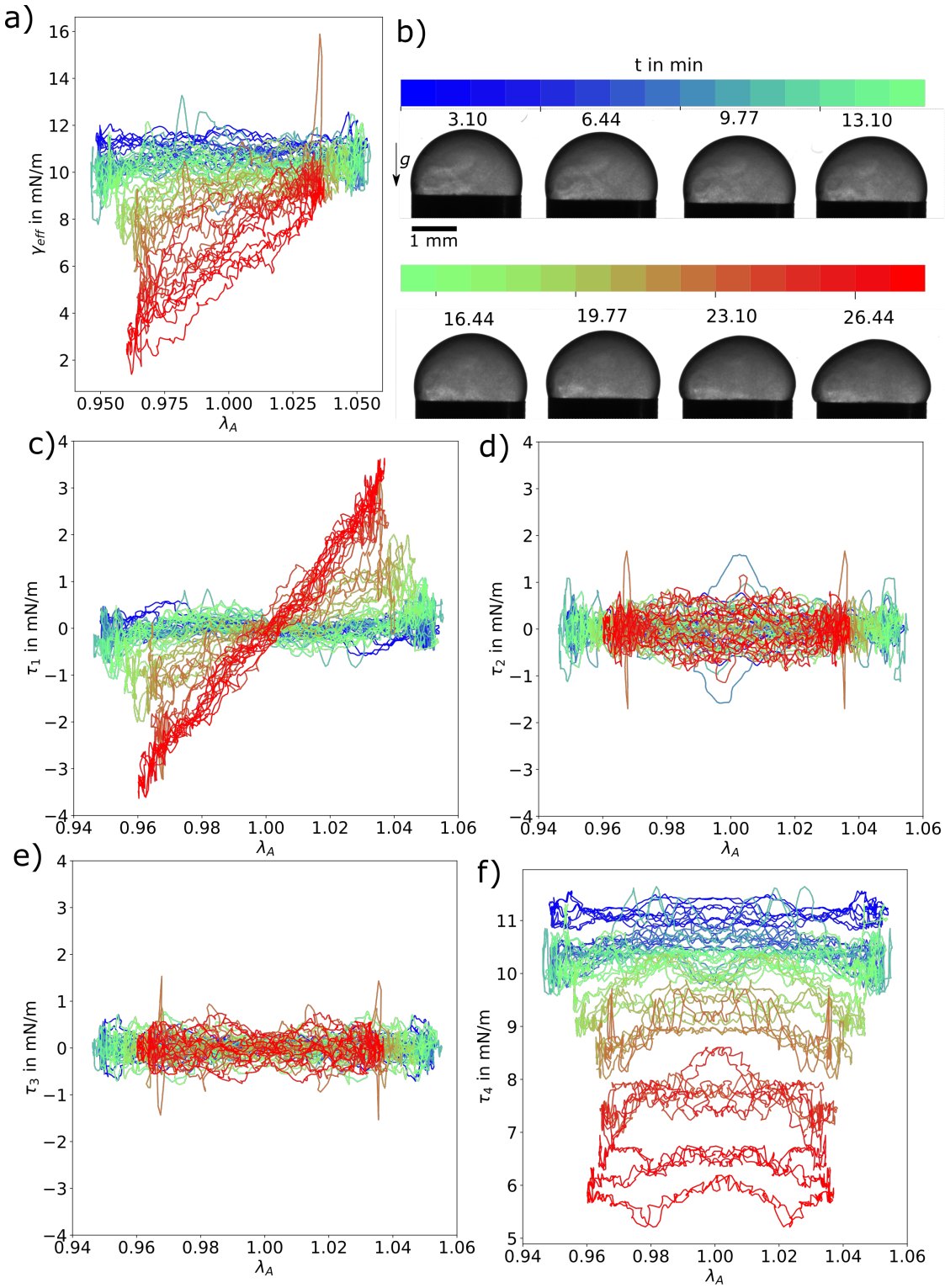

Figure 4.20: Results for dilational interfacial shear rheology (Section 4.3.6.2) for $S = 0.7$, $\Phi_d = 0.003$ and $\Phi_{cat} = 0.1$ of a sitting droploon: a) γ_{eff} from Equ. (4.15), b) Time legend with a series of images of the corresponding droploons, c) τ_1 from Equ. (4.32), d) τ_2 from Equ. (4.33), e) τ_3 from Equ. (4.34) and f) τ_4 from Equ. (4.35).

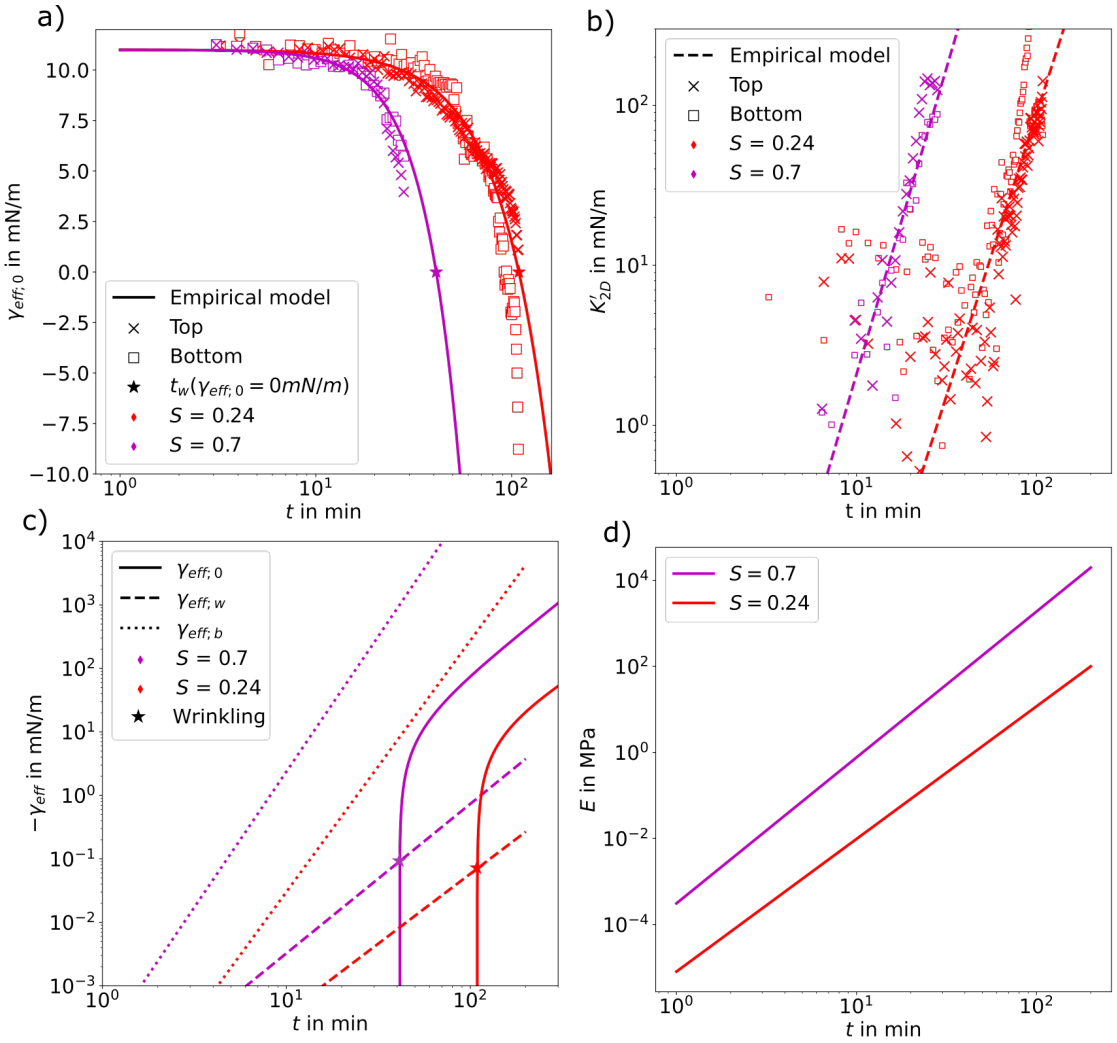

Figure 4.21: a) The measured mean effective tension $\gamma_{\text{eff};0}$ (Equ. (4.47)) in comparison to the fitted empirical laws from Equ. (4.48). b) The measured dilational elastic shear modulus (Equ. (4.26)) as a function in time for different S in comparison to the fitted empirical law from Equ. (4.49). c) The estimated effective buckling tension from Equ. (4.57) and winkling tension from Equ. (4.54) in comparison to the empirical obtained effective tension from Equ. (4.48) for different S. d) The theoretical Young's modulus E of the skin, assuming an isotropic skin and using the empirical laws for the skin thickness $\delta(t)$ (Equ. (4.36)) and the dilational elastic shear modulus (Equ. (4.49)) for different S. All measurements are made with an emulsion with $\Phi_{\text{cat}} = 0.1$ and $\Phi_{\text{d}} = 0.003$.

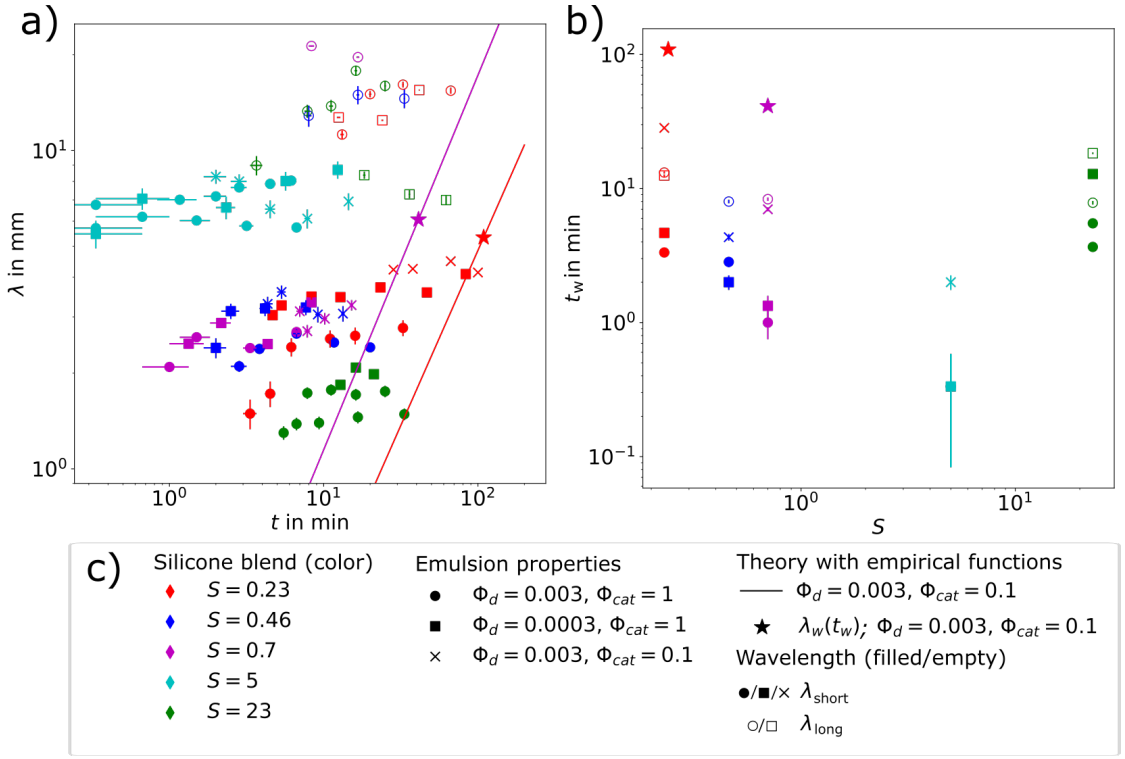

Figure 4.22: The experimental results from Fig. 4.15 are compared to the theory from Section 4.4.4.1 and the empirical laws for $\delta(t)$, $K'_{2D}(t)$ and $\gamma_{eff;0}(t)$. a) The wrinkling wave length λ against the time t, b) the wrinkling time t_w against S and c) the legend.

4.5 Conclusion

The mechanical properties of the catalyst-in-PEG emulsion droploon in reactive silicone oil is complete characterised, if the parameters $\gamma_{\text{eff};0}$, $K'_{2\text{D}}$ and δ are measured independently as a function of time. We showed in Section 4.4.3.1, that for a specific time period and some emulsion and silicone blend properties a measurement of $\gamma_{\text{eff};0}$ and $K'_{2\text{D}}$ as a function of time is possible (Fig. 4.21). For the first time we used the GSD (Section 4.3.6.2) for a liquid/liquid interface with a dynamic calibration. Thin skin growth $\delta(t)$ was modelled numerically and compared to some limited measurements to rather large skin thicknesses of a few hundreds of μm. The problem is that the time periods in which the skin thickness and the mechanical properties can be measured do not overlap.

The mechanical properties were tested on two known instabilities, in Section 4.4.1 on the wrinkling instability of elastic thin sheets on a liquid/liquid interface with a density difference and interfacial tension and in Section 4.4.3 on the buckling instability of droploons. Both instabilities depend on all three parameters $\gamma_{\text{eff};0}$, $K'_{2\text{D}}$ and δ (Fig. 4.21). The agreement between theory and experiments of the two instabilities is not perfect. Only qualitative statements can be made by comparison with the theory. This is probably mainly due to the poor skin thickness measurements and the imperfect model for skin growth especially for small times after the start of catalyst diffusion.

The main open question is why the skin expands parallel to the catalyst-in-PEG reactive silicone blend interface, which lowers $\gamma_{\text{eff};0}$ and thus causes the two instabilities. A first approach could be to test the hypothesis from Section 4.4.4 by analysing the structure of the skin as a function of the distance to the interface. However, the difficulty here is that the skin is very thin. It could also be tested whether similar observations can be made for other systems in which a reactant diffuses from an interface.

Furthermore, we demonstrated in Section 4.4.3 that the combination of emulsion and silicone blend properties as $S = 0.7$, $\Phi_{\text{d}} = 0.003$ and $\Phi_{\text{cat}} = 0.1$ could be used to investigate the interactions between two such droploons. Since the mechanical interface properties could be measured and the droploon remains axisymmetric over sufficient long time. The reaction should be stopped at the reaction time at which the desired properties are present. In addition, the measured mechanical properties could be compared more systematically with known other methods, such as in the article of M. Neubauer *et al.* [115], discussed in the introduction in Section 4.1.

Chapter 5

Droploon-droploon interactions

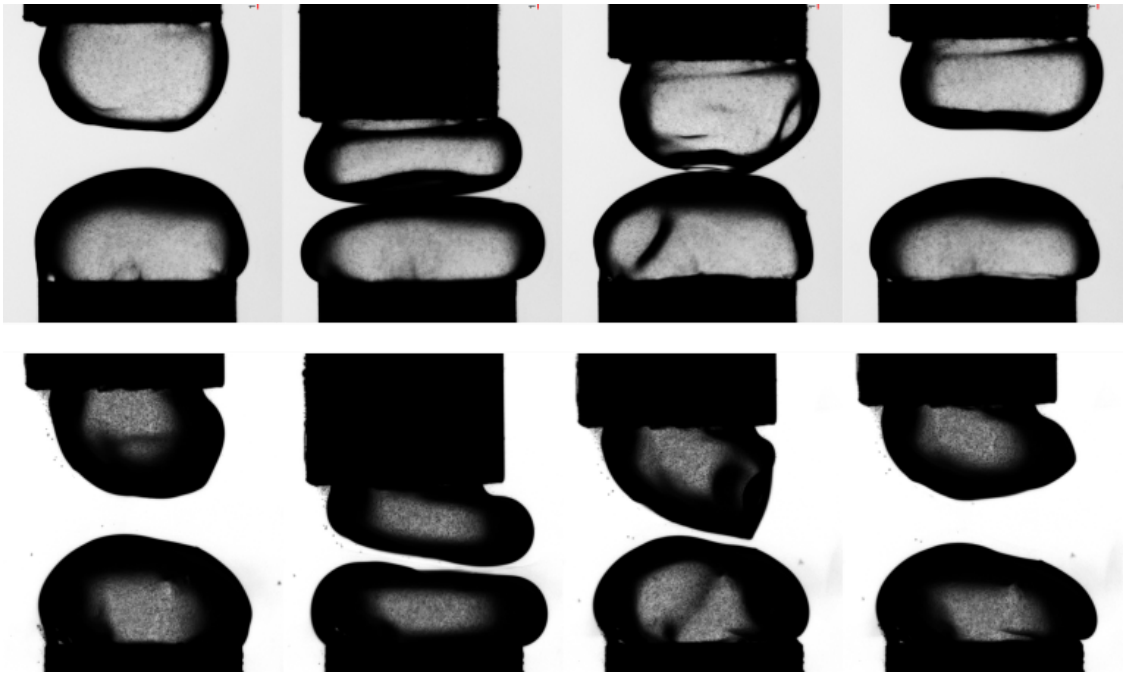

Contents

5.1 Introduction

As discussed in Chapter 4, droploons are used in many different areas. In most cases, the droploons serve as a means of transport (e.g. fragrances or medicines) and as protection against environmental influences. The mechanical properties of the droploons [100, 101, 102, 103] and the interactions between them are therefore of crucial importance for a save transport. But even to produce new materials with controlled mechanical properties, the interactions between the droploons or bubloons must first be understood and measured.

In this chapter we make a proof of concept, that it is possible to measure direct interactions between two very soft droploons with the new double bubble device, which was developed during this thesis and already used in Chapter 3 for the drop-drop interactions and in Chapter 4 for interfacial dilational rheology of silicone droploons. The device is represented in Fig. 3.6 and the droploons in Fig. 5.1b. To our knowledge, a similar experiment has so far only been carried out by A. Giustiniani *et al.* [2]. In this case, however, no pressure measurements were carried out, which is why the results are based only on the shape of the droploons. Other Studies on capsule-capsule interactions are mainly numerical and treat the coupled response of two capsules in a shear flow [134, 135]. Interactions through direct contact between two droploons have been mostly overlooked. Other studies focus more on the macroscopic response of droploon accumulations [136, 112, 2, 3] and do not look in detail at the direct interactions between two droploons. It is therefore important to close this knowledge deficit. In the following only primary results are presented to make a proof of concept. But the full quantitative exploitation have to be done in future work.

5.2 Methods

All results in this chapter are from the same two droploons. They were obtained using the same procedure described in Chapter 4. The catalyst-in-PEG emulsion has the following values: $\Phi_d = 0.0003$ and $\Phi_{cat} = 1$ and the silicone blend has $S = 10$. The volume of the droploons was kept constant during skin growth. Consequently, the mechanical

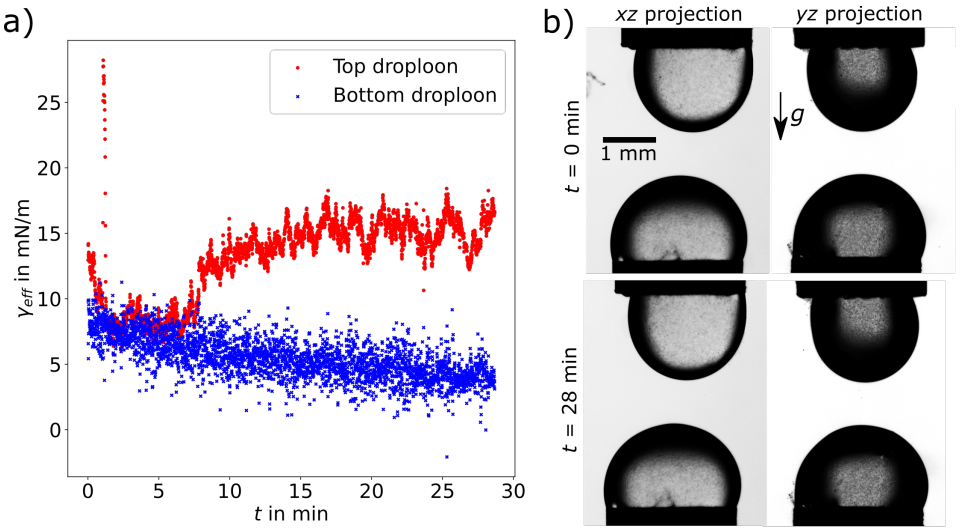

Figure 5.1: a) The effective interfacial tension γ_{eff} as a function in time for the bottom and top droploon obtained with Equ. (4.15). b) The projection of the droploons in the xz and yz plane at the beginning and the end of the droploon creation.

properties of the skin are not known as no GSD was performed (see Chapter 4). The pressure difference across the skin was determined using the same procedure as described in Chapters 3 and 4. The effetive interfacial tension γ_{eff} was obtained with Equ. (4.15) and plotted for the top and bottom droploon in Fig. 5.1a. It is used to validate the correctness of all pressure calibrations and the formation of the skin at the interface. Fig. 5.1b shows the xz and yz projection of the two droploons at the beginning and end of this measurement. The shapes of both droploons remain almost unchanged in time. The effective interfacial tension of the bottom droploon in Fig. 5.1a behaves as expected. At the beginning, γ_{eff} is around 11 mN/m and decreases progressively due to the skin formation. γ_{eff} of the top droploon shows irregular fluctuations, which cannot be explained by shape instabilities, as the shape is not changing. We therefore suspect that this is an artefact and that there are air entrapments in the tube system between the droploon and the pressure sensor, which disturb the measurement. Therefore, only the pressure at the bottom droploon is shown in Section 5.3 for measurements, where high accuracy is required.

In this preliminary experiments chemical reactions in the silicone blend were not stopped. However, as the catalyst-in-PEG emulsion has a very low catalyst concentration, the reaction only takes place very slowly. The influence on the subsequent measurements is therefore small.

5.2.1 Experimental procedure

Two different types of experiments were carried out, "contact experiments" and "sliding experiments", illustrated in Fig. 5.2. For a contact experiment (Fig. 5.2a), the upper droploon is first moved with a constant approaching velocity v_{a} in z direction forward the bottom droploon. At a distance h_{min} the movement is stopped and the two droploons stay in contact for a relaxation time t_{r}. At the end the upper droploon is moved upwards with the withdrawing velocity v_{w} until the two droploons loose their contact again.

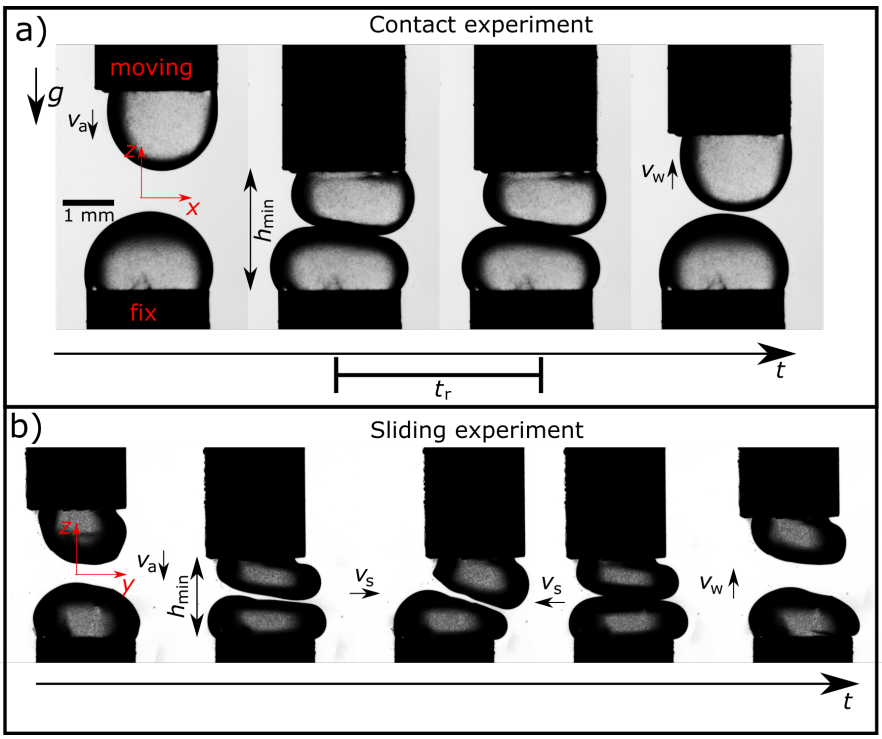

Figure 5.2: a) The principle procedure of a "contact experiment", with the approaching velocity v_a, the relaxation time t_r and the withdrawing velocity v_w. b) The principle procedure of a "sliding experiment" with the sliding velocity v_s.

The beginning and end of the sliding experiment (Fig. 5.2b) is the same as for a contact experiment. The top droploon approaches the bottom droploon with the veolocity v_a and is withdrawn at the end with the velocity v_w. During the contact duration (t_s), the top droploon is kept at constant distance h_{min} and moved in a horizontal direction at a speed v_s (Fig. 5.2b).

5.3 Results and discussion

The Table 5.1 shows in a chronological order five performed experiments with the two created droploons from the methods Section 5.2. The order is important since we expect a history-dependent response. The type of experiment, the figure showing the measurements, the minimal distance between the needles h_{min}, the approaching and withdrawing velocity $v_{a/w}$ are given in the Table 5.1. The experiments were carried out one after the other without much delay (in total after the skin formation 30 min). It can therefore be assumed that the chemical reaction between the first and last experiment did not cause a major change. The distances when the two droploons come into contact the first time at $h = h_{c;start}$ or when they loose the contact at $h = h_{c;end}$ are measured by eye. Since it is difficult to distinguish between the solid and liquid silicone, this values have a larger uncertainty $\pm 50\,\mu$m. If the two values are the same to this precision they are both called h_c.

Number	Type	Fig.	$h_{\min}$ in mm	v_a in μm/s	v_w in μm/s
1	contact	5.3	2.30	-8	8
2	contact	5.4	2.20	-20	20
3	contact	5.5	1.77	-80	18
4	sliding	5.6	1.95	-80	18
5	contact	5.7	1.85	-80	-

Table 5.1: The chronological order of the experiments carried out with the double-droploons. The table list the type of experiment, figure showing the corresponding results, the minimal distance between the needles $h_{\min}$, the approaching velocity v_a and the withdrawing velocity v_w.

5.3.1 First experiment: "contact"

The first experiment (Fig. 5.3) is a quasi static contact experiment. Very small approach and withdrawal velocities ($v_{a/w}$ in Table 5.1) were selected and the relaxation time is almost zero. $h_{\min}$ (Table 5.1) is rather large to ensure only elastic deformations. In Fig. 5.3a the pressure difference between the inside and outside of bottom droploon at the height of needle opening is plotted against the distance h between the two needles. Different symbols are chosen for the approaching (◀) and withdrawing (▷) process. Δp stays constant during the approach before the two capsules touch each other. From the distance h_c, when the droploons enter in contact, Δp increases continuously up to the distance $h_{\min}$. Increasing h again, Δp takes almost the same path back and reaches a fixed value a little below the initial Δp after the droploons detach at $h = h_c$. This change is probably caused by plastic deformation during the contact. This could be continued by a shape analysis in future work.

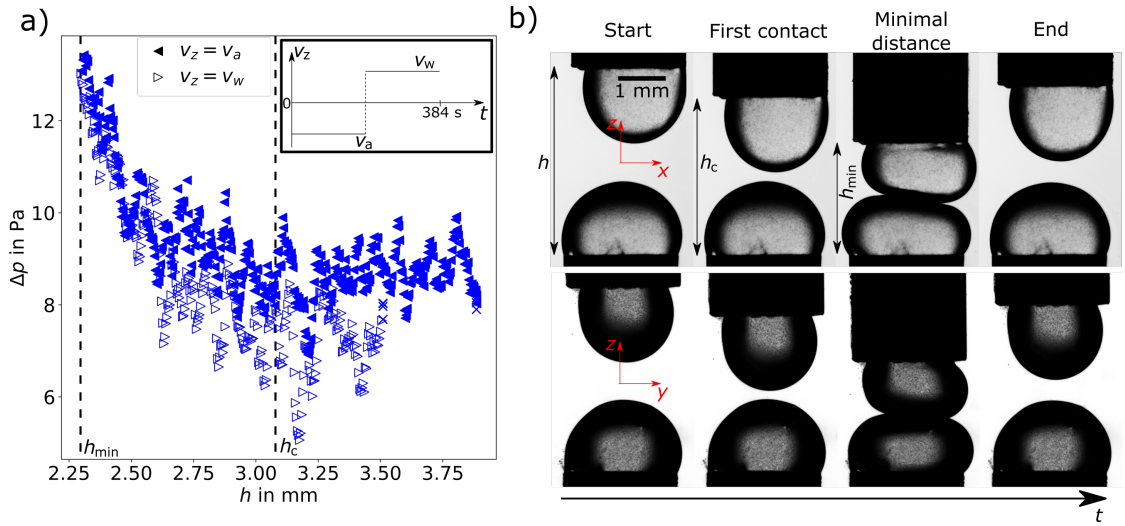

Figure 5.3: First experiment (contact, Table 5.1) with the two silicone droploons. a) The measured pressure difference Δp of the bottom droploon at $z = h/2$ (opening of the needle). b) xz and yz projections at different times. h_c is the height, where the two droploons touch each other for the first time. The inset in a) shows how the velocity in z direction changes, with $v_{a/w} = \mp 8\,\mu$m/s. For this experiment, the relaxation time is $t_r = 0$ s.

5.3.2 Second Experiment: "contact"

The second experiment (Fig. 5.4) is a contact experiment in which the two droploons are in contact with a needle distance $h_{\min} = 2.20$ mm for a relaxation time $t_r = 46$ s. Fig. 5.4 has the same organisation as Fig. 5.3. The differences are the measurements during the relaxation time symbolised with a cross ($\times$) in Fig. 5.4a and b. Fig. 5.4b, plots the change in Δp during t_r. We observe:

- The initial Δp in Fig. 5.4a is equal to the final Δp in Fig. 5.3a. Meaning the reaction has progressed little.
- During the relaxation (Fig. 5.4b) Δp has a decreasing trend.
- The initial Δp is clearly larger than the final Δp in Fig. 5.4a. The difference is approximately the change in pressure during the relaxation time t_r in Fig. 5.4b.
- By comparing the photographs in Fig.s 5.3b and 5.4c at the start and end of the experiments, one observes progressively small changes in the shape of the droploons, probably due to plastic deformations of the droploons.

5.3.3 Third experiment: "contact"

For the third experiment (Fig. 5.5), we increase v_a and decrease $h_{\min}$ (Table 5.1), to observe larger plastic deformations during the relaxation time and validate the previously observed trend. The effect is strong enough to be seen also for the top droploon (red in Fig. 5.5), despite the less accurate pressure measurements. The general behavior in Fig. 5.5a is the same as for the first (Fig. 5.3a) and the second experiment (Fig. 5.4a). Δp of the bottom and top droploon behave similarly in Fig. 5.5a and b. This is plausible, because both droploons have a similar volume and the two pressure differences Δp are coupled by the contact. The differences in shape between the top and bottom droploon appear to be of minor importance.

Let us take a closer look at the relaxation process at $h = h_{\min}$ in Fig. 5.5b and c. Fig. 5.5c shows the shapes before and after the relaxation. A clear difference in shape can be observed. At the end of the relaxation, the droploons resemble more a tilted bubble (TB) configuration from the Chapter 3. To reach this new shape, the two droploons have slipped along each other. Since the interfaces are no longer purely fluid as for the Chapter 3, there are other frictional forces that influence the slipping. This could explain the fluctuations in Δp in Fig. 5.5b during the relaxation. This is also supported by the fact that the fluctuations for the top and bottom droploon appear at the same time (Fig. 5.5b). The shape of the droploons in the forth photograph from the left in Fig. 5.5c shows a deformation, which is only explainable by attractive forces between the droploons. It is therefore the first time that we observe them in our experiments. The attractive forces could explain why Δp in Fig. 5.5a increases at specific h again for the withdrawing process and that h for the first contact $h_{c;\text{start}}$ is smaller then for the last contact $h_{c;\text{end}}$ (Fig. 5.5). The function $\Delta p(h)$ during the withdrawing resembles that of two drops in contact with a contact angle $\theta_c > 0°$ (Chapter 3). Since this behaviour could not be observed for the first two experiments from Fig.s 5.3 and 5.4, we conclude that the attractive forces are history-dependent.

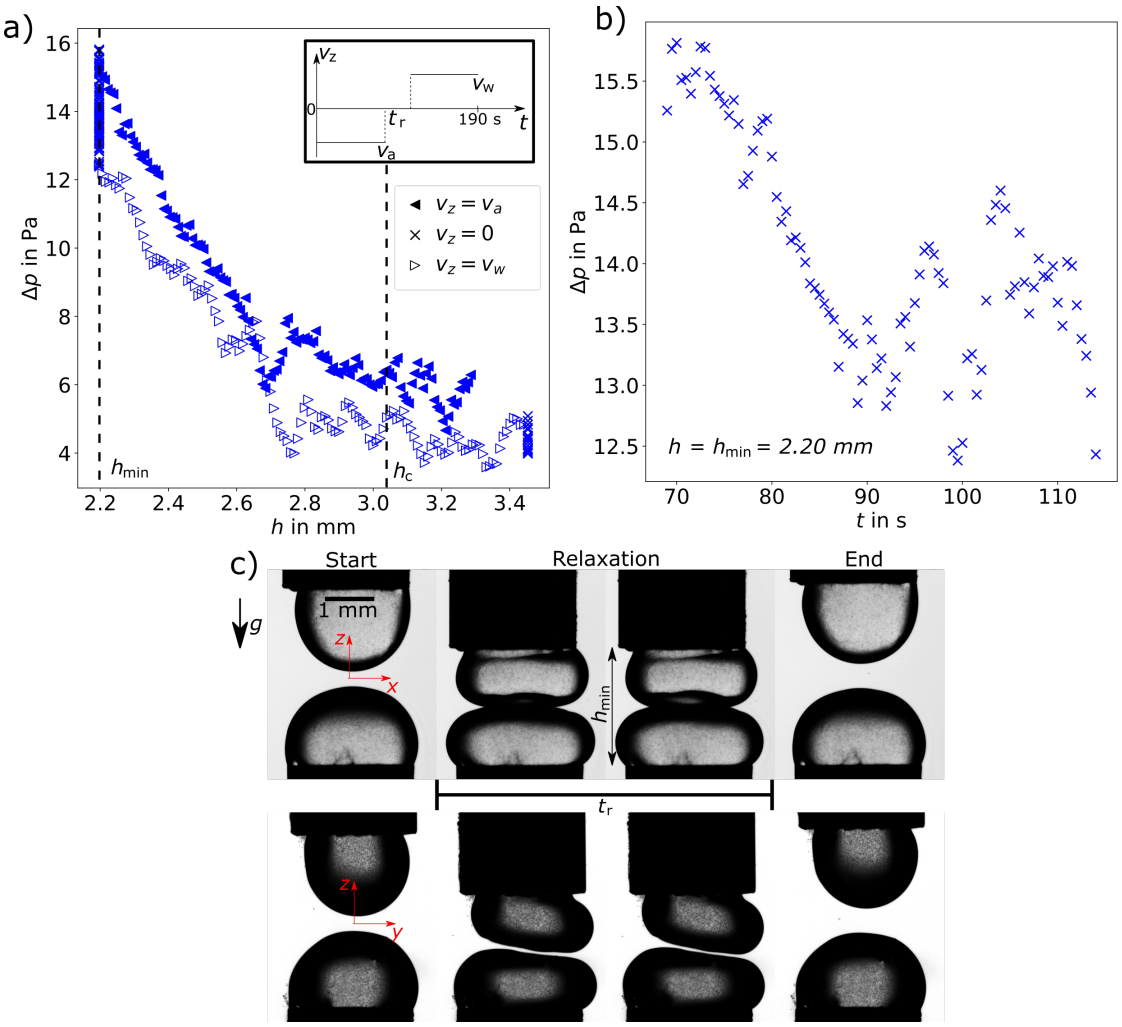

Figure 5.4: Second experiment (contact, Table 5.1) with the two silicone droploons. a) The measured pressure difference Δp at the bottom droploon at $z = h/2$ (opening of the needle) plotted against the distance between the two needles h. The inset shows how the velocity in z direction changes, with $v_{a/w} = \mp 20\,\mu$m/s and the relaxation time $t_r = 45$ s. b) Δp plotted against t in the time span t_r at $h = h_{min}$. c) xz and yz projections at different times.

The sliding of the two droploons over each other due to the droploon tilting instability (CB→TB in Chapter 3) or the high Δp due to the small h_{min} in the third experiment (Table 5.1 and Fig. 5.5) could have caused the attractive forces, which were not observed for the first and second experiment (Table 5.1). The contact time could also have an influence due to the ongoing chemical reaction, but plays probably a minor rule since the contact times of the three different experiments are not significant different.

5.3.4 Forth experiment: "sliding"

The forth experiment (Fig. 5.6 and Table 5.1) is a sliding experiment, in which we moved the top droploon horizontals to the left with the velocity v_s at the distance h_{min} over the time span t_s. Fig. 5.6c shows how Δp changes during t_s. The inset shows how v_s changes during t_s. Fig.s 5.6b and d show for different times the xz and yz projections

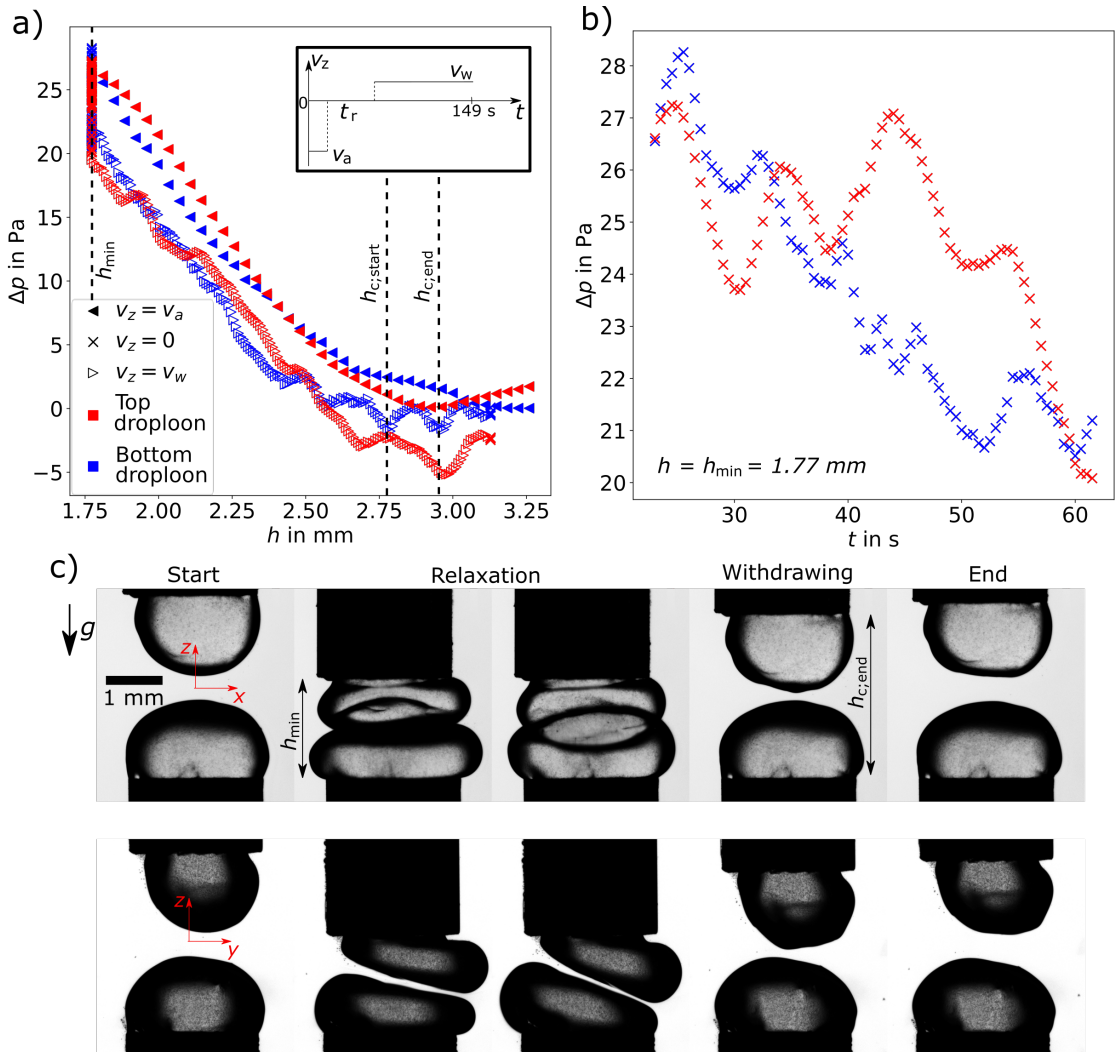

Figure 5.5: Third experiment (contact, Table 5.1) with the two silicone droploons. a) The measured pressure difference Δp at the top (red) and bottom (blue) droploons at $z = \pm h/2$ respectively (opening of the needles) plotted against the distance between the two needles h. The inset shows how the velocity in z direction changes, with $v_a = -80\,\mu$m/s, $v_w = 18\,\mu$m/s and the relaxation time $t_r = 39$ s. b) Δp plotted against t in the time span t_r. c) xz and yz projections at different times.

of the droploon shapes. Δp decreases by moving the droploons away from each other and increases by moving them towards each other (Fig. 5.6c). An exception is the top droploon for the first horizontal back and forth movement. We do not yet have an explanation for this.

The attractive forces during the withdrawing are stronger than in the third experiment (Fig. 5.5), clearly shown by the strong deformations of the droploons, a measurable contact angle θ_c in Fig. 5.6b and a pronounced minimum in Δp in Fig. 5.6a for both pressure measurements. Again the sliding, strong contact pressure or the long contact time could have been the cause for the contact forces.

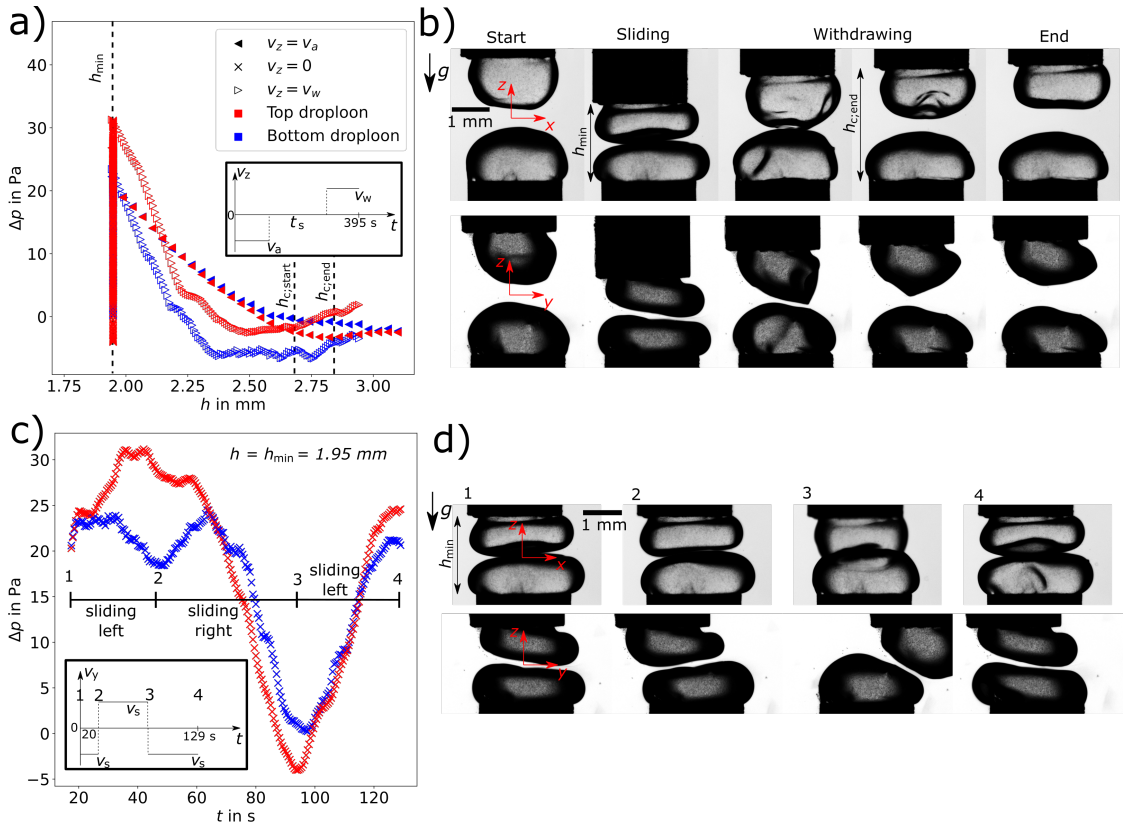

Figure 5.6: Forth experiment (sliding experiment) with the two silicone droploons. a) The measured pressure difference Δp at the top (red) and bottom (blue) droploons at $z = \pm h/2$ respectively (opening of the needles) plotted against the distance between the two needles h. The inset shows how the velocity in z direction changes, with $v_\mathrm{a} = -80\,\mu$m/s, $v_\mathrm{w} = 18\,\mu$m/s and the sliding time $t_\mathrm{s} = 105$ s. b) xz and yz projections at the approaching and withdrawing process. c) Δp plotted against t in the time span t_s. The inset shows how the velocity in y direction changes, with $v_\mathrm{s} = \pm 55\,\mu$m/s. d) xz and yz projections at the sliding process at four times also indicated in the scheme in c).

5.3.5 Fifth experiment: "contact"

The fifth experiment (Fig. 5.7 and Table 5.1) is a contact experiment, in which the bottom droploon broke. v_a is with -80 μm/s high. The minimal distance is with $h_\mathrm{min} = 1.85$ mm small but not the smallest (third experiment in Table 5.1). Fig. 5.7b shows how Δp changes after the two needles have stopped approaching each other. Δp for the top and bottom droploon behave similarly. In the beginning both Δp increase, reaching a maximum, decrease afterwards, and reaching a fixed value at the end. The skin of the bottom droploon breaks when the pressure reaches the maximum (Fig. 5.7c). Afterwards the bottom droploon releases liquid and both droploons start to relax, Δp decreases. The fixed pressure value at the end belongs to a new equilibrium state. The initial increase in pressure during relaxation (Fig. 5.7b) might be caused by effects of inertia. The needle stops moving and the droploon moves a little further due to inertia. In this case, however, one would also expect to see a reverse effect at the top droploon at the beginning of the measurement. This could not be measured significantly in the

fifth experiment. But in the third and forth experiments we could measure a decreasing pressure at the beginning of the measurement for at the top droploon, even though the droploons were not yet in contact (Fig.s 5.5a and 5.6a). This can only be explained by inertia effects. In the third and forth experiments we also worked with $v_a = -80\ \mu$m (Table 5.1).

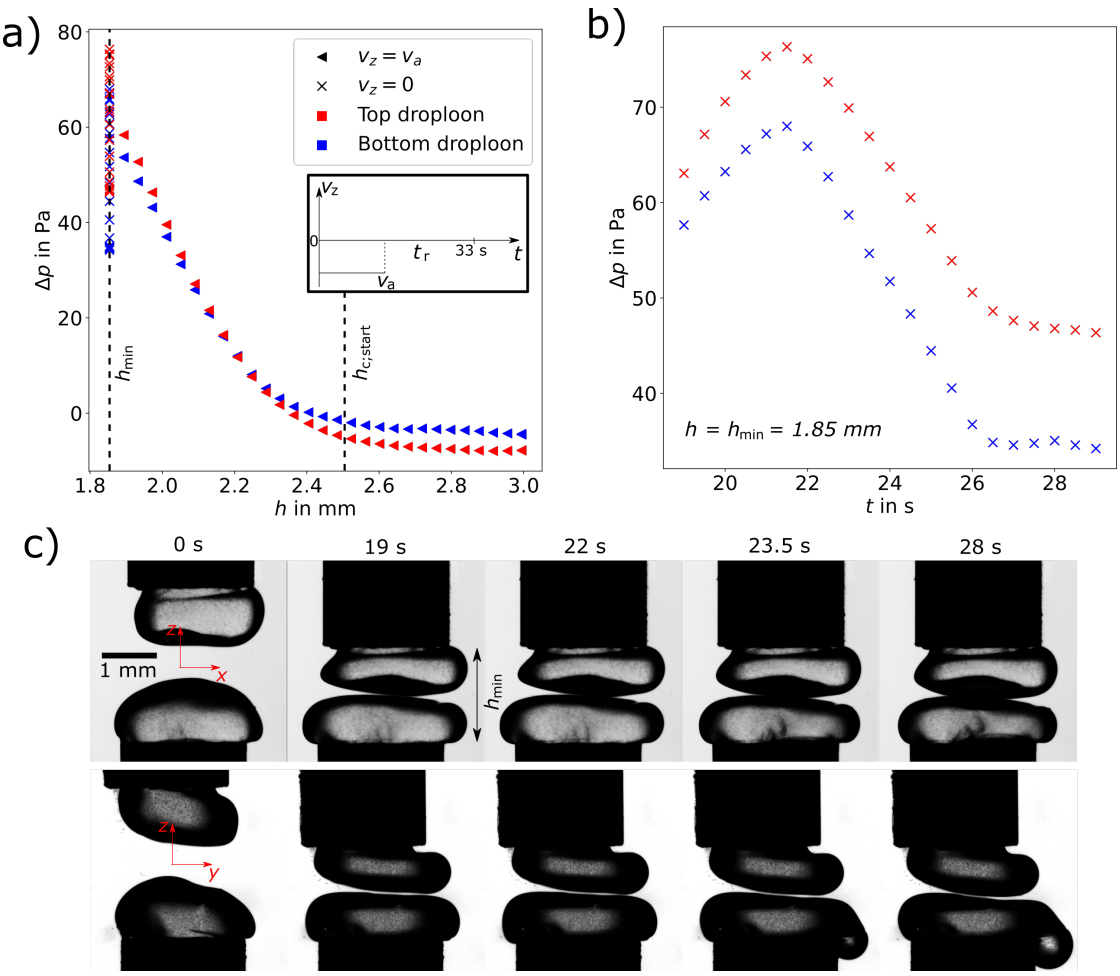

Figure 5.7: Fifth experiment (contact experiment) with the two silicone droploons. a) The measured pressure difference Δp at the top (red) and bottom (blue) droploons at $z = \pm h/2$ respectively (opening of the needles) plotted against the distance between the two needles h. The inset shows how the velocity in z direction changes, with $v_a = -80\,\mu$m/s and $t_r = 14$ s. b) Δp plotted against t in the time span t_r. d) xz and yz projections for different times.

5.4 Conclusion

In the presented preliminary experiments, we were able to show that our developed device has the necessary accuracy in pressure measurements, needle movements and image resolution to measure interactions between two droploons. Phenomena such as adhesion, friction and viscou-elastic or elastic-plastic deformations could already be analysed with very simple experimental procedures (contact and sliding experiment Fig. 5.2). The

results are not only qualitative due to the two cameras, but also quantitative due to the pressure measurements. Further measurements are necessary to obtain certainty about the different interpretations of the observed phenomena.

The axisymmetric structure of the setup (only contact experiments) allows comparatively simple to compare the complex physical system with theoretical models. However, it is of crucial importance that the droploons also remain axisymmetric to make general assumption about the interactions between the two skins of the droploons. Therefore, for the results shown in this chapter, only a statement about the behaviour of these two droploons for these particular deformations can be made. But Chapter 4 shows that we are able to fabricate axisymmetric droploons, from which we even know their effective interfacial properties. The comparison with theoretical models will therefore be part of future studies.

In the experiments from Section 5.3, it is noticeable, that there are many similarities with Chapter 3 (similar instabilities and pressure curves), in which interactions between drops with liquid interfaces and constant interfacial tension were investigated. The following questions arise: whether or how long droploons can be modelled with constant interfacial tension.

Chapter 6

Conclusion and outlook

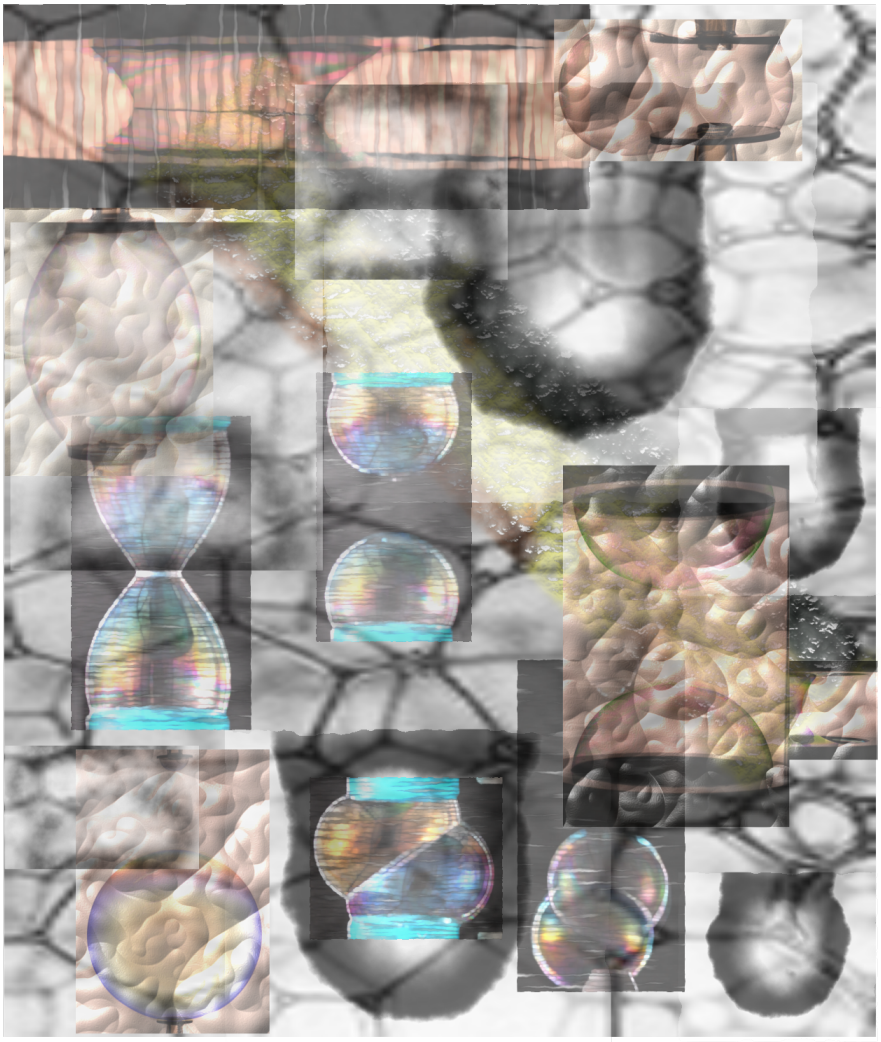

Contents

6.1 Conclusion

In this thesis interfaces with different properties, geometries and boundary conditions were investigated to develop methods and systems to systematically analyse the influence of complex interfaces on the properties of foams or emulsions. Complex here means the additional influence of adhesive, elastic or frictional forces between bubbles and drops. Forces, moments and pressures transmitted by the interfaces, the interface shape and stability were analysed with help of experiments, simulations and theory for different systems in the Chapters 2, 3, 4 and 5.

Chapter 2 deals with soap films between open, non-axisymmetric frames. The obtained shapes of the interfaces are minimal surfaces. We showed how the frame shape, their orientation and distance to each other affect the existence (Section 2.4.1) and shape (Section 2.4.2) of the connecting interface and the forces and moments exerted on the frames by the interfaces (Section 2.4.3). We compared the results to a new perturbation theory (Section 2.3), which has a very good qualitative and a good quantitative agreement to the experiments and simulations. All general trends in the force or moment to distance or angular orientation curves are in agreement. In contrast to previous studies, our approach is very general and simple and can be applied to arbitrary frame geometries. This makes it possible to predict forces and moments that do not exist for minimal surfaces between two identical frames. The quantitative agreement can be improved by normalising distances by characteristic lengths.

Chapter 3 deals with two drops/bubbles/soap bubbles in contact and also with one capillary bridge pinned on two closed circular frames for small Bond numbers Bo. The closed frames result in an additional volume constrain for the drops, bubbles and capillary bridges, which turns minimal surfaces into constant mean curvature surfaces. Therefore, we use for the axisymmetirc shapes the theory of Delaunay 3.3.3. We showed how adhesive forces between the drops or bubbles affect forces, pressures (Section 3.4.2) and shapes (Section 3.4.3) of the drops and bubbles. The strength of the adhesive forces is reflected in the size of the contact angle θ_c. We investigated three contact angles experimentally and all in the range of $0° \leq \theta_c \leq 90°$ theoretically and numerically. Therefore, the complete $\hat{R} - \hat{h} - \theta_c$ shape space is obtained and drawn for three slices with $\theta_c = 0°$, $60°$ and $90°$ in Fig. 3.20. In total, five different types of shapes were distinguished with five different shape transitions (Section 3.4.3). One is trivial (SB→CB), two were known from the literature (CB↔TB and CB→SB), but analysed experimentally and theoretically for different θ_c the first time in this depth and two were discovered and analysed by us (CB↔ShB and CB→DB). Although we carried out preliminary theoretical studies for the two non-axisymmetric instabilities (CB↔TB and CB↔ShB), a correct theoretical prediction has still to be made for the two instabilities.

Chapter 4 deals with the growth and characterisation of a silicone skin between a cayalyst-in-PEG emulsion and a silicone oil. The polymerization, which creates the skin at the interface, was analyzed at both a flat and spherical interface. It starts as

soon as the catalyst from the emulsion begins to diffuse into the silicone phase. The two-dimensional skin properties were measured as a function of time during growth by a pendant drop interfacial dilational rheology method. The effective tension-deformation signal was treated and analysed with a General Stress Decomposition (GSD), which was only very recently proposed for the analysis of interfaces [116]. We carried out the first investigation, known to us, with the GSD on a liquid-liquid interface. The mechanical properties of the skin were linked to wrinkling and buckling, both shape transitions, which we observed for the flat and spherical interface shape. We demonstrated that this characterisation can be performed simultaneously on two drops (one hanging and one sitting), on the same setup used for the drop-drop interaction investigations in Chapter 3.

With Chapter 4 we showed a possible model system, that has many of the desired properties:

- The two dimensional elasticity modulus K'_{2D} has a similar order of magnitude as the interfacial tension γ over a long reaction time period and is controlled by skin thickness δ and the chosen silicone blend S. The obtained elasto-capillary numbers are between $0 \leq \alpha \leq 10$.

- Good reproducible of the mechanical properties of the skin depending on the silicone blend.

- The skin growth can be stopped at a desired moment with help of an inhibitor with the drawback, that it must be dispersed homogeneously as fast as possible to achieve a homogeneous reaction stop.

Disadvantages of this system are:

- The skin is expanding tangentially to the interface, which makes it impossible to make investigations in an elastic stress-free state. But this is important, if one wants to compare the measurements to existing non-linear elastic models for capsules.

- The fabrication is complex, since the dynamic skin growth depends on the catalyst-in-PEG emulsion, which in itself is already a complex system. In addition, there is the reaction at the interface with large catalyst concentration gradients (Fig. 4.12b).

- The skin thickness is difficult to measure, because it has almost the same optical properties as the silicone oil.

Chapter 5 demonstrated with some preliminary experiments the potential of droploon-droploon experiments. We showed that the double drop device from Fig. 3.6a, for which the development was part of this thesis with the help of the engineer J. Dijoux, is capable to measure quantitative and qualitative small changes in the interface/skin due to droploon-droploon interactions. We gave a physical interpretation for different droploon-droploon interaction phenomena as elasticity, viscous and plastic deformations, adhesion and friction. For quantitative results a pre-analysis of every individual droploon, for example with a GSD analysis, is necessary. We demonstrated that this is possible with the same device. Due to the lack of time full exploitation of this experiments has to be done in future work.

6.2 Outlook

If the catalyst-in-PEG emulsion with reactive silicone is to be used to investigate droploon-droploon or capsule-capsule interactions in more depth, it would be important to understand the origin of the silicone skin expansion at the interface between the catalyst-in-PEG emulsion and silicone blend. The next step would be to increase progressively the elasto-capillary number α and compare pressure distance curves, shapes and shape instabilities with the fluid interface with $\alpha = 0$. The geometric parameters, such as the distance between the needles h, the volume of the drops V, the needle radius R can be used to manoeuvre into the interesting regimes. New parameters to investigate could be the contact time and history of the two objects in combination with the contact pressure or the skin thickness and the skin formulation. Measured quantities could be the hysteresis size for an approaching withdrawing experiment or the contact angle θ_c, which is in this case not constant, rather a function of all parameters and especially α and the adhesive forces between the two objects. Due to the axisymmetry a comparison with theory is practicable.

The next step could be the development of standardized characterisation methods for droploons, bubloons and capsules interactions. This would require the identification of sensitive, system-independent and easily measured and interpreted phenomena of this interactions. The standardised analysis would help to better compare materials and facilitate the choice of systems for potential new metamaterials with foams and emulsions. Existing applications of droploons, bubloons or capsules, for example in pharmaceuticals or agriculture, could also be optimised in this way. To achieve this, studies must be carried out that link the interactions between two individual droploons with the mechanical behaviour of a droploon accumulation.

Chapter 7

Synthèse en français

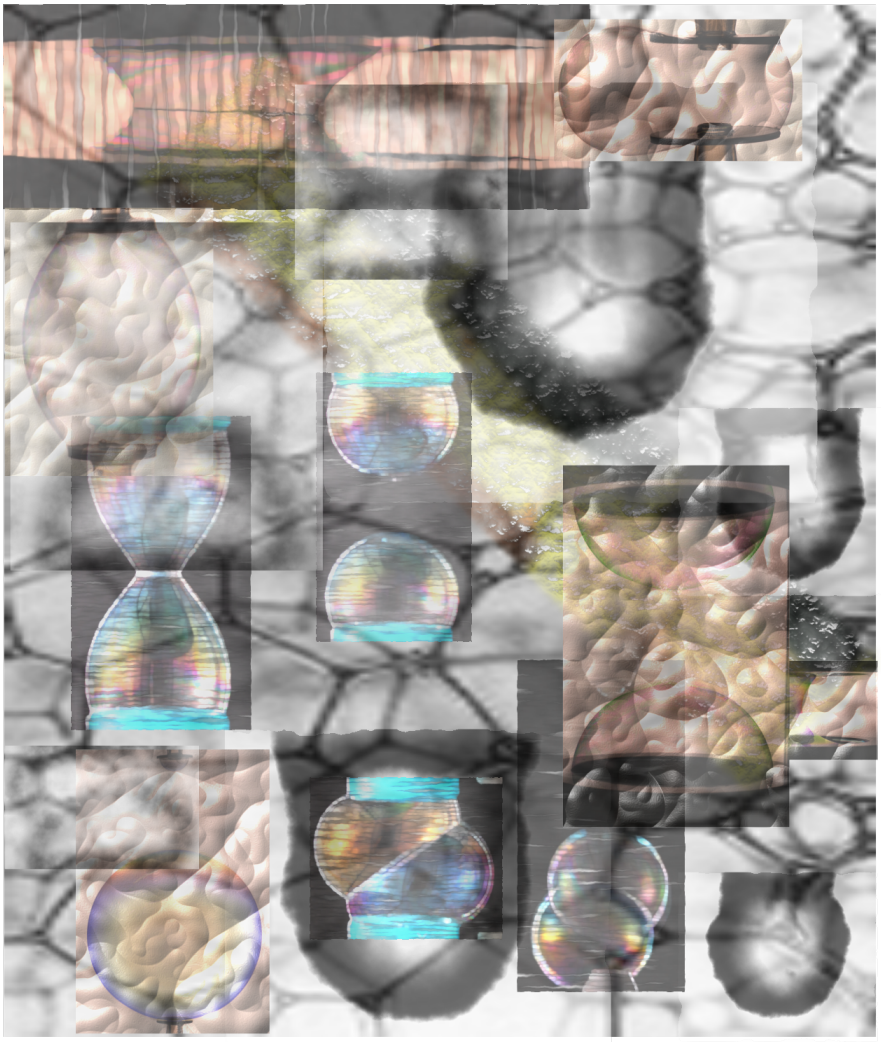

Contents

7.1 Motivation et contexte

Au fur et à mesure que la technologie progresse, le besoin en nouveaux matériaux combinant des propriétés complexes et multiples se fait de plus en plus sentir. Les matériaux dont les propriétés dépassent celles des matériaux traditionnels sont appelés méta-matériaux. Ils sont souvent constitués de différents composants/matières/structures qui sont asscociés selon des schémas répétitifs. La propriété globale du matériau combine alors les propriétés des différents éléments. Les mousses et les émulsions sont également composées de nombreux petits éléments, bulles ou gouttes, arrangés de manière plus ou moins périodique. Les propriétés macroscopiques du matériau sont alors déterminées par les propriétés et la disposition des bulles ou des gouttes. Toutes ces propriétés associées au fait que les bulles ou les gouttes s'agencent d'elles-mêmes, rendent les mousses et les émulsions intéressantes pour les méta-matériaux.
Les mousses et les émulsions sont des structures composées d'une phase continue et d'une phase dispersée. La mousse comporte une phase continue liquide et une phase dispersée gazeuse (les bulles). Une émulsion est constituée de deux liquides non miscibles, l'un étant la phase continue et l'autre la phase dispersée (les gouttes). Les mousses et les émulsions sont largement utilisées dans les applications et les processus industriels, par exemple dans les industries alimentaires (café spécialités ou pâtisserie), les produits de soins personnels et cosmétiques (crème solaire, crème pour la peau), les produits agrochimiques, les produits pharmaceutiques, les peintures, les industries pétrolières, les industries minières et les processus de recyclage, pour n'en citer que quelques-uns. On peut également observer fréquemment des mousses ou des émulsions dans la nature, par exemple sur les côtes après une tempête en présence de plancton, sur un volcan en activité ou dans des produits d'origine animale comme le lait. Il est donc crucial de comprendre leurs propriétés [4, 5, 6].
Les mousses et les émulsions présentent de nombreuses propriétés intéressantes. On peut citer le comportement macroscopique de fluide à seuil, les bonnes capacités d'isolation thermique, une absorption acoustique élevée, une faible fraction de volume continu par rapport au volume total, l'auto-assemblage des bulles ou des gouttes dans une mousse ou une émulsion, etc. Grâce aux méthodes de solidification, certaines de ces propriétés sont conservées dans les mousses solides. Cela élargit la gamme des applications, par exemple pour les matériaux de construction. D'autres propriétés jouent un rôle plus important, comme le module d'Young ou la rigidité. Toutefois, cela met en lumière un inconvénient majeur : le faible module de compression et la faible rigidité à la déformation des mousses. Cela est lié à la structure typique de la phase continue qui est

principalement définie par les lois de Plateau et de Young-Laplace. Cela réduit l'intérêt des mousses solides pour de nombreuses applications. On peut espérer, en modifiant les interactions bulle/bulle ou goutte/goutte dans une mousse ou une émulsion, accéder à des structures différentes avec des propriétés originales, et qui permettraient d'utiliser les avantages des mousses/émulsions en minimisant leurs inconvénients [137]. Le projet de recherche METAFOAM (ERC Consolidator Grant, agreement 819511 METAFOAM) vise à comprendre, à l'aide de différents systèmes modèles, l'influence de l'élasticité, de l'adhésion et de la friction en interaction avec la tension interfaciale sur les structures finales. Par la suite, les connaissances acquises seront utilisées pour produire des méta-matériaux avec les propriétés souhaitées. L'effet de l'auto-assemblage sera utilisé afin de travailler de manière reproductible et rentable.
Pour atteindre ces objectifs, il faut répondre à différentes questions :

- Quels sont les bons systèmes modèles ? Les critères utilisés sont la reproductibilité et le contrôle de l'espace des paramètres. Dans le cas idéal, les différents facteurs d'influence (tension de surface, élasticité, viscosité, adhésion et interaction des différents éléments) peuvent être étudiés séparément.

- Quelles sont les bonnes méthodes expérimentales et théoriques pour caractériser les différents facteurs pertinents ? Ici aussi, l'idéal est de pouvoir étudier ces facteurs d'influence séparément.

La première motivation de ma thèse est l'intérêt majeur pour la société de disposer de matériaux originaux aux applications novatrice. La seconde motivation, tout aussi importante, est de nature plus fondamentale et s'explique par la volonté de comprendre et d'expliquer l'inconnu. Les deux se conditionnent mutuellement. Mais les questions et donc les approches sont différentes.

- Qu'est-ce qui explique la structure et le changement de structure dans une mousse ou une émulsion ?

- Quelles formes peut-on générer avec des films de savon et lesquelles ne peut-on pas ? Quelle est l'influence des conditions limites ou d'autres contraintes ? Quelles sont les forces qui jouent un rôle ?

- Quelle est la relation entre la tension de surface, l'élasticité, l'adhésion et la friction ? Sont-elles interdépendantes ?

- et plus.

Nous commençons nos recherches avec le plus petit composant d'une mousse, des films, ici entre deux cadres, avec une distance h (Fig. 7.1 en haut à gauche). Nous analysons d'abord l'influence de la structure du cadre ; les cadres étant ouverts et donc le volume libre de s'ajuster. Ensuite, nous travaillons avec des cadres fermés, donc avec une contrainte de volume.
Afin d'analyser les interactions entre les bulles ou les gouttes, nous ajoutons un film de contact qui divise le volume en deux bulles ou gouttes (Fig. 7.1 en haut au milieu). Cela nous donne une base sur laquelle nous pouvons travailler pour étudier des systèmes plus complexes avec la viscoélasticité ou l'adhésion. Afin de nous concentrer entièrement sur les interactions entre des gouttes ou des bulles visco-élastiques et/ou adhésives, nous

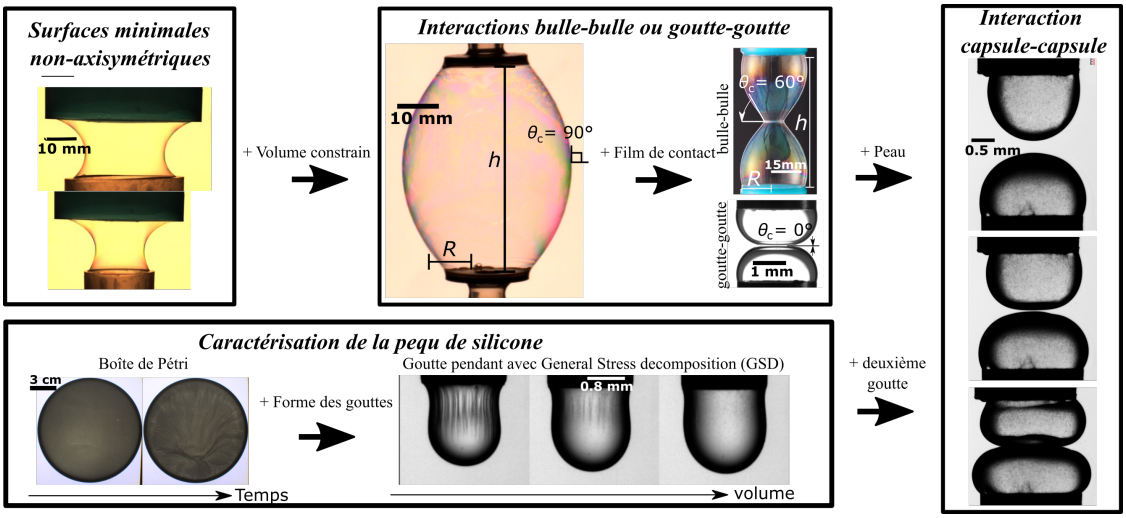

Figure 7.1: Vue d'ensemble des différentes étapes, de l'étude des surfaces minimales avec des films de savon (partie supérieure gauche), en passant par les interactions bulle-bulle et goutte-goutte (partie supérieure centrale), la caractérisation de la peau de silicone (partie inférieure gauche) et jusqu'aux interactions de la double capsule (partie droite).

étudions d'abord une interface unique (les interfaces qui n'interagissent pas avec d'autres interfaces). Nous avons combiné plusieurs méthodes pour obtenir les informations les plus pertinentes (Fig. 7.1, en bas à gauche). Finalement, nous observons les interactions entre deux interfaces présentant des propriétés mécaniques complexes (tension de surface, viscoélasticité et/ou l'adhésion) (Fig. 7.1, à droite).

7.2 Surfaces minimales non-axisymétriques

Les surfaces minimales apparaissent naturellement dans de nombreux systèmes de matière molle dont l'énergie libre est dominée par les énergies de surface ou d'interface. La forme, la stabilité et les contraintes mécaniques des surfaces minimales s'appuyant sur des contours géométriques spécifiques sont d'un intérêt particulier (problème de Plateau). La "caténoïde" est l'exemple le plus connu pour lequel on dispose d'une solution analytique décrivant la forme et la stabilité d'une surface minimale maintenue entre deux cadres circulaires concentriques parallèles. Nous étendons ici ce problème à des cadres parallèles non axisymétriques de différentes orientations, en développant une approche théorique de perturbation autour de la solution connue de la caténoïde. Nous démontrons que les prédictions de la théorie des perturbations concordent bien avec les expériences sur les films de savon et les simulations par éléments finis (Surface Evolver [64]). En combinant théorie, expérience et simulation, nous analysons en profondeur comment les formes, la stabilité et les propriétés mécaniques des surfaces minimales dépendent du type et de l'orientation des cadres elliptiques ou en forme de trèfle à trois feuilles [42]. Dans la limite de cadres non axisymétriques parfaitement alignés, nos prédictions montrent un excellent accord avec une théorie récente établie par Alimov *et al.* [1]. En outre, nous avons mis en évidence l'intrigante capacité des surfaces minimales non-axisymétriques à transmettre un couple mécanique, bien qu'elles soient complètement liquides. Ces forces pourraient être intéressantes à exploiter pour l'auto-assemblage mécanique de systèmes

de matière molle ou comme capteurs de force très sensibles. Des phénomènes également observés dans les mousses ou les émulsions peuvent être étudiés, en particulier à l'échelle des films (surface et épaisseur). Cependant, de nombreux autres phénomènes ne peuvent être étudiés parce que le modèle manque de complexité et que des conditions limites et des contraintes importantes sont omises, telles que le contact entre les bulles (ou les gouttes) ou la conservation du volume des bulles (ou des gouttes).

7.3 Interactions bulle-bulle ou goutte-goutte

Les interactions entre bulles ou gouttes jouent un rôle important dans de nombreux phénomènes physiques. Que l'on considère l'interaction entre deux bulles (gouttes) ou entre plusieurs bulles (mousses ou émulsions), ces interactions sont complexes et encore mal comprises. Un cas intéressant se présente lorsque deux bulles (gouttes) de volume égal et constant interagissent entre elles tout en étant maintenues par deux capillaires de section circulaire positionnés de manière axisymétrique – une configuration qui est fréquemment utilisée dans les dispositifs de caractérisation. Des études similaires, numériques et expérimentales, en 2D et 3D et entre parois parallèles, ont été menées par différents groupes de recherche [41, 81, 82, 79]. Par rapport au problème précédent, il prend également en compte les volumes et les interactions entre les gouttes ou les bulles. La minimisation de l'énergie de surface de cette configuration "double bulle" ou "double goutte", contrainte par le volume fixe et les limites des capillaires, crée un paysage complexe d'espaces de forme (Fig. 7.2 à gauche) où les formes stables sont séparées par différents types d'instabilités. En combinant l'expé-rience, la simulation par éléments finis [64] et la théorie [20] (Fig. 7.2 à droite), nous fournissons ici pour la première fois une analyse complète de ces espaces de forme, en considérant l'énergie adhésive entre les bulles ou les gouttes (exprimée par l'angle de contact) comme un paramètre de contrôle supplémentaire. Nous fournissons les diagrammes de forme complets pour différents angles de contact (0°, 60° et 90°), avec notamment une description détaillée de quatre types d'instabilités. Deux d'entre elles rompent l'axisymétrie tandis que les deux autres rompent la connectivité de l'ensemble. À notre connaissance, deux de ces instabilités n'ont jamais été signalées auparavant. Nous accompagnons l'analyse de la forme et de la stabilité avec une caractérisation mécanique détaillée à l'aide de mesures de force et de pression. Les expériences, les simulations et la théorie montrant un excellent accord. Ce travail sera utile pour guider l'exploitation des expériences de double bulle (double goutte) sur les capillaires. Il ouvre également la possibilité d'exploiter ces configurations pour la caractérisation d'interactions de bulles ou de gouttes de plus en plus complexes. L'angle de contact de 90° correspondant à un film "imaginaire" séparant les deux bulles, notre analyse inclut naturellement les formes et la stabilité d'un pont capillaire entre deux cadres circulaires (Fig. 7.2 à gauche der-nière colonne dans le tableau).

Name	Label	θ_c = 0°	θ_c = 60°	θ_c = 90°
Connected Bubbles	CB			
Separated Bubbles	SB			
Detached Bubbles	DB			
Tilted Bubbles	TB			
Shifted Bubbles	ShB			

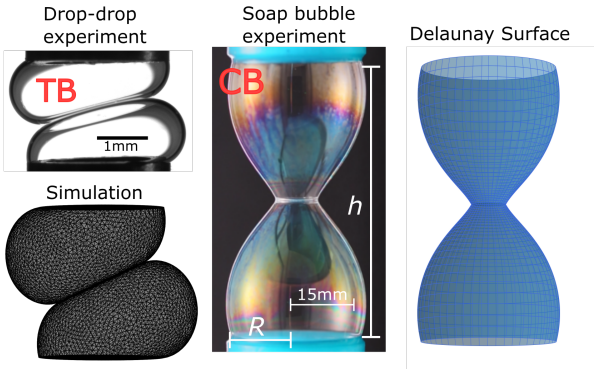

Figure 7.2: (Gauche) toutes les formes stables pour deux bulles ou deux gouttes en contact pour les trois angles de contact 0°, 60° et 90° sont représentées avec un nom, un pictogramme et une abréviation. (Droite) exemples de configurations obtenues numériquement, expérimentalement ou théoriquement.

7.4 Caractérisation des peaux elastiques

Pour produire une peau de silicone à la surface d'une goutte, nous utilisons deux types de siloxanes avec deux groupes réactifs différents, le triméthylsiloxane-méthylhydrosiloxane-terminé diméthylsi-loxane (MHDS) et le polydimethylsiloxane (PDMS) à terminaison vinyle. Les groupes réactifs réagissent entre eux en présence d'un catalyseur de platine. Pour que la réaction ne se produise qu'à une interface, nous préparons une PEG catalyseur de platine émulsion. Ensuite, nous mettons l'émulsion en contact avec un mélange des deux huiles de silicone reactif. Les gouttes de catalyseur de platine arrivent par diffusion à l'interface entre l'émulsion et l'huile de silicone et démarrent la réaction chimique. La peau croît alors à l'interface dans la phase silicone et crée une nouvelle phase solide (Fig. 7.3) [3, 2]. Nous sommes particulièrement intéressés par le régime dans lequel la peau peut encore être décrite comme une membrane ou une coquille, c'est-à-dire dans lequel elle peut être considérée comme un objet bidimensionnel. Différentes formes d'interfaces ont été utilisées, l'interface d'une goutte d'émulsion dans de l'huile de silicone et deux couches superposées d'émulsion et d'huile de silicone pour créer une interface plane. Les peaux de silicone sont des systèmes modèles prometteurs pour étudier la combinaison de l'élasti-cité et de la tension de surface. Leurs propriétés élastiques sont modifiables par le choix des polymères de silicone. Les paramètres importants avec lesquels nous contrôlons les propriétés élastiques sont la longueur des polymères et la proportion des différents groupes réactifs. D'autres facteurs influents sont étudiés, comme la vitesse de réaction ou la structure des polymères (nombre, espacement et répartition des groupes réactifs). Un autre paramètre important est l'épaisseur de la peau qui influence fortement les propriétés mécaniques. L'épaisseur de la peau augmente avec le temps de réaction. En effectuant nos mesures en fonction du temps de réaction, nous obtenons une évolution des propriétés mécaniques de la peau en fonction de son épaisseur. Il est souvent problématique de distinguer l'influence de l'épaisseur de la peau de celle des propriétés tridimensionnelles du matériau, car il n'est souvent pas possible d'effectuer des mesures en parallèle. La peau a été analysée selon deux méthodes (Fig. 7.1, en bas à gauche). Dans la boîte de Pétri, l'inter-face entre les deux liquides se trouve d'abord dans un plan et est exposée par le bas à une lumière perpendiculaire à l'interface. Au fur et à mesure que le temps de

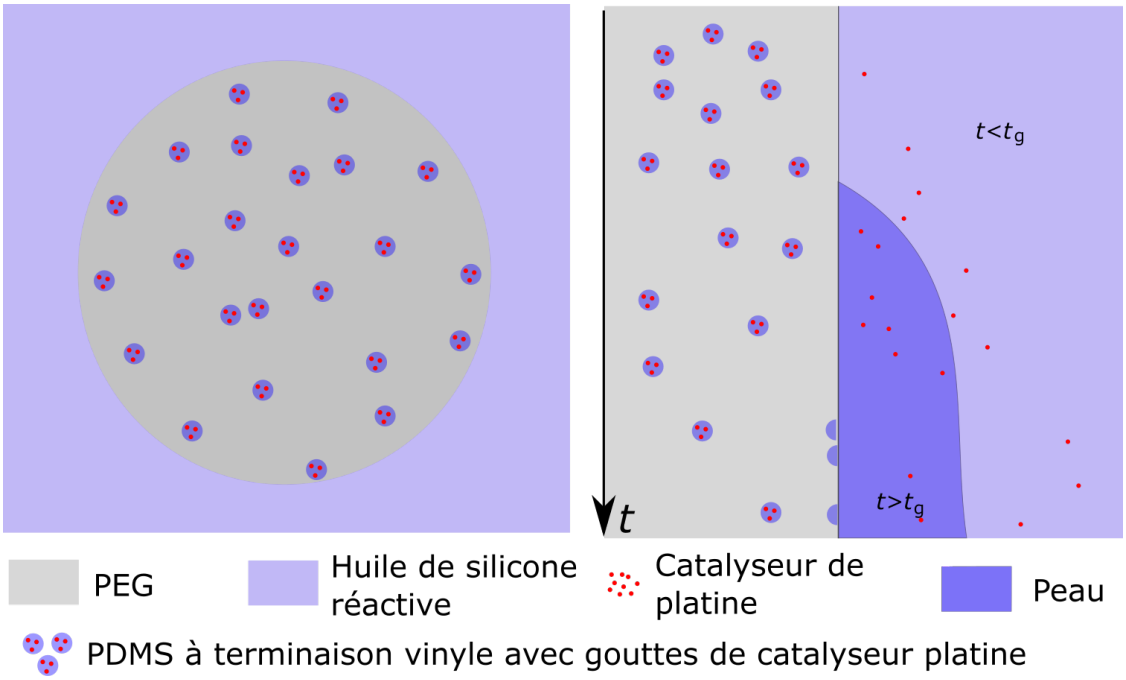

Figure 7.3: (Gauche) Goutte de PEG avec catalyseur de platine sous forme d'une émulsion entourée d'huile de silicone réactive. (A droite) La diffusion du catalyseur de platine et la modification de l'interface qui en résulte avec la formation de peaux.

réaction avance, la peau se déve-loppe et commence à former des rides. Le changement d'angle d'incidence de la lumière sur l'interface conduit à une figure de diffraction qui peut être mis en relation avec la longueur d'onde des rides. Cette méthode est également connue sous le nom de méthode de Schlieren et elle a été utilisée pour des études similaires [129, 130]. Ensuite, la longueur d'onde des rides peut être mise en relation avec l'épaisseur de la peau et les propriétés mécaniques du matériau. Dans la deuxième méthode, la peau se développe autour de l'interface d'une goutte. Pour caractériser la peau de la goutte, le volume de la goutte est modifié de manière sinusoïdale, le saut de pression sur l'interface et la peau est mesuré et mis en relation avec la déformation de la goutte, qui est détectée optiquement. Le signal obtenu est analysé à l'aide de la méthode de General Stress Decomposition (GSD). Cette technique d'analyse est connue en rhéologie volumique [116] et est également utilisée depuis peu en rhéologie d'interface [37, 36]. En utilisant différentes symétries, le signal peut être divisé en termes purement élastiques, purement visqueux et en termes de couplage. Ces termes peuvent ensuite être étudiés et analysés indépendamment les uns des autres (Fig.s A.8, 4.20, and **??**).

7.5 Interaction droploon-droploon

Pour comprendre les interactions entre deux interfaces avec des peaux, nous utilisons la configuration de la partie "Interactions Bulle-bulle ou goutte-goutte " et remplaçons le liquide des gouttes par une émulsion de PEG et du catalyseur de platine. Une peau de silicone se développe comme cela est décrit dans la partie "Caractérisation de la peau de silicone". En ajoutant un inhibiteur à la phase silicone, la réaction peut être arrêtée à

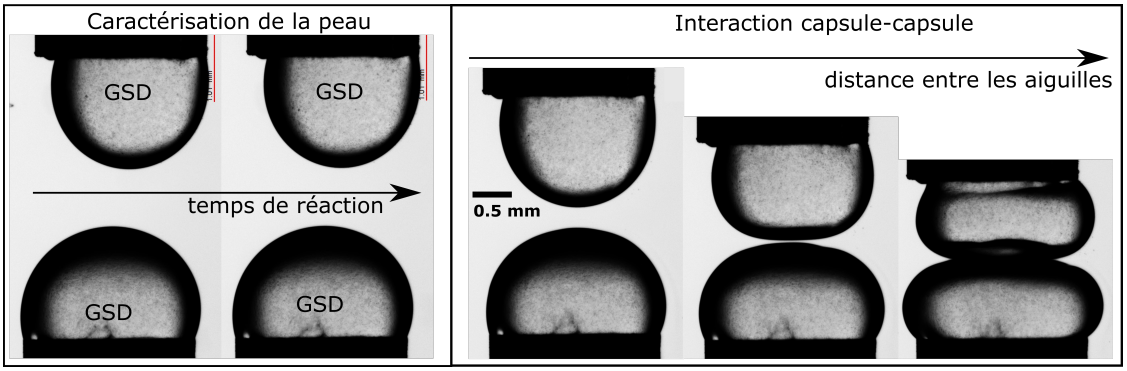

Figure 7.4: Procédure générale des expériences de double capsule. (Gauche) croissance de la peau avec caractérisation simultanée avec GSD, (A droite) Interactions entre deux capsules en les mettant en contact.

n'importe quel moment. Les deux interfaces sont mises en contact et on procède à une analyse qualitative et quantitative par analyse d'image et en mesurant le changement de la position relative des deux aiguilles et le saut de pression sur les deux interfaces (Fig. 7.4). Les formes à symétrie axiale, sans rides ni buckling sont privilégiées. Le choix des proportions des trois différents réactifs (MHDS, PDMS vinyl terminés et catalyseur de platine) se fait sur la base de la partie "Caractérisation de la peau de silicone".

7.6 Conclusion

En combinant des études expérimentales, numériques et théoriques nous avons développé différentes méthodologies pour étudier les surfaces minimales, les interactions entre les bulles, les gouttes ou les capsules et les interfaces avec ou sans visco-élasticité. Un système modèle pour l'étude des émulsions ou des mousses élastocapillaires a été développé avec des méthodes expérimentales combinant analyse de forme et mesures mécaniques. La question de l'influence des conditions limites sur les surfaces minimales ou les surfaces à courbure moyenne constante a également pu être résolue pour les conditions aux limites choisies. La question de l'influence de l'adhesion a également été adressée par l'observation des différents angles de contact entre les gouttes ou les bulles. Certaines questions sont encore sans réponse, d'autres ont reçu une réponse partielle. De nouvelles questions sont également apparues. Par exemple, il n'a pas été possible d'expliquer de ma-nière satisfaisante dans quelle mesure la tension de surface est indépendante de l'élasticité. Avec la décomposition générale des contraintes, il a été possible de séparer les différentes composantes (élastique, visqueuse et visco-élastique) de la réponse mécanique. Dans la plupart des cas, il est ainsi pos-sible de distinguer clairement les effets élastiques des effets visqueux. La méthodologie pour étudier les interactions entre les capsules est maintenant disponible. Mais il manque encore la compréhension théorique et la reproductibilité. Ces deux éléments sont en cours de développement et ne sont plus qu'une question de temps avant qu'ils ne soient complètement prêts à être utilisés. De nouvelles questions ont été soulevées par l'étude intensive des différentes instabilités de forme et de leur comportement. La position de certains points triples et la description théorique des formes non symétriques par rapport à l'axe ne sont que partiellement résolues. La question se pose également de savoir dans quelle mesure l'élasticité et la viscosité ont

une influence sur les formes et si de nouveaux types de formes peuvent être créés par l'association avec la tension de surface. Il serait intéressant de voir comment l'espace des formes se modifie avec une élasticité croissante par rapport à la tension de surface. Finalement, l'étude des interactions bulle-bulle ou goutte-goutte combinée à des mesures de balance de pression en couche mince pourrait donner lieu à une nouvelle méthode permettant d'étudier l'adhésion des interfaces de manière quantitative pour de nouveaux espaces de paramètres.

Chapter A
Appendix

Contents

A.1 Verticality and coaxiality of the two needles

The theoretical description of a problem is considerably simplified if axisymmetric boundary conditions are present. This is why we try to have boundary conditions that are as axisymmetric as possible in our experiments. In the following, we describe how this was achieved in the setup shown in Fig. 3.6a.
Therefore, we define the normal vector on the opening of the two needles with $\vec{n}^+$ and $\vec{n}^-$; with the indices "+" for upper and "−" for lower needle (Fig. A.1a). The normal vectors are obtained with our home-made lab-view code. To do this, we define the red boxes around the needles in the images, obtained with the two cameras (one for the xz-plane and one for the yz-plane. An example of one of this images is shown in A.1a. With the help of the strong intensity gradient at the edge of the needles we obtain the coordinates of the edges of the needles. The average of the two edges gives us the normal vector of the needle in the center for one needle and one plane. The needle opening is already axisymmetric due to their circular opening. However, it is also important that the acceleration due to gravity acts perpendicular to the needle opening. In order to fulfil this as best as possible, the angle between $\vec{n}^\pm$ and $\vec{g}$

$$\zeta^\pm = \arccos\left(\frac{\vec{n}^\pm \cdot \vec{g}}{|\vec{n}^\pm||\vec{g}|}\right), \tag{A.1}$$

must be as small as possible for both needles and both planes. The home-made lab-view program calculates $\zeta^\pm$ in real time with help of the cameras and the two vectors $\vec{n}^\pm$. By

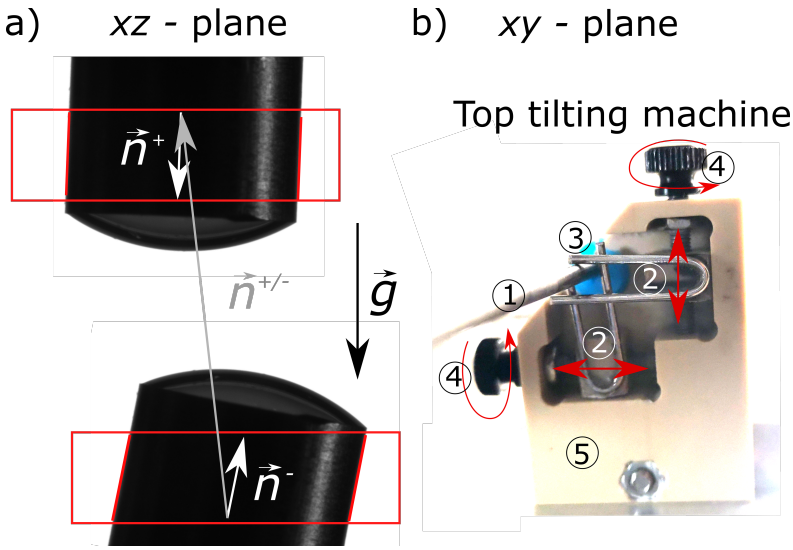

Figure A.1: a) Two needles in the xz-plane with the normal vectors on the needle openings $\vec{n}^+$ and $\vec{n}^-$ with the indices "+" for the upper needle and "−" for the lower needle. Obtained with the left and right edges of the needle, detected inside of the red squares for the upper and lower needle. The vector $\vec{n}^{+/-}$ connects the two beginnings of the two vectors $\vec{n}^+$ and $\vec{n}^-$. $\vec{g}$ is the direction of the earth acceleration. b) A picture of the upper tilting machine in the xy-plane with: 1) the needle, 2) the forks for the needle displacement, 3) a rubber fix point, 4) control buttons and 5) the framing of the tilting machine.

turning the control button ((4) in Fig. A.1b), the inclination of the needle changes in one of the two planes (xz- or yz-plane), as the needle is fixed by the rubber fix point ((3) in Fig. A.1b) and the point in contact with the fork ((4) in Fig. A.1b) moves. With this the angle $\zeta^{\pm}$ is minimized manually for both planes.
The two needles must then be aligned coaxially. To do this, the vector product

$$|\vec{n}^- \times \vec{n}^{+/-}| \tag{A.2}$$

is calculated with the home-made lab-view program and minimised by moving the upper needle with the micro-controller (Fig. 3.6a). The vector $\vec{n}^{+/-}$ starts the beginning of $\vec{n}^-$ and ends at the beginning of $\vec{n}^+$. The vector product is minimised separately for both planes.

A.2 Synchrotron absorption phase contrast silicon skin characterisations

We started our first investigations with the system of Gael Ginot [3], since we had access to the ANATOMIX beam line at the synchrotron Soleil for some hours. The ANATOMIX beam line uses absorption phase contrast of X-ray beams to measure very small density fluctuations with a pixel size between 0,13-20 µm [117].

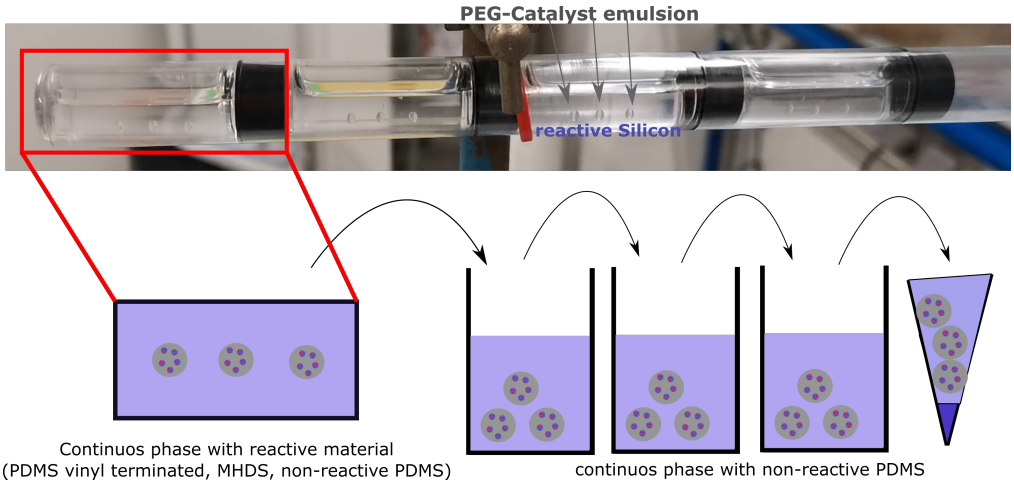

Figure A.2: The rotating cylindrical container with the silicon oil, a small amount of air and the PEG-catalyst emulsion drops in the top. In the bottom the washing procedure to stop the reaction with the conic container as the final sample container.

A.2.1 Sample preparation

To create closed capsules in the absence of capillaries or other supports, we dripped the PEG-Catalysator emulsion into a cyclindrical container filled with the silicon oil solution, Fig. A.2. After two to three drops, we closed the container and rotated it continuously with a small frequency so that the drops always fell downwards and never touched the wall of the container, Fig. A.2. After different times the reaction was stopped by taking the capsules out of the cylindrical container with a micro pipette and placed them in a solution with 100% non-reactive PDMS, Fig. A.2. This was repeated three times to be sure that the capsules are surrounded only by non-reactive PDMS, Fig. A.2. The last time the capsules where placed in a conic container with a suitable size for the measurements at ANATOMIX, Fig.s A.2 and A.3. Fig. A.3 shows all samples for different Φ_r and reaction times. With increasing reaction time and Φ_r the capsules start to buckle and loose there spherical shape. Only for short reaction times the capsules stay spherical.

A.2.2 Results of ANATOMIX

Due to the height resolution in space we where able to detect the interface between the drop and skin phase on a few µm precise, Fig. A.4. Fig. A.4a shows the 3D detected interface with help of a intensity threshold in the top and in the bottom the cross section through the interface with the normal vector $\vec{n}$ on the interface. The normal vector $\vec{n}$ is defined by the best fitting plane with the voxels with an intensity equal of the threshold in a small volume around the interface. Fig. A.4b plots the intensity of the voxels in direction of $\vec{n}$. The origin is on the detected interface. The red curve is the average of all detected profiles. The error bar is the standard derivation of the average.
The small drops on the interface are probably platin catalyst PDMS vinyl-terminated drops of the emulsion, which reached the interface after the skin was formed. They are not every where at the interface and We cannot say for sure whether they are solid or liquid. It is interesting that they form a contact angle. This could have to do with the

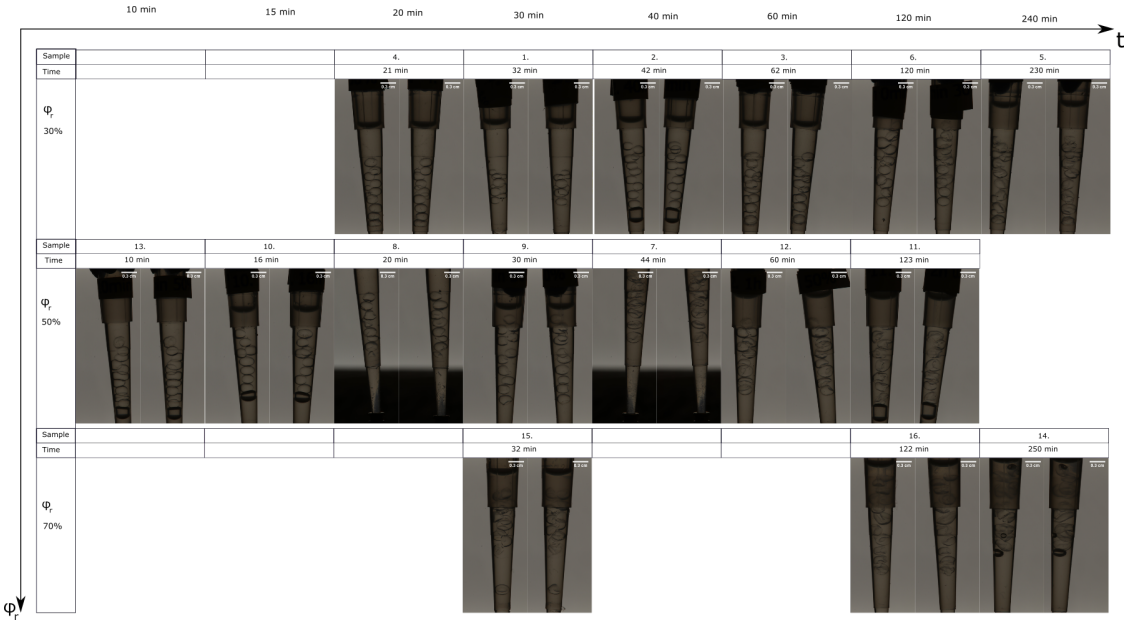

Figure A.3: Washed silicon capsules with different Φ_r and reaction times in there final conic container.

fact that they are solidified very quickly or that there is surface tension between the skin and the drops, even though they are both made of silicone. Another observation is the minimum and maximum of the intensity profile around the interface, A.4b. The distance to the interface and the intensity of the minimum and maximum is not changing a lot. The same characteristic occurred in all capsules analysed, regardless of Φ_r and whether the small droplets are located on the boundary surface as in Fig. A.4a.
To conclude, the intensity at the PEG-silicon interface shows a characteristic profile independent of Φ_r and the reaction time. In addition, small droplets could be identified on the interface. The exact origin of both phenomena could not be clarified. It remains open why the droplets form a contact angle, when they appear at the interface and whether they are solid or liquid. The exact relation between the density and the intensity at the interface is open as well.

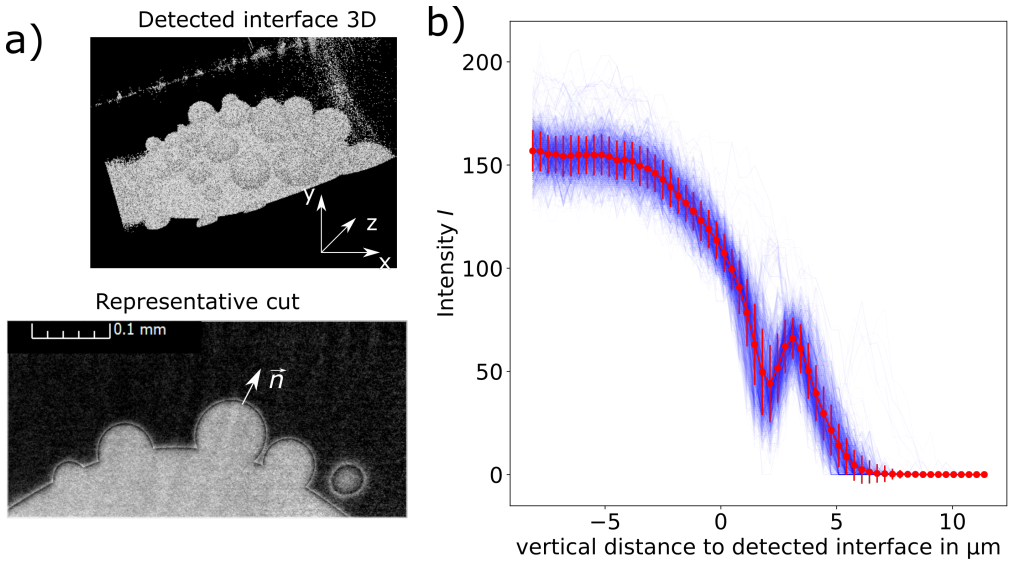

Figure A.4: a) Shows the 3D detected interface with help of a intensity threshold in the top and in the bottom the cross section through the interface with the normal vector $\vec{n}$ on the interface. b) plots the intensity of the voxels in direction of $\vec{n}$. The red curve is the average of all detected profiles. The error bar is the standard derivation of the average.

A.3 Petri dish experiments

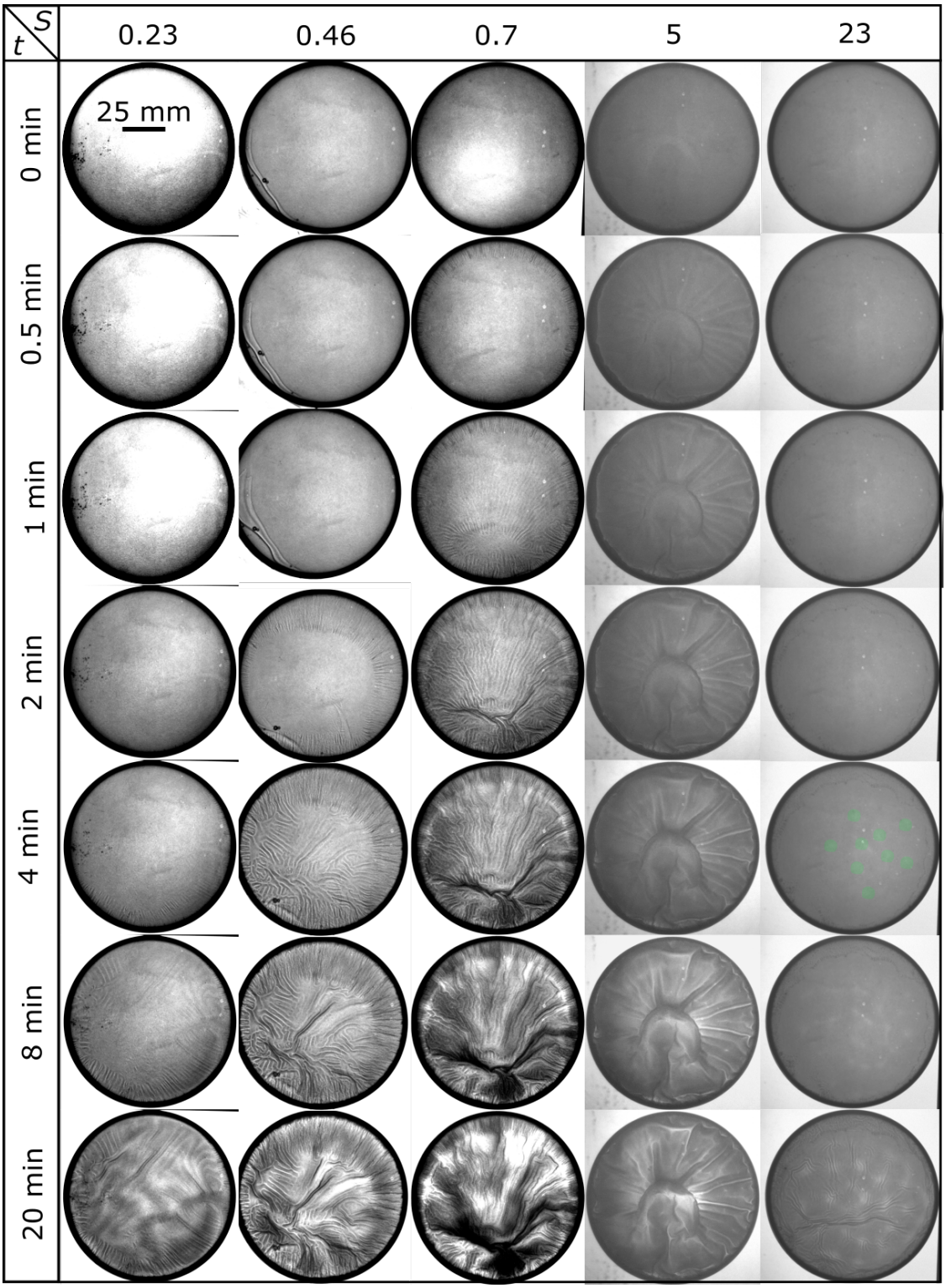

Figure A.5: Refraction pattern for the interface between the PEG-catalyst emulsion and the reactive silicon oil with increasing time in the columns form top to bottom and increasing S from left to right. The initial droplet concentration of the emulsion is for all $\Phi_{\mathrm{d}}(t_0) = 0.003$. The catalyst concentration in the droplets is $\Phi_{\mathrm{cat}} = 1$.

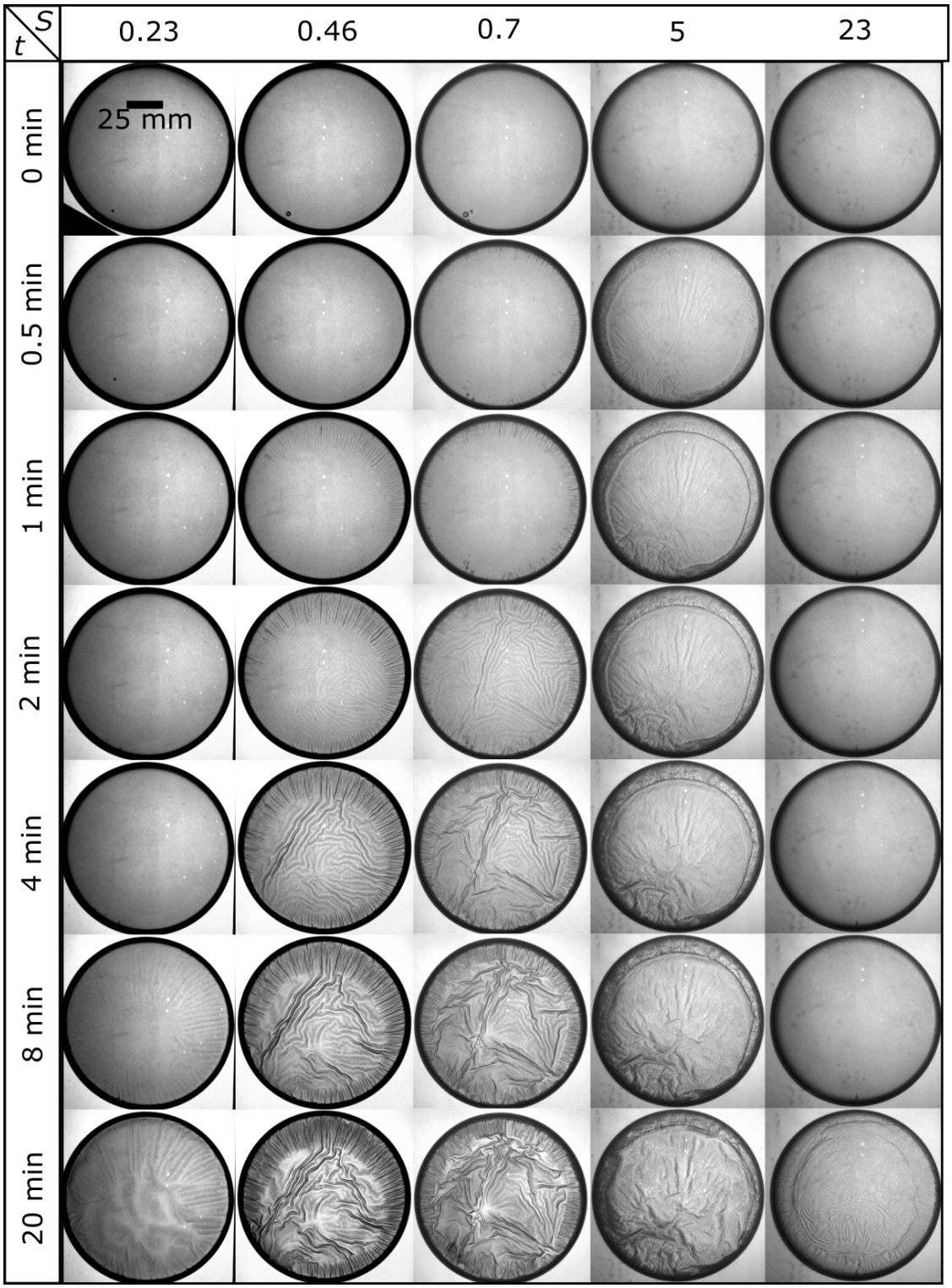

Figure A.6: Refraction pattern for the interface between the PEG-catalyst emulsion and the reactive silicon oil with increasing time in the column form top to bottom and increasing S in a row from left to right. The initial droplet concentration of the emulsion is for all $\Phi_{\mathrm{d}}(t_0) = 0.0003$. The catalyst concentration in the droplets is $\Phi_{\mathrm{cat}} = 1$.

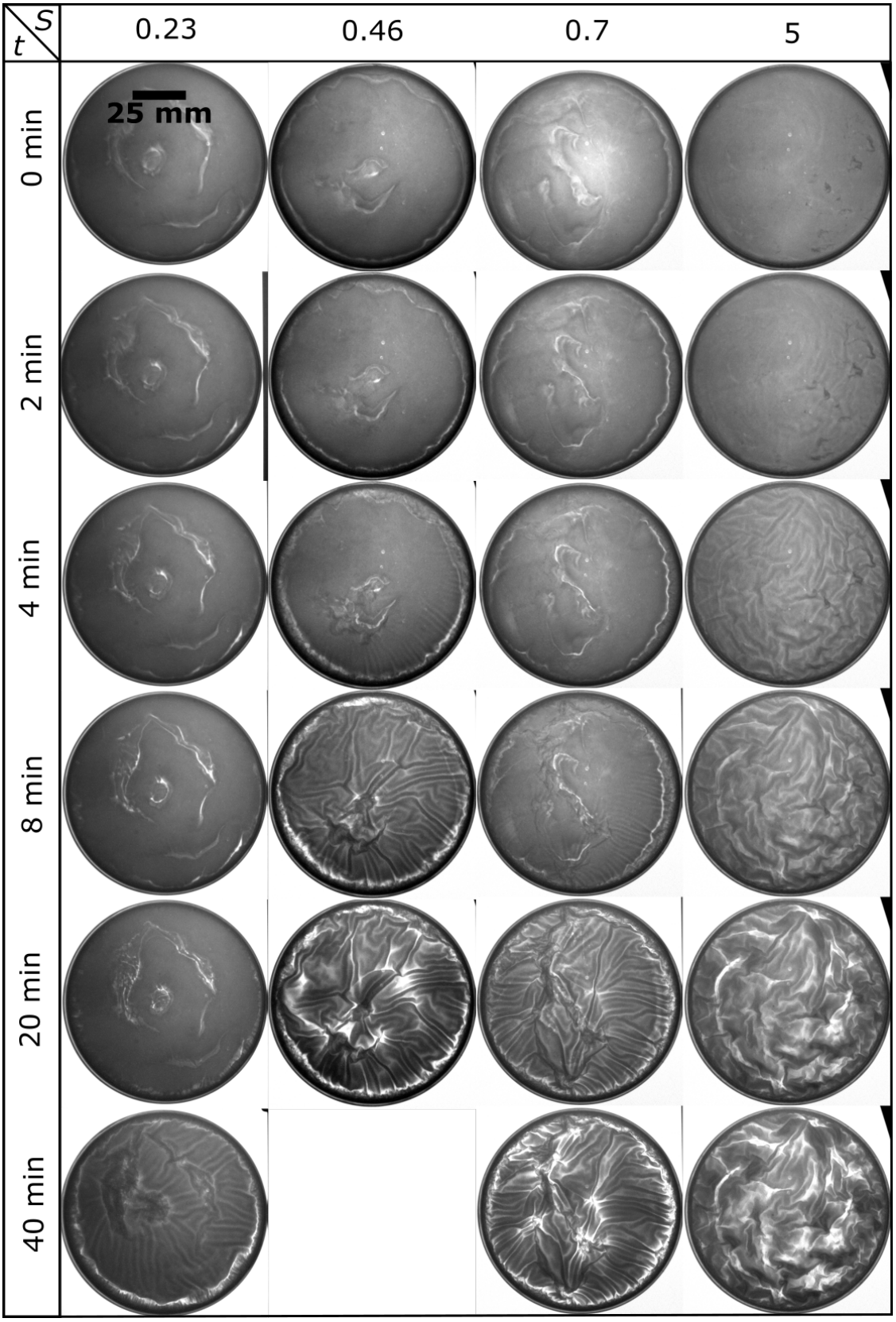

Figure A.7: Refraction pattern for the interface between the PEG-catalyst emulsion and the reactive silicon oil with increasing time in the column form top to bottom and increasing S in a row from left to right. The initial droplet concentration of the emulsion is for all $\Phi_{\mathrm{d}}(t_0) = 0.003$. The catalyst concentration in the droplets is $\Phi_{\mathrm{cat}} = 0.1$.

A.4 GSD Results

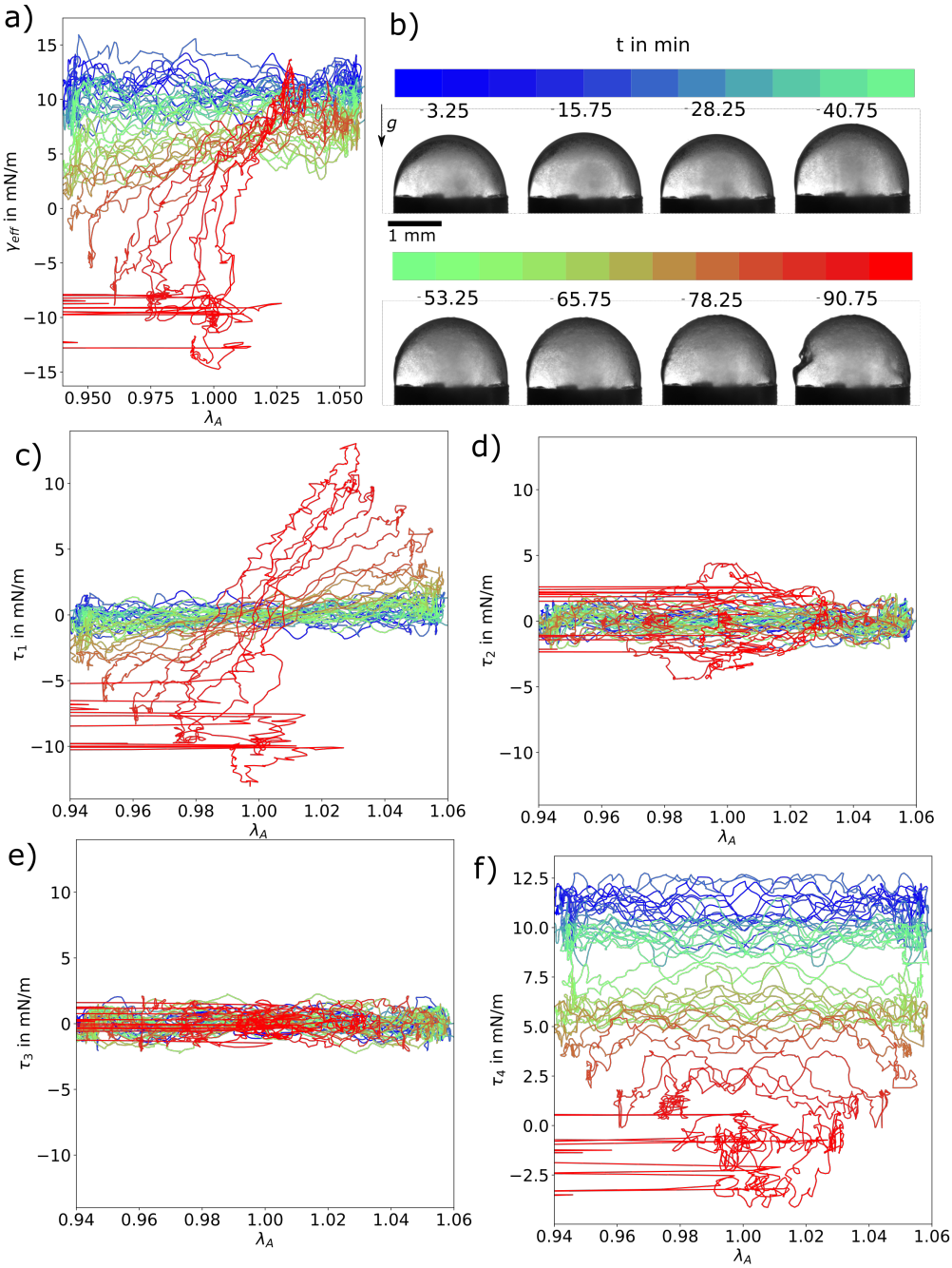

Figure A.8: Results for dilational interfacial shear rheology (Section 4.3.6.2) for $S = 0.24$, $\Phi_d = 0.003$ and $\Phi_{cat} = 0.1$ of a sessile drop: a) γ_{eff} from Equ. (4.15), b) Time legend with a series of images of the corresponding drops/droploons/capsules, c) τ_1 from Equ. (4.32), d) τ_2 from Equ. (4.33), e) τ_3 from Equ. (4.34) and f) τ_4 from Equ. (4.35).

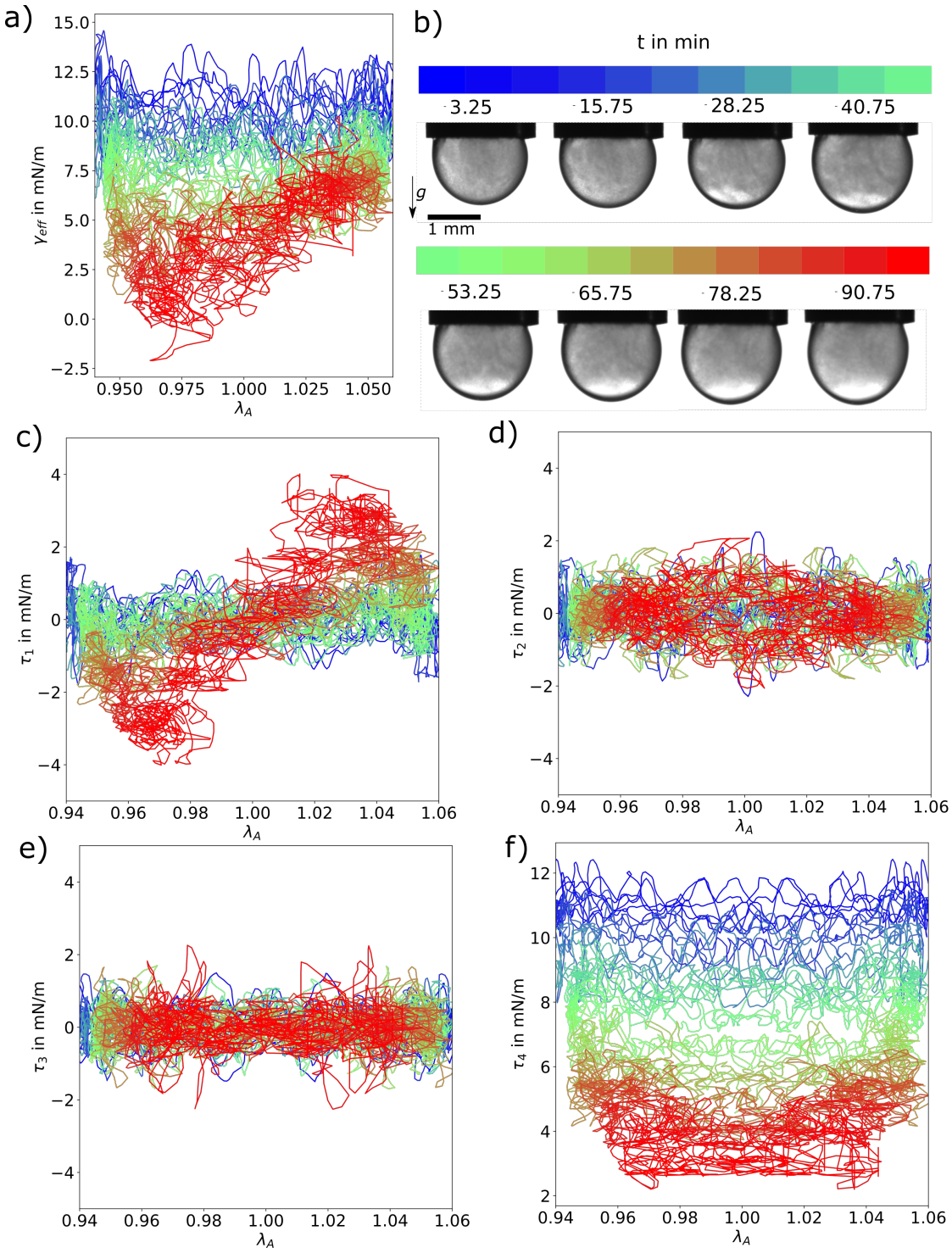

Figure A.9: Results for dilational interfacial shear rheology (Section 4.3.6.2) for $S = 0.24$, $\Phi_d = 0.003$ and $\Phi_{cat} = 0.1$ of a pendant drop: a) γ_{eff} from Equ. (4.15), b) Time legend with a series of images of the corresponding drops/droploons/capsules, c) τ_1 from Equ. (4.32), d) τ_2 from Equ. (4.33), e) τ_3 from Equ. (4.34) and f) τ_4 from Equ. (4.35).

Bibliography

[1] M. M. Alimov, A. V. Bazilevsky, and K. G. Kornev, *Soap film on two noncircular frames*, Physics of Fluids **33**, 052104 (2021). iii, 17, 18, 21, 26, 27, 41, 44, 47, 48, 53, 54, 166

[2] A. Giustiniani, S. Weis, C. Poulard, P. H. Kamm, F. García-Moreno, M. Schröter, and W. Drenckhan, *Skinny emulsions take on granular matter*, Soft Matter **14**, 7310–7323 (2018). iv, 104, 105, 106, 108, 110, 114, 148, 168

[3] G. Ginot, M. Hamann, L. Jacomine, F. Walzel, A. Egele, D. Favier, F. Schosseler, M. Legros, A. Carvalho, C. Foussat *et al.*, *PEG-in-PDMS drops stabilised by soft silicone skins as a model system for elastocapillary emulsions with explicit morphology control*, Journal of Colloid and Interface Science **628**, 1044–1057 (2022). iv, 104, 106, 108, 110, 113, 123, 148, 168, 174

[4] I. Cantat, S. Cohen-Addad, F. Elias, F. Graner, R. Höhler, O. Pitois, F. Rouyer, and A. Saint-Jalmes, *Foams: structure and dynamics* (OUP Oxford, 2013). 1, 3, 4, 164

[5] D. L. Weaire and S. Hutzler, *The physics of foams* (Oxford University Press, 1999). 1, 3, 164

[6] L. L. Schramm, *Emulsions, foams, suspensions, and aerosols: microscience and applications* (John Wiley & Sons, 2014). 1, 164

[7] T. F. Tadros, *Emulsion science and technology: a general introduction* (Wiley Online Library, 2009). 1

[8] T. F. Tadros, *Emulsion formation, stability, and rheology* (Wiley Online Library, 2013). 1

[9] R. Miller and L. Liggieri, *Interfacial rheology*, vol. 1 (CRC Press, 2009). 2, 14

[10] J. A. F. Plateau, *Statique expérimentale et théorique des liquides soumis aux seules forces moléculaires*, vol. 2 (Gauthier-Villars, 1873). 3, 18, 19

[11] J. Douglas, *Solution of the problem of Plateau*, Transactions of the American Mathematical Society **33**, 263–321 (1931). 6

[12] M. Deserno, *Elastic deformation of a fluid membrane upon colloid binding*, Physical Review E **69**, 031903 (2004). 6

[13] D. Hoffman and W. H. Meeks III, *Minimal surfaces based on the catenoid*, The American Mathematical Monthly **97**, 702–730 (1990). 6, 7

[14] H. F. Scherk, *Bemerkungen über die kleinste Fläche innerhalb gegebener Grenzen.*, (1835). 7

[15] H. Karcher, *Embedded minimal surfaces derived from Scherk's examples*, Manuscripta mathematica **62**, 83–114 (1988). 7, 94

[16] *MathWorld: The Web's Most Extensive Mathematics Resource*, URL: https://mathworld.wolfram.com/. 7

[17] P. S. marquis de Laplace, *Traité de mécanique céleste*, vol. 5 (Chez JBM Duprat, libraire pour les mathématiques, quai des Augustins, 1825). 8

[18] T. Young, *An essay on the cohesion of fluids*, in Abstracts of the Papers Printed in the Philosophical Transactions of the Royal Society of London (The Royal Society London, 1832), 1, pp. 171–172. 8

[19] J. L. M. Barbosa and A. G. Colares, *Minimal surfaces in R 3*, vol. 1195 (Springer, 2006). 8

[20] C. Delaunay, *Sur la surface de révolution dont la courbure moyenne est constante*, Journal de mathématiques pures et appliquées **6**, 309–315 (1841). 8, 59, 69, 99, 167

[21] L. Euler, *Methodus inveniendi lineas curvas maximi minimive proprietate gaudentes sive solutio problematis isoperimetrici latissimo sensu accepti*, vol. 1 (Springer Science & Business Media, 1952). 8, 18, 19

[22] J. Meusnier, *Mémoire sur la courbure des surfaces, Mém. div. sav*, (1785). 8, 18, 19

[23] R. Courant, *Soap Film Experiments with Minimal Surfaces*, The American Mathematical Monthly **47**, 167–174 (1940). URL: https://doi.org/10.1080/00029890.1940.11990957. 8, 19

[24] *The Calculus of Variations* (John Wiley & Sons, Ltd, 1989), chap. 4, pp. 164–274. URL: https://onlinelibrary.wiley.com/doi/abs/10.1002/9783527617210.ch4. 8

[25] J. N. Israelachvili, *Intermolecular and surface forces* (Academic press, 2011). 9, 10

[26] B. Toshev and D. Platikanov, *Disjoining pressure, contact angles and line tension in free thin liquid films*, Advances in colloid and interface science **40**, 157–189 (1992). 10

[27] A. Scheludko, B. Radoev, and T. Kolarov, *Tension of liquid films and contact angles between film and bulk liquid*, Transactions of the Faraday Society **64**, 2213–2220 (1968). 10, 11

[28] J. Seknagi, *Structure et perméabilité des mousses liquides en présence d'une interaction attractive entre les bulles*, Ph.D. thesis, Sorbonne Universite (2022). 11

[29] J. Bibette, T. Mason, H. Gang, D. Weitz, and P. Poulin, *Structure of adhesive emulsions*, Langmuir **9**, 3352–3356 (1993). 11, 99

[30] E. Ventsel, T. Krauthammer, and E. Carrera, *Thin plates and shells: theory, analysis, and applications*, Appl. Mech. Rev. **55**, B72–B73 (2002). 12, 13

[31] I. Müller and P. Strehlow, *Rubber and rubber balloons: paradigms of thermodynamics*, vol. 637 (Springer Science & Business Media, 2004). 13

[32] G. Ginot, F. S. Kratz, F. Walzel, J. Farago, J. Kierfeld, R. Höhler, and W. Drenckhan, *Pressure–deformation relations of elasto-capillary drops (droploons) on capillaries*, Soft Matter **17**, 9131–9153 (2021). 13, 24, 119, 121

[33] M. Nagel, T. A. Tervoort, and J. Vermant, *From drop-shape analysis to stress-fitting elastometry*, Advances in colloid and interface science **247**, 33–51 (2017). 13

[34] J. Hegemann, S. Knoche, S. Egger, M. Kott, S. Demand, A. Unverfehrt, H. Rehage, and J. Kierfeld, *Pendant capsule elastometry*, Journal of colloid and interface science **513**, 549–565 (2018). 13, 14

[35] R. Myrvold and F. K. Hansen, *Surface elasticity and viscosity from oscillating bubbles measured by automatic axisymmetric drop shape analysis*, Journal of colloid and interface science **207**, 97–105 (1998). 14

[36] S. Pivard, L. Jacomine, F. S. Kratz, C. Foussat, J.-P. Lamps, M. Legros, F. Boulmedais, J. Kierfeld, F. Schosseler, and W. Drenckhan, *Interfacial rheology of linearly growing polyelectrolyte multilayers at the water–air interface: from liquid to solid viscoelasticity*, Soft Matter **20**, 1347–1360 (2024). 14, 106, 120, 122, 169

[37] A. de Groot, J. Yang, and L. M. Sagis, *Surface stress decomposition in large amplitude oscillatory interfacial dilatation of complex interfaces*, Journal of Colloid and Interface Science **638**, 569–581 (2023). 14, 106, 119, 120, 122, 169

[38] S. Vandebril, A. Franck, G. G. Fuller, P. Moldenaers, and J. Vermant, *A double wall-ring geometry for interfacial shear rheometry*, Rheologica Acta **49**, 131–144 (2010). 14

[39] G. Domokos, P. Holmes, and B. Royce, *Constrained euler buckling*, Journal of Nonlinear Science **7**, 281–314 (1997). 14

[40] S. Hutzler, J. Ryan-Purcell, A. Mughal, and D. Weaire, *A continuum description of the buckling of a line of spheres in a transverse harmonic confining potential*, Royal Society Open Science **10**, 230293 (2023). 14

[41] G. Bradley and D. Weaire, *Instabilities of two liquid drops in contact*, Computing in Science & Engineering **3**, 16–21 (2001). 15, 58, 78, 79, 87, 99, 167

[42] F. Walzel, A. Requier, K. Boschi, J. Farago, P. Fuchs, F. Thalmann, W. Drenckhan, P. Muller, and T. Charitat, *Perturbing the catenoid: Stability and mechanical properties of nonaxisymmetric minimal surfaces*, Physical Review E **106**, 014803 (2022). 17, 166

[43] C. Lagrange, *Essai d'une nouvelle méthodes pour déterminer les maxima et les minima*, Misc. Taur. **2**, 356–357 (1760). 18

[44] J. C. Nitsche, *Lectures on minimal surfaces: vol. 1* (Cambridge university press, 1989). 18

[45] W. Meeks and J. Pérez, *A Survey on Classical Minimal Surface Theory*, University lecture series (American Mathematical Society, 2012). URL: https://books.google.fr/books?id=tSyU7A7XfaAC. 18

[46] M. Emmer, *Minimal Surfaces and Architecture: New Forms*, NEXUS NETWORK JOURNAL **15**, 227–239 (2013). 18

[47] S. Torquato, S. Hyun, and A. Donev, *Multifunctional Composites: Optimizing Microstructures for Simultaneous Transport of Heat and Electricity*, Phys. Rev. Lett. **89**, 266601 (2002). URL: https://link.aps.org/doi/10.1103/PhysRevLett.89.266601. 18

[48] S. Zhou and Q. Li, *The relation of constant mean curvature surfaces to multiphase composites with extremal thermal conductivity*, Journal of Physics D: Applied Physics **40**, 6083–6093 (2007). URL: https://doi.org/10.1088/0022-3727/40/19/048. 18

[49] Y. Chen, S. Zhou, and Q. Li, *Multiobjective topology optimization for finite periodic structures*, Computers & Structures **88**, 806–811 (2010). URL: https://www.sciencedirect.com/science/article/pii/S0045794909002600. 18

[50] S. C. Kapfer, S. T. Hyde, K. Mecke, C. H. Arns, and G. E. Schröder-Turk, *Minimal surface scaffold designs for tissue engineering*, Biomaterials **32**, 6875–6882 (2011). URL: https://www.sciencedirect.com/science/article/pii/S0142961211006776. 18

[51] J. Douglas, *Solution of the problem of Plateau*, Bulletin of the American Mathematical Society pp. 143–259 (1927). 19

[52] R. Courant, *The Existence of a Minimal Surface of Least Area Bounded by Prescribed Jordan Arcs and Prescribed Surfaces*, Proceedings of the National Academy of Sciences **24**, 97–101 (1938). URL: https://www.pnas.org/content/24/2/97. 19

[53] M. A. Erle, R. Gillette, and D. Dyson, *Stability of interfaces of revolution with constant surface tension—the case of the catenoid*, The Chemical Engineering Journal **1**, 97–109 (1970). 19, 90

[54] V. A. Toponogov, *Differential geometry of curves and surfaces* (Springer, 2006). 19

[55] H. Sagan, *Introduction to the Calculus of Variations* (Courier Corporation, 1992). 19

[56] L. Durand, *Stability and oscillations of a soap film: An analytic treatment*, American Journal of Physics **49**, 334–343 (1981). URL: https://doi.org/10.1119/1.12506. 19

[57] M. B. Amar, P. P. da Silva, N. Limodin, A. Langlois, M. Brazovskaia, C. Even, I. Chikina, and P. Pieranski, *Stability and vibrations of catenoid-shaped smectic films*, The European Physical Journal B-Condensed Matter and Complex Systems **3**, 197–202 (1998). 19

[58] S. Jana and S. Kar, *Perturbative stability of catenoidal soap films*, The European Physical Journal Plus **128**, 108 (2013). URL: https://doi.org/10.1140/epjp/i2013-13108-y. 19

[59] S. A. Cryer and P. H. Steen, *Collapse of the soap-film bridge: quasistatic description*, Journal of colloid and interface science **154**, 276–288 (1992). 19

[60] R. E. Goldstein, A. I. Pesci, C. Raufaste, and J. D. Shemilt, *Geometry of catenoidal soap film collapse induced by boundary deformation*, Phys. Rev. E **104**, 035105 (2021). URL: https://link.aps.org/doi/10.1103/PhysRevE.104.035105. 19

[61] L. Salkin, A. Schmit, P. Panizza, and L. Courbin, *Influence of boundary conditions on the existence and stability of minimal surfaces of revolution of soap films*, American Journal of Physics pp. 839–850 (2014). 19, 29, 46

[62] K. A. Brakke, *Surface Evolver manual.*, (2013). 21

[63] M. M. Alimov, A. V. Bazilevsky, and K. G. Kornev, *Minimal surfaces on mirror-symmetric frames: a fluid dynamics analogy*, Journal of Fluid Mechanics **897**, A36 (2020). 21

[64] K. Brakke, *The Surface Evolver*, Experimental Mathematics **1**, 141–165 (1992). URL: http://dx.doi.org/10.1080/10586458.1992.10504253. 23, 78, 99, 166, 167

[65] K. A. Brakke, *The surface evolver and the stability of liquid surfaces*, Philosophical transactions of the royal society of london. series a: mathematical, physical and engineering sciences **354**, 2143–2157 (1996). 25

[66] P. Grandgeorge, N. Krins, A. Hourlier-Fragette, C. Laberty-Robert, N. Sébastien, and A. Antkowiak, *Capillary-induced folds fuel extreme shape changes in thick wicked membranes*, Science pp. 296–299 (2018). 53

[67] R. Hohler and S. Cohen-Addad, *Many-body interactions in soft jammed materials*, Soft Matter **13**, 1371–1383 (2017). URL: http://dx.doi.org/10.1039/C6SM01567K. 57

[68] R. Höhler and D. Weaire, *Can liquid foams and emulsions be modeled as packings of soft elastic particles?*, Advances in Colloid and Interface Science (2018). URL: http://www.sciencedirect.com/science/article/pii/S0001868618302744. 57

[69] G. Ginot, R. Höhler, S. Mariot, A. Kraynik, and W. Drenckhan, *Juggling bubbles in square capillaries: an experimental proof of non-pairwise bubble interactions*, Soft Matter **15**, 4570–4582 (2019). URL: http://dx.doi.org/10.1039/C8SM02477D. 57

[70] Y. Rotenberg, L. Boruvka, and A. Neumann, *Determination of surface tension and contact angle from the shapes of axisymmetric fluid interfaces*, Journal of colloid and interface science **93**, 169–183 (1983). 57

[71] J. D. Berry, M. J. Neeson, R. R. Dagastine, D. Y. Chan, and R. F. Tabor, *Measurement of surface and interfacial tension using pendant drop tensiometry*, Journal of colloid and interface science **454**, 226–237 (2015). 57

[72] F. S. Kratz and J. Kierfeld, *Pendant drop tensiometry: A machine learning approach*, Journal of Chemical Physics **153**, 094102 (2020). 57

[73] D. Y. Chan, E. Klaseboer, and R. Manica, *Film drainage and coalescence between deformable drops and bubbles*, Soft Matter **7**, 2235–2264 (2011). 57

[74] R. Han, S. Li, A. Zhang, and Q. Wang, *Modelling for three dimensional coalescence of two bubbles*, Physics of Fluids **28**, 062104 (2016). 57

[75] H.-H.-Q. Dinh, E. Santanach-Carreras, M. Lalanne-Aulet, V. Schmitt, P. Panizza, and F. Lequeux, *Effect of a surfactant mixture on coalescence occurring in concentrated emulsions: the hole nucleation theory revisited*, Langmuir **37**, 8726–8737 (2021). 57

[76] T. Morokuma and Y. Utaka, *Variation of the liquid film thickness distribution between contacting twin air bubbles during the coalescence process in water and ethanol pools*, International Journal of Heat and Mass Transfer **98**, 96–107 (2016). 57

[77] A. S. Vishen, J. Prost, and P. Sens, *Quantitative comparison of cell–cell detachment force in different experimental setups*, The European Physical Journal E **47**, 22 (2024). 57

[78] R. F. Tabor, H. Lockie, D. Mair, R. Manica, D. Y. C. Chan, F. Grieser, and R. R. Dagastine, *Combined AFMConfocal Microscopy of Oil Droplets: Absolute Separations and Forces in Nanofilms*, The Journal of Physical Chemistry Letters **2**, 961–965 (2011). URL: https://doi.org/10.1021/jz2003606, doi: 10.1021/jz2003606. 57

[79] J. M. Frostad, M. C. Collins, and L. G. Leal, *Cantilevered-Capillary Force Apparatus for Measuring Multiphase Fluid Interactions*, Langmuir **29**, 4715–4725 (2013). URL: https://doi.org/10.1021/la304115k, doi: 10.1021/la304115k. 57, 58, 80, 167

[80] K. Li, W. Wang, F. Xiao, Y. Ge, H. Jin, Z. Yu, J. Gong, W. Gao, and Z. Peng, *Atomic Force Microscopy Study of Non-DLVO Interactions between Drops and Bubbles*, Langmuir **37**, 6830–6837 (2021). URL: https://doi.org/10.1021/acs.langmuir.1c00937, doi: 10.1021/acs.langmuir.1c00937. 57

[81] S. Bohn, *Bubbles under stress*, The European Physical Journal E **11**, 177–189 (2003). URL: https://doi.org/10.1140/epje/i2003-10014-x. 58, 79, 80, 87, 99, 167

[82] M. A. Fortes, M. E. Rosa, M. F. Vaz, and P. I. Teixeira, *Mechanical instabilities of bubble clusters between parallel walls*, European Physical Journal E **15**, 395–406 (2004). 58, 79, 87, 99, 167

[83] K. Mittal, *Advances in Contact Angle, Wettability and Adhesion, Volume 2*, Adhesion and Adhesives: Fundamental and Applied Aspects (Wiley, 2015). URL: https://books.google.fr/books?id=Ol-aCgAAQBAJ. 62

[84] C. Cohen, B. Darbois Texier, E. Reyssat, J. H. Snoeijer, D. Quéré, and C. Clanet, *On the shape of giant soap bubbles*, Proceedings of the National Academy of Sciences **114**, 2515–2519 (2017). 68

[85] K. Kenmotsu, *Surfaces with constant mean curvature*, 221 (American Mathematical Soc., 2003). 69

[86] B. G. Chen and R. D. Kamien, *Nematic films and radially anisotropic delaunay surfaces*, European Physical Journal E **28**, 315–329 (2009). 70

[87] B. Athukorallage, T. Paragoda, and M. Toda, *Roulettes of conics, Delaunay surfaces and applications*, . 70, 71

[88] Wikipedia, *Conic sections*, (2023). URL: https://en.wikipedia.org/wiki/File:Conic_Sections.svg. 73

[89] R. Gillette and D. Dyson, *Stability of fluid interfaces of revolution between equal solid circular plates*, The Chemical Engineering Journal **2**, 44–54 (1971). 75, 88

[90] J. H. Maddocks, *Stability and Folds*, . 75

[91] L. Salkin, A. Schmit, P. Panizza, and L. Courbin, *Influence of boundary conditions on the existence and stability of minimal surfaces of revolution made of soap films*, American Journal of Physics **82**, 839–847 (2014). 76

[92] X. Zhang, R. S. Padgett, and O. A. Basaran, *Nonlinear deformation and breakup of stretching liquid bridges*, Journal of Fluid Mechanics **329**, 207–245 (1996). 88

[93] T. I. Vogel, *Stability of a liquid drop trapped between two planes*, (1987). URL: http://www.siam.org/journals/ojsa.php. 88, 99

[94] S. Cox, A. Kraynik, D. Weaire, and S. Hutzler, *Ideal wet two-dimensional foams and emulsions with finite contact angle*, Soft Matter **14**, 5922–5929 (2018). 99

[95] D. Filip, V. Uricanu, M. H. Duits, D. Van den Ende, J. Mellema, W. Agterof, and F. Mugele, *Microrheology of aggregated emulsion droplet networks, studied with AFM- CSLM*, Langmuir **22**, 560–574 (2006). 99

[96] C. Stubenrauch and R. Von Klitzing, *Disjoining pressure in thin liquid foam and emulsion films—new concepts and perspectives*, Journal of Physics: condensed matter **15**, R1197 (2003). 100

[97] S. Andrieux, P. Muller, M. Kaushal, N. S. M. Vera, R. Bollache, C. Honorez, A. Cagna, and W. Drenckhan, *Microfluidic thin film pressure balance for the study of complex thin films*, Lab on a Chip **21**, 412–420 (2021). 100

[98] G. Andersson, E. Carey, and C. Stubenrauch, *Disjoining pressure study of formamide foam films stabilized by surfactants*, Langmuir **26**, 7752–7760 (2010). 100

[99] N. C. Christov, K. D. Danov, Y. Zeng, P. A. Kralchevsky, and R. von Klitzing, *Oscillatory structural forces due to nonionic surfactant micelles: Data by colloidal-probe AFM vs theory*, Langmuir **26**, 915–923 (2010). 100

[100] K. Kataoka, A. Harada, and Y. Nagasaki, *Block copolymer micelles for drug delivery: design, characterization and biological significance*, Advanced drug delivery reviews **64**, 37–48 (2012). 104, 148

[101] B. B. C. Youan, T. L. Jackson, L. Dickens, C. Hernandez, and G. Owusu-Ababio, *Protein release profiles and morphology of biodegradable microcapsules containing an oily core*, Journal of controlled release **76**, 313–326 (2001). 104, 148

[102] S. Rokka and P. Rantamäki, *Protecting probiotic bacteria by microencapsulation: challenges for industrial applications*, European Food Research and Technology **231**, 1–12 (2010). 104, 148

[103] A. Madene, M. Jacquot, J. Scher, and S. Desobry, *Flavour encapsulation and controlled release–a review*, International journal of food science & technology **41**, 1–21 (2006). 104, 148

[104] F. Sopeña, C. Maqueda, and E. Morillo, *Controlled release formulations of herbicides based on micro-encapsulation*, Ciencia e investigación agraria **36**, 27–42 (2009). 104

[105] M. A. Salem, W. Al-Zayadneh, and A. J. Cheruth, *Water conservation and management with hydrophobic encapsulation of sand*, Water resources management **24**, 2237–2246 (2010). 104

[106] A. Ammala, *Biodegradable polymers as encapsulation materials for cosmetics and personal care markets*, International journal of cosmetic science **35**, 113–124 (2013). 104

[107] G. Nelson, *Application of microencapsulation in textiles*, International journal of pharmaceutics **242**, 55–62 (2002). 104

[108] C. E. Akers Jr and J. X. Sun, *Encapsulated pigment for ink-jet ink formulations and methods of producing same*, (2008). US Patent 7,354,962. 104

[109] B.-W. Park, D.-Y. Yoon, and D.-S. Kim, *Recent progress in bio-sensing techniques with encapsulated enzymes*, Biosensors and Bioelectronics **26**, 1–10 (2010). 104

[110] D. G. Shchukin, D. O. Grigoriev, and H. Möhwald, *Application of smart organic nanocontainers in feedback active coatings*, Soft Matter **6**, 720–725 (2010). 104

[111] V. A. A. Raj and R. Velraj, *Review on free cooling of buildings using phase change materials*, Renewable and Sustainable Energy Reviews **14**, 2819–2829 (2010). 104

[112] S. Abang, E.-S. Chan, and D. Poncelet, *Effects of process variables on the encapsulation of oil in ca-alginate capsules using an inverse gelation technique*, Journal of microencapsulation **29**, 417–428 (2012). 105, 148

[113] Q. Chen, N. Singh, K. Schirrmann, Q. Zhou, I. L. Chernyavsky, and A. Juel, *Robust fabrication of ultra-soft tunable PDMS microcapsules as a biomimetic model for red blood cells*, Soft Matter **19**, 5249–5261 (2023). 105

[114] S.-H. Kim, J. W. Kim, J.-C. Cho, and D. A. Weitz, *Double-emulsion drops with ultra-thin shells for capsule templates*, Lab on a Chip **11**, 3162–3166 (2011). 105

[115] M. P. Neubauer, M. Poehlmann, and A. Fery, *Microcapsule mechanics: From stability to function*, Advances in colloid and interface science **207**, 65–80 (2014). 105, 145

[116] W. Yu, P. Wang, and C. Zhou, *General stress decomposition in nonlinear oscillatory shear flow*, Journal of Rheology **53**, 215–238 (2009). 106, 119, 121, 122, 123, 161, 169

[117] T. Weitkamp, M. Scheel, J. Giorgetta, V. Joyet, V. Le Roux, G. Cauchon, T. Moreno, F. Polack, A. Thompson, and J. Samama, *The tomography beamline ANATOMIX at Synchrotron SOLEIL*, in Journal of Physics: Conference Series, vol. 849 (IOP Publishing, 2017), vol. 849, p. 012037. 109, 174

[118] K. Herrmann, *Härteprüfung an Metallen und Kunststoffen: Grundlagen und Überblick zu modernen Verfahren; mit 66 Tabellen* (expert verlag, 2007). 110

[119] L. Cheng, X. Xia, W. Yu, L. Scriven, and W. W. Gerberich, *Flat-punch indentation of viscoelastic material*, Journal of Polymer Science Part B: Polymer Physics **38**, 10–22 (2000). 110

[120] A. H.-F. F. S. L. J. W. D. Qiwei Li, Luca Fiorucci, *Optimization of Silicone Formulations for Architected Silicone Materials*, Internship report (2023). 113

[121] R. Pecora, *Dynamic light scattering measurement of nanometer particles in liquids*, Journal of nanoparticle research **2**, 123–131 (2000). 113

[122] T. Gaillard, M. Roché, C. Honorez, M. Jumeau, A. Balan, C. Jedrzejczyk, and W. Drenckhan, *Controlled foam generation using cyclic diphasic flows through a constriction*, International Journal of Multiphase Flow **96**, 173–187 (2017). 113

[123] H. Mehrer, *Continuum theory of diffusion*, Diffusion in Solids: Fundamentals, Methods, Materials, Diffusion-Controlled Processes pp. 27–36 (2007). 124

[124] A. Einstein, *Über die von der molekularkinetischen Theorie der Wärme geforderte Bewegung von in ruhenden Flüssigkeiten suspendierten Teilchen*, Annalen der physik **4** (1905). 124

[125] C. Zoldesi, I. Ivanovska, C. Quilliet, G. Wuite, and A. Imhof, *Elastic properties of hollow colloidal particles*, Physical Review E—Statistical, Nonlinear, and Soft Matter Physics **78**, 051401 (2008). 132

[126] A. Fery, F. Dubreuil, and H. Möhwald, *Mechanics of artificial microcapsules*, New journal of Physics **6**, 18 (2004). 132

[127] S. Knoche and J. Kierfeld, *Buckling of spherical capsules*, Physical Review E—Statistical, Nonlinear, and Soft Matter Physics **84**, 046608 (2011). 132, 135, 138

[128] S. Knoche and J. Kierfeld, *The secondary buckling transition: wrinkling of buckled spherical shells*, The European Physical Journal E **37**, 1–21 (2014). 132, 135

[129] F. Brau, P. Damman, H. Diamant, and T. A. Witten, *Wrinkle to fold transition: influence of the substrate response*, Soft Matter **9**, 8177–8186 (2013). 135, 137, 169

[130] E. Jambon-Puillet, *Folds in floating membranes: from elastic sheets to granular rafts*, Ph.D. thesis, Université Pierre et Marie Curie-Paris VI (2016). 135, 137, 169

[131] J. Huang, M. Juszkiewicz, W. H. De Jeu, E. Cerda, T. Emrick, N. Menon, and T. P. Russell, *Capillary wrinkling of floating thin polymer films*, Science **317**, 650–653 (2007). 135, 137

[132] J. Huang, B. Davidovitch, C. D. Santangelo, T. P. Russell, and N. Menon, *Smooth cascade of wrinkles at the edge of a floating elastic film*, Physical review letters **105**, 038302 (2010). 135, 137

[133] C. Gao, E. Donath, S. Moya, V. Dudnik, and H. Möhwald, *Elasticity of hollow polyelectrolyte capsules prepared by the layer-by-layer technique*, The European Physical Journal E **5**, 21–27 (2001). 138

[134] D.-V. Le and K.-H. Chiam, *Hydrodynamic interaction between two nonspherical capsules in shear flow*, Physical Review E—Statistical, Nonlinear, and Soft Matter Physics **84**, 056322 (2011). 148

[135] A. Alexeev, R. Verberg, and A. C. Balazs, *Modeling the interactions between deformable capsules rolling on a compliant surface*, Soft Matter **2**, 499–509 (2006). 148

[136] M. Gross, T. Krüger, and F. Varnik, *Rheology of dense suspensions of elastic capsules: normal stresses, yield stress, jamming and confinement effects*, Soft matter **10**, 4360–4372 (2014). 148

[137] G. Ginot, *Interfacially-controlled soft granular matter: from non-pairwise to elasto-capillary interactions in foams and emulsions stabilised by polymeric skins*, Ph.D. thesis, Université de Strasbourg (2021). 165

Nomenclature

Generalities

g	Gravitational acceleration
t	Time
$\dot{(\,)}$	Derivation with respect to time
$\mathcal{E}$	Free energy
W	Work per surface area
Π	Disjoining pressure
Bo	Bondnumber

Material properties

Φ	Liquid fraction of the continuous phase
Φ_{cat}	Volume platinum catalyst fraction
Φ_{d}	Volume drop fraction of the catalyst-in-PEG emulsion
γ	Interfacial tension
γ_{eff}	Effective interfacial tension
ρ	Volumic density
μ	Liquid viscosity
α	Elastocapillary number
D	Diffusion coefficient
S	Ratio between -H and vinyl groups
K'_{2D}	Dilational elastic interfacial shear modulus
K''_{2D}	Dilational viscous interfacial shear modulus

E	Young's modulus

Geometrical variables

θ	Angle between r(z) profile and the horizontal plane
θ_{c}	Contact Angle between two bubbles or drops
r	Radius in cylindrical coordinates
z	Vertical coordinate in cylindrical and Cartesian coordinates
φ	Angle of cylindrical coordinates
R	Capillary, frame, needle radius
R_{mean}	Average frame radius
u, v	Parametrisation of a surface
A	Surface area
$\vec{r}$	Position vector from a surface
$\vec{n}$	Normal vector of a surface
φ_0	Rotation angle between frames
φ_Γ	Angle between z-axe and Γ_r
φ_F	Angle between z-axe and F_r
a	Neck radius
H	Mean curvature
V	Bubble/drop volume
h	Distance between frames/needles
δ	Film/skin thickness
ω	Rolling angle of cone sections
e	Eccentricity
λ_{long}	Long wrinkle wave length
λ_{short}	Short wrinkle wave length

Loads

Δp	Laplace pressure and more general pressure jump above an interface or skin

γ	Interfacial tension
$\vec{F}$	Force vector
F_r	Force in radial direction on the frame
F_z	Force in z direction on the frame
$\underline{\sigma}$	Real stress tensor
$\vec{\Gamma}$	Moment vector
Γ_z	Moment in z direction on the frame
Γ_r	Tilt moment in radial direction on the frame

Normalisation

$\tilde{(\,)}$	Normalised with the mean curvature with equations...
$\hat{(\,)}$	Normalised with the third rood of the bubble Volume with equations...

Mathematical objects

$\underline{H}$	Hessian matrix
λ	Eigenvalue
$\mathcal{L}$	Lagrangian
$(\,)_{,ji}$	Derivation with respect to j and i
$(\,)_{,j}$	Derivation with respect to j
w	Complex number
$\overline{w}$	Conjugate complex of w

04/11/2024

Des interaction entre bulles et gouttes aux capsules élastiques: analyse de la forme, des propriétés mécanique et de la stabilité

Résumé : La thèse traite des interactions entre les films de savon, les bulles, les gouttes et les capsules. Le lien entre les propriétés mécaniques de l'interface et la réponse mécanique des assemblages de bulles est étudié. La stabilité des différentes formes et les transitions entre ces formes sont analysées en détail. Le premier chapitre utilise la théorie des surfaces minimales pour décrire les films de savon avec des conditions aux limites non axisymétriques proches de la solution axisymétrique de la caténoïde. Le deuxième chapitre considère deux bulles/gouttes ou un pont capillaire maintenu par deux capillaires circulaires coaxiaux. En faisant varier la distance entre les deux capillaires ou le volume des bulles/gouttes/capillaires, on observe une variété de formes et de transitions de forme. Les observations sont étayées par des méthodes théoriques et numériques. Le troisième chapitre traite de la formation et de la caractérisation mécanique d'une peau de polymère à l'interface entre une émulsion de polyéthylène glycol – catalyseur de platine et une huile de silicone réactive. La caractérisation a lieu directement pendant la réaction chimique qui peut donc être suivie dans le temps. Le dernier chapitre étudie les interactions de deux peaux de ce type à l'interface entre deux gouttes d'émulsion.

Mots clés : Surfaces minimales, Catenoide, Surfaces de Delauney, Bulles, Gouttes, Interactions, Elastocapillarite, Polymerisation interfaciale

04/11/2024

From interacting bubbles and drops to soft capsules: shape, mechanics and stability analysis

Abstract : The thesis deals with the interactions of soap films, bubbles, drops and capsules. The mechanical properties of the interface are related to the mechanical response of the shapes. Therefore, the stability of the different shapes and there shape transitions are analysed. The first chapter uses the theory of minimal surfaces to describe soap films with non-axisymmetric boundary conditions close to the axisymmetric solution of the catenoid. The second chapter considers two bubbles/drops or a capillary bridge held by two coaxial circular capillaries. By varying the distance between the two capillaries and the dimensions of the bubbles/drops/capillaries, a variety of tensions, shapes and shape transitions are observed. The observations are supported by theoretical and numerical methods. The third chapter deals with the formation and mechanical characterisation of a polymer skin at the interface between a polyethylene glycol - platin catalyst emulsion and a reactive silicone oil. The characterisation takes place directly during the chemical reaction and can therefore be followed over time. The last chapter considers the interactions of two such skins at the interface between two emulsion droplets.

Keywords : Minimal surfaces, Catenoid, Delauney surfaces, Bubbles, Drops, Interactions, Elastocapillarity, Interfacial polymerisation